Performance Characteristics of Centrifugal Pump Impeller for Heart Failure Therapy: Numerical and In-vitro Approach

Paula Andrea Ruiz Hincapié

Queen Mary
University of London
School *of* Engineering *and* Materials Science

A thesis submitted in fulfilment of the requirements of

The Degree of Doctor of Philosophy

at the University of London

October 2015

Declaration

I hereby declare that this thesis titled

Performance Characteristics of Centrifugal Pump Impeller for Heart Failure Therapy: Numerical and In-vitro Approach

and the work reported herein was composed by and originated entirely from me. Information derived from the published and unpublished work of others has been acknowledged in the text and references are given in the list of sources. This work has not been submitted for any other qualification.

London – 2015 ______________________________

(signature)

To Balazs, Tina and Alexis.

Acknowledgements

Firstly, I would like to thank my supervisor, Professor Theodosios Korakianitis, for allowing me to take on research studies in the field of cardiovascular technologies. Also, to my sponsor the Westfield Trust for supporting my PhD studies.

I also would like to give a special thank you to Dr. Akbar Rahideh for his unconditional support throughout my PhD studies. Also, thanks to Mr Mike Collins and Mr Dennis Ife for the technical guidance and excellent manufacturing skills.

Above all, I am most grateful to my husband, Balazs, whose never ending patience and continuous support kept me going. And, to my parents and sister for their patience and moral support.

Abstract

Heart failure (HF) is a common cause of hospitalisation and mortality across industrialised countries. The number of hospitalisations and deaths attributed to heart failure is increasing, and this trend is predicted to continue. Numerical and in-vitro simulations of the human cardiovascular system constitute the basic tools for enhancing diagnostic and therapeutic technologies for HF and this would in turn, have significant effects on morbidity, mortality, and healthcare expenditure. Mechanical Circulatory Support (MCS) as a destination therapy for HF is rising significantly as it provides a cost-effective alternative to long-term treatment and cardiac transplantation. However, long-term versatility is far from ideal and incidence of transient and permanent neurological events is still high. To this end, evolution of MCS devices calls for more sophisticated design and evaluation methods.

The purpose of this work is to develop a numerical model and to implemented a novel in-vitro model of the cardiovascular system with the intention of evaluating the performance characteristics of a purposely selected centrifugal pump impeller for the treatment of both Class III and IV HF conditions when placed in series with the heart at two different anatomic locations: Ascending Aorta and Descending Aorta.

An existing lumped-parameter model of the CV system, that included models for the heart, the pulmonary and the systemic circulatory loops by adapting a modified version of the fourth-element Windkessel model was enhanced by dividing the systemic circulation into six parallel vascular beds, and by including an autoregulatory system to control both pressures and volumes throughout the system. As part of the novelty of the present work, a volume reflex loop was included with the purpose of simulating volume overload conditions, as commonly found in HF conditions, and obtaining a more realistic analysis of volume displacement, while using a MCS device.

The in-vitro model implemented in this work adopted most of the features included in the mathematical counterpart with the purpose of validating the numerical results. As a result of the combination of models and proper optimisation of the system parameters, predictions of pathophysiological trends and MCS usage are satisfactorily obtained.

The models implemented in this work offer a valuable tool for the selection and performance evaluation of MCS devices for the treatment of HF conditions.

Thesis Supervisor: Prof. Theodosios Korakianitis

Contents

List of Figures

Nomenclature

Greek

α	cardiovascular model vector of parameters, see equation (3.5), page 59
β	Gaussian distribution shape , see equation (3.4), page 55
β	blade angle, see equation (5.7), page 82
Δ	parameter/variable variation , see equation (2.8), page 39
μ	blood viscosity , see equation (3.1), page 50
$\nabla\cdot$	divergence operator, see equation (5.34), page 92
ω	angular velocity , see equation (5.0), page 79
ρ	blood density , see equation (3.2), page 50
σ	Gaussian distribution variance , see equation (3.4), page 55
τ	cardiac cycle period , page 47
θ	circumferential coordinate (or blade wrap angle), see equation (5.14), page 86

Latin

A	area , see equation (5.8), page 82
a	ellipse semi-major axis , page 89

b	blade width , see equation (5.10), page 82
b	ellipse semi-minor axis , page 89
bpm	beats per minute , page 44
C	absolute velocity, see equation (5.3), page 81
C	compliance , see equation (2.12), page 41
D	diameter , page 78
E	elastance, see equation (2.1), page 34
e	elastance action , see equation (2.5), page 37
G	static gain value , page 46
gc	Gaussian distribution peak value location , see equation (3.4), page 55
GGI	general grid interface , see equation (5.55), page 101
gh	Gaussian distribution highest value , see equation (3.4), page 55
gl	Gaussian distribution lowest value , see equation (3.4), page 55
H	pump head, see equation (5.1), page 80
k	valve flow dynamic characteristic, page 35
k_U	impeller entrance pre-rotation constant , see equation (5.4), page 81
L	inertance , see equation (2.11), page 41
l	length , see equation (3.1), page 50
m'	normalized meridional coordinate, see equation (5.17), page 88
N	rotational speed in rpm , page 78

n	number of elements , see equation (3.1), page 50
N_s	pump specific speed , page 90
P	Bezier curve control point, see equation (5.15), page 86
P	pressure, see equation (2.1), page 34
Q	flow , see equation (2.3), page 36
R	resistance , see equation (2.11), page 41
r	radius , see equation (3.1), page 50
rpm	revolutions per minute , page 23
S	distance along meridional curve, see equation (5.16), page 87
s	normalized distance along meridional curve, see equation (5.16), page 87
SF	sigmoid transform scaling factor , see equation (2.13), page 44
T	heart period , see equation (2.6), page 38
t	thickness , page 78
t	time, see equation (2.1), page 34
U	peripheral velocity, see equation (5.1), page 80
V	volume, see equation (2.1), page 34
W	relative velocity , see equation (5.4), page 81
w	valve opening dynamic characteristic , see equation (2.8), page 39
z	axial location, see equation (5.16), page 87
z	number of blade sets, see equation (5.14), page 84

Subscripts

0	nominal value, page 35
1	inlet , page 78
2	outlet , page 78
a	atrium , see equation (2.7), page 38
ac	beginning of atrial contraction phase, see equation (2.7), page 38
af	beginning of atrial filling phase, see equation (2.7), page 38
coil	common iliac artery , page 148
covb	coronary vascular bed , page 148
cvb	cerebralvascular bed , page 148
cvd	cerebral vascular bed , page 61
gfr	glomerular filtration rate , page 62
i	element index , see equation (2.10), page 41
ivc	inferior vena cava , page 60
la	left atrium, page 35
laao	lower abdominal aorta artery , page 148
llvb	lower limb vascular bed , page 148
lv	left ventricle, page 35
m	meridional component, see equation (5.3), page 81
max	maximal value , see equation (2.5), page 37

min	minimal value , see equation (2.5), page 37
par	pulmonary arteriole , page 148
pat	pulmonary artery , page 148
pcp	pulmonary capillary , page 148
ps	blade pressure side , page 89
psv	pulmonary small vein , page 148
pta	pulmonary terminal artery , page 148
pvl	pulmonary venule , page 148
pvn	pulmonary vein , page 148
ra	right atrium, page 35
ref	reference point , page 62
rv	right ventricle, page 35
rvb	renal vascular bed , page 148
rvd	renal vascular bed , page 61
sap	systemic arterial pressure , page 62
sar	systemic arteriole , page 148
sat	systemic artery , page 148
scp	systemic capillary , page 148
se	valve flow ejection speed, page 35
ss	blade suction side , page 89

ssv	systemic small vein , page 148
sta	systemic terminal artery , page 148
svb	splachnic vascular bed , page 148
svb	splanchnic vascular bed , page 61
svc	superior vena cava , page 148
svl	systemic venule , page 148
svn	systemic vein , page 148
tao	thoracic aorta artery , page 148
uaao	upper abdominal aorta artery , page 148
ulvb	upper limb vascular bed , page 148
v	ventricle , see equation (2.6), page 38
vc	beginning of ventricular contraction phase, see equation (2.6), page 38
vf	beginning of ventricular filling phase, see equation (2.6), page 38

Acronyms and abbreviations

AAo	ascending aorta , page 18
ANP	atrial natriuretic peptide , page 12
ANS	autonomic nervous system, page 7
AoPW	aortic pressure waveform , page 71
AoV	aortic valve, page 35
BNP	brain natriuretic peptide , page 12

BTT	bridge to transplant , see equation (1.2), page 16
CHF	congestive heart failure , page 11
CMR	cardiac magnetic resonance , page 53
CNS	central nervous system , page 45
CO	cardiac output, page 7
CV	cardiovascular, page 2
CVP	central venous pressure, page 59
DAo	descending aorta , page 24
DT	destination therapy , page 17
ECF	extracellular fluid , page 14
EDP	end diastolic pressure, page 5
EDV	end diastolic volume, page 5
EF	ejection fraction, see equation (1.2), page 10
ESP	end systolic pressure, page 67
ESV	end systolic volume, page 5
GA	genetic algorithms, page 52
GFR	glomerular filtration rate , page 45
HF	heart failure, page 1
HR	heart rate , page 43
IABC	intra-aortic balloon counterpulsation, see equation (1.2), page 16

IPFM	integral pulse frequency modulator , page 47
ISF	interstitial fluid , page 14
LA	left atrium , page 26
LA-AAo	left atrium to ascending aorta , page 19
LEP	leading edge profile, see equation (5.17), page 88
LV	left ventricle, page 5
LV-AAo	left ventricular apex to ascending aorta , page 18
LVAD	left ventricular assist device , page 18
LVAS	left ventricular assist system , page 18
LVSV	left ventricular stroke volume, page 67
LVSW	left ventricular stroke work, page 67
MAP	mean arterial pressure , page 44
MCD	mechanical circulatory devices , page 33
MCS	mechanical circulatory support, page 2
MiV	mitral valve, page 35
MPAP	mean pulmonary artery pressure , page 74
NYHA	New York Heart Association, page 9
ODE	ordinary differential equation , page 66
PoV	pulmonary valve, page 35
PSP	peak systolic pressure, page 5

PV	pressure-volume , page 33
PWV	pulse wave velocity , page 73
RAA	renin-angiotensin-aldosterone , page 8
RANS	Reynolds-Averaged Navier-Stokes , page 96
RCL	resistance, capacitance and inductance , page 33
REMATCH	randomised evaluation of mechanical assistance for the treatment of congestive heart failure , page 17
RV	right ventricle, page 5
SCVL	simulator of cardiovascular loops , page 107
SV	stroke volume, page 5
TAH	total artificial heart , page 16
TiV	tricuspid valve, page 35
TPR	total peripheral resistance, page 67
US	United States, page 1
VAD	ventricular assist device, see equation (1.2), page 16
VAS	ventricular assist system , page 19

Chapter 1

Introduction

Heart failure (HF) is a common cause of hospitalisation and mortality across industrialised countries. The number of hospitalisations and deaths attributed to heart failure is increasing, and this trend is predicted to continue [1]. Numerical and in-vitro simulations of the human cardiovascular system constitute the basic tools for enhancing diagnostic and therapeutic technologies for HF and this would, in turn, have significant effects on morbidity, mortality, and healthcare expenditure, which in the United Kingdom alone were estimated to be £715.7 millions in 1995 [2]. According to the Heart Disease and Stroke Statistics 2012 Update conducted in the United States (US) [3], an estimated 5.7 million Americans over the age of 20 have HF. It was also reported that in 2010, approximately 6.6 million US adults over 18 years of age had HF, and that by 2030, approximately 3 million people will suffer the condition. The incidence of HF is about 10 per 1000 population beyond 65 years of age, and according to the Framingham study, the most prevalent etiologic precursor is hypertension in 75% of the cases [4]. In both Europe and North America, there are over 7 million HF patients, 60% of whom have systolic dysfunction; 1.2% of whom are younger than 65 years of age amounting to over 200 thousand potential transplant-eligible patients between the two continents.

The present work focuses on enhancing an existing grey-box model of the human cardiovascular (CV) system, developed by Prof. Korakianitis, by including cardiovascular control elements that represent the autonomic nervous system with the purpose of studying the effect of a centrifugal pump connected in-series with the heart while the system was set to mimic a HF condition. It was also the intention of this study to select a centrifugal pump impeller, with a pressure rise of 70 mmHg against a flow of 5 lt/min for an existing centrifugal pump volute and to analyse its effect in a cardiovascular system simulator while concurrently mimicking HF.

This chapter starts by briefly describing the human cardiovascular system and its main functions. It then focuses on the vascular and neuroendocrine mechanisms that influence changes in regional blood flow and sodium/water retention commonly found in HF. Next, it briefly looks into a historical review of heart failure device management and describes some of the available mechanical circulatory support (MCS) devices and their operating conditions. Finally, the chapter presents the motivation of the present study, its aims and objectives, and an outline of the thesis.

1.1 Human cardiovascular physiology

The CV system is composed of three main elements, namely, the heart, vasculature and blood. Its main functions are: to distribute oxygen and nutrients to all body tissues; to unburden the same tissues from carbon dioxide and waste products; to control body temperature [5]. These functions are primordially achieved by the circulation of blood to and from the body tissues.

1.1.1 The heart as a pump

In the average 70-kg man, there are about 5.5 litres of blood composed of plasma and blood cells. Blood is pumped through the vasculature by means of a pulsating motion generated by the heart muscle. The heart muscle or myocardium is composed of striated, multinucleated, slow-rate contracting cells that are linked by intercalated disks forming the muscle mass that makes up the heart [6, 7]. In turn, the heart is made up of two pumps: left- and right-sided pumps, and each of these pumps are in turn composed of two chambers: one atrium and one ventricle. On arrival to the right-sided pump, via the inferior and superior vena cava, blood enters the right atrium (whose main function is to fill or prime the right ventricle) and then flows through the atrio-ventricular valve into the right ventricle, where it is ejected to the lungs for oxygenation. Oxygenated blood returns to the left-sided pump via the pulmonary veins. Once on the left pump, blood is finally ejected to the systemic circulation to supply oxygen to all body tissues. Unidirectional flow through each heart chamber is achieved by four one-way heart (check) valves; these are: mitral, tricuspid, pulmonary, and aortic. The mitral and tricuspid valves are placed at the atrio-ventricular interface, whereas the pulmonary and aortic valves are located at the arterio-ventricular coupling. Fig.1.1 shows the four chambers of the heart and illustrates the pathway of blood flow through the heart.

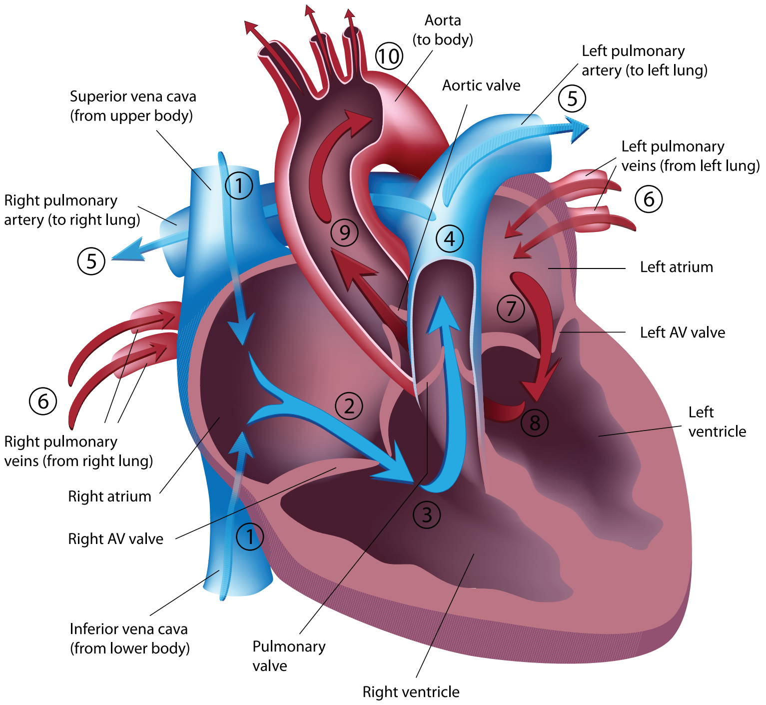

Figure 1.1. The pathway of blood flow through the heart. The arrows and numbers indicate the direction of blood flow. Adapted from Guyton, A. & Hall, J. [6]

1.1.2 Cardiac cycle

The native heart chambers have a very complex functioning and can be widely viewed as having two main phases: systolic and diastolic. Over the duration of a single cardiac cycle, the cardiac chambers have changes in volume and pressure according to the phase in which they are. In broad terms, a systolic phase would be one where contraction of the heart muscle takes place, which translates into an increase in pressure and a decrease of a chamber's volume. A diastolic phase, by contrast, allows for the blood return to take place by increasing the chamber's size; this can be thought of as a suctioning mechanism that draws blood back in. This suctioning event in turn, lowers the chamber's pressure.

Considering a cardiac cycle with a period of 0.9 s and starting from a resting position, the ventricular diastolic phase can be arbitrarily selected as the precursor of the cyclical process. The ventricular diastole starts at the concurrent closing of inlet and outlet heart valves (see point **c** in Fig.1.2), allowing the ventricles to become close chambers and to become ready to initiate the filling process. This event, in which inlet and outlet valves are closed, is known as the isovolumetric relaxation of the ventricles, where volume remains constant and lasts for approximately 0.08 s; this can be viewed in Fig.1.2 being depicted by a light blue band. Once the isovolumetric relaxation has taken place, the atrioventricular valves open (see point **d** in Fig.1.2), initiating the filling process; the atria empty rapidly into the ventricles, producing a sharp fall in pressure denominated as the Y descent. The ventricular filling commonly lasts for 0.5 s and is initially fast-paced up to the point where the ventricular natural relaxed volume is achieved; thereafter, the filling slows down and terminates with an extra blood volume injected by means of the atrial contraction (see the A wave in Fig.1.2) commonly known as the atrial kick or boost. The blood volume at the end of the filling process is known as the End Diastolic Volume (EDV), which is about 110-120 ml on the average 70-kg man; the corresponding End Diastolic Pressure (EDP) is about 9 mmHg in the Left Ventricle (LV) and 4 mmHg in the Right Ventricle (RV). Following the atrial boost, the ventricular contraction takes place. The ventricular systole typically lasts for 0.35 s and is divided into two further phases:

a short isovolumetric contraction phase of about 0.05 s (see light green band in Fig.1.2) and a long ejection phase lasting for approximately 0.3 s. The former is characterised by a simultaneous closure of the inlet and outlet heart valves (see point **a** in Fig.1.2) and and can be identified by the C wave in the atria pressure, allowing for the blood volume to remain constant while increasing the chamber's pressure. The latter is characterised by the opening of the outlet valves (see point **b** in Fig.1.2), by means of the steep increment in pressure in the ventricles with respect to that of the central arteries, creating a rapid ejection; in the atria this can be seen as a sharp fall in pressure denominated as the X descent. Three-quarters of the stroke volume (SV) are displaced into the elastic vessels during this rapid ejection phase. Once the pressure in the ventricle falls below that of the central arteries, the outlet valves close allowing the ventricles to become closed chambers again. In the meantime, the atria have been refilling during the ventricular ejection and are ready to boost the ventricular blood volume, giving rise to a new cardiac cycle [5].

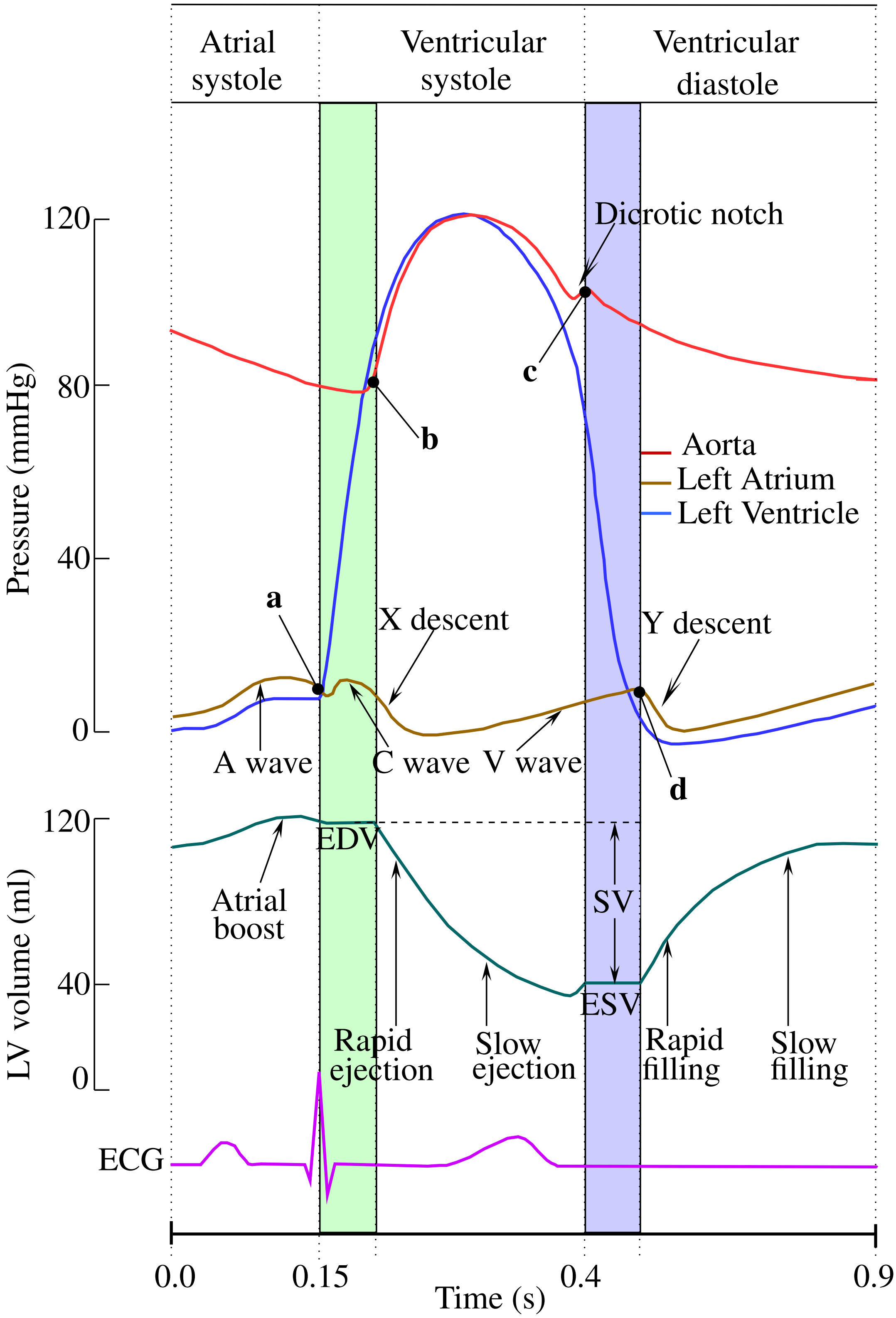

Figure 1.2. Schematic diagram of the human cardiac cycle. Top: Changes in pressure in the aorta artery, the left ventricle, and the left atrium. Bottom: Changes in volume in the left ventricle where EDV, end-diastolic volume; ESV, end-systolic volume; and SV is the stroke volume as given by the difference between EDV and ESV. The electrocardiogram (ECG) signal is shown to provide an indication of the cardiac cycle timings. Adapted from Levick, JR [5]

1.1.3 Cardiac Output Regulation

Cardiac output (CO) is adopted throughout this work as the main haemodynamic variable and measure of cardiac functionality. In general, CO is defined as the amount of blood ejected from the left ventricle into the aorta artery per minute and is modulated by two complex regulatory systems namely, the autonomic nervous system (ANS) and the intrinsic regulation of the heart [6]. The former responds to the local blood flow demands; whereas, the latter responds to the summation of all the local blood flows that converge into the heart, a process that is better known as the venous return. In the 70-kg man, CO is about $5-5.6$ lt/min during resting condition and can increase up to 4 times this amount during exercise, in which oxygen consumption and tissue metabolic rates are increased. In disease conditions such as HF, CO is commonly found to be reduced at about 3.5 lt/min.

1.1.3.1 Autonomic regulation

Regulation of the cardiovascular (CV) system is brought about by a combination of several feedback control mechanisms that are continuously determining the difference between a reference value and an actual one obtained via sensor sites [8]. The mechanical sensors, or mechanoreceptors, responsible for blood pressure regulation are of two types: pressure sensors and volume sensors. The former, better known as baroreceptors, respond to changes in arterial pressure and are located in the left ventricle and central arteries, specially in the carotid sinus and in the renal juxtaglomerular apparatus. The latter are mainly associated with the renal perfusion and the sodium-water homeostasis [9]. Both of these types of sensors are tightly linked to the peripheral resistance that essentially regulates CO; this relationship is an inversely proportional one, that is, at greater levels of peripheral resistance, CO decreases; conversely, at lower peripheral resistance, CO increases. The information gathered at the sensor sites is both conveyed to the central nervous system (CNS), via the afferent pathways, and locally interpreted by the renal juxtaglomerular apparatus. The result is an autonomic reflex that is converged to the CV system via efferent pathways, either parasympathetic or sympathetic, and the activation of the renin-angiotensin-aldosterone (RAA) system according to the required action. In general, locally synthesised angiotensin II regulates vascular function by contracting the arterioles and promoting sympathetic nervous transmission; a sympathetic signal would increase heart rate and contractility as well as modulate the resistance and capacitance of the blood vessels, while a parasympathetic one will oppose the effect of a sympathetic stimulus [6, 10].

The heart is greatly innervated by sympathetic fibres, but scarcely innervated by parasympathetic ones. The latter are mainly found in the atria, where the heart rate modulation centre or sinus node is located, and has as major effect to decrease heart rate as supposed to decreasing contractility.

1.1.3.2 Intrinsic regulation of the heart

In addition to the autonomic regulation, the heart has an intrinsic regulation system, commonly known as the Frank-Startling mechanism, which determines the stroke volume generated per cardiac cycle. This mechanism is entirely controlled by the amount of blood flowing into the heart from the vein reservoir, and holds a linear relationship between the lengthening of the heart muscle due to the amount of returned blood volume and the force of contraction generated by the heart. In other words, the greater the returning blood volume or heart muscle stretch is, the greater the force of contraction is [5, 6, 11]. In a similar linear fashion, increased stretch of the right atrial wall is related to the modulation of heart rate, with the objective of displacing the extra amount of blood entering the heart. Nevertheless, it is worth noting that the intrinsic regulation of the heart is weak when compared to the autonomic one.

1.2 Heart failure

HF can be described as a combination of several symptoms including: shortness of breath, fatigue, and congestion that are brought about by inadequate tissue perfusion, water retention, and elevated ventricular filling pressure [12]. To sustain life, the heart must pump enough blood to supply nutrients for all tissues. In providing this perfusion, the ventricles must generate enough force to overcome the resistance imposed by the systemic and pulmonary circulations; this function can be cleverly described with an electrical analogy by using Ohm's law, in which voltage is equal to the current by the resistance of the circuit, where the voltage is analogue to pressure and current to flow; this relationship can be expressed with the following equation

$$P(t) = Q(t) \times R \tag{1.1}$$

where $P(t)$ is the instantaneous pressure, R is the resistance, and $Q(t)$ is the flow which is commonly known as the cardiac output. Succinctly, HF can be defined as a disability of the left ventricle to fill or empty adequately. This results in decreased cardiac output, initially during exercise and eventually at rest. The neuroendocrine systems respond to this lack of perfusion with regional blood flow vasoconstriction in both the pulmonary and systemic circulations, renal retention of sodium, and pulmonary congestion; this in turn, increases the load required by the heart to eject blood, thereby creating further heart failure [12, 13]

HF patients are commonly classified into 4 categories (I, II, III, IV) with higher class suggesting more severe symptoms, physical activity limitation, and poorer prognosis. In 1928, the New York Heart Association (NYHA) developed this classification system to aid clinicians categorise HF patients based on symptoms as reported by the patient, medical history and cardiac performance tests [14]. Table 1.1 summarises the NYHA functional classification system.

In advanced HF or NYHA class IV the typical clinical findings include: severe congestion

Table 1.1. Functional classification system by The New York Heart Association [15]

Class	functional classification
I	Patients have cardiac disease, but without the resulting limitations of physical activity. Ordinary physical activity does not cause undue fatigue, palpitation, dyspnoea or anginal pain
II	Patients have cardiac disease resulting in slight limitation of physical activity. They are comfortable at rest. Ordinary physical activity results in fatigue, palpitation, dyspnoea, or anginal pain
III	Patients have cardiac disease resulting in marked limitation of physical activity. They are comfortable at rest. Less than ordinary physical activity causes fatigue, palpitation, dyspnoea, or anginal pain
IV	Patients have cardiac disease resulting in inability to carry out any physical activity without discomfort. Symptoms of cardiac insufficiency or anginal syndrome may be present even at rest. If any physical activity is undertaken, discomfort is increased

associated with reduced left ventricular ejection fraction (EF) and pulmonary hypertension in addition to unresponsive pharmacotherapy [13]. A further subcategory is applied to NYHA class IV patients according to their systolic function as having a reduced or preserved systolic function. In the work by Dauterman et al. [16], a reduced systolic function is defined by an ejection fraction that is lower than 40%, where ejection fraction relates the ejected blood volume to the diastolic blood volume and can be expressed by the following equation

$$\mathrm{EF} = \frac{\mathrm{EDV} - \mathrm{ESV}}{\mathrm{EDV}} \tag{1.2}$$

where EDV is the end diastolic volume and ESV is the end systolic volume.

1.3 Autoregulation in HF

Patients with HF have raised blood levels of neurohormonal factors, including: norepinephrine, angiotensin, aldosterone that are detrimental in the progression of HF. These factors have direct and indirect effects on the heart. Indirectly, they alter the structure and function of the heart in response to sodium retention and peripheral vasoconstriction; and directly, they alter the myocytes performance and phenotype [17]. Important changes take place in the cardiovascular system in response to HF. These changes are brought about by activation of the neurohormonal systems that regulate fluid volume and vascular tone. The activation of these systems may be attributable to abnormal baroreceptor function which is a feature commonly found in HF patients [13]. Blunted baroreceptor sensitivity in HF is associated with, increased circulating catecholamines and renal sympathetic activity in addition to parasympathetic withdrawal [9, 18]. In patients with congestive heart failure (CHF), the increased sympathetic activity is reflected on high plasma concentrations of norepinephrine; moreover, greater the concentration, more severe the disease [19]. In general, a decrease in myocardial contractiliy leads to a decrease in cardiac output and blood pooling; concurrently, the fractional CO distribution to renal, limb and splachnic systems decreases [20]. Disrupted renal hemodynamics, particularly low renal perfusion contributes to sodium and water retention in response to the release of strong vasoactive substances such as renin [21–23]. By contrast, blood flow to the brain and heart is preserved; nevertheless, in patients with low ejection fraction (EF), cerebral autoregulation may be impaired by high levels of circulating catecholamines [18, 24].

The kidneys play a very important role in the control of systemic blood pressure. This control is mediated by either regulating the extracellular fluid volume or modifying the vascular tone. In low perfusion conditions such as CHF, arterial pressure is controlled by increasing contraction of systemic arterioles [10, 25]. This vasoconstriction is the result of the activation the renin-angiotensin system, which in turn acts on the kidneys to cause sodium (Na^+) and water retention. Angiotensin plays another crucial role in the development of HF; it causes the adrenal glands to secrete aldosterone and this in turn increases salt and water reabsorption by the kidney's tubules, thus increasing extracellular Na^+ [18]. From this point onwards, a negative feedback loop is initiated in an attempt to maintaining extracellular Na^+ homeostasis; the resulting effect is the increased in total blood volume leading to further congestion; see the flowchart presented in Fig.1.3 for a summary of the effect of the RAA system in response to hypoperfusion in CHF. In patients with CHF, increased activity of the RAA system is known to directly correlate with mortality [26].

Similar to the kidneys, the heart produces a family of vasoactive peptides that have important effects on cardiovascular and renal functions. Two main types of peptides are produced by the heart; these are: atrial natriuretic peptide (ANP) and brain natriuretic peptide (BNP). ANP is chiefly synthesised by atrial myocytes whereas BNP is primarily produced in ventricular tissue, although a small proportion of BNP is produced by the atrial myocytes [27].

ANP is released in a prompt response to atrial wall stretch or mechanical strain from increased blood volume, whereas BNP is released within an hour from the initial wall stretch [28]. In normal conditions, the natriuretic peptides have a vasodilator effect on blood vessels; however, in HF patients, this effect is markedly blunted; what is more, ANP and BNP plasma levels are increased in HF patients and this is directly related with the severity of HF [27]. Other functions of the natriuretic peptides include: myocardial and vascular remodelling, regulation of myocardial perfusion [28].

1.3.1 Body Fluid Volume Regulation

Sodium and water retention are hallmarks of HF [18]. Regulation of sodium and water excretion, hence total body fluid volume, is mainly attributed to the arterial-tree fluid compartment, which is responsible for the perfusion of vital organs. In the average 70-kg man, the total body fluid volume is about 42 lt, 1.7% of which resides in the arterial compartment whereas over 60% is found in the veins. This can only imply that body fluid volume homeostasis is regulated by the smallest fluid compartment, further imply-

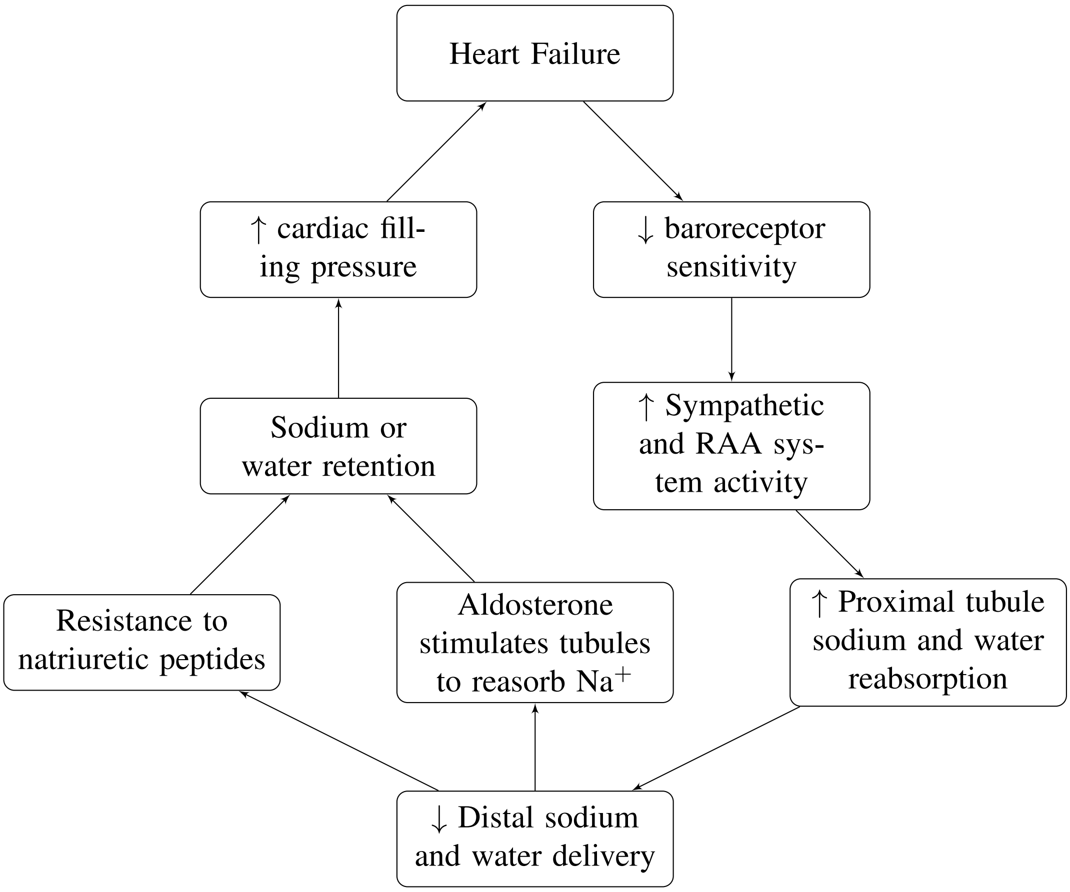

Figure 1.3. The Heart failure vicious cycle. Decreased baroreceptor sensitivity in HF patients promotes further cardiac failure by triggering the RAA system and sympathetic activity; concurrently, raised aldosterone level promotes a negative feedback loop for the extracellular Na^+ homeostasis; this in turn, results in fluid retention and blunted response to natriuretic peptides. Adapted from Schrier et al. [18].

ing that the system is over sensitive to small changes in fluid volume [26]. Increased fluid volume can increase cardiac pre-load, and ultimately create cardiac dilation and myocardial remodelling, heart valve insufficiency, especially of the mitral valve, and promote pulmonary hypertension [18]. Until recently, it was uncertain whether renal dysfunction promotes the progression of HF or whether it reflected the severity of the condition. The data published by Dries et al [29], suggested that impaired renal function is independently associated with all-cause mortality in patients with mild to moderate heart failure. However, other studies suggested that worsening renal function occurs often among elderly patients admitted with heart failure and this was in turn associated with higher mortality, increased length of stay, and higher costs [30]. It is now recognized that renal dysfunction is an important predictor of morbidity and mortality in HF [18, 30, 31].

The kidneys play a major role in the regulation of blood pressure, both via pressure and body fluid volume control mediated by pressure sensors. High-pressure receptors, located in the juxtaglomerular apparatus within the kidney's afferent arterioles, respond to decreased renal perfusion commonly found in CHF by activating the sympathetic and RAA systems in an attempt to increase the arterial pressure by promoting further sodium and water retention [21–23, 32, 33]. In addition to the regulating factor brought about by the kidneys, stretch receptors in the left atrium and pulmonary veins respond to intravascular volume expansion by releasing ANP [9, 34, 35]. These two regulating systems are commonly known as the atrial-renal sympathetic reflex and have been found to have a direct correlation between left atrial pressure and renal sodium excretion in the dog [34]; however, this reflex is blunted in CHF [36, 37]. The experiments carried out by Volpe et al., citeVolpe1991, showed that cardiorenal and hormonal regulation, in response to acute volume expansion, are critically diminished in patients with dilated cardiomyopathy and mild heart failure; particularly, the inability to increase plasma ANP levels in response to an acute rise of cardiac preload. While plasma ANP levels were almost doublefold in normal subjects, in those with dilated cardiomyopathy there was no increase, thus confirming previous observations of impaired ANP activity obtained in animal models of acute and chronic congestive heart failure [37]

Table 1.2. Body Fluid Volume Distribution [26].

Compartment	Amount	Volumes in 70-kg Man
Total body fluid	60% of body weight	42 lt
Intracellular fluid	40% of body weight	28 lt
Extracellular fluid (ECF)	20% of body weight	14 lt
Interstitial fluid (ISF)	2/3 of ECF	9.4 lt
Plasma fluid	1/3 of ECF	4.6 lt
Venous fluid	85% of plasma fluid	3.9 lt
Arterial fluid	15% of plasma fluid	0.7 lt

1.4 Mechanical Circulatory Support

The two main therapeutic modalities for managing advanced HF are pharmacotherapy and cardiac transplantation. Cardiac transplantation remains the gold standard therapy for class-IV patients; however, the great immunosuppression hurdle and the organ donation not meeting the high demand make this therapy the most limited of them all [38]. Current pharmacotherapy can alleviate HF symptoms [12] and can even be successful in terms of life expectancy [39]; however, in many cases, HF remains refractory to pharmacotherapy, especially in advanced cases. In these cases, MCS therapy could prove beneficial. Over the last three decades, MCS therapy has evolved enormously and is currently considered as a standard one in many industrialised countries [40]. The MCS therapy goals span from relief of circulatory congestion symptoms and increasing tissue perfusion to prolonging life by slowing or even reversing both structural damage and blunted neurohormonal mechanisms [12, 38]. Nowadays, there is a wide selection of MCS devices allowing for an adequate selection of treatment according to duration and level of support. In general, short-term devices may be used to support patients during heart surgery or even to reverse mild HF brought about by myocardial infarction, while long-term devices are mainly used in advanced HF stages as a bridge to cardiac transplantation and even as destination therapy [41].

1.4.1 Heart Failure Device Management: brief historical review

The first clinical usage of MCS therapy was done in 1953 during a cardiopulmonary bypass by implementing a heart-lung machine. From this point onwards, several therapies were developed for different cardiac disorders; however, special interest was focused in enhancing circulatory support technologies [42]. The starting point for today's MCS devices was led by several researchers including Dr John H. Gibbon Jr., who pioneered the extracorporeal circulation machine usage in open heart surgery [43].

In 1960, counterpulsation techniques were studied and developed by Masopuolos et al.

[44]; they mainly consisted of inflating an elongated balloon inserted in the aorta via a small calibre catheter during diastole and deflating it during systole. This technique is still the most widely used, mainly because it is minimally invasive and operates in-series with the native heart. Although this technique does not cause haemolysis, it cannot be used in patients with aortic dissection, aortic valve regurgition, amongst other conditions. The most noteworthy limitation of the Intra-Aortic Balloon Counterpulsation (IABC) technique is that it is not beneficial when systolic aortic pressure is lower than 60 mmHg [44].

In 1963, BeBakey et al. [43] implanted a pulsatile ventricular assist device (VAD) consisting of a double-lumen silicon elastomer tube reinforced with polyethylene terephthalate fibre (Dacron), with a compressible silicone elatomer blood chamber actuated by pressurised air and ball valves at inlet and outlet ports to ensure unidirectional flow.

In 1969, the first clinical bridge to transplant (BTT) was performed swhen a critically ill 47-year old man was implanted with a total artificial heart (TAH). The device consisted of two diaphragm pumps pneumatically driven by an extracorporeal control console. The patient was successfully supported for a period of 64 hours while waiting for a donor heart to be transplanted [45].

In 1978, a patient with acute bacterial endocarditis was implanted with an intracorporeal partial artificial heart for almost 6 days while waiting for a donor heart. The device was implanted in the abdominal region [46, 47].

In 1979, utilization of a nonpulsatile biventricular bypass research on animals was reported by Nosé et al. at the Cleveland Clinic Foundation [48]. However, for the next 20 years, mechanical cardiac assistance development remained focused on pulsatile perfusion devices. In 1982, the implantation of a permanent total artificial heart (TAH) was performed by William DeVries. The implanted TAH was the Jarvik-7 designed by Robert Jarvik. During implantation time, the incidence of infection and embolic events were 36% and 9%, respectively; moreover, the 1-year survival rate for all patients receiving the Jarvik-7 was only 37% [49].

In 1990s, the axial-flow-device generation emerged increasing versatility and reliability over their pneumatic counterpart. In the same decade, the European and US regulatory bodies approved the use of the first BTT device. A decade later, the US Food and Drug Administration (FDA) approved the first device for destination therapy (DT) as a result of the Randomised Evaluation of Mechanical Assistance for the Treatment of Congestive Heart Failure (REMATCH) trial, which compared optimal medical management with long-term use of LVADs for patients with NYHA class IV HF who were ineligible for orthotopic heart transplantation [38, 50].

1.4.2 Continuous vs. Pulsatile Flow Circulatory Support

Over the last three decades, MCS devices have significantly varied in both type and number; in general, they can be subdivided into two categories: pulsatile-flow and continuous-flow devices. The former are mainly pneumatic devices with several moving parts while the latter are mainly rotary devices, either axial or centrifugal pumps, with a single moving component. The continuous-flow devices offer several advantages over the pulsatile ones including: minimisation of thrombus formation and bacterial growth due to lack of blood pooling; shorter implantation periods and less invasive surgical procedures; greater durability and reliability [51]. Table 1.3 summarises the main pulsatile-flow and continuous-flow devices.

1.4.2.1 HearMate XVE

The HeartMate XVE is an FDA-approved pulsatile Left Ventricular Assist Device (LVAD) device indicated to NYHA class IV patients use as a BTT or DT [52]. It consists of a flexible polyurethane diaphragm bonded to a pusher plate, which is actuated by compressed air. The inflow and outflow conduits are both made out of woven Dacron with a 25-mm diameter porcine xenograft heart valve in each of them for adequate unidirectional flow [53]. Implantation is performed with the patient under total cardiopulmonary bypass. The pump housing is placed inside or outside the peritoneal cavity, just bellow the left diaphragm, in a left ventricular apex to ascending aorta (LV-AAo) bypass configuration; see Fig.1.4. The maximum stroke volume is 83 ml corresponding to a pressure rise of 100 mmHg [53].

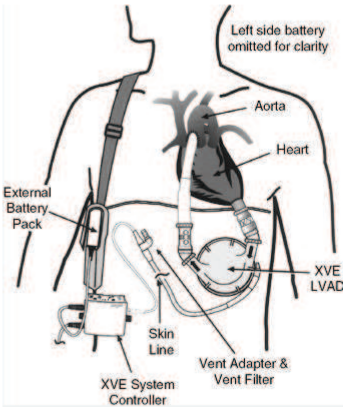

Figure 1.4. Schematic of the HearMate XVE placement in the human body. From [52]

1.4.2.2 Novacor LVAS

Novacor (Baxter Healthcare Corp) is a pulsatile Left Ventricular Assist System (LAVS) that completely takes over the LV workload. The pump consist of a polyurethane diaphragm, actuated by compressed air via two pusher plates, and a 21-mm diameter bioprosthetic heart valve to ensure unidirectional flow [42]. The drive unit is implanted in the abdominal wall just below the diaphragm. The system is connected in parallel to the native system in a LV-AAo configuration, see Fig.1.5, while the patient is under cardiopulmonary bypass [54]. The drive-line exits through the abdominal wall and it is then connected to the external control unit.

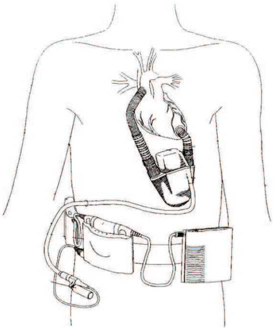

Figure 1.5. Schematic of the Novacor placement in the human body. From [55]

1.4.2.3 Thoratec VAS

Thoratec is a paracorporeal Ventricular Assist System (VAS) that can be used for univentricular or biventricular support. It consists of a pneumatically driven polyurethane sac within a polycarbonate housing. The inflow and outflow cannula have tilting-disk valves to achieve unidirectional flow. It has a maximum stroke volume of 65 ml and can be operated at a maximum flow of 6.5 lt/min with a corresponding pressure rise of 100 mmHg [42, 56]. The implantation technique is via median sternotomy with cardiopulmonry bypass in most cases. For LV support, the system is implanted in a LV-AAo or left atrium appendage to ascending aorta (LA-AAo) bypass configuration. For RV support, a right atrium appendage to the main pulmonary artery (RV-Pa) bypass configuration is implemented. The inflow and outflow conduits exit below the rib cage (subcostally) to be attached to the pump(s) [42], see Fig. 1.6.

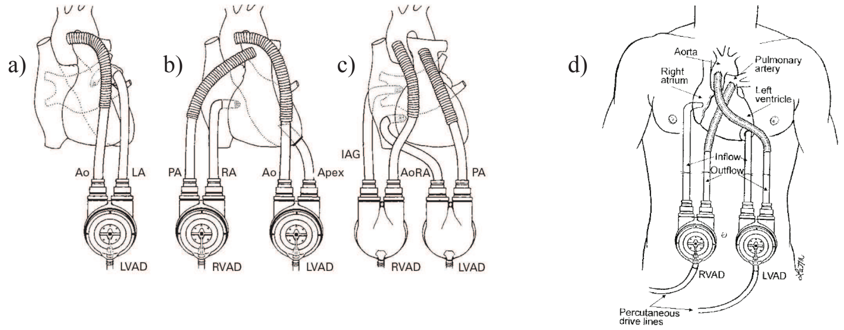

Figure 1.6. Thoratec VAS: a) Univentricular leaft heart support; b) and c) biventricular support. From [56]; d) Schematic of the Thoratec VAS placement in the human body. From [42]

1.4.2.4 MEDOS VAD

The MEDOS VAD is a paracorporeal pneumatically driven MCS device for children. The system is available in three different sizes of 10, 25, and 60 ml maximum LV stroke volume. It is made of polyurethane and allows visualisation of the filling and emptying processes while observing for any unwanted air during installation or clot formation while in prolonged usage; see Fig.1.7. The inflow and outflow conduits are fitted with trileaflet valves to ensure unidirectional flow [57]. The pump can generate pressures between 300 mmHg and -80 mmHg at a maximum rate of 180 beats/min [57]. The implantation technique is via median sternotomy with cardiopulmonry bypass. For LV support, the inflow conduit is sewn to the right superior pulmonary vein and exits through the superior abdominal wall (right epigastrium), while the outflow conduit is internalised through the left epigastrium and sewn to the aorta.

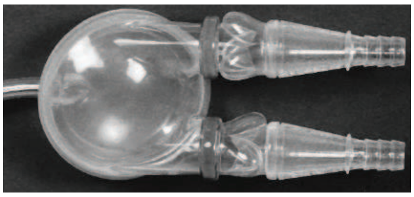

Figure 1.7. 60-ml sized MEDOS VAD for left ventricular support. From [57]

1.4.2.5 CardioWest TAH

The CardioWest Total Artificial Heart (TAH) is a pulsatile biventricular heart replacement system. It consists of a polyurethane membrane actuated pneumatically, the outlets of each chamber house a Medtronic-Hall mechanical heart valve to ensure unidirectional flow. After removal of both native ventricles, the CardioWest is implanted within the mediastinal space [42, 58]; see Fig.1.8. It weighs 160 g and displaces 400 ml of volume. It has a maximum stroke volume of 70 ml and can deliver up to 9 lt/min.

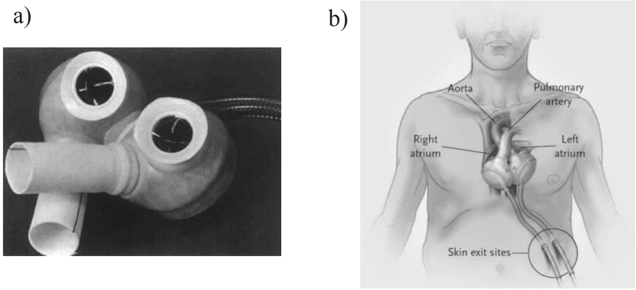

Figure 1.8. The Incor (Berlin Heart) axial flow pump: a) Actual device displaying the pump cradled between inlet and outlet elbow connectors; b) Schematic of the CardioWest TAH placement in the human body. From [58]

1.4.2.6 HeartMate II LVAS

The HeartMate II LVAS (ThermoCardiosystems, Inc, Woburn, MA) is an axial flow rotary VAD composed of a blood pump, percutaneous lead, and external power and system driver designed for long-term use. It is implanted in the abdominal wall or preperitoneally in a LV-AAo bypass configuration; see Fig.1.9. The pump features a single moving part, a 3-bladed rotor that spins on two ball-and-cup bearings. It operates at rates of $8,000-9,000$ rpm with pressure differentials of $80-100$ mmHg with corresponding flows of $3-4$ lt/min [59].

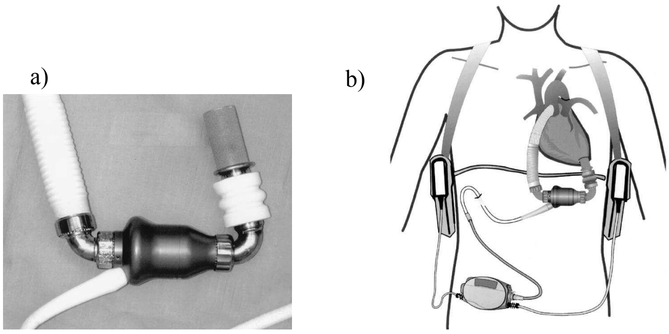

Figure 1.9. The HeartMate II VAD axial flow pump: a) Actual device displaying the pump cradled between inlet and outlet elbow connectors; b) Schematic of the CardioWest TAH placement in the human body. From [59]

1.4.2.7 MicroMed DeBakey VAD

The MicroMed DeBakey is an electromagnetically actuated, implantable axial flow pump. It consists of a titanium inflow conduit, a housing containing the rotor and a motor, and a vascular graft outflow; all internal components have a total weight of 93 g. The pump is designed to operate at a flow of 5 lt/min corresponding to a pressure rise of 100 mmHg at a speed of 10,000 rpm. The implantation technique is via median sternotomy and cardiopulmonary bypass; the pump is housed in a small preperitoneal pocket and is attached to the native circulation in a LV-AAo bypass configuration; see Fig.1.10. The drive-line exits the abdominal wall at the left lower quadrant to be connected to the controller [60]. Ongoing improvement and optimisation of the MicroMed DeBakey VAD resulted in the design of the HeartAssit 5™ [61].

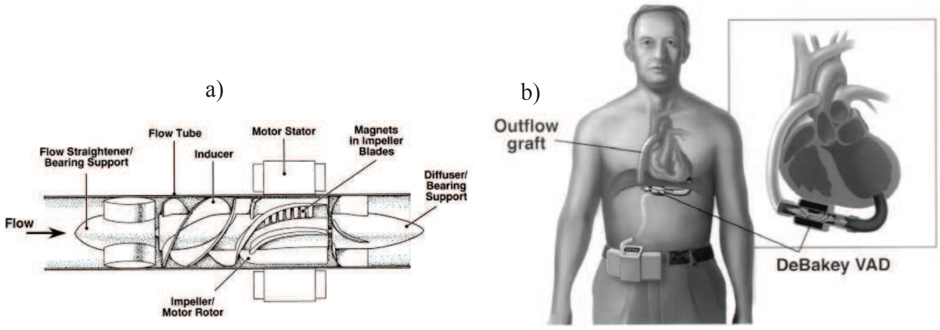

Figure 1.10. DeBakey VAD axial flow pump: a) Schematic of the essential components of DeBakey/-NASA axial flow pump; b) Schematic of the CardioWest TAH placement in the human body. From [62]

1.4.2.8 Jarvik 2000 VAS

The Jarvik 2000 is an electromagnetically actuated, implantable axial flow pump with a single rotating part held in position by two ceramic bearings, designed for either DT or BTT [63, 64]. It consist of a 16-mm outflow graft, a blood pump, a speed controller, a percutaneous power cable, and a direct-current power supply. It can operate at $8,000-12,000$ rpm generating an average flow rate of $3-6$ lt/min. The implantation technique is via left thoracotomy or sternotomy with partial cardiopulmonary bypass. The pump is placed within the LV through the apex while the outflow conduit may be placed in either the ascending or descending aorta [63], see Fig.1.11.

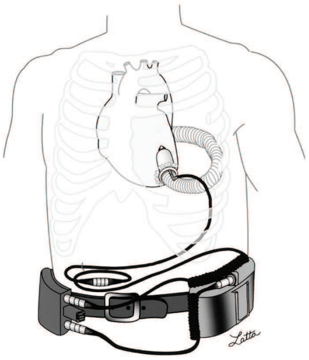

Figure 1.11. Schematic of the Jarvik 2000 VAS placement in the human body. From [63]

1.4.2.9 Incor

The Incor (Berlin Heart AG, Berlin) is an axial flow pump that weights about 200 g, 30 mm in diameter and can rotate at speeds of up to $10,000$ rpm, which corresponds to a blood flow of 7 lt/min against a pressure rise of 150 mmHg. The impeller is held by a magnetic bearing and has no physical contact with any other parts of the system. The implantation technique is via median sternotomy supported with extracorporeal circulation and is placed in a LV-AAo bypass configuration, see Fig.1.12. The inflow conduit, made out of silicone, is inserted and fixed via a Dacron ring to the left ventricular apex. The pump housing is placed in the pericardial cavity, while its drive-line exits through the abdominal wall. The outflow conduit, made out of silicone, is sutured to the ascending aorta [65].

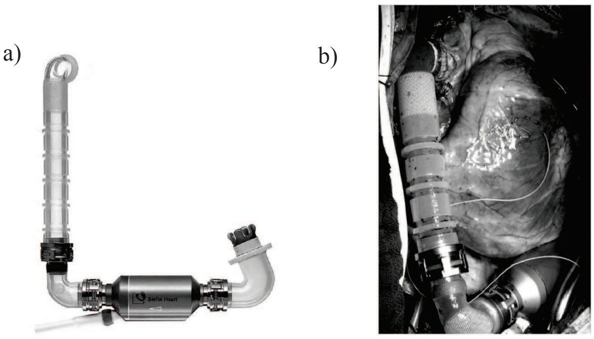

Figure 1.12. The Incor (Berlin Heart) axial flow pump: a) Actual device displaying the pump cradled between inlet and outlet elbow connectors. From [66]; b) Intraoperative view of the inserted device. From [65]

1.4.2.10 HeartWare (HVAD)

The HeartWare VAS is designed to support a dysfunctional LV. It consists of a 21-mm diameter inflow conduit, a centrifugal blood pump (registered as the HVAD$^{®}$ pump), an outflow graft, a percutaneous drive-line and an external controller; the implantable parts weigh a total of 160 g. The drive-line cable features a tissue in-growth polyester fabric. The impeller is the only moving component suspended by magnetic and hydrodynamic forces; it rotates at about $1,800-4,000$ and can generate flow rates up to 10 lt/min. The small size of the inflow conduit and pump housing allow for pericardial placement without the need for abdominal pockets. The HeartWare® is implanted via median sternotomy and cardiopulmonary bypass. The device is placed in a LV-AAo or a LV-DAo bypass configuration, see Fig.1.13. The driveline is externalised through the right upper quadrant of the abdomen [67, 68].

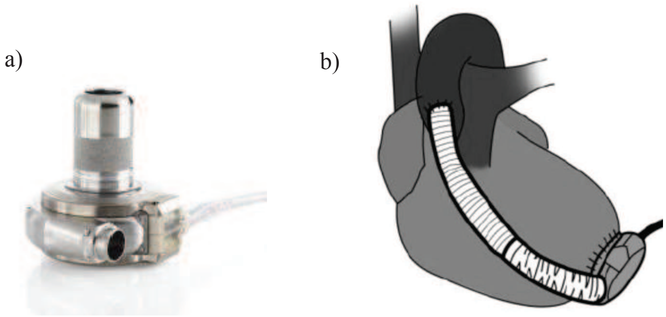

Figure 1.13. The HeartWare® VAS: a) Actual device displaying the inflow conduit and housing; b) Schematic of the placement in the native heart. From [68]

1.4.2.11 DuraHeart LVAS

The DuraHeart (Terumo Heart, Inc., Ann Arbor, Michigan, USA) is the first approved magnetically supported LVAS for long-term circulatory support. It consists of an inflow conduit, a centrifugal pump, an outflow conduit and an external controller. The impeller is the only moving part and is suspended by three electromagnets; hence it neither requires a rotating shaft or shaft seals. The DuraHeart™ can generate flows up to 8 lt/min corresponding to a pressure rise of 120 mmHg. It can operate in a wide pressure range from 50 mmHg at $1,200$ rpm to 180 mmHg at $2,400$ rpm. The DuraHeart™ benefits from drug-eluting blood contacting surfaces to reduce the risk of thrombus formation. The device is implanted via median sternotomy and cardiopulmonary bypass in a LV-AAo bypass configuration; see Fig.1.14.

1.4.2.12 VentrAssits LVAD

VentrAssist is a third-generation implantable rotary LVAD designed for long-term circulatory support. It consists of inflow and outflow conduits, a centrifugal pump, a percutaneous lead, and a controller. The impeller is the only moving part, composed of

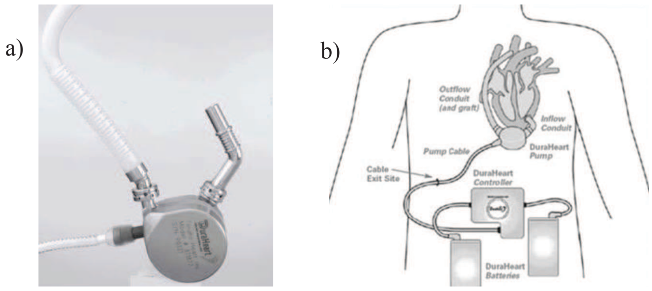

Figure 1.14. The DuraHeart$^{\text{TM}}$ LVAS: a) Actual device displaying the pump cradled between inlet and outlet elbow connectors; b) Schematic of the DuraHeart$^{\text{TM}}$ placement in the human body. From [69]

four blades with embedded permanent magnets, which are suspended by hydrodynamic bearings; it rotates at $1,800-3,000$ rpm in the normal setting [70, 71]. The device is implanted via median sternotomy and cardiopulmonary bypass in a LV-AAo bypass configuration; see Fig.1.15. The pump is placed in a pocket bellow the diaphragm. The VentrAssits features a diamond-like carbon coating in the blood contacting surfaces to reduce the risk of platelet activation and hence thrombus formation [71].

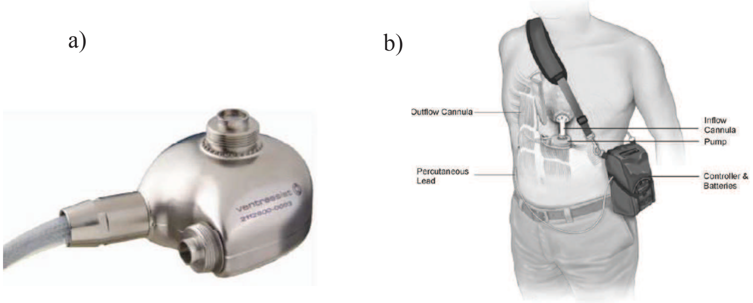

Figure 1.15. The VentrAssits$^{\text{TM}}$ LVAS: a) Actual device displaying the pump titanium housing and silicone percutaneous lead; b) Schematic of the VentrAssist$^{\text{TM}}$ placement in the human body. From [71]

1.4.2.13 Levacor LVAD

The Levacor LVAD, formerly ‘HeartQuest’, is a third generation implantable radial flow pump. It is designed for long-term circulatory support in BTT and DT applications. The impeller is magnetically suspended reducing wear. The device can generate flows ranging from $0-10$ lt/min [72].

1.4.2.14 EVAHEART LVAS

The EVAHEART is a third generation implantable LVAS designed for long-term circulatory support. The impeller rotates on a shaft supported with hydrodynamic journal bearings that are lubricated with water. The device is implanted in a LV-AAo bypass configuration. Flows over 12 lt/min with a corresponding pressure rise of 100 mmHg are achieved at $2,600$ rpm [73, 74].

1.4.2.15 Synergy Pocket Micro-pump

Synergy Pocket Micro-pump (CircuLite®) is an axial implantable micro blood pump designed to partially support the ventricles in patients with advanced heart failure who are not eligible for implantation with a contemporary full support LVAD. It consists of a nitinol reinforced silicone inflow cannula, a pump, an 8-mm polytetrafluoroethylene outflow graft, a driveline and a controller. The device is implanted via mini-thoracotomy; the distal end of inflow cannula is guidewired into the left atrium (LA), while the proximal end of the inflow cannula exits through the second intercostal space to meet the main body of the pump already placed in a small subcutaneous pocket. The outflow graft is anastomosed to the subclavian artery. The driveline exits through the upper right quadrant of the abdomen. The pump operates at speeds as high as $22,000-24,000$ corresponding to a flow of approximately 3 lt/min [75, 76].

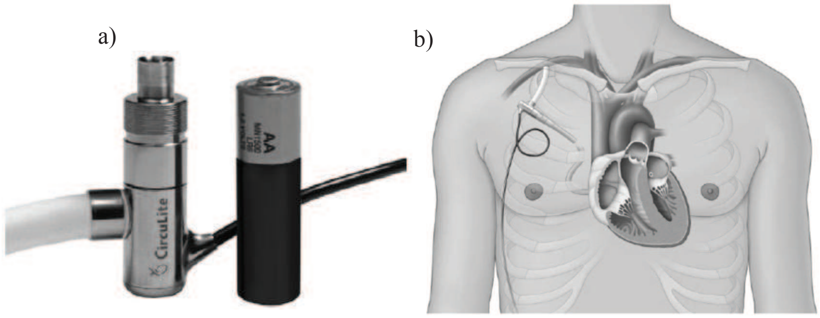

Figure 1.16. The Synergy Pocket Micro-pump LVAS: a) Actual device being compared in size to an AA battery. From [77]; b) Schematic of the Synergy placement in the human body. From [76]

Table 1.3. Continuous-flow and pulsatile-flow devices

Device	**Pump mechanism**	**Revolutions per minute**	**Q (Lt/min)**	**ΔP (mmHg)**	**Implantation site**	**Type of support**	**EU approvals**	**FDA approvals**	**Reference**
HeartMate XVE	Electromechanically driven; Opposing pusher plates	NA	2-10	100	LV-AAo; external drive	LVAD	CE Mark	BTT, DT	[52, 53, 78]
Novacor	Electromechanically driven; Opposing pusher plates pneumatically actuated	NA	2-5	-	Pre-peritoneal pocket with external control unit; LV-AAo	LVAD	CE Mark	BTT, DT	[42, 54]
Thoratec	Pneumatic (diaphragm pump)	NA	5.0 ± 0.9	100	Paracorporeal; LV-AAo or LA-AAo	BiVAD or UniVAD	CE Mark	PC, BTT	[42, 56]
MEDOS VAD	Pneumatic (diaphragm pump)	NA	LV: 10, 25 & 60 ml; RV: 9, 22.5 & 54ml	$-80-300$	Paracorporeal	BiVAD or UniVAD	CE Mark	-	[57]
CardioWest TAH	Pneumatic (diaphragm pump)	NA	< 9 lt/min	-	Mediastinal space, requires excision of both ventricles	Total	CE Mark	BTT	[58, 79]

Table 1.3. Continuous-flow and pulsatile-flow devices

Device	Pump mechanism	Revolutions per minute	Q (Lt/min)	ΔP (mmHg)	Implantation site	Type of support	EU approvals	FDA approvals	Reference
HeartMateII	Internal axial pump; ball-and-cup bearings; external system driver	8,000 – 9,000	3 - 4	80 - 100	LV-AAo	LVAD	CE Mark	BTT DT	[42, 59, 78, 80]
MicroMed DeBakey	Axial pump	10,000	5	100	LV-AAo	LVAD	CE Mark	BTT DT	[60, 62]
HeartAssist 5	Axial pump; blood-immersed bearings	7,500 – 12,500	3-10	50-150	LV-AAo	LVAD	CE Mark	IDE trial ongoing for BTT	[61, 81]
Jarvik2000	Axial pump; ceramic bearings	8,000 – 12,000	3-6	70-74	Intraventricularly postioned and anastomosed to the AA	LVAD	CE Mark	IDE trial ongoing for BTT	[63, 64, 82]
Incor	Axial pump; magnetic bearing	6,000 – 7,000	4-5	150	LV-AAo	LVAD	CE Mark	IDE trial ongoing for BTT	[65, 83]

Table 1.3. Continuous-flow and pulsatile-flow devices

Device	Pump mechanism	Revolutions per minute	Q (Lt/min)	ΔP (mmHg)	Implantation site	Type of support	EU approvals	FDA approvals	Reference
HeartWare (HVAD)	Centrifugal pump; hydrodynamic bearing	1,800 – 4,000	3 - 8	-	Pericardial space; LV-Ao or LV-DAo; percutaneous driveline	BiVAD or UniVAD	CE Mark	IDE trial ongoing for BTT	[67, 68]
DuraHeart LVAS	Centrifugal pump; bearingless; magnetically levitated impeller	1,200 – 2,400	8 Lt/min (120 mmHg)	50 - 120	LV-AAo	LVAD	CE Mark	IDE trial ongoing for BTT	[69]
Levacor LVAD	Centrifugal pump; bearingless magnetically levitate impeller	2,500	6.5	100		LVAD	CE Mark trials terminated	IDE trial for BTT terminated	[72]
EVAHEART LVAS	Centrifugal pump	2,600	12	100	Pre-peritoneal pocket; LV-AAo	LVAD	Complete trial in Japan; PMDA pending	IDE trial for BTT	[73, 74, 84, 85]

Table 1.3. Continuous-flow and pulsatile-flow devices

Device	Pump mechanism	Revolutions per minute	Q (Lt/min)	ΔP (mmHg)	Implantation site	Type of support	EU approvals	FDA approvals	Reference
VentrAssist LVAD	Centrifugal pump; hydrodynamic suspended rotor	$1,800 - 3,000$ rpm	4.8	125	Left sub-diaphragmatic pocket; LV-AAo	BiVAD or UniVAD	CE Mark	IDE trial for BTT	[70, 71]
CircuLite Synergy	Axial pump; magnetic bearing	$22,000 - 24,000$	~ 3	-	Subcutaneous placement; LA-SA	PVSD	CE Mark trial ongoing	IDE pilot trial initiated in 2013 for BTT and DT	[75, 76]

AAo, ascending aorta; LA-AAo, Left atrium to ascending aorta bypass configuration; BiVAD, biventricular assist device; BTT, bridge to transplant; CE Mark, conformity mark in European Economic Area; DT, destination therapy; FDA, Food and Drug Administration; IDE, investigational device exemption; LA-SA, Left atrium to subclavian artery bypass configuration; LV-AAo, Left Ventricle apex to Aorta bypass configuration; LVAD, left ventricular assist device; LV-DAo, Left Ventricular apex to descending aorta bypass configuration; PC, post-cardiotomy; PMDA, Pharmaceutical and Medical Device Agency (Japan); PVSD, Partial Ventricular Support device; TAH, total artificial heart; UniVAD, univentricular assist device.

1.5 Motivation

The use of MCS devices as a DT for HF treatment is rising significantly as it provides a cost-effective alternative to long-term treatment and cardiac transplantation. The most significant result of the REMATCH trial has been its role in proving the utility of MCS devices as DT. However, long-term versatility is far from ideal and incidence of transient and permanent neurological events is still high [86]. More recently, it has been reported that at low-flow low-pressure CV support, there is lower incidence of neurologic dysfunction [87]. To this end, evolution of MCS devices calls for more sophisticated design and evaluation methods.

1.6 Objective

The objective of this work is to develop a method to identify the effect of performance characteristics, pressure and flow rate, of mechanical circulatory support (MCS) devices on the human cardiovascular system. The evaluation will be carried out both numerically and experimentally.

1.7 Specific Aims

The research outlined in this thesis has the following specific aims:

1. To enhance an existing computational model of the human cardiovascular system that is capable of simulating normal and diseased conditions.
2. To implement a purposely built multi-chamber cardiovascular test rig to evaluate haemodynamic variables at several sites of the system while connected to a MCS device .
3. To modify an off-the-shelf centrifugal pump impeller with the purpose of unloading the left ventricle from high filling pressures and to re-establish a normal cardiac

output.

4. To evaluate the capabilities of a new centrifugal pump impeller as an alternative NYHA Class III and IV HF therapy.

1.8 Thesis Outline

Chapter 2 will describe the mathematical formulation used to simulate Class III and IV HF conditions. In Chapter 3, a local sensitivity analysis of the mathematical formulation is performed. In Chapter 4, transient simulations are run with the objective of identifying the centrifugal pump operating condition adequate for optimal perfusion in Class III and IV HF conditions. Chapter 5 starts by describing the method for centrifugal pump impeller blade generation and concludes by providing performance results from both numerical and experimental procedures. In Chapter 6, the numerical results are compared against those from a novel cardiovascular test rig. Lastly, Chapter 7 gives a brief conclusion and provides a suggestion for future research.

Chapter 2

Mathematical Model of The Human Cardiovascular System

2.1 Justification of the 0-D Model

In general, there are many models of the human cardiovascular system including those that emphasize on the mechanics of the left ventricle [88–92], or the arterial tree [93–96], the ones that include both the systemic and pulmonary circulations [97–101], those that are coupled to mechanical circulatory devices (MCD) [102–105], and the latest approach the multidomain models [91, 106–110]. The great majority of them make use of the 0-D Windkessel model given its simplicity, its good estimation of essential central hemodynamic variables (particularly CO [111]) and its potential estimation of hemodynamic variables that takes as input a patient's specific variables including age, gender, etc., [112].

The present cardiovascular model includes: systemic and pulmonary circulations; instantaneous pressure-volume (PV) relation of the four chambers of the heart; a modified valve model; and adapts a modified version of the fourth-element Windkessel model, by including resistance, capacitance and inductance (RCL) elements for each of the vessel segments in the model.

A very important issue in cardiovascular modelling is the accurate analysis of the PV relation of the heart chambers. Many cardiovascular models [88, 92, 100] have used the time-varying elastance model introduced by Suga et al. [88], in which the PV relation is formulated as

$$P(t) = E(t)[V(t) - V_0] \tag{2.1}$$

where $P(t)$ and $V(t)$ are the LV pressure and volume respectively, $E(t)$ is the variable elastance, and V_0 is a fixed volume-axis intercept. This equation assumes that all isochrones (curves that connect PV data points occurring at the same time) are linear and have a common volume intercept in the PV graph. This is problematic because for a similar left ventricular end-systolic pressure (LVESP) and volume ratio, the volume intercept varies depending on the cardiac abnormality [113]. It has been shown that the left-ventricle has a non-linear PV relation [114–117]. Claessens et al. [116] found that the shape of the isochrones, was best simulated by a quadratic or logarithmic function with a variable volume intercept as a function of time. Langewouters et al. [114] formulated an arctangent model for the pressure-area plot of the aorta; this translates into tangentially curved isochrones when formulated as a PV relation [118]. Shroff et al. [115] developed a PV relation model that includes ventricular resistive behaviour; however, this model is identical to the work of Suga et al. [88] when the aortic flow is equal to zero [118]. Campbell et al. [117] suggested that to improve time-varying elastance models, it is necessary to include the dynamic effects of volume variation over pressure variation. In their model, the dynamic left ventricular elastance was determined by integrating the dynamic relations between muscle-fiber force and fibre length into PV relationships. In the present model, Campbell's concept is adopted, in a modified manner, by including an elastance function generator and its rate of change with respect to time to represent muscle-fiber action, since the normalized time-varying elastance waveform does not change in either normal condition or various cardiovascular diseases [119–121].

Many of the previous numerical studies have described heart valve models by: forward flow as depicted by the orifice flow model [122, 123]; effective orifice area [124]; Boolean values to decide whether blood flows through the valves [112]; the diode analogue with finite resistance [125, 126]. Others, have used more sophisticated and realistic models, which simulate both the forward flow and the reverse flow phases [92, 100, 127, 128]. However, an easier to tune valve model, is generally more preferable. In this work a model in terms of electrical analogies is implemented. This is achieved by representing the heart valves as modified diodes, with decaying leakage current (flow) to model physiological reverse flow.

2.2 Hemodynamic Model

Components of the whole circulation system are modelled in three main parts: heart, systemic, and pulmonary circulation loops. The heart is modelled as a four-chamber pump with variable elastance, and four heart valves that control the blood flow direction. The circulation loops, are modelled as modified Windkessel model with repetitive RCL units arranged in a similar fashion to [100, 101, 129–131] to represent the different vascular compartments. The vascular compartments are in turn divided into 9 groups according to their size and function.

2.2.1 Heart model

The concept of a variable capacitor is used as an electrical analogue of the heart chambers; see Fig. 2.1. In this figure each chamber is represented by a time-varying capacitor, and the heart valves are modified diodes. Compliance is analogous to capacitance, which is generally expressed as the volume over pressure [6]. The inverse of compliance, known as elastance, represents the contractile property of the heart chambers. The heart model parameters are listed in Table 2.1.

A modified PV relation is proposed in this model in which the instantaneous pressure in

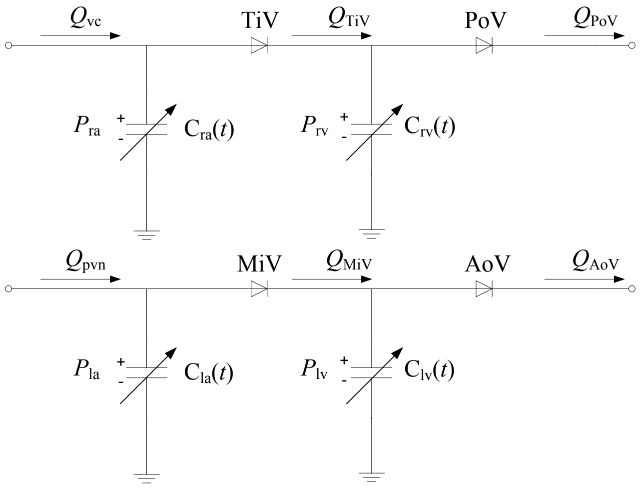

Figure 2.1. Schematic representation of the electrical analogy of the heart chambers and heart valves.

Table 2.1. List of parameters for heart chambers.

Left Heart	Value	Ref.	Right Heart	Value	Ref.	Unit
$E_{\mathrm{lv,\ max}}$	3.20	[132–137]	$E_{\mathrm{rv,\ max}}$	1.0	[132–137]	mmHg/ml
$E_{\mathrm{lv,\ min}}$	0.10	[132–137]	$E_{\mathrm{rv,\ min}}$	0.1	[132–137]	mmHg/ml
$E_{\mathrm{la,\ max}}$	1.00	[132–137]	$E_{\mathrm{ra,\ max}}$	0.3	[132–137]	mmHg/ml
$E_{\mathrm{la,\ min}}$	0.10	[132–137]	$E_{\mathrm{ra,\ min}}$	0.1	[132–137]	mmHg/ml
$V_{\mathrm{lv,0}}$	90.00	[132–137]	$V_{\mathrm{rv,0}}$	64.0	[132–137]	ml
$V_{\mathrm{la,0}}$	23.00	[132–137]	$V_{\mathrm{ra,0}}$	23.0	[132–137]	ml
$P_{\mathrm{lv,0}}$	0.00	[132–137]	$P_{\mathrm{rv,0}}$	4.0	[132–137]	mmHg
$P_{\mathrm{la,0}}$	0.00	[132–137]	$P_{\mathrm{ra,0}}$	4.0	[132–137]	mmHg

any heart chamber is governed by the contractile property of the chamber, $E(t)$, and the returning blood volume, $V(t)$, according to

$$V(t) = \frac{P(t)}{E(t)} \tag{2.2}$$

and its time derivative is calculated as the flow difference between the inlet and the outlet of the chamber. In the left ventricle, it is given by the mitral and aortic flow difference (see Fig. 2.1) according to

$$\frac{\mathrm{d}V_{\mathrm{lv}}(t)}{\mathrm{d}t} = Q_{\mathrm{MiV}}(t) - Q_{\mathrm{AoV}}(t) \tag{2.3}$$

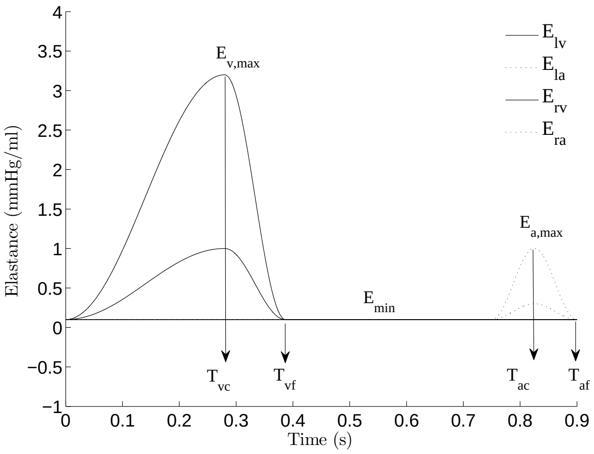

Figure 2.2. Varying elastance waveforms for the four cardiac chambers during one heart cycle, where T_c is the time to reach maximum contraction, T_f is the time to initiate chamber filling, E_{max} and E_{min} are the maximum and minimum elastances for each chamber accordingly.

therefore, the dynamic relations between elastance variation and volume variation to generate the instantaneous pressure change in the left ventricle can be obtained by applying the product rule of differentiation to Eq. 2.2 as follows

$$\frac{\mathrm{d}P_{\mathrm{lv}}(t)}{\mathrm{d}t} = E_{\mathrm{lv}}(t)\frac{\mathrm{d}V_{\mathrm{lv}}(t)}{\mathrm{d}t} + \mathrm{V}_{\mathrm{lv}}(t)\frac{\mathrm{d}E_{\mathrm{lv}}(t)}{\mathrm{d}t} \tag{2.4}$$

where $E_{\mathrm{lv}}(t)$ represents the time-varying elastance as a function of the maximum and minimum elastances of the chamber (E_{max} and E_{min}) as used by [132–137].

$$E_{\mathrm{lv}}(t) = \mathrm{E}_{\mathrm{lv,min}} + \frac{\mathrm{E}_{\mathrm{lv,max}} - \mathrm{E}_{\mathrm{lv,min}}}{2}e(t) \tag{2.5}$$

and, $e(t)$, describes the muscle contraction and the relaxation phases in the heart chamber as seen in Fig. 2.2 for which the following functions are proposed.

For the ventricle $e(t)$ is given by

$$e_v(t) = \begin{cases} 1-\cos\left(\dfrac{t}{\mathrm{T_{vc}}}\pi\right) & : \quad 0 \le t < \mathrm{T_{vc}} \\ 1+\cos\left(\dfrac{t-\mathrm{T_{vc}}}{\mathrm{T_{vf}}-\mathrm{T_{vc}}}\pi\right) & : \quad \mathrm{T_{vc}} \le t < \mathrm{T_{vf}} \\ 0 & : \quad \mathrm{T_{vf}} \le t < \mathrm{T} \end{cases} \tag{2.6}$$

where T_{vc} and T_{vf} are related to the time to reach the maximum contraction and that to initiate chamber filling of the ventricle respectively.

For the atrium $e(t)$ is given by

$$e_{\mathrm{a}}(t) = \begin{cases} 0 & : \quad 0 \leq t < \mathrm{T}_{\mathrm{ac}} \\ 1 - \cos\left(\dfrac{t - \mathrm{T}_{\mathrm{ac}}}{\mathrm{T}_{\mathrm{af}} - \mathrm{T}_{\mathrm{ac}}} 2\pi\right) & : \quad \mathrm{T}_{\mathrm{ac}} \leq t < \mathrm{T}_{\mathrm{af}} \\ 0 & : \quad \mathrm{T}_{\mathrm{af}} \leq t < \mathrm{T} \end{cases} \tag{2.7}$$

where T_{ac} and T_{af} are related to the time to reach the maximum contraction and that to initiate chamber filling of the atrium respectively. The time parameters are listed in Table 2.2.

Table 2.2. List of time parameters for a normal condition.

Parameter	Value	Unit
HR	66.70	bpm
T	0.90	s
T_{vc}	0.28	s
T_{vf}	0.39	s
T_{ac}	0.75	s
T_{af}	0.90	s

2.2.2 Valve flow model

Accurate modelling of the dynamic flow characteristics of the heart valves plays a crucial role in modelling the atrium-to-ventricle and ventricle-to-artery interactions. She et al. [138] described the instantaneous $Q(t) - \Delta P(t)$ relation for different prosthetic heart valves in pulsatile flow as having a deformed 8-shape trace during a whole cardiac cycle. In this model we adopt this dynamic characteristic by implementing a modified diode with decaying leakage current (flow) which models physiological reverse flow; for this purpose Shockley diode model [139] (see Fig. 2.3a), is implemented as follows

$$Q(t) = \mathrm{k}_{\mathrm{max}} \left[\mathrm{e}^{\mathrm{k}_{\mathrm{min}} \Delta P(t)} - 1 \right] w(t) \tag{2.8}$$

where $\mathrm{k}_{\mathrm{max}}$ and $\mathrm{k}_{\mathrm{min}}$ are constants that control maximum and minimum flows, $\Delta P(t)$ is the pressure difference across the valve as a function of time, and $w(t)$ is the valve opening, whose dynamics can be described by

$$\frac{\mathrm{d}w(t)}{\mathrm{d}t} = \frac{\tanh(\mathrm{k}_{\mathrm{se}} \Delta P(t) + 1)}{2\mathrm{k}} - \frac{w(t)}{\mathrm{k}} \tag{2.9}$$

where k_{se} and k are constants that control the speed of ejection and the dynamic characteristic, respectively. The valve flow model parameters are listed in Table 2.3.

Table 2.3. List of parameters for valve flow model.

Left Heart	Value	Ref.	Right Heart	Value	Ref.	Unit
$\mathrm{k}_{\text{max, MiV}}$	400.00	†	$\mathrm{k}_{\text{max, TiV}}$	200.0	†	mmHg^{-1}
$\mathrm{k}_{\text{min, MiV}}$	0.15	†	$\mathrm{k}_{\text{min, TiV}}$	0.18	†	mmHg^{-1}
$\mathrm{k}_{\text{se, MiV}}$	2.50	†	$\mathrm{k}_{\text{se, TiV}}$	2.0	†	mmHg^{-1}
$\mathrm{k}_{\text{max, AoV}}$	400.00	†	$\mathrm{k}_{\text{max, PoV}}$	300.0	†	mmHg^{-1}
$\mathrm{k}_{\text{min, AoV}}$	0.28	†	$\mathrm{k}_{\text{min, PoV}}$	1.5	†	mmHg^{-1}
$\mathrm{k}_{\text{se, AoV}}$	2.50	†	$\mathrm{k}_{\text{se, PoV}}$	2.5	†	mmHg^{-1}
k	0.01	‡	k	0.01	‡	s

† Selected values are similar to those found in [132–137] but have different units as the valve mechanism is different in this work;
‡ Assumed value.

Fig. 2.3 shows a diagrammatic representation of the $\Delta P(t) - Q(t)$ relation of the present model. As previously described in She et al., [138] the following phases are identified. Starting from a closed position at *a*; see Fig. 2.3b, the curve quickly rises into the positive $\Delta P(t)$ axis constituting the isovolumetric contraction of the muscle. Once the valve has opened, a rapid ejection phase initiates at *b* until the maximum flow is reached at *c*. From this point, a slow ejection phase takes place up to the point where the curve turns into the negative flow axis (reverse flow phase) at *d*. The curve quickly turns into the negative

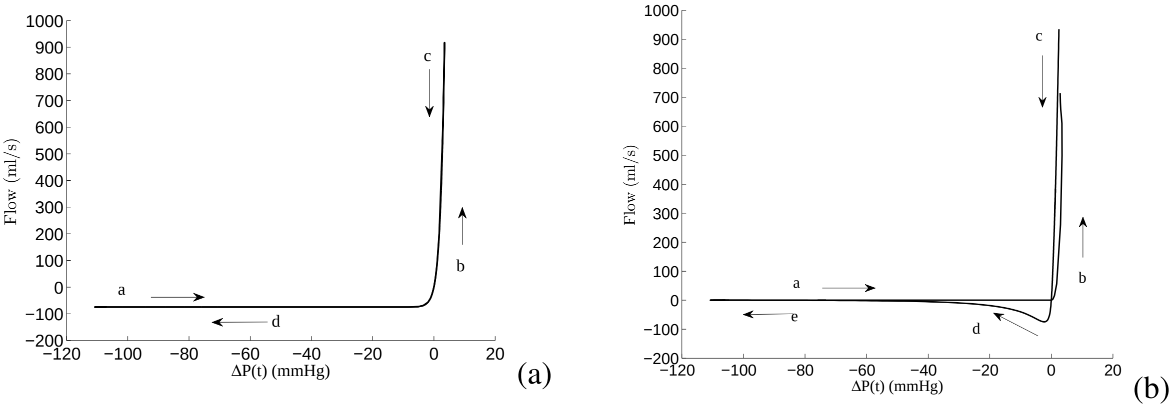

Figure 2.3. Illustration of Pressure difference, $\Delta P(t)$, and flow relation of the aortic valve during a cardiac cycle: a) Shockley diode model and b) proposed modified diode with variable inflow-outflow characteristics and reverse flow.

$\Delta P(t)$ axis to finally go back to the close position at e and allow chamber filling. When comparing a normal diode to present valve model, is clearly noticed that the model results in a good prediction of valve flow dynamics; such as decaying leakage current (shown in Fig. 2.3).

2.2.3 Blood Circulation Loops

The various components of both the systemic and pulmonary circulation loops are represented by a lumped parameter model (shown in Fig. 2.5). In this work, the systemic circulation was divided into six-parallel vascular beds representing head, coronary, upper limb, splanchnic, renal and lower limbs circulations with the intention of properly distributing the total blood volume; see Fig. 2.5. Each vascular bed is divided into nine segments: central artery; large arteries; terminal arteries; arterioles; capillaries; venules; small veins; large veins; and central vein. Each Local resistance to flow, compliance, and inertance of each of these segments are modelled as resistance, compliance, and inertance effects respectively. An illustration of two RCL segments in series is shown in Fig. 2.4. At each node, e.g. N_i, the following equations for volume, flow and pressure are obtained

$$\frac{\mathrm{d}V_i(t)}{\mathrm{d}t} = Q_{i-1}(t) - Q_i(t) \tag{2.10}$$

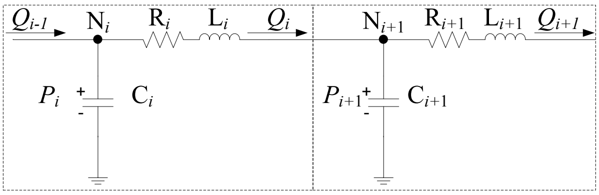

Figure 2.4. Illustration of two RCL units in series.

Flow rate $Q_i(t)$, is given by

$$\frac{\mathrm{d}Q_i(t)}{\mathrm{d}t} = \frac{P_i(t) - P_{i+1}(t) - \mathrm{R}_i Q_i(t)}{\mathrm{L}_i} \tag{2.11}$$

where R_i is the segment's resistance to flow, L_i is the flow inertance of each segment, C_i is the compliance of each segment, and $P_i(t)$ is the pressure in the segment given by

$$P_i(t) = \frac{V_i(t) - \mathrm{V}_0}{\mathrm{C}_i} + \mathrm{P}_0 \tag{2.12}$$

The pulmonary loop model is similar to that of the systemic loop with different values for system parameters.

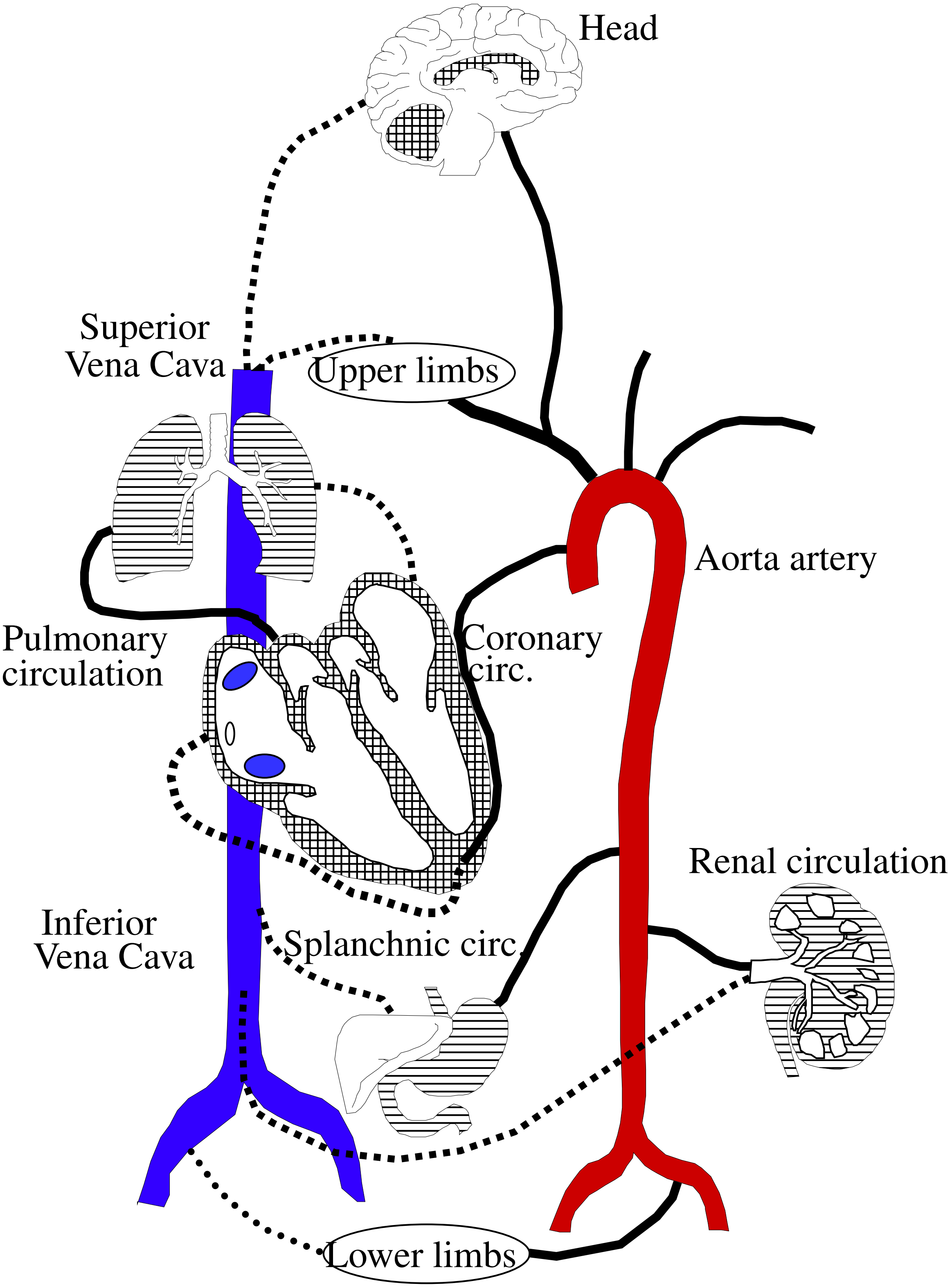

Figure 2.5. Schematic of the pulmonary and systemic circulation loops. Each loop is composed of nine RCL units in series (shown in Fig. 2.4). The solid lines represent the arterial tree originating from the aorta (vessel in red) while the broken lines represent the venous tree which converges into the inferior vena cava and superior vena cava (vessel in blue)

2.3 Autoregulation model

In this work, the cardiovascular control model includes three main systems representing the ANS function: arterial baroreflex; volume reflex; and heart rate (HR) variability; see Fig. 2.6.

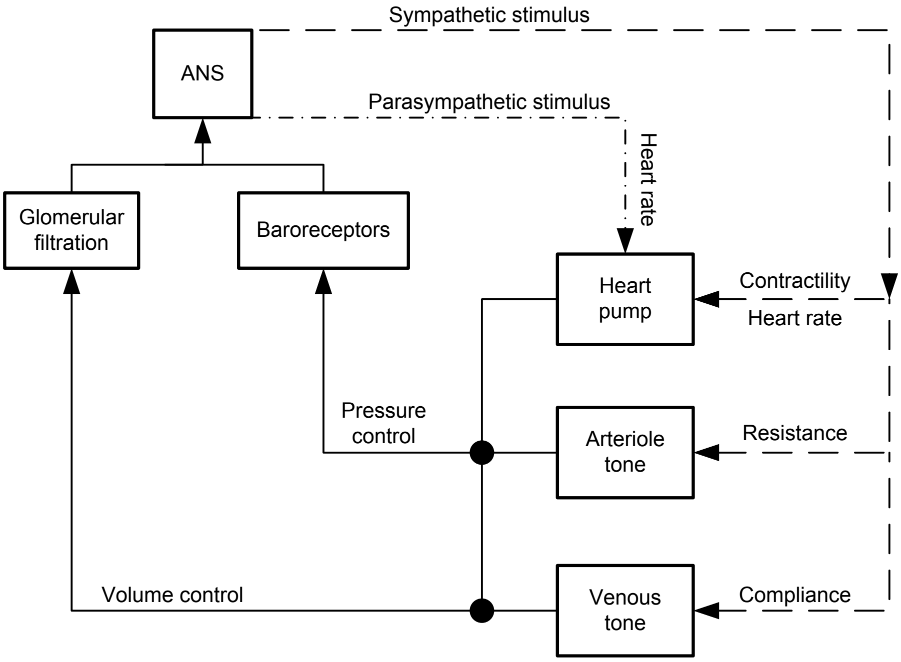

Figure 2.6. Diagrammatic representation of the cardiovascular control model where the broken lines represent the effector stimulus and the solid lines represent the afferent signals. The heart's contractility is assumed to be modulated solely by the sympathetic nerve control; resistance is assumed to be controlled only at the arterioles as these are the main resistive vessels [5]; vascular compliance is only controlled at the veins as they are the main capacitive vessels in the whole circulation [140]. This figure is a modification of the works undertaken by Heldt et al. [141] and Shim et al. [142]

Regulation of pressure is controlled by the sympathetic and parasympathetic innervation throughout the cardiovascular system. They are the efferent subdivisions of the ANS. The sympathetic fibres richly innervate: the cardiac chambers; the heart pacemaker; vascular smooth muscle, whereas the parasympathetic innervation mainly focuses on the heart's pacemaker [5, 143]. In general, sympathetic stimulation increases cardiac contractility and HR, and produces vasoconstriction in the arterioles mainly; whereas parasympathetic stimulation reduces HR and induces vasodilation on the peripheral vasculature. In Fig. 2.7, it is shown that for changing levels of atrial pressure the amount of blood pumped per minute can be increased or decreased according to the levels of sympathetic and parasympathetic stimulus, respectively [144]. Sympathetic stimulus can increase HR, up to 200 beats per minute (bpm), and double the force of contraction, therefore increasing CO and mean arterial pressure (MAP). By contrast, parasympathetic stimulation can decrease HR and CO to as low as zero.

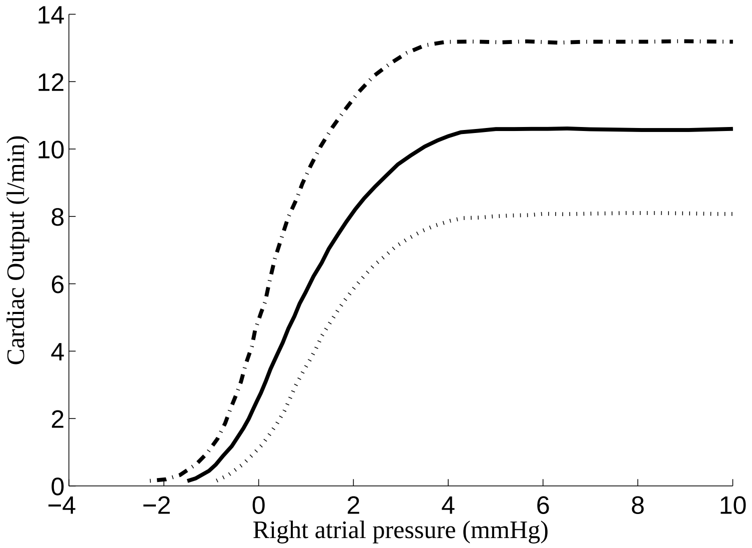

Figure 2.7. Changes in CO in response to nerve stimulation. The figure shows three different conditions: zero stimulation (solid line) where optimal condition is found around the middle of the curve; parasympathetic stimulation (dotted line); normal sympathetic stimulation (broken line). (The data in this figure was extrated from Guyton [144])

The baroreflex and volume reflex are responsible for the regulation of pressure and volume respectively, and are model as reference-point controllers that aim at minimizing an error signal. In the pressure control reflex loop the error signal, $P_{\mathrm{error}}(t)$, is the difference between the mean arterial pressure, $\bar{P}_{\mathrm{cs}}(t)$, over a full sample of carotid pressures in a cardiac cycle, τ, and a pre-defined reference pressure $P_{\mathrm{cs}}^{\mathrm{ref}}$; see Fig. 2.8 for a diagrammatic representation. This difference is then scaled by a sigmoid transform to represent the experimentally-observed sigmoidicity of the stimulus-response curves as shown in Fig. 2.7. The sigmoid transform is given as follows

$$P_{\mathrm{eff}}(t) = \mathrm{SF}\tan^{-1}\left(\frac{\bar{P}_{\mathrm{cs}}(t) - P_{\mathrm{cs}}^{\mathrm{ref}}}{\mathrm{SF}}\right) \tag{2.13}$$

where SF is the scaling factor. The carotid sinus is used in this work as the main baroreceptor site as this is how it is found in the human body [145]. The pulmonary baroreflex is modelled similarly to its systemic counterpart but with different model parameters.

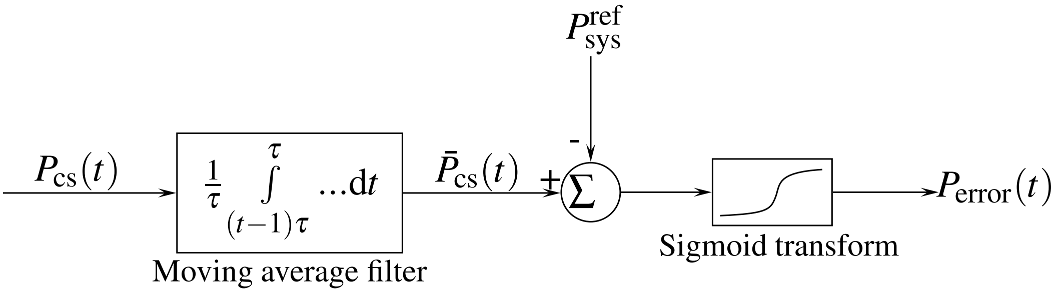

Figure 2.8. Arterial baroreflex model where $P_{cs}(t)$ is the instantaneous carotid pressure, $\bar{P}_{cs}(t)$ is the arithmetic mean of the carotid pressure in a cardiac cycle, $P_{\mathrm{sys}}^{\mathrm{ref}}$ is the reference systemic arterial pressure, $P_{\mathrm{error}}(t)$ is the scaled error signal and τ is the period of the cardiac cycle

The volume reflex is model by simulating the stretch of the atria caused by sensing increased returning blood volume and consequent dilation of the afferent arterioles in the kidneys brought about by ANS activity [146]. In general, a decreased arteriolar resistance in the kidneys causes the glomerular capillary pressure to rise resulting in increased glomerular filtration rate (GFR). Simultaneously, the CNS reduces the reabsorption of water from the kidney tubules, thus increasing the fluid loss and consequently reducing the increased blood volume back to normal. This feedback mechanism, intrinsic to the kidneys, normally keeps the renal blood flow and GFR relatively constant even in the presence of significant changes in arterial blood pressure. In Fig. 2.9 it is noted that the stimulus curve appears similar to that of the baroreflex system (see Fig. 2.7) with this in mind, an error signal for the RA volume, V_{ra}, is produced in a similarly manner to that for the baroreflex model and scaled by a sigmoid transform in order to regulate MAP as function of the extracellular volume. In previous cardiovascular models that included automatic pressure control [107, 141, 142, 147, 148], the volume reflex loop has been neglected as these studies mainly concentrated in acute pressure control, particularly in hypotensive conditions. As this study requires the simulation of chronic conditions, such as hypertension and congestive heart failure, kidney autoregulation becomes an important mechanism to maintain constant CO and adequate MAP [6, 33, 149–152].

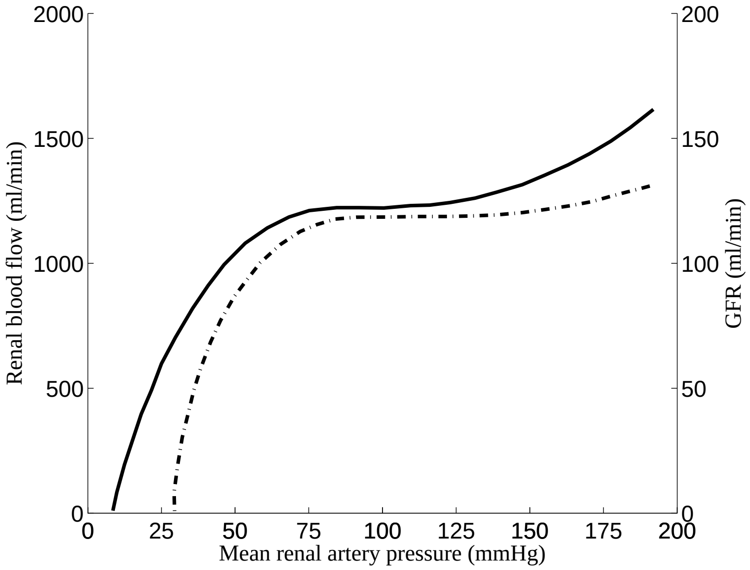

Figure 2.9. Autoregulation of the renal blood flow and glomerular filtration rate during changes in renal mean arterial pressure where the solid line shows the renal blood flow and the broken line GFR. (Data extracted from [6])

The summation of the error signal from the baroreflex loop and the volume reflex loop constitutes the effector variable $Y(t)$. This variable represents the ANS response signal, either a sympathetic or a parasympathetic signal, that ultimately governs the effector mechanisms, namely: the variation of heart elastance; arteriolar resistance variation; glomerular filtration rate; venous compliance of the systemic circulation and the pulmonary circulation. The response signal, $Y(t)$, is scaled by static gain values, G_X, where X denotes any of the effector mechanisms as illustrated in Fig. 2.6. The static gain parameters implemented in this model are listed in Table 2.4.

Table 2.4. List of static gain values for a normal condition.

Effector	Value	Unit	Reference
$\mathrm{G}_{\mathrm{E}_{\mathrm{lv}}}$	0.01	mmHg/ml	[141]
$\mathrm{G}_{\mathrm{E}_{\mathrm{rv}}}$	-0.005	mmHg/ml	
$\mathrm{G}_{\mathrm{C}_{\mathrm{svn}}}$	0.05	ml/mmH	
$\mathrm{G}_{\mathrm{C}_{\mathrm{pvn}}}$	-0.05	ml/mmH	
$\mathrm{G}_{\mathrm{R}_{\mathrm{sar}}}$	0.005	mmHg.s/ml	[141]
$\mathrm{G}_{\mathrm{R}_{\mathrm{par}}}$	-0.005	mmHg.s/ml	
$\mathrm{G}_{\mathrm{gfr}}$	-0.05	ml/s	

2.3.1 Heart Rate

HR variability is simulated by an integral pulse frequency modulator (IPFM) model of the sino-atrial node (also known as the heart's pace maker). In this model an input signal, consisting of the mean HR, m_0, and the modulating signal, $m(\tau)$, which describes the variations in HR according to the autonomic activity, is integrated until a threshold, R, is reached at which time an action potential is triggered off; the integrator is then reset to zero and the procedure is repeated. The threshold, R, defines the mean interval length between successive events [153]. The resulting signal can be viewed as the charging of the membrane potential of the sino-atrial node. The following mathematical expression represents the IPFM model,

$$\int_{t_{n-1}}^{t_n} (m_0 + m(\tau))d\tau = R, \quad n = 1, ..., N \tag{2.14}$$

where n is an integer that indexes the n^{th} heart beat.

A summary of all the parameters implemented in the present mathematical model is given in Appendix A.

Chapter 3

Parameter Estimation and Sensitivity Analyses

3.1 Parameter Estimation Model

The cardiovascular model described in Chapter 2 was developed with the intention of following the main physical properties encountered in the native system. Particular attention was given to the optimisation of the venous compliance values, representing the capacitance of the venous tree, and the volume reflex, which are commonly neglected in most models. In addition to modelling the physical properties of the vasculature in the various loops, representing the perfusion to the internal organs and limbs, the CV model also included the reflex system. However, the present model has as main downside that it has a very large number of parameters. With this in mind, a method to estimate the majority of the model parameters is presented in this chapter.

System parameters for resistances, compliances and inertances were identified in a 4-stage process. The first three stages implemented a simpler model of the CV system which consisted of two main circulatory loops, namely pulmonary and systemic loops; see Fig. 3.1 for an illustration of this simplified model. Each circulatory loop is composed of nine vascular compartments or RCL units that included: central artery; large arteries; terminal arteries; arterioles; capillaries; venules; small veins; large veins; and central vein. In the last stage, the full CV model, as described in Chapter 2, was implemented. The final optimised system parameters are provided in Appendix A.

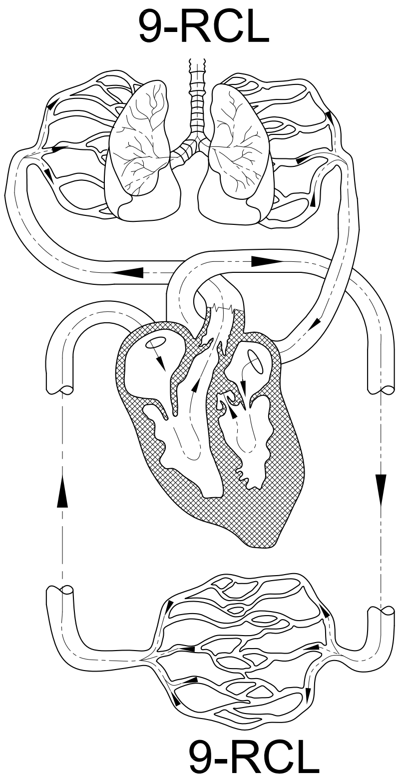

Figure 3.1. Schematic of the pulmonary and systemic circulation loops. Each loop is built of nine RCL units in series (shown in Fig. 2.4)

In the first stage, the majority of parameters were assigned values as found in the literature [100, 127, 141, 147, 154–158]. These values served as stepping stones to proceed with the overall optimisation. However, whenever the parameters from the literature where found unsuitable for the CV model, the following equations for resistance and inertance were implemented

$$R = \frac{8\mu l_i}{\pi r_i^4 \mathrm{n}_i} \tag{3.1}$$

$$L = \frac{\rho l_i}{\pi r_i^2 \mathrm{n}_i} \tag{3.2}$$

where μ is the blood viscosity taken as 4 mPa s, ρ is the blood density taken as 1060 $\mathrm{kg/m^3}$, l is the vessel length, r is the vessel radius, and n is the number of vessels, considered in a parallel configuration in relation to the aorta, per compartment or vascular bed (all numerical data necessary to implement Eq. 3.1 and 3.2 was extracted from J.R Levick; Appendix 1 [5]).

Table 3.1. List of RCL parameters for the systemic loop.

Segment	R(mmHg.s/ml)	C(ml/mmHg)	L(mmHg.s^2/ml)
Central artery	0.003	0.0800	6.20e-05
Large arteries	0.050‡	1.6000	6.20e-04‡
Terminal arteries	0.283‡	0.0017	1.70e-05‡
Arterioles	0.630	0.2000	1.07e-06
Capillaries	0.283	0.0100	2.75e-08‡
Venules	0.0179‡	18.620	5.62e-07‡
Small veins	0.001‡	66.600	6.75e-05‡
Large veins	0.001‡	20.500	6.32e-04‡
Central vein	0.075	1.5000	1.97e-04‡

‡ Denotes the parameters calculated using Eq. 3.1 and 3.2

Table 3.2. List of RCL parameters for the pulmonary loop.

Segment	R(mmHg.s/ml)	C(ml/mmHg)	L(mmHg.s^2/ml)
Central artery	0.002	0.180	5.20e-05
Large arteries	0.003 ‡	3.800	9.23e-04‡
Terminal arteries	0.092‡	0.017	1.7e-05 ‡
Arterioles	0.050	0.200	1.6e-07
Capillaries	0.025	0.100	4.13e-09‡
Venules	0.00179‡	5.000	8.43e-08‡
Small veins	0.001‡	66.60	1.01e-05‡
Large veins	0.001‡	20.50	9.45e-05‡
Central vein	0.006	1.500	2.97e-05‡

‡ Denotes the parameters calculated using Eq. 3.1 and 3.2

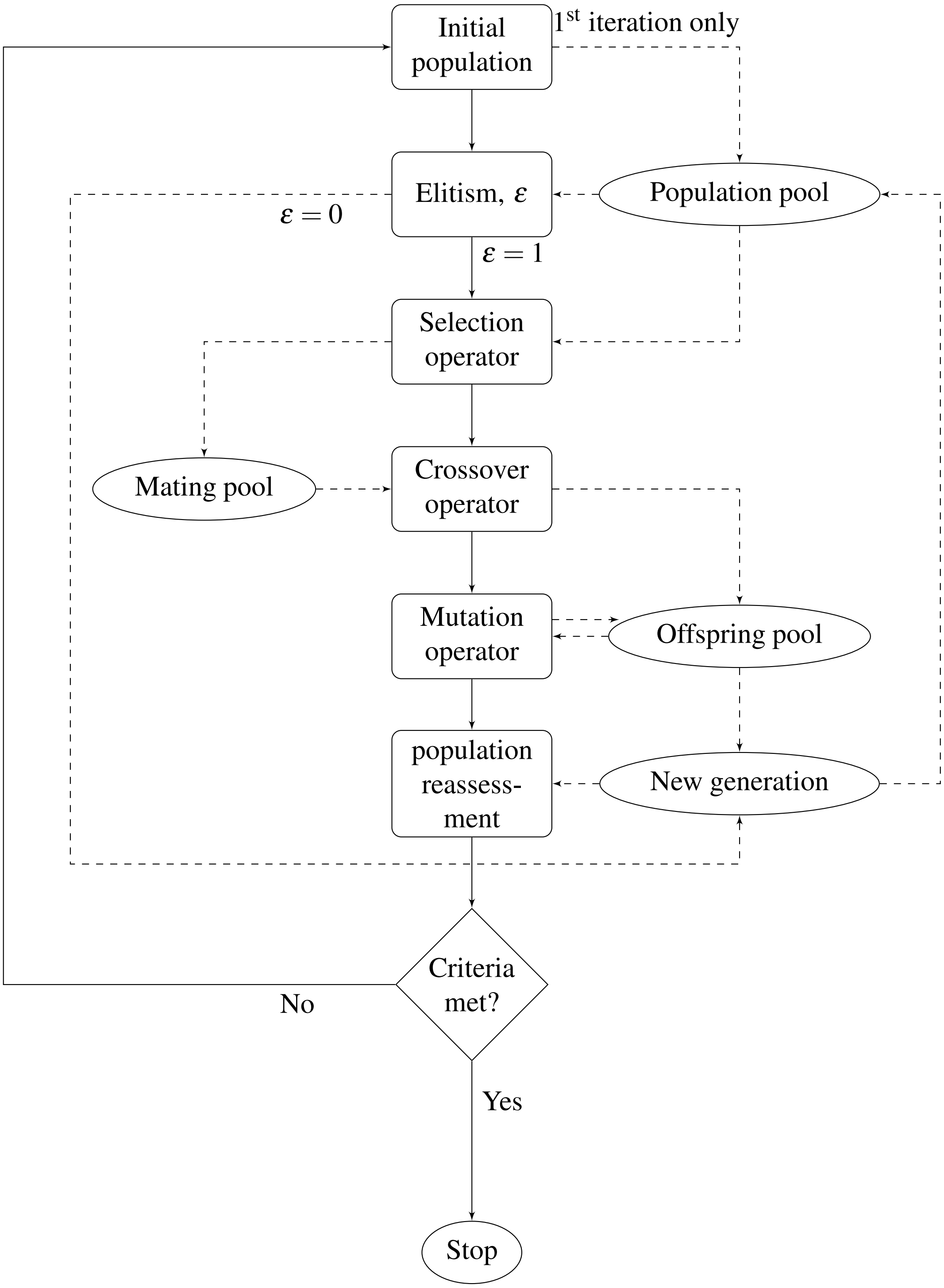

Figure 3.2. Genetic algorithm flow chart where the solid lines represent the control flow and the broken lines the data flow. Adapted from Rahided et al., [159].

In the second stage, a meta-heuristic optimisation technique, called the genetic algorithm (GA), was employed to optimally identify the systemic and pulmonary compliances given that many local optima exist in this particular problem.

GAs are mathematical optimisation algorithms that are inspired in nature's survival-of-fittest selection mechanism, in particular the one found in the field of genetics. The search process is initialised with a population of guesses that are processed by operators with the intention of directing the initial population towards an ultimate goal or global optimum. These operators are selection, crossover and mutation. Selection, evaluates the best performing individuals and push them forward as mating individuals. Crossover, is characterised by an exchange of information amongst the fitter individuals, thus, creating a new offspring. Mutation, randomly changes information in the offspring with the intention of improving the individuals' performance. After the three operators have been applied, a new generation is created. The process is continued until either a number of generations have been reached or the criterion for convergence has been met [160]. Fig. 3.2 shows a schematic representation of the GA. In this work, an existing GA model, developed by Dr A. Rahideh, was implemented; the reader is then referred to the work by Rahideh et al. [159], for further information.

The vascular compliances are the most challenging parameters to be identified and are the driving characteristics to correctly simulate the different elements of the cardiovascular system [157, 161–163]. The resistance values were made to adopt a normal distribution (being highest at the arterioles and lowest at the central arteries and central veins), and the inertance values were made to adopt an inverted normal distribution (being highest at the central arteries and central veins and lowest at the arterioles, capillaries and venules), with the purpose of optimising the compliances values according to them.

The objective of the optimisation problem is to minimize the error between clinically measured and numerically calculated LV volumes, shown in Fig. 3.4c. Semiautomated software (CMRtools; Cardiovascular Imaging Solutions, London, UK) was used to derive LVEDV and LVESV of a control subject using a previously described technique [164]. A comparison between the CMR measurement and the numerical data is shown in Fig. 3.4.

The objective function, Ω, implemented in this work is the least squares cost function as given by

$$\Omega = \sum_{i=1}^{n} (\bar{y}_i - y_i)^2 \tag{3.3}$$

where $\bar{y}$ is the measured data (in this case LV volume over one cardiac cycle), y is the predicted value, and n is the number of data points. The method calculates the sum squared of the vertical distance between the measured LV volume and the one predicted by the CV model. The objective function will be at a minimum when the difference between measured and predicted data approaches zero [160].

The initial population of the GA consists of the compliance parameters found in the first stage and some randomly generated individuals [165]. The parameters for the GA are listed in Table 3.3.

Table 3.3. List of parameters for the genetic algorithms [**159**].

Parameter	Value
Number of individuals	200
Number of elite individuals	5
Number of generations	50
Crossover rate	0.9
Mutation rate	0.025

The values for the systemic and pulmonary vessel compliances obtained in the second stage were found to continue to display a bell-shaped distribution as initially imposed at that stage of the optimisation process. In the third stage, non-linear regression analysis was implemented (MATLAB's nlinfit model for non-linear regression was used) to fit a Gaussian distribution model to the compliance values obtained in the second stage. The estimated regression coefficients aimed at minimising the sum of squared differences between predicted and actual values.

This fitting was aimed at facilitating parameter estimation while maintaining common

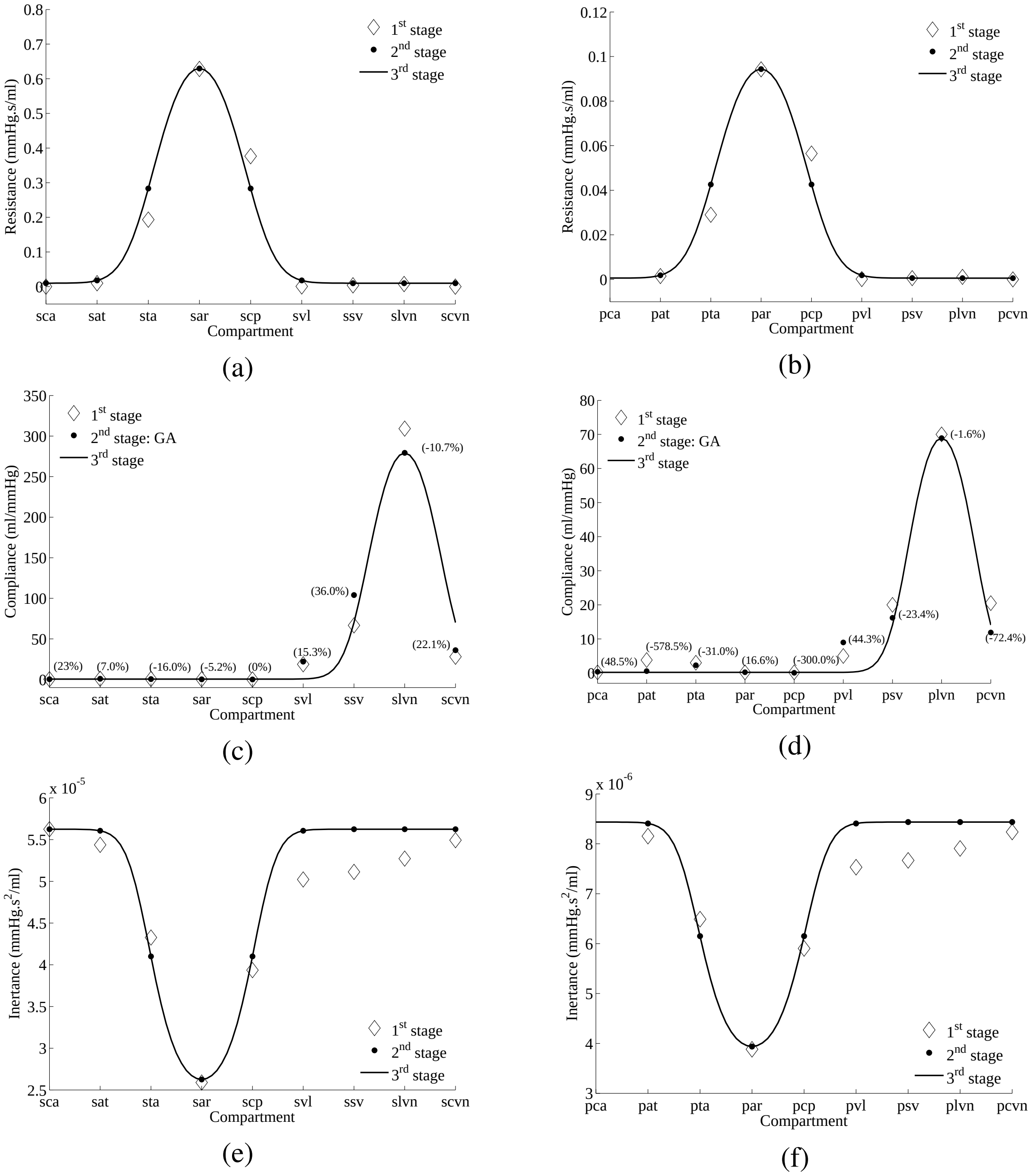

Figure 3.3. Illustration of the parameters for blood vessels as described in Tables 3.1 and 3.2: a) systemic resistance, b) pulmonary resistance, c) systemic compliance , d) pulmonary compliance (showing within brackets the percent change of the paremeter from stage 1 to stage 2), e) systemic inertance and f) pulmonary inertance.

physiological trends, namely: stroke volume within the 70-80 ml range; CO in the 4-7 l/min range; central systemic blood pressure close to 120/80 mmHg; and pulmonary artery pressure close to 25/10 mmHg. The implemented Gaussian model is mathematically expressed as

$$f(x) = \frac{\mathrm{gh}}{1+\mathrm{e}^{\left[\beta\left(\frac{x_i-gc}{\sigma}\right)^2\right]}} + \mathrm{gl} \tag{3.4}$$

where β, gc, σ, gh and dl are coefficients (generated by the nonlinear regression analysis) which govern the characteristics of the bell-shaped curve, x_i is the value of the independent parameter, in this case the location, where i takes values from 1 to 9 representing the vascular tree distribution from central arteries (1) to central veins (9). The coefficients β, σ and gh control the peak value and dilation factor of the curve, respectively, and can therefore be regarded as the variance; gc shifts the curve sideways whereas gl controls the lowest value of the bell-shaped curve. As these two parameters cause no modification to the shape of the curve they can be constrained as the location of highest vessel compliance and the lowest compliance value as found in stage 2, respectively. All Gaussian coefficients are summarised in Table 3.4

Table 3.4. Gaussian fitting coefficients.

Coefficient	C_s	C_p	L_s	L_p	R_s	R_p
β	42.04	33.45	50	30	53.18	52.78
gl (constrained)	0.43	0.18	17782	118550	0.01	5.80e-4
gc (constrained)	8.00	8.00	4	4	4.00	4.00
σ	4.65	3.91	9	10	5.18	5.20
gh	553.00	137.44	28535	19023	1.29	0.20

The choice of values for the model's parameters, as presented in Fig. 3.3a-f, show the highest systemic resistance occurring at the arteriole vessels and the lowest in the central vessels; this is consistent with the small diameters found towards the periphery as resistance is inversely proportional to the radius raised to the fourth power, r^4, as described by Eq. 3.1. Conversely, inertance is mainly influential in the central vessels and very insignificant at the periphery as inertance is inversely proportional to the squared of the radius, r^2, as described by Eq. 3.2; hence, it plays a significant role in large diameter vessels. The pulmonary loop parameter values for both resistance and inertance were calculated as being 15% of their systemic counterpart. Vascular compliance or the ability of the vessels to store blood per pressure change is significantly higher in the veins when compared to the corresponding arteries with about 64% of the total blood volume stored in the systemic venules, small veins and vena cava [6]; Fig. 3.3 (c) and (d) show that the results from the third optimisation stage approximate this fact, with the peak compliance value occurring at the large veins.

In the fourth and final optimisation stage, the systemic loop, as implemented in stages 1 to 3, was divided into six parallel loops representing coronary, head, upper limb, splanchnic, renal and lower limb circulations (see Fig. 2.5); each of which having nine vascular compartments or RCL units, and connected to the heart by a lumped-parameter representation of the aorta and the vena cava, as described in Chapter 2. The fitted Gaussian coefficients gh and gl, as identified in the third stage, were divided into the mentioned vascular beds according to CO distribution percentage as follows: coronary 3.0%, head 13%, upper limb 11%, splanchnic 32%, renal 28% and lower limb 13%. The remaining Gaussian coefficients were not changed for any of the vascular beds given that each of the loops has the same amount of vascular compartments, but most importantly because the haemodynamic properties of all vascular beds behave in the same fashion. GA optimisation was once again employed to identify the maximum and minimun values for TPR, total vascular compliance and total vascular inertance that would in turn control the Gaussian coefficients gh and gl for all vascular beds as a function of CO distribution. The objective function of this optimisation problem was the same as in the second stage, that is, to minimise the error between the clinically measured LV volume and the numerically calculated LV volume. The Gaussian coefficients obtained in stage 4 are summarised in Table 3.5

Table 3.6 gives a quantitative representation of the changes that took place from stages 1

Table 3.5. Gaussian parameters for all systemic vascular beds

Vacular bed	R		C		L	
	gh	gl	gh	gl	gh	gl
Coronary	10.00	1.00	12	0.0112	0.0021	3.514e-4
Head	3.33	0.28	90.00	0.0120	0.0113	1.933e-6
Upper limb	8.89	0.89	48.00	0.0120	0.0103	1.757e-5
Splanchnic	1.60	0.22	180.00	0.0120	0.0247	4.217e-6
Renal	2.00	0.28	144.00	0.0029	0.0196	3.338e-6
Lower limb	11.11	1.11	60.00	0.0012	0.0082	1.757e-5

Table 3.6. Output measures from stages 1 to 4 of the optimisation process.

Variable	Control	Stage 1	Stage 2	Stage 3	Stage 4	Unit
CO	4-7	6.0	5.7 (-8.1%)	5.6 (-1.8%)	5.6 (0%)	l/min
MSAP	70-100	101.7	98.5 (-3.1%)	97.5 (-1.0%)	102.7 (5.3%)	mmHg
MPAP	9-18	19.6	17.6 (-10.2%)	18.4 (4.5%)	18.8 (2.2%)	mmHg
CVP	3-8	8.0	8.1 (1.3%)	8.4 (3.7%)	3.7 (-55.9%)	mmHg

Quantitative information about the changes in output measures from stage 1 to stage 2 to stage 3 to stage 4 of the optimisation process is given within the brackets.

to 4 of the optimisation process. From Table 3.6 it can be seen that the parameters used in stage 1 resulted in a relatively good fit when compared to the control values therefore making of them a good estimate for stage 2 of the optimisation process; the Gaussian fitting performed in stage 3 did not vary greatly the output measures with respect to stage 2 as identified with the GA tool; lastly, the comparison of the output measures from stages 3 and 4, although presented with greater variation than for the other stages, proves that the Gaussian fit for estimation of the model's parameters works well for both the simple and the complex CV model. However, as the output measures listed in Table 3.6 are cycle-averaged values no time histories of the simulation details can be assessed. When comparing the clinical LV volume with the calculated LV volume at stage 1 as found in Fig. 3.4a it can be seen that the there are many inaccuracies throughout the cardiac cycle as depicted by the error bars. When comparing the numerical LV volume obtained at stage 4 to that of stage 3 (see Fig. 3.4c and d), it can be appreciated that very small changes occur making the implementation of the Gaussian fit for estimation of the model's parameters a useful tool.

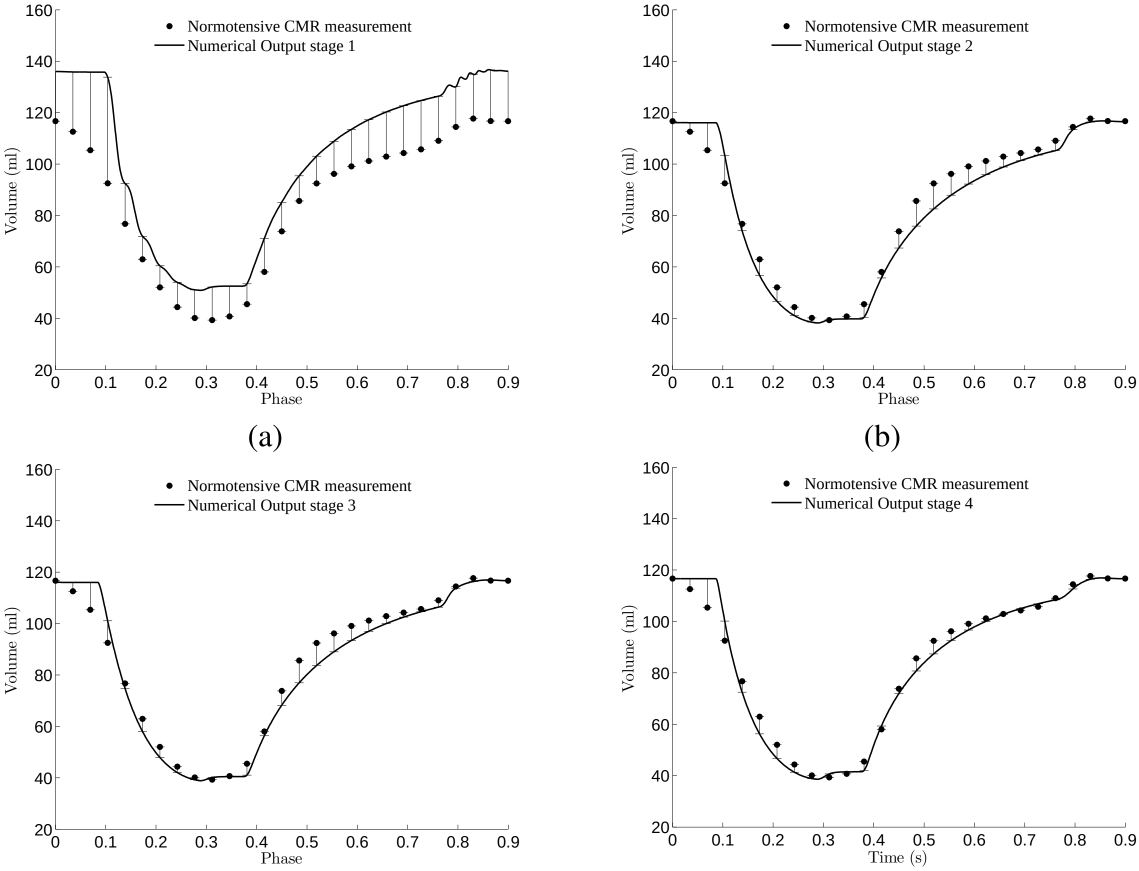

(a) (b)

(c) (d)

Figure 3.4. Comparison of calculated left ventricular volume vs normal clinical measurement throughout the 4-stage optimisation process. (a) stage 1, (b) stage 2, (c) stage 3 and (d) stage 4.

3.2 Sensitivity Analyses

The present model, although has as main intention to produce a heart failure model, is intended to be robust enough to simulate normal and diseased cardiovascular conditions. The intention of this sensitivity analysis is therefore, to find the main influencing parameters of the CV model over a set of output variables. A deterministic method, requiring as many model evaluations as there are parameters in the model, is used in this work to carry out a local sensitivity analysis or derivative based analysis in which the sensitivity of the cost function is evaluated with respect to each of the model's parameters. The sensitivity analysis is performed in two separate parts: 1. Analysis of the sensitivities of the uncontrolled CV model in steady state; 2. Analysis of the sensitivities of the CV model with automated regulation.

In this work, particular interest was given to finding the most significant parameters that affect CO as a derived feature of the aortic valve outflow, MAP, MPAP and central venous pressure (CVP) on a beat-by-beat basis. These four cost functions are chosen here because these are the gold standards of cardiac condition assessment [111]. Investigation of parametric sensitivities is achieved by assessing the difference between the nominal response (output y) and perturbed values Δy brought about by imposing small changes, $\Delta\alpha$, in the model's parameters, α. The output, y, consists of the cycle-averaged values of cost function over one cycle. The local sensitivity of a cost function with respect to a given parameter, α_i, is equal to the partial derivative of the cost function with respect to each of the model's parameters α_i, this can be mathematically expressed as follows

$$\left(\frac{\partial \mathrm{CO}}{\partial \alpha}\right)\left(\frac{\alpha_i^0}{\mathrm{CO}^0}\right)_{i=1,\ldots,n} \tag{3.5}$$

where n is the number of independent parameters in the model, the superscript 0 denotes the nominal value and $\partial\mathrm{CO}/\partial\alpha$ is the local sensitivity of the cost function CO with respect to small variations in the model's parameters. A forward difference approximation was implemented as used in [143]

$$\left(\frac{\partial \mathrm{CO}}{\partial \alpha_i}\right) = \frac{\mathrm{CO}(\alpha_i^0 + \Delta\alpha_i) - \mathrm{CO}(\alpha_i^0)}{\Delta\alpha_i}, \quad (i = 1, \ldots, \mathrm{n}) \tag{3.6}$$

where $\Delta\alpha_i$ is the parameter variation with step sizes of 10% and 25% in increment from the nominal parameter values. Tables 3.7, 3.9, 3.10 and 3.8 present numerical results for the relative sensitivities of CO, MSAP, MPAP and CVP, respectively, to the top 15 most significant parameters out of the total 492 model parameters for the uncontrolled CV model. The parameters are ordered from high to low according to their absolute values. Tables 3.11, 3.13, 3.14 and 3.12 present the results for the autoregulated CV model.

3.2.1 Results and Discussion

From Tables 3.7, 3.9, 3.10, 3.8 it can be appreciated that 8 parameters repeatedly appear to have a significant influence over the output variables for the uncontrolled analysis, these are: heart period, T, total blood volume, $\mathrm{V}_{\mathrm{total},0}$, onset of atria filling T_{af}, right ventricular volume, $\mathrm{V}_{\mathrm{rv},0}$, right ventricular minimum elastance, $\mathrm{E}_{\mathrm{rv},\ \mathrm{min}}$, venous compliance of the splanchnic vascular bed, $\mathrm{C}_{\mathrm{svn,svb}}$, inferior vena cava resistance, $\mathrm{R}_{\mathrm{ivc}}$ and splanchnic arteriolar resistance $\mathrm{R}_{\mathrm{sar,svb}}$.

This result is consistent with mechanisms that drive CO, mainly heart rate and stroke volume. The latter is in turn affected by venous return and onset of atria filling through the Frank-Starling mechanism.

According to Table 3.7 the main determinants of CO are heart period, T, total blood volume, $\mathrm{V}_{\mathrm{total},0}$, right ventricular diastolic elastance, $\mathrm{E}_{\mathrm{rv},\ \mathrm{min}}$, splanchnic arteriolar resistance $\mathrm{R}_{\mathrm{sar,svb}}$ and right ventricular volume, $\mathrm{V}_{\mathrm{rv},0}$. This result is consistent with mechanisms that drive CO, mainly heart rate and stroke volume. Stroke volume, in turn, is determined by the right ventricular end-diastolic volume (RVEDV), which is mainly governed by venous return, minimum right ventricular elastance, $\mathrm{E}_{\mathrm{rv},\ \mathrm{min}}$, and onset of atria filling,T_{af}. Other main factor influencing CO is TPR, the splanchnic vascular bed has the largest CO

Table 3.7. Relative sensitivities of CO for the uncontrolled CV model

Parameter $[\alpha_i]$	Relative Sensitivity $\left[\frac{\Delta\alpha_i}{\alpha_i^0}\right] = 0.10$	$\left[\frac{\Delta\alpha_i}{\alpha_i^0}\right] = 0.25$
T	1.233	1.083
$V_{\text{total,0}}$	0.979	0.966
$E_{\text{rv, min}}$	0.717	0.712
$R_{\text{sar,svb}}$	0.706	0.707
$V_{\text{rv,0}}$	0.555	0.559
$R_{\text{sar,rvb}}$	0.402	0.402
$V_{\text{lv,0}}$	0.298	0.300
$P_{\text{rv,0}}$	0.141	0.143
$E_{\text{rv, max}}$	0.097	0.122
T_{af}	0.275	0.107
$E_{\text{rv, min}}$	0.101	0.096
$P_{\text{lv,0}}$	0.106	0.093
T_{vf}	0.053	0.085
T_{vc}	0.078	0.085
R_{ivc}	0.074	0.080

distribution hence, splanchnic arteriolar resistance ranked highest amongst other vascular beds.

The sensitivity spectrum for CVP; see Table 3.8, displays an expected overlap with some of the determinants of CO and this in turn being a consistent result with the Frank-Starling mechanism of the heart. CVP is determined by the addition of all the systemic veins flow into the right atrium. The sensitivity spectrum is found to be consistent with this fact given that the most influencing parameters are related to venous return to the heart such as right ventricular volume, $V_{\text{rv,0}}$, onset of atria filling,T_{af}, venous compliance of the splanchnic, $C_{\text{svn,svb}}$, and renal, $C_{\text{svn,rvb}}$, vascular beds since over 50% of the total circulating blood volume resides within those beds.

The sensitivity spectrum for MSAP; see Table 3.9, displays an overlap with both the CO and CVP sprectra hence overstating the presence of a strong Frank-Starling mechanism in the CV model. In the native system, increased arterial pressure is connected to a series of events starting from an increased circulating blood volume which in turn increases venous return to the heart ultimately increasing CO and arterial pressure.

The sensitivity spectrum for MPAP; see Table 3.10, displays an expected overlap with

Table 3.8. Relative sensitivities of CVP for the uncontrolled CV model

Parameter $[\alpha_i]$	Relative Sensitivity $\left[\frac{\Delta\alpha_i}{\alpha_i^0}\right] = 0.10$	$\left[\frac{\Delta\alpha_i}{\alpha_i^0}\right] = 0.25$
$V_{rv,0}$	0.972	0.977
T_{af}	0.740	0.296
$C_{svn,svb}$	0.433	0.406
$V_{total,0}$	0.407	0.401
$V_{svb,0}$	0.369	0.367
R_{ivc}	0.361	0.352
$C_{svn,rvb}$	0.354	0.332
$V_{rvb,0}$	0.321	0.320
$R_{svn,svb}$	0.321	0.297
$E_{rv,\ min}$	0.272	0.238
$P_{rv,0}$	0.269	0.272
$R_{sar,svb}$	0.261	0.243
$E_{rv,\ max}$	0.239	0.217
$R_{ssv,svb}$	0.238	0.226
T	0.216	0.217

both CO and CVP sensitivity spectra given that all returning blood first enters the pulmonary circulation. In addition to these, pulmonary arteriolar resistance, R_{par}, ranked top three amongst the most influencing parameters of MPAP.

The same parameters that rank high in the sensitivity spectra of the uncontrolled system rank high in the corresponding spectra of the controlled system. However, the heart rate controller and the pressure and volume reflex reference points were commonly found in the sensitivity spectra of the autoregulated system. From Tables 3.11, 3.8, 3.13 and 3.14 it can be appreciated that 7 parameters repeatedly appear to have a significant influence over the output variables for the controlled analysis, these are: CO reference point CO_{ref}, onset of ventricular filling T_{vf}, total blood volume $V_{total,0}$, systemic arterial baroreflex gain G_{sap}, GFR gain G_{gfr}, right atrium volume reference point $V_{ra,ref}$ and the heart rate set-point T_{ref}.

Table 3.9. Relative sensitivities of MSAP for the uncontrolled CV model

	Relative Sensitivity	
Parameter $[\alpha_i]$	$\left[\frac{\Delta\alpha_i}{\alpha_i^0}\right] = 0.10$	$\left[\frac{\Delta\alpha_i}{\alpha_i^0}\right] = 0.25$
$V_{total,0}$	1.655	1.715
$V_{rv,0}$	0.492	0.495
T	0.329	0.333
$V_{lv,0}$	0.307	0.311
T_{af}	0.235	0.091
$R_{sar,svb}$	0.159	0.150
$R_{sar,rvb}$	0.128	0.122
$P_{rv,0}$	0.127	0.125
$P_{lv,0}$	0.106	0.096
$E_{rv,\ min}$	0.104	0.098
$C_{svn,svb}$	0.101	0.085
$R_{sar,cvd}$	0.099	0.098
$E_{lv,\ min}$	0.098	0.093
$E_{rv,\ max}$	0.090	0.107
$V_{svb,0}$	0.089	0.081

Table 3.10. Relative sensitivities of MPAP for the uncontrolled CV model

	Relative Sensitivity	
Parameter $[\alpha_i]$	$\left[\frac{\Delta\alpha_i}{\alpha_i^0}\right] = 0.10$	$\left[\frac{\Delta\alpha_i}{\alpha_i^0}\right] = 0.25$
$V_{rv,0}$	0.832	0.834
$V_{total,0}$	0.770	0.730
R_{par}	0.714	0.705
$V_{lv,0}$	0.346	0.342
$P_{rv,0}$	0.212	0.217
T	0.196	0.196
$E_{rv,\ max}$	0.208	0.187
$E_{rv,\ min}$	0.210	0.180
R_{ivc}	0.145	0.140
$C_{svn,svb}$	0.144	0.138
$V_{svb,0}$	0.132	0.136
T_{vf}	0.142	0.128
$P_{lv,0}$	0.121	0.122
$V_{rvb,0}$	0.115	0.117
$C_{svn,rvb}$	0.120	0.115

Table 3.11. Relative sensitivities of CO for the autoregulated model

	Relative Sensitivity	
Parameter $[\alpha_i]$	$\left[\frac{\Delta\alpha_i}{\alpha_i^0}\right] = 0.10$	$\left[\frac{\Delta\alpha_i}{\alpha_i^0}\right] = 0.25$
$\mathrm{CO_{ref}}$	9.403	6.336
$\mathrm{T_{vf}}$	0.097	4.059
$\mathrm{T_{ref}}$	9.098	3.608
$\mathrm{V_{total,0}}$	9.128	3.285
$\mathrm{P_{s,ref}}$	1.410	2.922
$\mathrm{R_{sar,svb}}$	1.935	1.742
$\mathrm{E_{lv,\ min}}$	1.422	1.733
$\mathrm{G_{sap}}$	0.565	1.610
$\mathrm{G_{gfr}}$	9.504	1.293
$\mathrm{E_{lv,\ max}}$	1.075	0.986
$\mathrm{V_{p,0}}$	1.075	0.986
$\mathrm{V_{lv,0}}$	0.939	0.902
$\mathrm{V_{ao,0}}$	0.977	0.780
$\mathrm{R_{ivc}}$	0.638	0.583
$\mathrm{R_{sar,rvb}}$	0.678	0.488

Table 3.12. Relative sensitivities of CVP for the autoregulated model

	Relative Sensitivity	
Parameter $[\alpha_i]$	$\left[\frac{\Delta\alpha_i}{\alpha_i^0}\right] = 0.10$	$\left[\frac{\Delta\alpha_i}{\alpha_i^0}\right] = 0.25$
$\mathrm{CO_{ref}}$	0.877	1.262
$\mathrm{V_{total,0}}$	0.986	1.180
$\mathrm{T_{ref}}$	0.917	0.922
$\mathrm{G_{gfr}}$	0.201	0.602
$\mathrm{V_{ra,ref}}$	0.420	0.580
$\mathrm{V_{svb,0}}$	0.444	0.444
$\mathrm{G_{sap}}$	0.123	0.421
$\mathrm{C_{svn,svb}}$	0.473	0.420
$\mathrm{C_{ivc}}$	0.431	0.412
$\mathrm{V_{rvb,0}}$	0.386	0.385
$\mathrm{C_{svn,rvb}}$	0.408	0.361
$\mathrm{T_{vf}}$	0.003	0.356
$\mathrm{E_{lv,\ max}}$	1.089	0.340
$\mathrm{R_{sar,svb}}$	0.366	0.327
$\mathrm{R_{ivc}}$	0.329	0.310

Table 3.13. Relative sensitivities of MSAP for the autoregulated model

Parameter $[\alpha_i]$	Relative Sensitivity $\left[\frac{\Delta\alpha_i}{\alpha_i^0}\right] = 0.10$	 $\left[\frac{\Delta\alpha_i}{\alpha_i^0}\right] = 0.25$
$\mathrm{CO_{ref}}$	4.362	5.183
$\mathrm{P_{syst,ref}}$	0.864	2.550
$\mathrm{k_{gfr}}$	0.058	1.755
$\mathrm{V_{total,0}}$	3.734	1.348
$\mathrm{V_{ra,ref}}$	0.500	1.301
$\mathrm{E_{lv,\ min}}$	1.317	1.237
$\mathrm{E_{lv,\ max}}$	4.506	0.878
$\mathrm{k_{sap}}$	0.818	0.681
$\mathrm{T_{vf}}$	0.670	0.577
$\mathrm{T_{af}}$	0.595	0.535
$\mathrm{V_{p,0}}$	0.595	0.535
$\mathrm{R_{sar,svb}}$	0.603	0.505
$\mathrm{R_{sar,rvb}}$	0.477	0.457
$\mathrm{V_{rv,0}}$	0.511	0.425
$\mathrm{R_{sar,cvb}}$	0.478	0.394

Table 3.14. Relative sensitivities of MPAP for the autoregulated model

Parameter $[\alpha_i]$	Relative Sensitivity $\left[\frac{\Delta\alpha_i}{\alpha_i^0}\right] = 0.10$	 $\left[\frac{\Delta\alpha_i}{\alpha_i^0}\right] = 0.25$
$\mathrm{CO_{ref}}$	0.593	1.355
$\mathrm{V_{rv,0}}$	0.819	0.825
$\mathrm{P_{pul,ref}}$	0.814	0.813
$\mathrm{V_{ra,ref}}$	0.500	0.594
$\mathrm{k_{pap}}$	0.532	0.532
$\mathrm{k_{sap}}$	0.323	0.530
$\mathrm{V_{total,0}}$	0.477	0.517
$\mathrm{E_{lv,\ max}}$	1.142	0.455
$\mathrm{T_{vf}}$	0.251	0.298
$\mathrm{P_{rv,0}}$	0.217	0.215
$\mathrm{T_{ref}}$	0.297	0.187
$\mathrm{E_{rv,\ min}}$	0.193	0.159
$\mathrm{k_{GFR}}$	0.154	0.139
$\mathrm{E_{rv,\ max}}$	0.126	0.110
$\mathrm{E_{lv,\ min}}$	0.101	0.109

Chapter 4

Simulations and Selection of Centrifugal Pump Operating Condition

This Chapter will be concerned with the calculation of the hemodynamic variables in the healthy or control condition and their comparison with experimental data extracted from the literature review carried out on this topic. It also considers the simulation of HF Class III and IV with and without a MCS device.

The model written by Prof. T. Alexander was originally solved explicitly in C language with a fourth-order Runge-Kutta formulation [100]; this implementation was found to be computationally costly. To overcome this issue Simulink software (MathWorks®) is implemented in this work to solve the set of ordinary differential equations (ODE) that represent the mathematical model of the CV system as presented in Chapter 2. The selected solver is ode15s (stiff/NDF) given that the present CV model becomes unstable if a large step size is used; in other words, the set of ODEs are stiff. A varible-step solver is hereby used to obtain satisfactory results. Other important parameters are specified in Table 4.1.

The simulations reach periodic solution after the forty fourth heart cycles; see Fig. 4.1. In all simulated cases the converged solution of the 100^{th} second is presented in the figures; however, to facilitate discussion of results, the time scale is normalised by the time period.

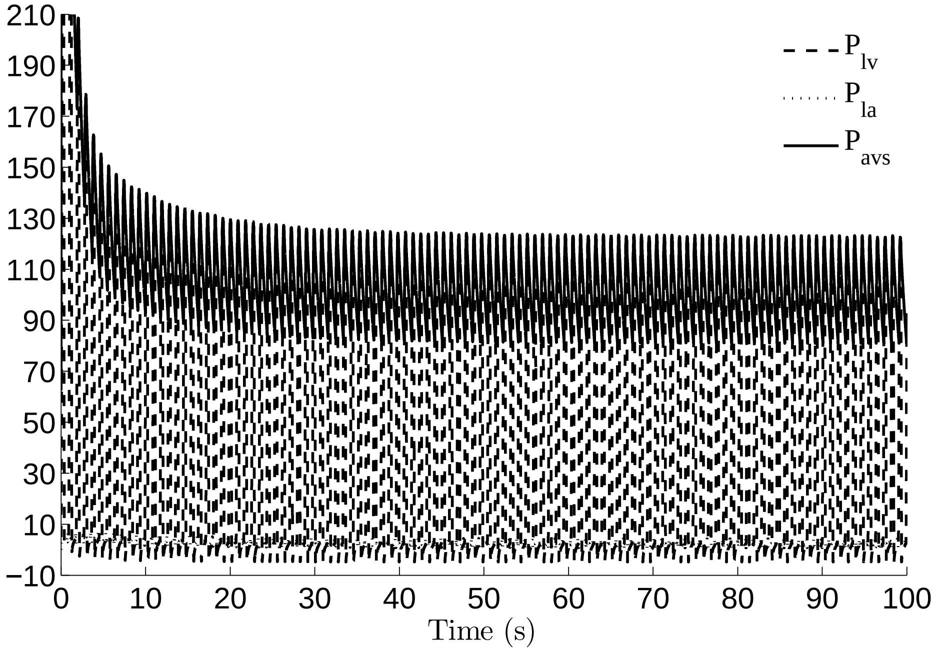

Figure 4.1. System response with cardiovascular model in normal or control state. Periodic solution obtained after the forty fourth heart cycle (40^{th} second).

4.1 Modelling Healthy or Control Condition

Fig. 4.2 shows the simulation results for pressure, flow and volume changes in the four cardiac chambers during normal or control state. In general, the pulmonary artery pressure is 25.7/12.3 mmHg, aortic pressure 124/82 mmHg, total pulmonary resistance of 0.185 mmHg.s/ml, total peripheral resistance (TPR) 1.27 mmHg.s/ml, CO 5.6 lt/min, LVSV 79 ml, and left ventricular stroke work (LVSW) 1.1 J. Other important commonly used clinical parameters are summarized in Table 4.2. In this Table a comparison between calculated and experimental data extracted from the literature review is provided. In general, it can be appreciated that the model gives a good estimate of cycle-averaged haemodynamic varibles but when compared with full time pressure histories there are several features that are not adequately represented; see Fig. 4.4 (a) and (c). Nevertheless, the model is adequate enough for the purpose set out in this work.

The combination of the modified PV relation and valve models predicted several important features in the pressure, flow and volume calculations of the cardiac chambers. In the atrial model, the V-wave, Y-descent, and A-wave were evidently seen. They indicate the

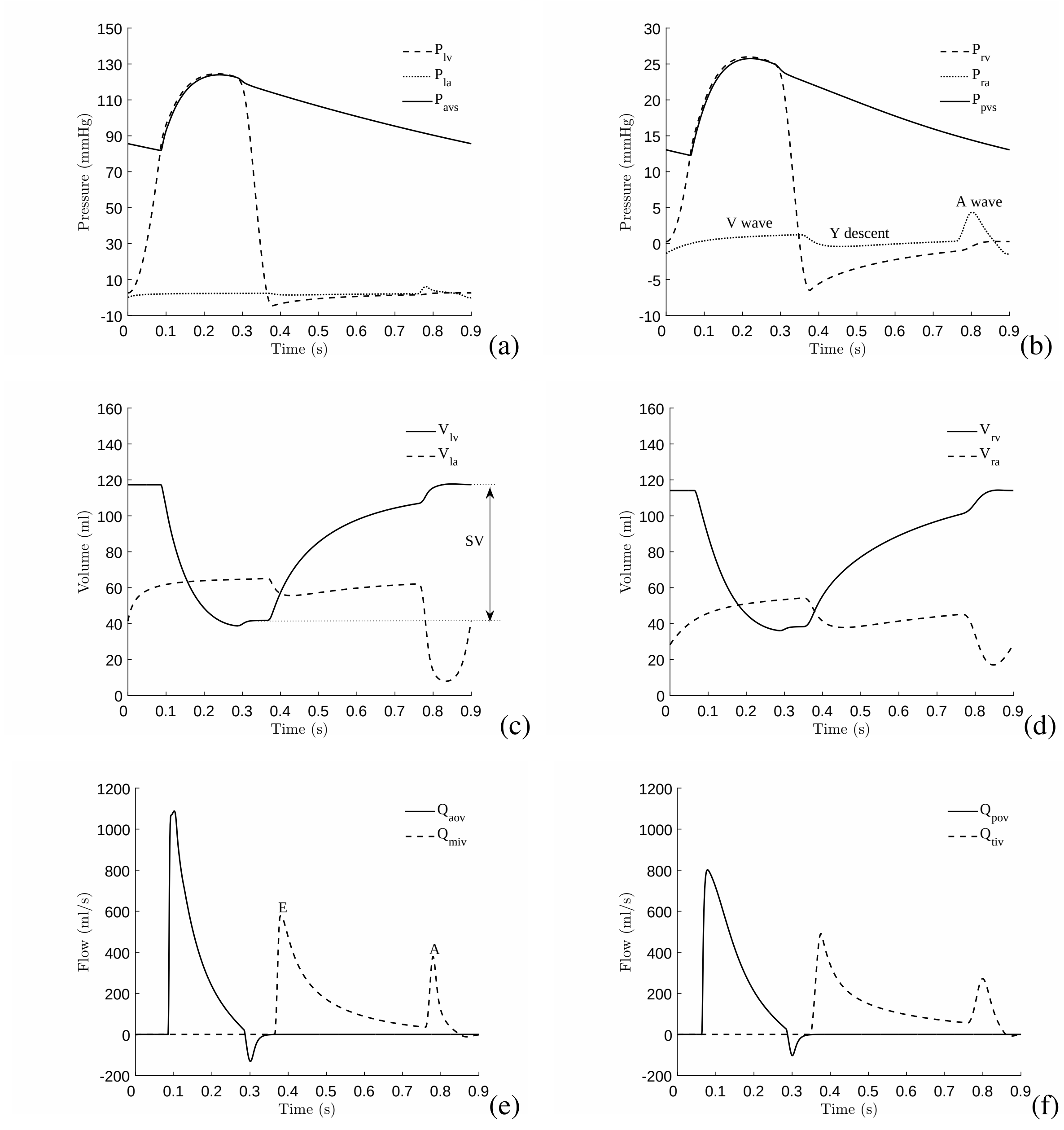

Figure 4.2. System response with cardiovascular model in normal or control state: (a) left heart pressure waveforms; (b) right heart pressure waveforms, (c) left heart volume waveforms, (d) right heart volume waveforms, (e) aortic and mitral valvular flow and (f) pulmonary and tricuspid valvular flow.

Table 4.1. Simulation configuration parameters

Parameter	Value/specification
Solver	ode15s (stiff/NDF)
Type	variable step
Max. step size	0.001
Min. step size	auto
Initial step size	auto
Relative tolerance	1e-3
Absolute tolerance	1e-6
Solver reset method	Fast
Maximum order	3
No. of consecutive min. steps	1
Solver Jacobian method	sparse perturbation ‡

‡ Sparse methods are beneficial for models having a large number of states; the run-time performance is also improved.

changes in pressure according to the filling pressure, the opening of the atrio-ventricular valves and the actual atrial contraction, respectively as seen in Fig. 4.3. In the ventricular model, a realistic description of the chamber volume is achieved, the instances of isovolumetric contraction, isovolumetric relaxation, rapid-ejection phase, filling phase and the atrial boost (due to the atrio-ventricular interaction), are clearly identified as seen in Fig. 4.2(c)-(d). The atrio-ventricular valve flow is also realistically modelled, showing two main peaks better known as the E and A velocities as seen in Fig. 4.2(e)-(f).

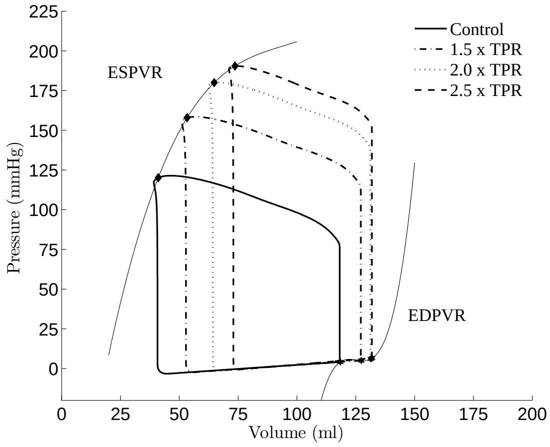

Figure 4.3. Illustration of validation test for calculated PV relation.

To further validate the model's trends, a test was carried out in a similar way as Smith

Table 4.2. Comparison of calculated and experimental data in control condition.

Variable	Simulation	Measurement (range)	Unit
$P_{\text{avs,s}}$	124.0	90 – 140 [166]	mmHg
$P_{\text{avs,d}}$	82.0	60 – 90 [166]	mmHg
$P_{\text{avs,mean}}$	96.0	70 – 105 [166]	mmHg
$P_{\text{svn,mean}}$	3.8	4 – 13 [143]	mmHg
$P_{\text{pvs,s}}$	25.7	15 – 30 [166]	mmHg
$P_{\text{pvs,d}}$	12.3	5 – 15 [166]	mmHg
$P_{\text{pvs,mean}}$	19.0	10 – 20 [166]	mmHg
$P_{\text{pvn,mean}}$ ‡	2.2	3 – 15 [166]	mmHg
$P_{\text{ra,mean}}$	0.46	$-2-2$ [143]	mmHg
$P_{\text{rv,s}}$	26.0	15 – 30 [166]	mmHg
$P_{\text{rv,d}}$	0.26	0 – 8 [166]	mmHg
$P_{\text{la,mean}}$	2.1	2 – 12 [143]	mmHg
$P_{\text{lv,s}}$	124.5	90 – 140 [166]	mmHg
$P_{\text{lv,d}}$	2.1	4 – 12 [166]	mmHg
TPR	1.27	0.85 – 0.13 [166]	mmHg.s/ml
SV	79	70 – 80 [5]	ml
LVSW	1.1	1(mean) [5]	J
MiV E/A Ratio	1.81	0.98 (mean) [167]	-
CO	5.6	4 – 7 lt/min [5]	lt/min

‡ Comparable to Pulmonary capillary wedge pressure

et al. [92]. This test consists of increasing TPR by 50% each time. Four PV loops were obtained and two representative isochrones were plotted. The non-linear isochrones obtained with the modified PV relation model were found to follow physiological trends as described by Lankhaar et al, [118] in which the end-systolic pressure-volume relation (ESPVR) showed a concavity towards the volume axis; see Fig. 4.3. In general it was found that, the higher the resistance the higher the stroke work and the smaller the CO.

4.2 Modelling Heart Failure

In order to validate the present CV model, a series of cases representing the development and progression of left ventricular systolic dysfunction (LVSD) were simulated, see Fig. 4.4(a)-(h). The simulations initiate by modelling a healthy condition (see Fig. 4.4(a)-

(b)), typical of a young healthy subject; then progress to established hypertension (see Fig. 4.4(c)-(d)) in which LV hypertrophy is commonly found and begins the process of systolic heart failure [168]; see Fig. 4.4(e)-(f). Finally, a severe heart failure (HF) condition is simulated, see Fig. 4.4(g)-(h). The progression from normal condition to severe heart failure was achieved by decreasing systemic compliance while concurrently increasing TPR; total volume was also increased with the purpose of mimicking volume overload as frequently found in hypertensive patients and strongly correlated with progression to HF [169, 170]. To mimic depressed cardiac contractility, as consistently observed even in the mildest early stages of heart failure [169, 171], $E_{\text{lv,max}}$ was decreased and $E_{\text{lv,min}}$ was increased [172]. Lastly, static gain values, G_X, that modify the ANS signal response, $Y(t)$ (as described in Chapter 2 section 2.3), were reduced to a third of their normal value to mimic the abnormal function of the baroreflex system given that is a commonly found feature in patients with HF [13].

From Fig. 4.4(a)-(h), it can be observed that the CV model follows the clinically measured AoP waveforms (shown in the dotted curves in Fig. 4.4 (a), (c), (e) and (g)); moreover, it accurately predicts LV volume, in particular, it captures the increase in LVEDV as heart failure progresses.

The main disadvantage of the present CV model is the lack of a pressure wave propagation model. This results in a poor representation of the early stages of the systolic AoPW and an elevated area under the diastolic portion of the AoPW; see Fig. 4.4(a) and (c). In the native system, the aortic pressure waveform (AoPW) consists of a forward-travelling wave generated by LV work, and a backward-travelling wave generated by the reflection of the forward wave from different sites along the arterial tree [168]; see the purple shaded area in Fig. 4.5. This area under the systolic portion of the reflected wave represents the required LV effort necessary to overcome the augmented pressure. Nonetheless, when simulating HF conditions the AoPW appears to be better represented; this can be appreciated in Fig. 4.4(e) and (f). The reason for this false improvement is that wave reflection is directly affected by the elastic properties of the arterial tree; in HF conditions, the arterial

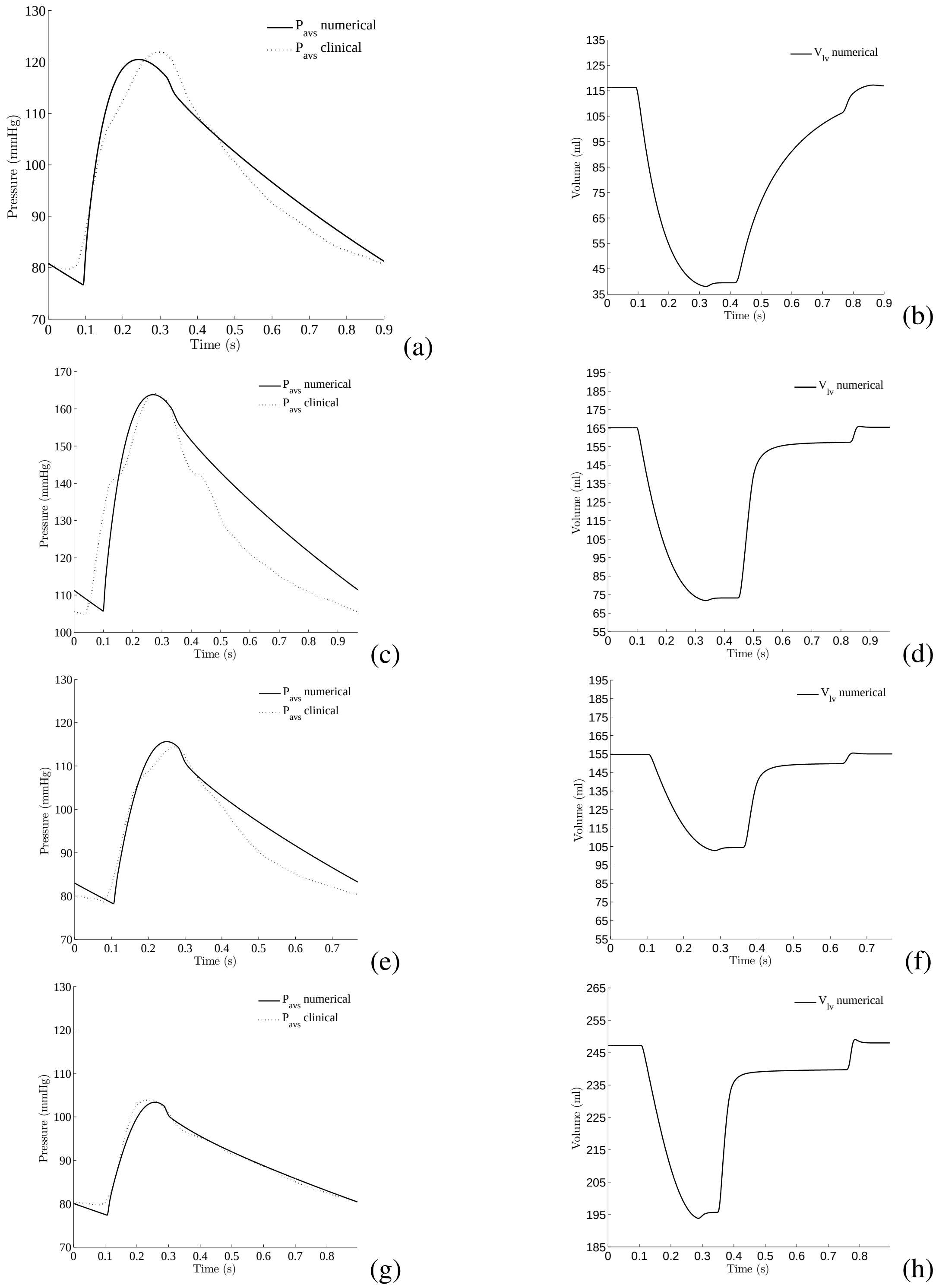

Figure 4.4. System response during different simulated cases showcasing changes that occur in the central aortic pressure waveform (AoPW) and left ventricular volume (LVV) during the development and progression of LVSD. (a-b) Young normal AoPW; (c-d) established hypertension in the elderly; (e-f) mild heart failure; (g-h) severe LVSD. Solid curves indicate the calculated AoPW; dotted curves, clinical AoPW. Clinical data was extracted from Denardo et al. [168].

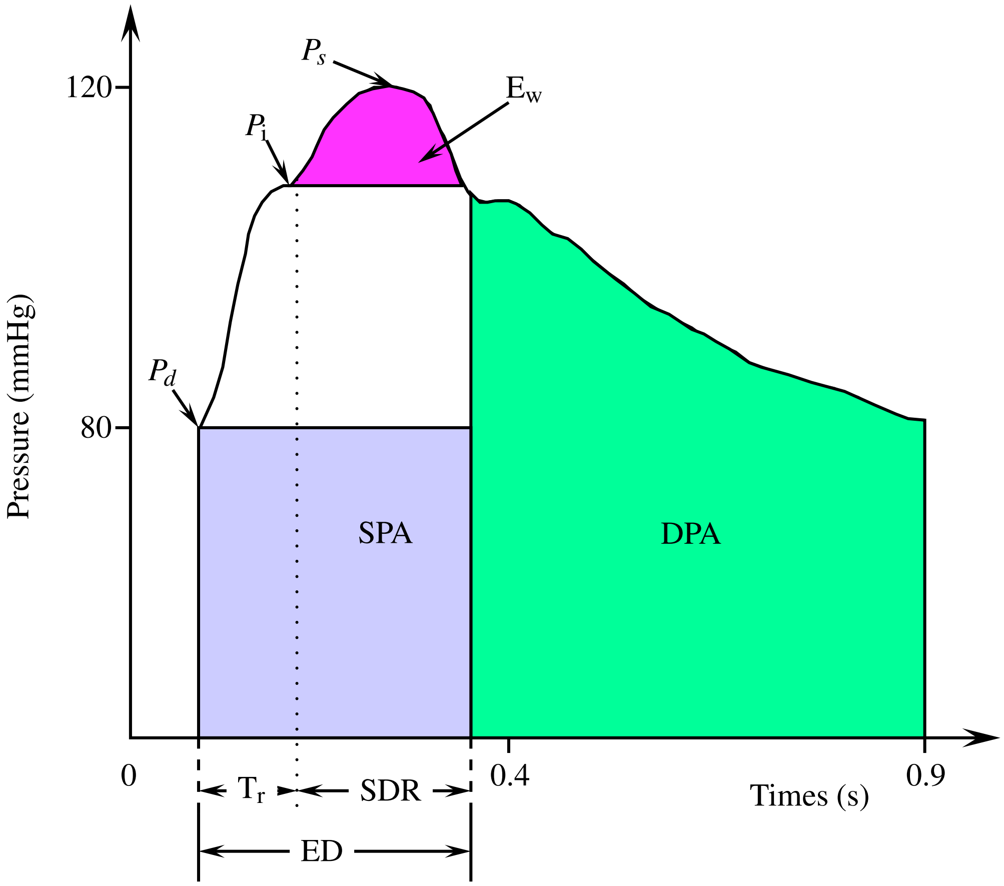

Figure 4.5. A central aortic pressure waveform. P_d: diastolic pressure; P_s: systolic pressure; P_i: inflection point (merging point of the forward and reflected waves); SPA: systolic pressure area; DPA: diastolic pressure area; ED: ejection duration; T_r: round-trip travel time of the pressure wave to and from the major reflecting SDR: systolic duration of reflected wave; E_w: LV wasted effort. Adapted from Denardo et al. [168]

tree is very stiff resulting in faster pulse wave velocities (PWV) and faster arrival of the backward-travelling wave; see Fig. 4.4 (e) and (g). This can be identified by the variable T_r in Fig. 4.5 representing the time difference between the occurrence of the diastolic pressure, P_d, and that of the point of inflection, P_i.

4.3 Transient Response with MCS device

In this section, a MCS device is installed in series with the left ventricle in two different locations, AAo and DAo, with the intention of numerically identifying an adequate pump operating point. This was achieved by heuristically modifying ΔP_{pump} while the cardiovascular system is set up to mimic two diseased conditions; namely, mild HF (NYHA Class III) and advanced HF (NYHA Class IV). An adequate pump design point was considered as one that would established a normal CO without compromising cerebral perfusion. The transient haemodynamic responses of MAP, mean pulmonary arterial pressure (MPAP), HR and CO to MCS support before and after the MCS device is switched on were evaluated for the above diseased conditions. A summary of these variables is presented in Tables 4.3 and 4.4.

Table 4.3. Calculated haemodynamic variables in HF Class III condition with MCS device.

Installation site	Variable	Value	Unit
Pump at AAo	$P_{\text{avs,mean}}$	81.4	mmHg
	$P_{\text{pvs,mean}}$	23.9	mmHg
	$P_{\text{ca,mean}}$	137.1	mmHg
	$P_{\text{re,mean}}$	130.8	mmHg
	HR	75.1	bpm
	CO	5.9	lt/min
	$Q_{\text{re,mean}}$	1095.0	ml/min
	U_{out}	3.1	ml/min
Pump at DAo	$P_{\text{avs,mean}}$	91.6	mmHg
	$P_{\text{pvs,mean}}$	21.1	mmHg
	$P_{\text{ca,mean}}$	79.8	mmHg
	$P_{\text{re,mean}}$	139.4	mmHg
	HR	73.6	bpm
	CO	6.0	lt/min
	$Q_{\text{re,mean}}$	1254.0	ml/min
	U_{out}	3.4	ml/min

In all modelled transient-response cases the hemodynamic variables CO, renal flow, Q_{re} and urinary output are normalised 5 seconds after the MCS device is switched on. However, in the mild HF case; see Fig. 4.6, MPAP increases from 20 mmHg to 23.42 mmHg indicating that the pulmonary circulation is not coping well with the increased CO.

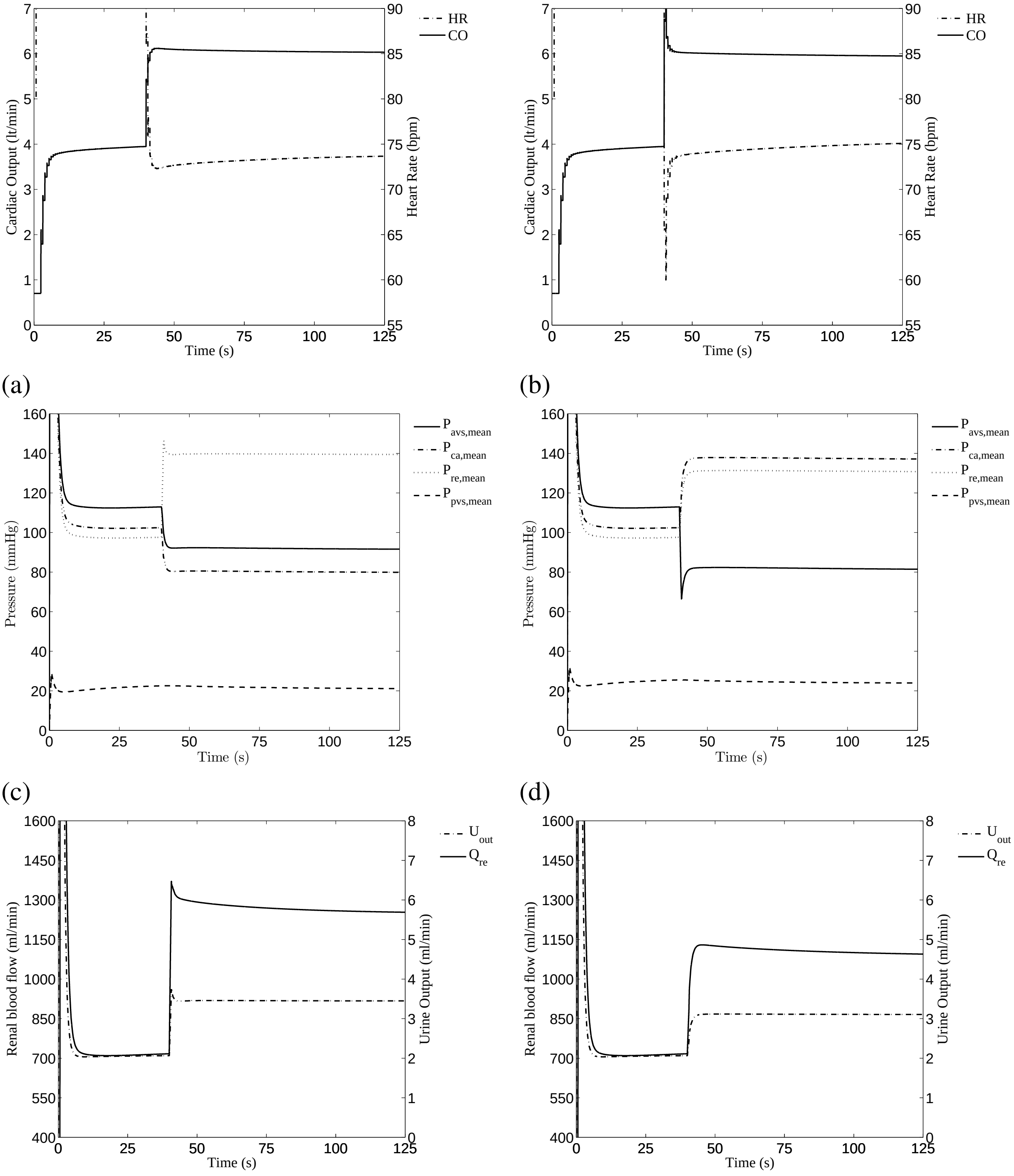

(a) (b)

(c) (d)

(e) (f)

Figure 4.6. Comparison of transient responses to MCS device installed at descending aorta (left) and ascending aorta (right) in Class III HF.

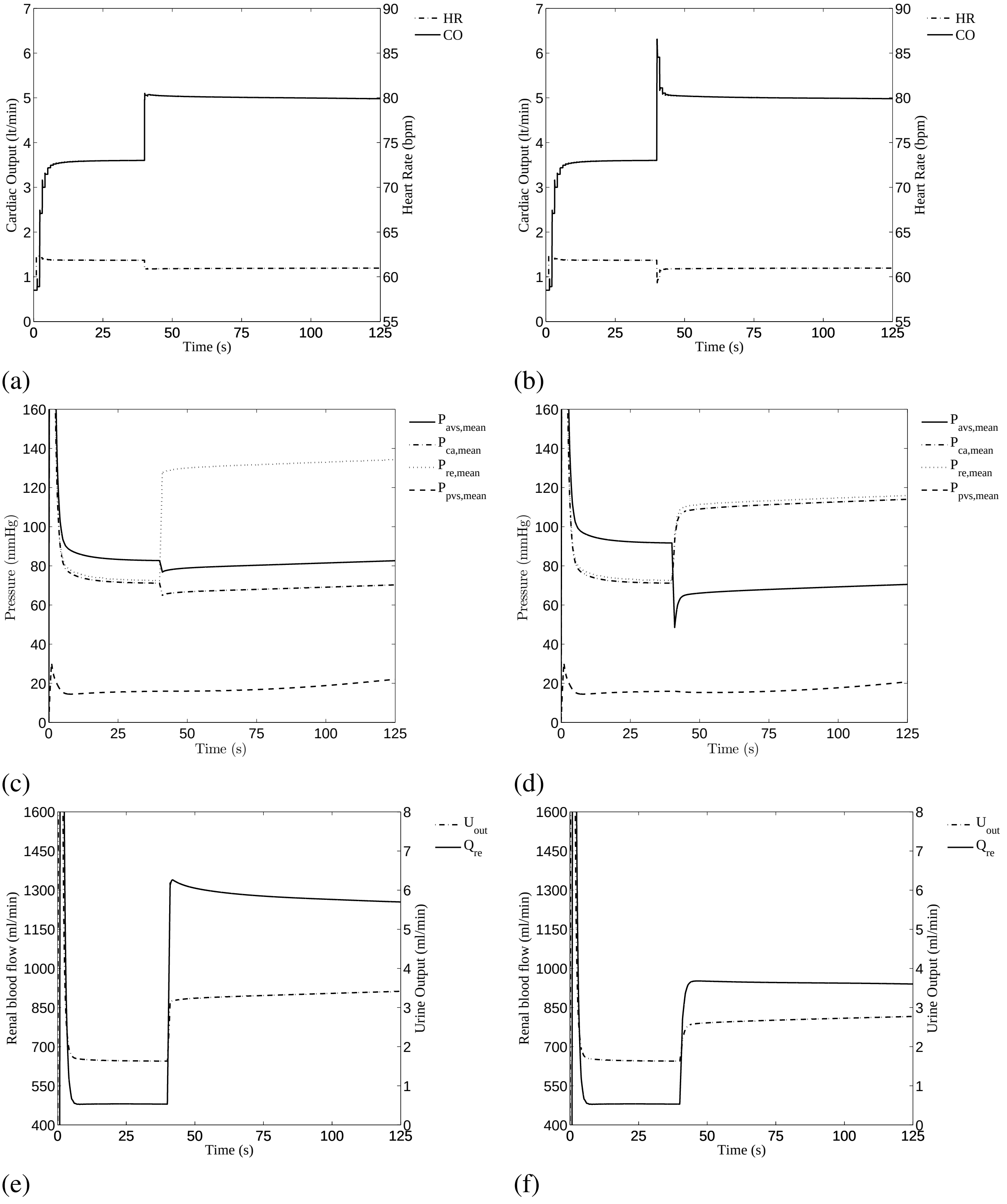

Figure 4.7. Comparison of transient responses to MCS device installed at descending aorta (left) and ascending aorta (right)in Class IV HF.

Table 4.4. Calculated haemodynamic variables in HF Class IV condition with MCS device.

Installation site	Variable	Value	Unit
Pump at AAo	$P_{\text{avs,mean}}$	70.4	mmHg
	$P_{\text{pvs,mean}}$	20.61	mmHg
	$P_{\text{ca,mean}}$	113.8	mmHg
	$P_{\text{re,mean}}$	115.8	mmHg
	HR	60.1	bpm
	CO	5.0	lt/min
	$Q_{\text{re,mean}}$	940.2	ml/min
	U_{out}	2.8	ml/min
Pump at DAo	$P_{\text{avs,mean}}$	82.5	mmHg
	$P_{\text{pvs,mean}}$	21.8	mmHg
	$P_{\text{ca,mean}}$	70.2	mmHg
	$P_{\text{re,mean}}$	134.2	mmHg
	HR	60.1	bpm
	CO	5.0	lt/min
	$Q_{\text{re,mean}}$	1255.0	ml/min
	U_{out}	3.4	ml/min

In Fig. 4.7 the selection of a pressure difference of 70 mmHg corresponding to a flow of 5 lt/min appears to have a better haemodynamic response when compared to that of a system with Class III HF; see Fig. 4.6. In particular, placing the MCS device in ascending aorta accomplishes better perfusion to the head and kidneys as depicted by a $P_{\text{ca,mean}}$ of 71.71 mmHg and $P_{\text{re,mean}}$ of 130.2 mmHg. A $P_{\text{ca,mean}}$ of 71.71 mmHg is well above the lower limit of 60 mmHg necessary to maintain an adequate cerebral perfusion [6, 20]. In Fig. 4.6, it can be appreciated that placing a device in the ascending aorta increases $P_{\text{ca,mean}}$ from 94 mmHg to 140 mmHg; however, $P_{\text{ca,mean}}$ falls right on the upper limit for adequate autoregulated cerebral perfusion; it then could be a risky choice with high possibilities of intra-cranial haemorrhage.

Chapter 5

Centrifugal Pump: Impeller Selection and testing

This chapter is concerned with the selection of an adequate impeller blade profile, inlet and outlet angles, and outer impeller diameter in order to satisfy the design point as mathematically found in Chapter 4, that is, a pressure difference, ΔP, equal to 70 mmHg and a flow rate, Q equal to 5 lt/min. Four different Hozelock pond pumps (Hozelock Ltd., Midpoint Park, Birmingham, England) were initially characterised according to head, flow and rotational speed. The criteria used in selecting an available model was a hydraulic performance that was close to the design conditions determined in Chapter 4 and a rotational speed within $1,200-4,000$ rpm as found in literature review made on commercial LVAD devices operating with centrifugal pumps [67–74, 84, 85]. This allows for a good initial starting point given that the design of a centrifugal blood pump takes into consideration many geometric parameters which leads to a very large number of cases to be analysed. The main disadvantages of using off-the-shelf pond pumps is that the speed cannot be controlled as the motor is sealed (waterproof) and the pump casing cannot be changed; see Fig. 5.1. However, for the purpose of achieving the set out operating condition the existing geometric parameters produce a satisfactory result. Table 5.1 summarises the design constraints and parameters for the pump.

Table 5.1. List of pump design constraints and parameters

	Parameter	Value/Assignment
Operating point	Flow rate	5 lt/min
	Pressure rise	70 mmHg
Geometric constraints	Maximum wall shear stress	< 150 Pa [173]
	Impeller diameter (D_2)	< 33 mm ‡
	Suction inlet diameter (D_1)	20 mm ‡
	Shaft diameter	1.5 mm ‡
	Rotational speed (N)	$2,800$ rpm ‡
	Impeller height	< 7.5 mm ‡
	Minimum blade thickness	> 1 mm †

‡ denotes the constraints imposed by the existing Hozelock pump, model 3378-0000.
† manufacturing constraint imposed by the in-house rapid prototyping machine.

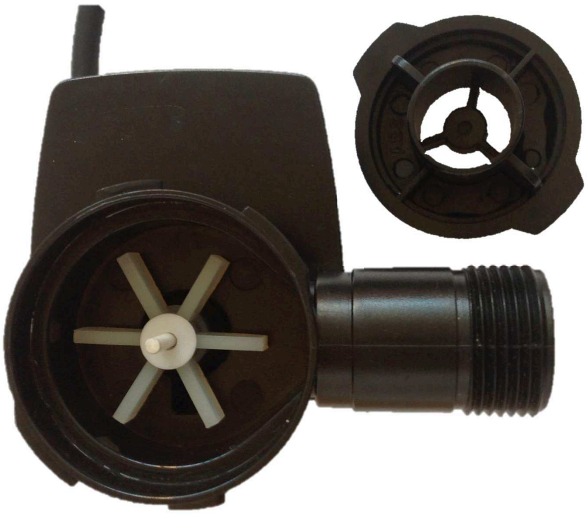

Figure 5.1. Pump casing implemented in this work. Hozelock pond pump model 3378-0000.

5.1 Pump Design Theory

5.1.1 Selection of Impeller Blade angles

Velocity triangles are drawn at two places: inlet and outlet of impeller blades. The relative velocity of flow is considered relative to the impeller. The absolute velocity is equal to the vectorial sum of the relative velocity and the peripheral velocity of the impeller ($U = \omega r$). The liquid in this impeller enters with a tangential component and therefore the mathe-

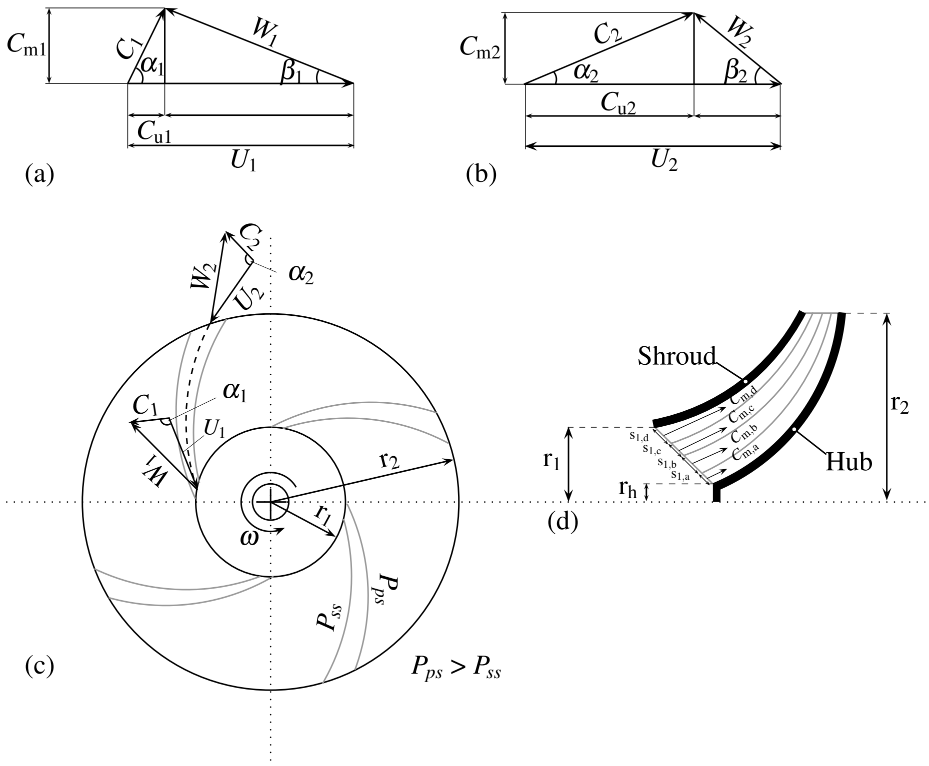

Figure 5.2. Centrifugal pump impeller with the velocity triangles at inlet and outlet. a) entry velocity triangle, b) discharge velocity triangle, c)Velocities in an impeller, d) impeller inlet velocity distribution. Adapted from [174–176]

matical expression for the theoretical head is given as follows

$$H_{\text{theory}} = \frac{U_2 C_{U2} - U_1 C_{U_1}}{g} \tag{5.1}$$

According to this expression the head is built up gradually as both C_{U_2} and U_2 are steadily increased. It also shows that relative velocity does not contribute to an increase in pressure [174].

According to the work by Kovas [175] dynamic depression at the impeller eye is highest at the leading edge of the impeller blades. To achieve the lowest dynamic depression at the impeller entry, the relation between peripheral velocity U_1 and the meridional component of the absolute velocity C_{m_1} must be arranged in such way that the resulting relative velocity W_1 is markedly reduced and the absolute velocity C_1 is slightly higher than C_{m_1}.

From Fig. 5.2(a) the following velocity expression can be derived

$$
\begin{aligned}
C_1^2 &= C_{m1}^2 + C_{U_1}^2 \qquad (5.2)\\
&= C_{m1}^2 + (1-k_U)^2 C_1^2 \qquad (5.3)
\end{aligned}
$$

and

$$W^2 = C_{m1}^2 + ku^2 \qquad (5.4)$$

In order to reduce hydraulic losses a slanted leading edge is implemented. This configuration reduces W_1^2 [175, 177] particularly at the shroud where the curvature of the streamlines is smaller when compared to that of the hub. With this in mind a small pre-rotation at the entrance with a value of 0.1 is implemented [175], that is, $(1-k_U)U_1 = 0.1$ therefore the value of choice for k_U is 0.9. The circulating fluid gains rotation as it approaches the impeller's flow passages; ideally, as it approaches the impeller, the flow should enter in a direction that results in the least flow resistance which is dependent on the blade's inlet angle β_1 [174], this angle can be calculated as follows

$$\tan\beta_1 = \frac{C_{m1}}{U_1 - C_{U_1}} \qquad (5.5)$$

where C_{m1}, for an oblique leading as seen in Fig. 5.2a, is equal to the sum of the partial channels as given by

$$C_{m1} = \sum_{i=1}^{n} \frac{Q}{D_{1,i}\pi b_{1,i}} \left(1 - \frac{s_{1,i}}{t}\right) \qquad (5.6)$$

where s is the circumferential spacing at the leading edge, t is the blade thickness measured along direction of U_1, and n is the number of subdivisions of the leading edge. In this work 4 subdivisions are used.

In this work, the radius was kept constant along the trailing edge of the blade, therefore the outlet was kept constant for all blade spans. The following expression was used to calculate the outlet angle

$$\tan\,\beta_2 = \frac{C_{m2}}{U_2 - C_{U_2}} \tag{5.7}$$

where C_{m2}, U_2 and C_{uU_2} are given as follows

$$C_{m2} = Q/A_2 \tag{5.8}$$

$$U_2 = \omega r_2 \tag{5.9}$$

$$C_{u2} = \frac{Hg}{U_2} \tag{5.10}$$

5.1.2 Selection of Impeller Diameter

According to the hydraulic performances of the 4 available pumps, pump No. 3 was chosen as the starting point with an impeller diameter (D_2) of 33 mm, a rotational speed of $2,800$ rpm and an inlet diameter (D_1 of 20 mm. The latter dimension represents a good selection since it approximates to the values found in the human aorta artery, commonly 29 mm at AAo and 20 mm at DAo [158]. Given that many of the geometric parameters were constrained, this work only pursued to redefine the blade exit width, b_2; the blade angles, β_1 and β_2, and to achieve smooth curves for the blade profile with the ultimate goal of achieving the target operating point as specified in Chapter 4.

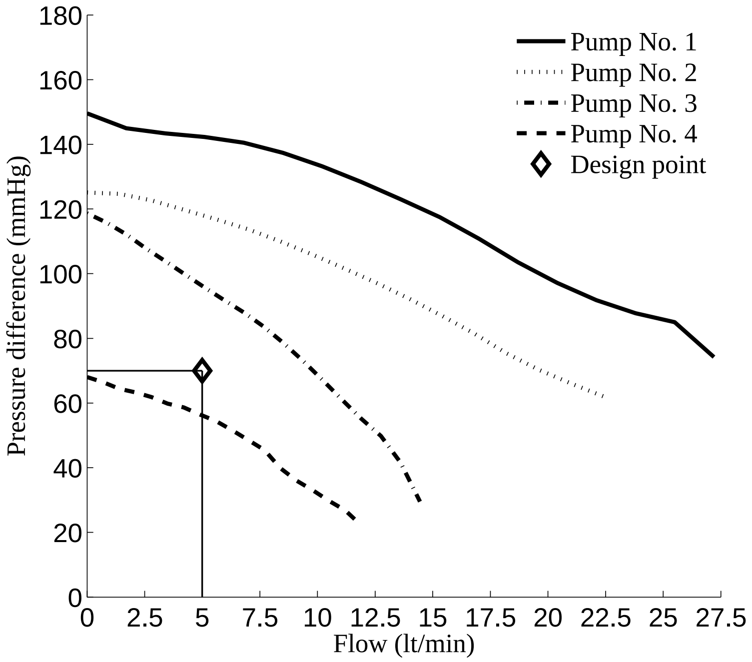

Figure 5.3. Pump performance curves for different Hozelock pump models

5.1.3 Selection of Blade Exit Width

The calculation of the blade exit width departs from the operating point found in Chapter 4, the given rotational speed of 2,800 rpm from the existing Hozelock pump, and assuming a target efficiency of 80%, $\eta = 0.8$. By implementing the coefficient of flow, ϕ, and head coefficient, ψ chart; see Fig. 5.4, the exit width can be calculated as follows

$$\psi = \frac{gH}{\eta U_2^2} \tag{5.11}$$

From Eq. 5.11 the head coefficient is equal to 0.5

$$\phi = \frac{Q}{\pi D_2 b_2 U_2} \tag{5.12}$$

Solving for b_2 gives

$$b_2 = \frac{Q}{\phi \pi D_2 U_2} \tag{5.13}$$

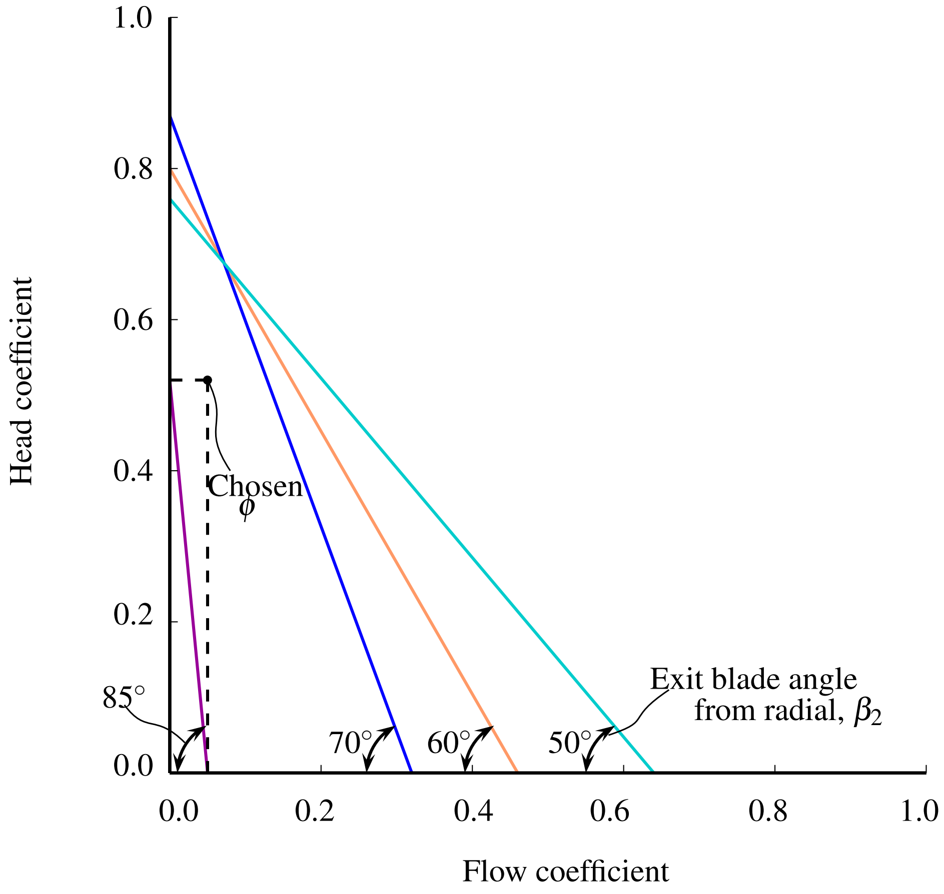

Figure 5.4. Head and flow coefficient diagram. Adapted from [176]

5.1.4 Selection of Number of Blade Sets

The selection of number of blades greatly influences a pump performance. A large number of blade sets reduces recirculation, or slip, given that the impeller passages become narrower. In low-speed low-flow pumps, flow separation is not a dominant feature consequently viscous effects must dominate the flow [178]. The higher the viscosity of a fluid the greater the disc friction and hydraulic losses suggesting that a large number of blade sets could result in a drop in efficiency as a product of a larger surface area [179, 180]. Commonly, the Karl Pfleiderer equation for selection of number of blade sets is used, this equation is given by

$$z = 6.5\frac{r_2 + r_1}{r_2 - r_1}\sin\frac{\beta_1 + \beta_2}{2} \tag{5.14}$$

In section 5.1.1, the inlet and outlet angles were found to be 49.6° and 86°, respectively. When using Eq. 5.14, it was found that the number of blade was high at thirteen blade sets. With this in mind, several cases were simulated in which the number of blades was varied. Table 5.2 summarises the effect of variation of the number of blade sets on pump efficiency, pressure rise, and wall shear stress. It is worth mentioning that only a maximum of eleven blade sets was possible to mesh, any higher than eleven blades resulted in very poor meshes and solver issues.

From Table 5.2, it can be concluded that the impeller with eleven blade sets was the only one to achieve the set out operating point, however, it can also be appreciated that wall shear stress increased as the number of blade sets increased. It is also noticeable that the total efficiency drops as the wall shear stress increases.

Table 5.2. Pump performance results with different number of blade sets

Number of blade sets (z)	Static Head at outlet (m)	Efficiency (%)	Max. Wall Shear (Pa)
6	1.07	60.75	253.25
7	1.06	59.83	267.52
8	1.03	59.33	284.87
9	0.99	58.69	313.32
10	0.94	57.76	403.51
11	0.95	56.63	422.76

5.1.5 Impeller Blade Shape

The meridional coordinate system is used here given its convenience in studying axisymmetric flow as found in impellers. The coordinate axes are axial, Z, radial, R, and circumferential, θ. The latter is the angle measured about the axis of rotation from a rotating reference plane. Having selected the inlet diameter, D_1, exit diameter, D_2, exit width, b_2 blade inlet, β_1, and outlet angles, β_2, a detailed streamwise contour of the blade's angle distribution is next on the blade design process. The shape of the blades and the resulting flow pattern in the impeller determine how energy is transferred to the fluid [176]. In general, the blade shapes can be classified as:

- Backward-curved blades ($\beta_2 < 90°$)
- Radial blades ($\beta_2 = 90°$)
- Forward-curved blades ($\beta_2 > 90°$)

According to the exit velocity diagram; see Fig. 5.2(b), high values of β_2 leads to very high values of C_2 or high kinetic energy; however, its transformation to static pressure can only be appropriately achieved if diffusion takes place in a reasonably sized fixed casing [177]. Since the volute in this work is one of the design constraints, the forward-curved blades were opted out of the selection process; moreover, the blade's outlet angle was found to be lower than 90°. Radial blades have as main advantages that are relatively easy to manufacture and produce the highest pressure when compared with the other two configurations.

5.1.6 Blade Meridional Profile

The calculation of each streamline was achieved by implementing Bezier curves, see Fig.5.5. In this work, a cubic Bezier curve was implemented as it is simple to control yet produces smooth profiles. This type of curve can be mathematically expressed by

$$\mathrm{P}_0^3 = (1-t)^3\mathrm{P}_0 + 3(1-t)^2 t\mathrm{P}_1 + 3(1-t)t^2\mathrm{P}_2 + t^3\mathrm{P}_3 \tag{5.15}$$

where P represents a control point and t is the curve's parameter value.

The inter-displacement of the streamlines is kept equidistant from one another. At the leading edge, an inclination of 32° from axial (Z) was implemented with the purpose of creating a slanted leading edge; see Fig. 5.5(a). The trailing edge, however, was kept parallel to the axis rotation, Z. The radius of curvature at the bend, where the flow direction changes from axial to radial, was made as large as possible from hub to shroud

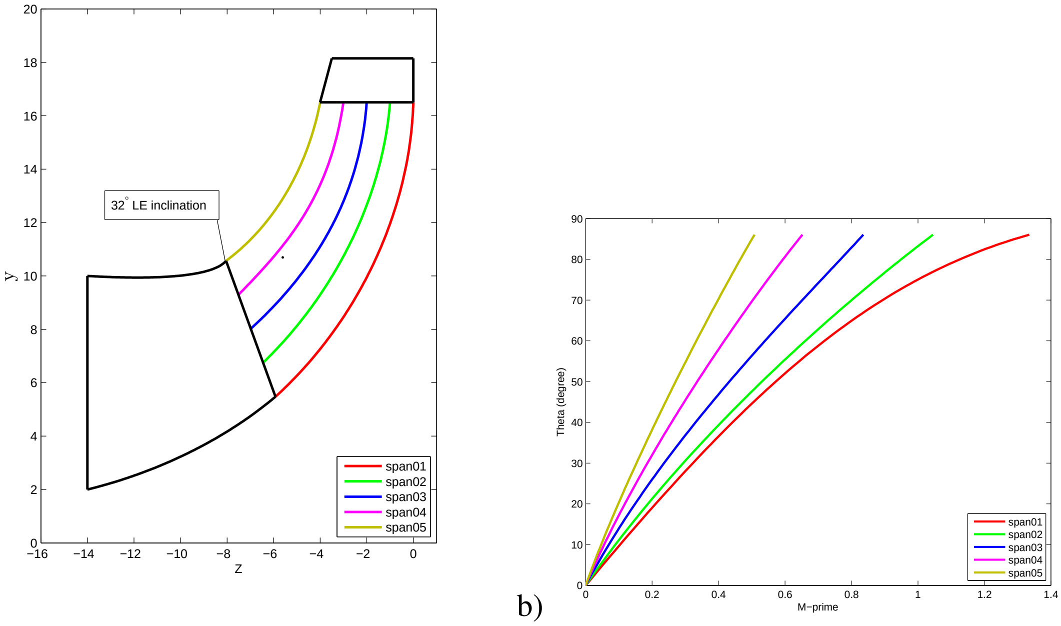

a) b)

Figure 5.5. Graphical representation of: a) blade meridional profiles, and b) blade wrap angles

in order to achieve an adequate performance given that small radius of curvature yields high flow velocity and possible flow separation after the bend, this in turn reduces the total efficiency [177].

5.1.7 Pressure and suction sides

Having identified the inlet and outlet blade angles, β_1 and β_2 respectively, and blade exit width, the setting of the coordinates of the camber line (m,θ) is next in the design process. The angle distribution, β, along the blade was calculated by using a cubic Bezier curve, see Eq. 5.15. The meridional coordinate, m, is expressed as the relationship between the axial and radial locations along the meridional curves or streamlines and can be mathematically written as

$$m = \int_0^S \sqrt{\left(\frac{\mathrm{d}r}{\mathrm{d}s}\right)^2 + \left(\frac{\mathrm{d}z}{\mathrm{d}s}\right)^2}\,\mathrm{d}s \tag{5.16}$$

where s is the distance along the meridional curve, S is the normalized distance along

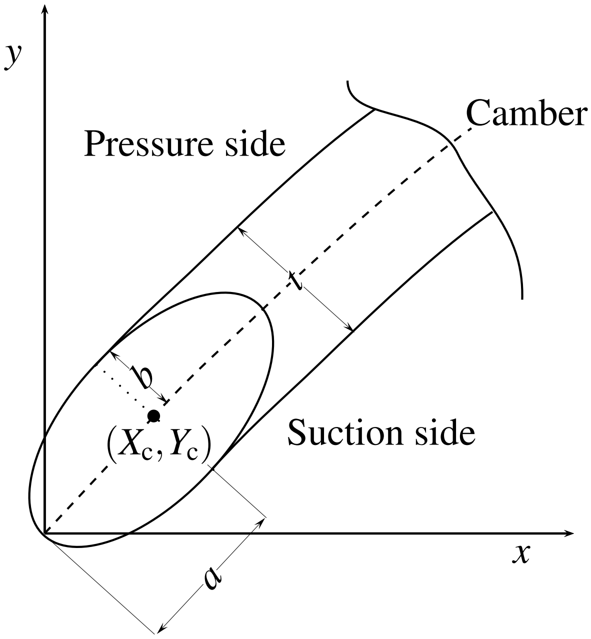

Figure 5.6. Superposition of thickness distribution (including elliptical profile at LE) on the camber line. Adapted from Miloş [181].

meridional curve, r is the radial location, and z is the axial location. The normalized meridional coordinate is given by

$$m' = \int_0^S \left[\frac{\sqrt{\left(\frac{\mathrm{d}r}{\mathrm{d}s}\right)^2 + \left(\frac{\mathrm{d}z}{\mathrm{d}s}\right)^2}}{r} \right] \mathrm{d}s \tag{5.17}$$

The thickness distribution, t, of the blade profile was determined by using a cubic Bezier curve, see Eq. 5.15. The thickness is calculated as gradually increasing from inlet to outlet in order to to provide an uniform change in area from inlet to outlet of impeller flow passage [177]. At the leading edge half ellipse is used for shockless entry [177, 181], see Fig. 5.6. The coordinates of the elliptical leading edge profile (LEP) are determined with the following equations

$$\frac{x_{\mathrm{lep}}^2}{a^2}+\frac{y_{\mathrm{lep}}^2}{b^2}=1 \tag{5.18}$$

$$x_{\mathrm{lep}}=a-X_{\mathrm{c}} \tag{5.19}$$

$$y_{\mathrm{lep}}=\frac{b}{a}\sqrt{a^2-x_{lep}^2} \tag{5.20}$$

where a and b are the semi-major and semi-minor axes of the ellipse respectively, X_{c} and Y_{c} represent the x and y coordinates of the centre of the ellipse, respectively [181].

The next step is to superimpose the thickness distribution on the camber line to create the pressure and suction sides. These can constructed by using the following equations

$$x_{\mathrm{ps}}=r_i\cos\theta_i \tag{5.21}$$

$$y_{\mathrm{ps}}=r_i\sin\left(\theta_i+t_i\right) \tag{5.22}$$

$$x_{\mathrm{ss}}=r_i\cos\theta_i \tag{5.23}$$

$$y_{\mathrm{ss}}=r_i\sin\left(\theta_i-t_i\right) \tag{5.24}$$

where i specifies the variation of radius, r, thickness, t, and angle, θ, from inlet to outlet, x_{ps} and y_{ps} are the x and y coordinates of the pressure side, and x_{ss} and y_{ss} are the x and y coordinates of the suction side. The thickness distribution, t, is given as an angle offset from the camber line, and θ is the blade wrap angle which can be mathematically expressed as

$$\theta=\int\frac{\mathrm{d}m\tan\beta}{r} \tag{5.25}$$

where m is the meridional coordinate as previously described in Eq. 5.16. Fig. 5.6 shows a schematic of the superposition method.

5.1.8 Selection of Impeller Type

Impellers can be classified into opened, semi-opened and closed. An opened impeller has neither hub nor shroud; a semi-opened impeller has a hub but not shroud; a closed impeller has both hub and shroud. In general, opened and semi-opened impellers are subjected to hydraulic friction losses associated with leakage over the clearance between two adjacent impeller blades and the stationary volute wall [174]. However, high specific speed pumps favour from opened impellers given that hydraulic friction losses are balanced [174]. By contrast, in a closed impeller friction losses are associated with flow relative to the inner side of the shroud [174]. A closed type impeller is then selected in this work given that the specific speed, N_s, is not too high at 1594. Specific speed was calculated by the following expression

$$N_s = \frac{NQ^{0.5}}{H^{0.75}} \tag{5.26}$$

5.2 Numerical Method

5.2.1 Governing Equations

The incompressible flow through the rotating impeller is solved in a moving frame of reference with constant rotational speed equal the rotational speed of the impeller. The flow through the stationary parts of the pump is solved in a stationary reference frame. The governing equations for the impeller are formulated below.

Considering water as a constant density fluid, conservation of mass states that the change of mass with respect to time is zero, that is, the mass contained in a given volume, $\forall$, must remain constant [182]. This can be mathematically expressed as

$$m = \int_{\forall} \rho \mathrm{d}\forall \tag{5.27}$$

and the substantial derivative is given by

$$\frac{\mathrm{D}m}{\mathrm{D}t} = \frac{\mathrm{D}}{\mathrm{D}t}\int_{\rlap{-}V} \rho \mathrm{d}\rlap{-}V = 0 \tag{5.28}$$

Applying the Reynolds transport formula the integral becomes

$$\frac{\mathrm{D}}{\mathrm{D}t}\int_{\rlap{-}V} \rho \mathrm{d}\rlap{-}V = \int_{\rlap{-}V} \left(\frac{\partial \rho}{\partial t} + \nabla \cdot (\rho \mathbf{V})\right) \mathrm{d}\rlap{-}V = 0 \tag{5.29}$$

given that the integrand in the bracket must be equal to zero then the continuity equation for unsteady and compressible may be written as

$$\frac{\partial \rho}{\partial t} + \nabla \cdot (\rho \mathbf{V}) = 0 \tag{5.30}$$

where $\nabla \cdot (\rho \mathbf{V})$ is the divergence of the product of a scalar times a vector and can be expanded as follows

$$\nabla \cdot (\rho \mathbf{V}) \equiv (\rho \nabla \cdot \boldsymbol{V}) + (\boldsymbol{V} \cdot \nabla \rho) \tag{5.31}$$

Substituting Eq. 5.31 into Eq. 5.30 the following expression is obtained

$$\underbrace{\frac{\partial \rho}{\partial t} + (\boldsymbol{V} \cdot \nabla \rho)}_{\frac{\mathrm{D}\rho}{\mathrm{D}t}} + (\rho \nabla \cdot \boldsymbol{V}) = 0 \tag{5.32}$$

for incompressibility condition the substantial change of density must be equal to zero, this can be mathematically expressed as follows

$$\frac{\mathrm{D}\rho}{\mathrm{D}t} = \frac{\partial \rho}{\partial t} + \rho \nabla \cdot \boldsymbol{V} = 0 \tag{5.33}$$

substituting Eq. 5.33 into 5.32 the continuity equation for an incompressible flow reduces to

$$\nabla \cdot \boldsymbol{V} = 0 \tag{5.34}$$

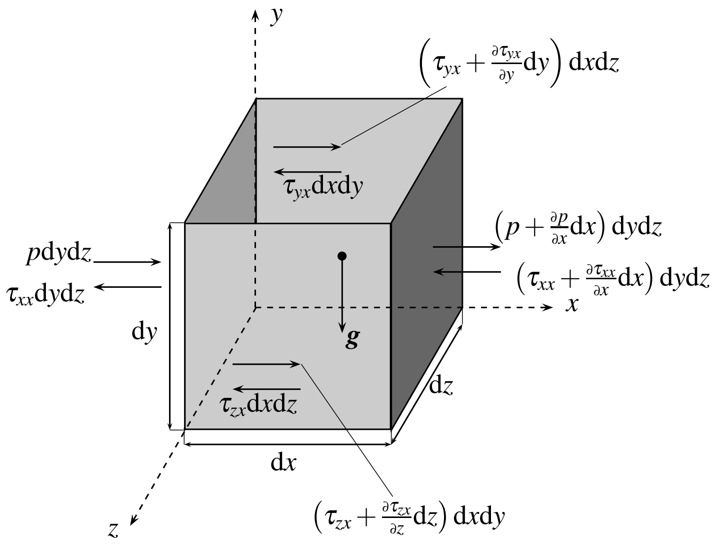

Figure 5.7. Infinitesimally small, moving fluid element. By convention τ_{zx} denotes a stress in the x direction acting on the plane. Adapted from [183]

5.2.2 Equation of Motion

The calculation of the entire flow field through the impeller blade channels requires the equation of motion in differential form

Applying Newton's second law of motion to the moving fluid element in Fig. 5.7 and considering the x component alone the following expression is defined

$$F_x = ma_x \tag{5.35}$$

where a_x and F_x are the acceleration and force acting on the x-component, respectively. The force component is equal to the sum of the surface forces acting on the x-component, including shear and normal stress distributions, and body forces such as the gravitational force. The net surface force in the x-component, $F_{x,s}$, of the element in question can be written as

$$\begin{aligned} F_{x,s} = \left[P - \left(P + \frac{\partial P}{\partial x}\mathrm{d}x\right)\right]\mathrm{d}y\mathrm{d}z + \left[\left(\tau_{xx} + \frac{\partial \tau_{xx}}{\partial x}\mathrm{d}x\right) - \tau_{xx}\right]\mathrm{d}y\mathrm{d}z \\ + \left[\left(\tau_{yx} + \frac{\partial \tau_{yx}}{\partial y}\mathrm{d}y\right) - \tau_{yx}\right]\mathrm{d}x\mathrm{d}z \\ + \left[\left(\tau_{zx} + \frac{\partial \tau_{zx}}{\partial z}\mathrm{d}z\right) - \tau_{zx}\right]\mathrm{d}x\mathrm{d}y \end{aligned} \tag{5.36}$$

the body force per unit mass in the x-component, $F_{x,b}$, acting on the fluid element can be expressed as

$$F_{x,b} = \rho f_x(\mathrm{d}x\mathrm{d}y\mathrm{d}z) \tag{5.37}$$

where $\mathrm{d}x\mathrm{d}y\mathrm{d}z$ represents the volume of the fluid element. Combining Eq. 5.36 and 5.37, the total force in the x direction, F_x, can be found

$$F_x = \left[-\frac{\partial P}{\partial x} + \frac{\partial \tau_{xx}}{\partial x} + \frac{\partial \tau_{yx}}{\partial y} + \frac{\partial \tau_{zx}}{\partial z}\right]\mathrm{d}x\mathrm{d}y\mathrm{d}z + \rho f_x(\mathrm{d}x\mathrm{d}y\mathrm{d}z) \tag{5.38}$$

given that the mass of the fluid element is fixed it can be expressed as

$$m = \rho\mathrm{d}x\mathrm{d}y\mathrm{d}z \tag{5.39}$$

recalling that the acceleration of the fluid element is the time rate of change of its velocity and considering a moving fluid element, it can be expressed by following substantial derivative

$$a_x = \frac{\mathrm{D}u}{\mathrm{D}t} = \underbrace{\frac{\partial u}{\partial t}}_{\text{Local}} + \underbrace{u\frac{\partial u}{\partial x} + v\frac{\partial u}{\partial y} + w\frac{\partial u}{\partial z}}_{\text{Convective}} = \frac{\partial u}{\partial t} + \nabla \cdot \boldsymbol{V}u \tag{5.40}$$

substituting Eq. 5.38, 5.39, 5.40 into 5.35, the x component of the equation of motion for a viscous flow is found

$$\rho\frac{\mathrm{D}u}{\mathrm{D}t} = -\frac{\partial P}{\partial x} + \frac{\partial \tau_{xx}}{\partial x} + \frac{\partial \tau_{yx}}{\partial y} + \frac{\partial \tau_{zx}}{\partial z} + \rho f_x \tag{5.41}$$

the y and z components can be obtained in a similar manner to that of the previously found x component.

writing Eq. 5.41 in terms of substantial derivative definition gives

$$\rho\frac{\mathrm{D}u}{\mathrm{D}t} = \rho\frac{\partial u}{\partial t} + \rho\nabla\cdot\boldsymbol{V}u \tag{5.42}$$

where $\rho\frac{\partial u}{\partial t}$ can be written as

$$\rho\frac{\partial u}{\partial t} = \frac{\partial(\rho u)}{\partial t} - u\frac{\partial \rho}{\partial t} \tag{5.43}$$

and $\rho\nabla\cdot\boldsymbol{V}u$ can be written as

$$\rho\nabla\cdot\boldsymbol{V}u = \nabla\cdot(\rho u\boldsymbol{V}) - u\nabla\cdot(\rho\boldsymbol{V}) \tag{5.44}$$

rearranging Eq. 5.42 by substituting in Eq. 5.43 and 5.44 gives

$$\rho\frac{\mathrm{D}u}{\mathrm{D}t} = \frac{\partial(\rho u)}{\partial t} - u\frac{\partial \rho}{\partial t} + \nabla\cdot(\rho u\boldsymbol{V}) - u\nabla\cdot(\rho\boldsymbol{V}) \tag{5.45}$$

$$= \frac{\partial(\rho u)}{\partial t} - u\left[\frac{\partial \rho}{\partial t} + \nabla\cdot(\rho\boldsymbol{V})\right] + \nabla\cdot(\rho u\boldsymbol{V}) \tag{5.46}$$

the term within the square brackets can be recognised as the continuity equation, see Eq. 5.33; hence the above equation reduces to

$$\rho\frac{\mathrm{D}u}{\mathrm{D}t} = \frac{\partial(\rho u)}{\partial t} + \nabla\cdot(\rho u\boldsymbol{V}) \tag{5.47}$$

substituting Eq. 5.47 into 5.41 results in the Navier-Stokes equation in the x component

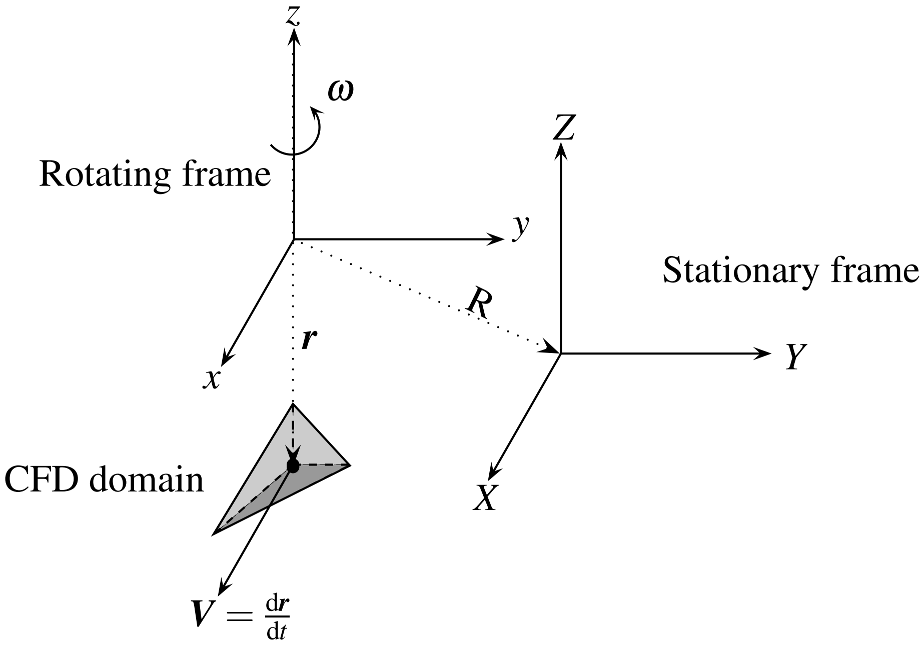

Figure 5.8. Coordinate system representing a rotating reference frame in the vicinity of a stationary reference frame. The stationary frame is denoted by the upper case letters X, Y, Z while the rotating frame is denoted by the lower case letters x, y, z. The rotating reference frame rotates with an angular velocity ω and is placed at a distance $\boldsymbol{R}$ from the stationary frame. Adapted from [184]

in conservation form

$$\frac{\partial(\rho u)}{\partial t} + \nabla \cdot (\rho u \boldsymbol{V}) = -\frac{\partial P}{\partial x} + \frac{\partial \tau_{xx}}{\partial x} + \frac{\partial \tau_{yx}}{\partial y} + \frac{\partial \tau_{zx}}{\partial z} + \rho f_x \tag{5.48}$$

rearranging

$$\frac{\partial u}{\partial t} + \nabla \cdot (u\boldsymbol{V}) = -\frac{1}{\rho}\left[\frac{\partial P}{\partial x} - \nabla \cdot \boldsymbol{\tau}_x\right] + f_x \tag{5.49}$$

In this work, a rotating frame of reference with angular velocity ω about the z-axis was considered. From a stationary point of view, a fluid particle passing through a rotating frame at an arbitrary time, t, has position $\boldsymbol{r}$ and relative velocity $\boldsymbol{W}$. The inherited rotation of the frame causes the fluid particle to rotate with velocity $\omega \times \boldsymbol{r}$, therefore the velocity is given by

$$\boldsymbol{V} = \boldsymbol{W} + \omega \times \boldsymbol{r} \tag{5.50}$$

substituting Eq. 5.50 into 5.40 to find the substantial acceleration gives

$$a_x = \frac{\mathrm{D}u}{\mathrm{D}t} = \frac{\partial(\boldsymbol{W}+\omega\times\boldsymbol{r})\cdot\boldsymbol{i}}{\partial t} + (\boldsymbol{W}+\omega\times\boldsymbol{r})\cdot\nabla(\boldsymbol{W}+\omega\times\boldsymbol{r})\cdot\boldsymbol{i} \tag{5.51}$$

rearranging and simplifying the equation reduces to

$$a_x = \frac{\partial u}{\partial t} + \nabla\cdot(u\boldsymbol{V}) = \frac{\partial W_x}{\partial t} + \frac{\partial \omega_x}{\partial t}\times\boldsymbol{r} + \boldsymbol{W}\cdot\nabla W_x + [\omega\times(\omega\times\boldsymbol{r}) + 2\boldsymbol{W}\times\omega]\cdot\boldsymbol{i} \tag{5.52}$$

where $\frac{\partial W_x}{\partial t}$ represents the local acceleration of the velocity field within the relative frame of reference; $\frac{\partial \omega_x}{\partial t}\times\boldsymbol{r}$ the angular acceleration; $\boldsymbol{W}\cdot\nabla W_x$ the convective term within the relative frame of reference; $\omega\times(\omega\times\boldsymbol{r})$ the centripetal acceleration and $2\boldsymbol{W}\times\omega$ the Coriolis acceleration [185]. The latter two terms appear as a result of the rotational component of the velocity. The centrifugal acceleration acts in the radial direction whereas the Coriolis acceleration acts tangentially and in opposite direction to the tangential velocity [176]. Replacing the acceleration in Eq. 5.49 by the expression in Eq. 5.52 and recalling that for a steady rotating reference frame $\frac{\partial \boldsymbol{r}}{\partial t} = 0$ and $\omega =$ constant the equation of motion in rotating frame reference is obtained

$$\frac{\partial W_x}{\partial t} + \boldsymbol{W}\cdot\nabla W_x + [\omega\times(\omega\times\boldsymbol{r}) + 2\boldsymbol{W}\times\omega]\cdot\boldsymbol{i} = -\frac{1}{\rho}\left[\frac{\partial P}{\partial x} - \nabla\cdot\boldsymbol{\tau}_x\right] + f_x \tag{5.53}$$

5.2.3 Turbulence Model

In this work, turbulence is simulated with the standard $k-\omega$ model. This model utilises the Reynolds-Averaged Navier-Stokes (RANS) model in which mean flow properties are calculated by splitting the instantaneous properties into a time-average component and a fluctuating component [186], this can be mathematically expressed as follows

$$\underbrace{\boldsymbol{V}_i(x,y,z,t)}_{\text{Instantaneous component}} = \underbrace{\overline{\boldsymbol{V}}_i(x,y,z,t)}_{\text{time-average component}} + \underbrace{\boldsymbol{V}'_i(x,y,z,t)}_{\text{fluctuating component}} \tag{5.54}$$

In the $k-\omega$ model the turbulence viscosity, μ_t, is related to the turbulence kinetic energy and turbulence frequency through the following expression

$$\mu_t = \rho \frac{k^2}{\omega} \tag{5.55}$$

where k is the turbulent kinetic energy and ω is the turbulent frequency [186].

In ANSYS CFX, the near-wall treatment for the $k-\omega$ model is achieved with an automatic function that gradually switches from a scalable wall function formulation to a low-Reynolds number one to capture the details of the boundary layer profile. The scalable wall function formulation is useful in that it is less computationally costly as it is able to model near-wall high gradient shear layers with relatively coarse meshes [186]. By contrast, the low-Reynolds number approach resolves complex details of the boundary layer by using very small mesh length scales in the direction normal to the wall or inflation layers; for this purpose, the model requires a near-wall mesh resolution of at least $y^+ < 2$ [186]. With this in mind, ten nodes from the wall were used to resolve the boundary layer given that in this work it is of great importance to gain an appreciation of typical wall shear stresses present in the flow passage. This in turn, would have a significant effect in the preservation of red blood cells. Having reported on the importance of studying wall shear stress, it is worth noting that in this study water was implemented as the working fluid, however, if a blood-like working fluid was implemented the resultant wall shear stresses would have been about 4 times higher than those obtained with water.

5.3 CFD Implementation

Numerical flow analyses were conducted to investigate the flow characteristics the pump assembly. The commercial software ANSYS-CFX was implemented in all studied cases. Steady state analyses were performed in all cases studied in this work. Water was selected as the working fluid and was set as being isothermal and having an incompressible behaviour.

5.3.1 Computational Domain

The methods used to generate the model of the pump components were of two main types: 1) x, y and z coordinate data generated with a purposely built MATLAB program (see Appendix B); 2) typical lofting, surface, and extrusion tools implemented in the commercial software Autodesk Inventor.

5.3.1.1 Impeller

A MATLAB program was written by implementing the pump theory as reported in section 5.1. This program produces x, y and z coordinate data that can be imported into ANSYS TurboGrid for impeller mesh generation purposes. Fig. 5.9 displays the blade and the flow passage obtained with the bespoke program. Table 5.3, summarises the dimensions of the impeller geometry.

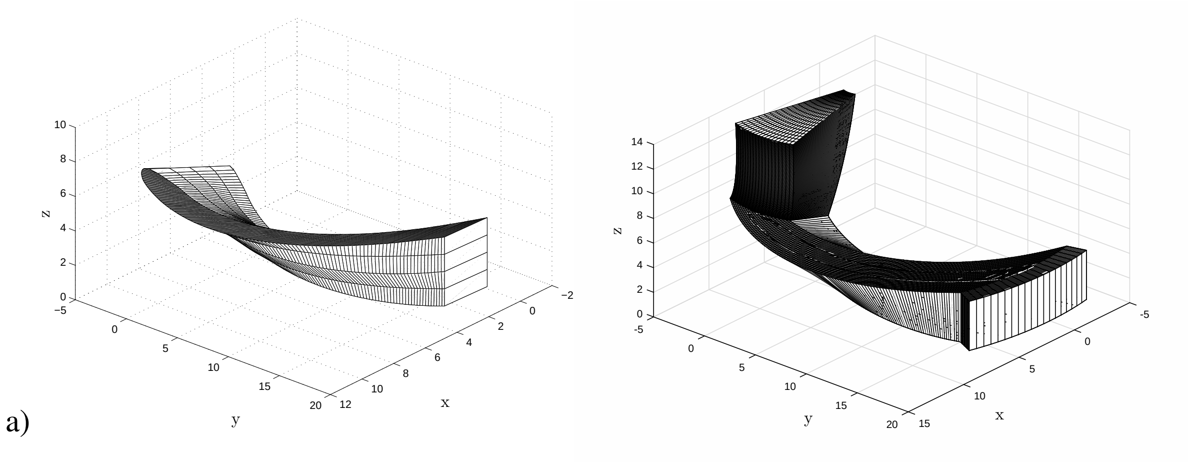

Figure 5.9. 3D geometry definition: a) blade constructed with 5 curves, b) flow passage construction.

5.3.1.2 Volute, suction inlet and outlet pipes

The commercial software Autodesk Inventor was implemented to generate the volute, and the suction inlet and outlet pipes. Modelling silicone was used to measure the dimensions of the exiting volute and outlet pipe. The resulting CAD files were saved as IGES files to be imported into the commercial mesher ANSYS ICEM CFD.

Table 5.3. List of impeller dimensions.

Parameter	Value	Unit
Inlet diameter at hub $D_{1,h}$	11	mm
Inlet diameter at tip $D_{1,t}$	21	mm
Outlet diameter at hub D_2	33	mm
Inlet width b_1	6	mm
Outlet width b_2	4	mm
Number of blade sets	11	-
Mean blade thickness t	1	mm
Mean Blade inlet angle	39	deg
Blade outlet angle	86	deg

5.3.2 Mesh Generation

5.3.2.1 Mesh Refinement Study

A comparison of the static and total head at the impeller outlet against various grid sizes was carried out. In Fig. 5.10, it is noticeable that at coarser mesh sizes both the static and total head are larger. The head starts to plateau at about $400,000$ elements, however, a satisfactory result is achieved with $160,000$ elements. The variation in static head from the last two finest grid sizes is about 0.01% for both the static and total head rise.

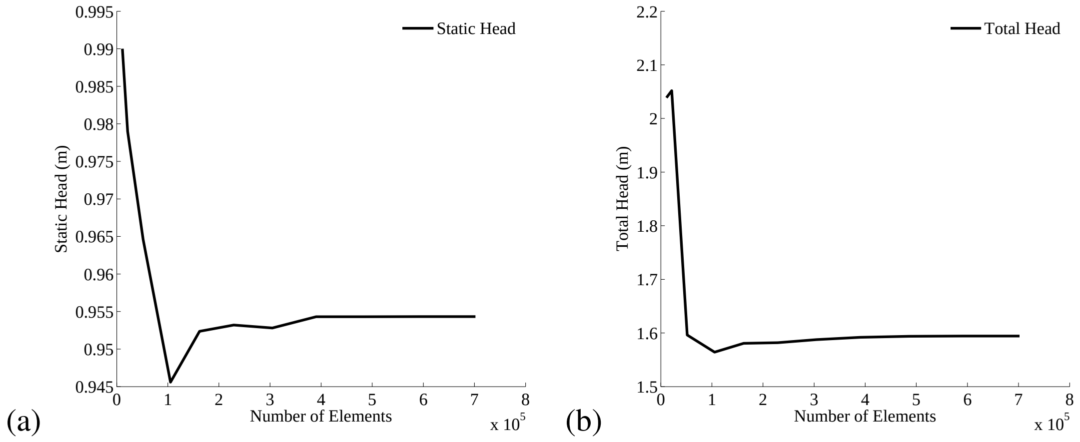

Figure 5.10. Comparisson of the effect of grid size on (a) static head and (b) total head.

5.3.2.2 Impeller

ANSYS TurboGrid was used to generate the computational grid for a single flow passage. The topology was defined by selecting a placement on curves with control points, the control points were preserved in all layers to improve the mesh quality. One-to-one node matching on corresponding periodic surfaces was achieved by imposing a rotational periodicity, this is of particular importance when generating the full assembly model of the impeller. The topology method used was a J-Grid type with an embedded O-Grid that surrounds the blade; this method was implemented with the purpose of resolving the details of the boundary layer near the blade. Near wall element size specification was implemented with the Y Plus method by specifying a target $y^+ = 1$ on the passage, hub and shroud, and the Reynolds number based on the chord length ($Re_L = 99,600$). Next, the mesh Data Object was modified to adjust the number of nodes; at first the mesh was generated with a lower density then the mesh was refined. A total of 244,101 elements were implemented per passage as this was found to produce a satisfactory result for static and total head; see Fig. 5.10. In all layers a face angle criterion ranging from 15° to 165° was imposed to achieve a good mesh quality. Fig. 5.11 shows the generated mesh for a single flow passage.

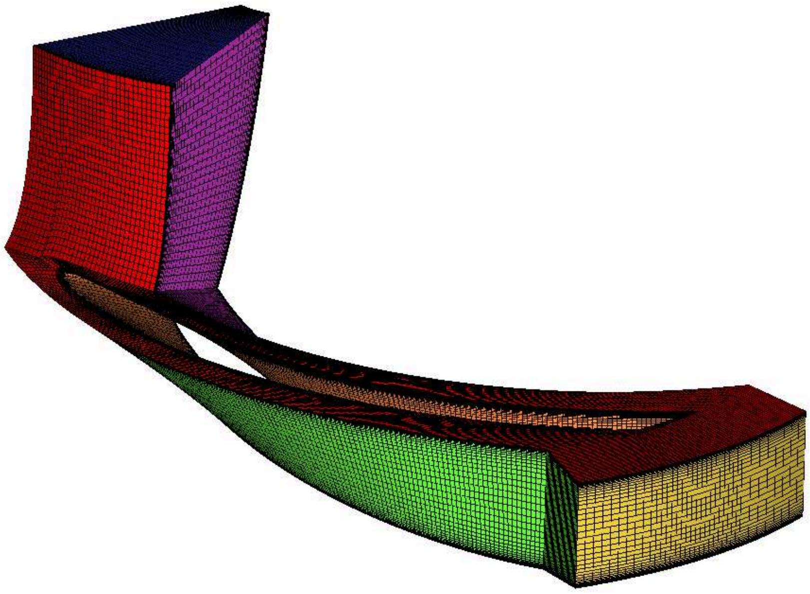

Figure 5.11. Structured mesh for a single flow passage.

5.3.2.3 Volute, suction inlet and outlet pipes

ANSYS ICEM CFD was used to generate the computational grid for the volute, suction inlet and outlet pipes. A blocking technique was implemented to achieve only hexahedral element and to ensure good mesh quality. In all cases a face angle criteria ranging from 15° to 165° was imposed to achieve a good mesh quality. Table 5.4 summarises the main mesh quality parameters for all the components of the pump.

Table 5.4. List of mesh quality parameters.

	Parameter	Value	Unit
Suction inlet	Minimum angle	27	deg
	Maximum angle	144	deg
	Min. orthogonal qual.	0.55	-
	Determinant ($3 \times 3 \times 3$)	0.6	-
	Total elements	261,708	-
Flow passage	Minimum angle	15	deg
	Maximum angle	165	deg
	Total elements	244,101	-
Volute & Outlet	Minimum angle	18	deg
	Maximum angle	162	deg
	Min. orthogonal qual.	0.1	-
	Determinant ($3 \times 3 \times 3$)	0.3	-
	Total elements	195,950	-

The assembly mesh consists of 3.14 million hexahedral elements. Fig. 5.12 displays the assembly mesh used for the numerical analyses.

5.3.2.4 Pre-processing

The frozen rotor frame change model was selected for the numerical analyses as it produces satisfactory solutions and is less computationally costly than a transient study. Domain interfaces were created for each of the assembly components. The interface connections between the suction pipe and the impeller's inlet, and the impeller's outlet and the volute's inlet was achieved by using General Grid Interface (GGI) connection as these allow to connect two surfaces with non-matching node locations.

For the rotational periodic interfaces, one-to-one connections were implemented as these

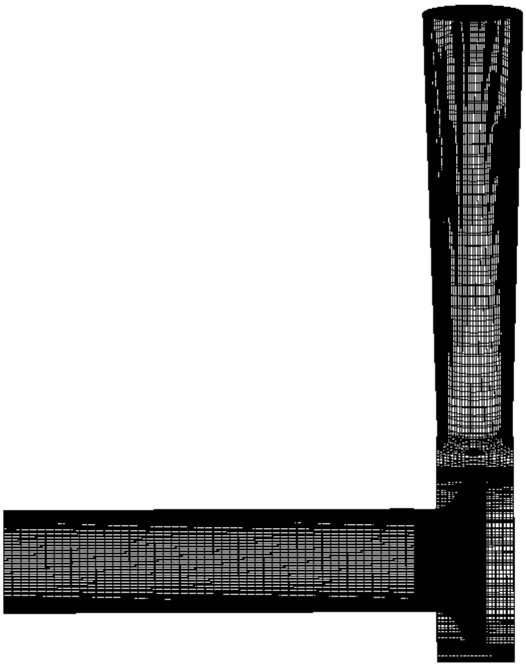

Figure 5.12. Centrifugal pump mesh assembly. Number of elements: 3.14 million

produce the highest accuracy. The rotating frame elements (i.e. the blade, hub and shroud) were set to a wall type boundary. Finally, the solver control parameters were set to high resolution for the advection scheme and the turbulence numerics. A physical time step of 5.95×10^{-5} s is used, this is equivalent 360 time steps per one rotor rotation. The convergence criteria selected was a residual target of 1×10^{-4} for the root mean square (RMS) normalized values of the momentum and mass equations residuals.

5.4 Numerical Results

Fig. 5.13 shows a plane view of the total pressure contours (right column) and velocity vectors (left column) of the blades and volute for the designed flow rate at different exit blade widths. The rotational direction of the rotor is the clockwise direction. Secondary flows (denoted with the letter A) were found in all blade widths at each of the blade-to-blade flow distributions but they were more predominant as b_2 was increased; see Fig. 5.13(g). This can also be appreciated in Fig. 5.13(h) from the negative pressures present near the suction surface of the blade. The interaction between the blade outlet flow and the volute was rather chaotic at $b_2 = 2$ mm with some of the velocity vectors pointing in the opposite direction of the rotor motion; this is denoted with the letter B. Secondary flows were also found at the volute throat at all blade widths; this is denoted with the letter C in Fig. 5.13 (a), (c), (e) and (g). From Table 5.5, the maximum wall shear stress is found to increase as the flow increases, and similarly for the efficiency.

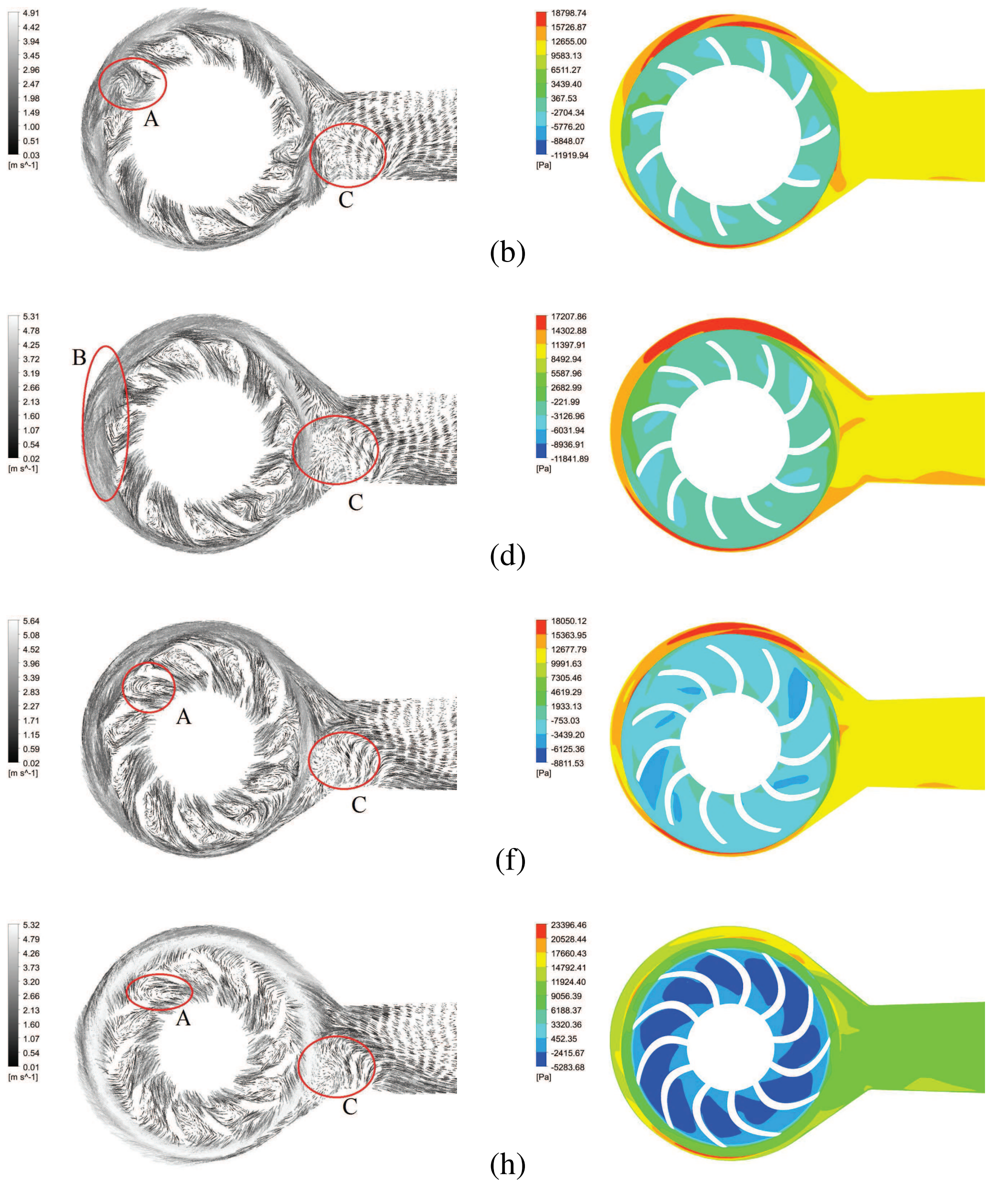

(a) (b)

(c) (d)

(e) (f)

(g) (h)

Figure 5.13. Numerical results at different blade widths, b_2, at the design flow rate $Q = 5$ lt/min. Left column: velocity vectors; Right column: total pressure distributions.

Table 5.5. Pump performance results with different flow conditions.

Flow (lt/min)	Static Head at outlet (m)	Efficiency (%)	Max. Wall Shear (Pa)
1	1.16	48.68	108.1
2	1.09	49.10	213.4
3	1.04	49.95	298.2
4	1.01	50.48	347.2
5	0.95	51.32	422.8
6	0.90	52.02	484.7
7	0.87	52.77	573.1
8	0.83	52.74	617.1
9	0.78	52.31	646.9
10	0.71	50.60	686.2
11	0.63	47.99	711.3
12	0.56	45.78	739.8

5.5 Validation

The hydraulic pump performance of the centrifugal pump was evaluated using a typical simple loop, by circulating water at room temperature. Flow rate was recorded within the range of $0-12$ lt/min with simultaneous recording of the static head. Fig. 5.14 shows the relationship between pump flow rate and static head. In general, it can be seen that the design point was achieved with the new impeller and that there is agreement between the experiment and the numerical result for the design point. For flows ranging from $0-6$ lt/min the numerical static pressure result appears to represent satisfactorily the experimental results; however, for flows ranging between $7-12$ lt/min the numerical result does not agree with the experimental results.

5.6 Discussion

The main target pump performance of 70 mmHg against 5 lt/min was successfully achieved, however, the maximum shear wall stress condition was not met. In Table 5.5, it can be seen that the maximum wall shear stress was 422.8 Pa; this value is well above the thresh-

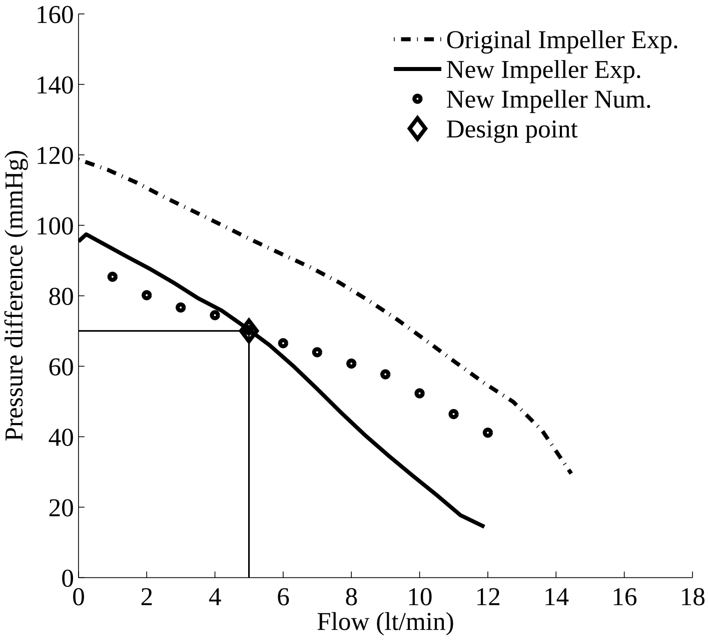

Figure 5.14. Numerical and experimental comparison of the new impeller performance.

old level of 150 Pa as found in the work by Leverett et al. [173]. In the latter, two primary determinants of haemolysis were hypothesised: shear stress and exposure time. Particularly, cells exposed to stress for very short times, can withstand very high stresses without fragmentation. On the other hand, prolonged exposure at much lower stresses results in lysis. In the work by Sutera et al.[187], red blood cells fragmentation became apparent at shear stress values of 250 Pa and at exposure time of 4 minutes. From this work, it was inferred that the presence of turbulence is not adverse by itself provided that the time-averaged shear stress does not exceed the threshold level. Later works by Paul et al. [188], suggested that to observe a significant increase in blood damage shear stresses should be greater than 425 Pa and exposure times greater than 620 ms are required. From Table 5.5, it can be appreciated that at greater flows the wall shear stress is also higher suggesting that lower flows should be used to avoid red blood cells rupture (haemolysis). From a clinical usage stand point, perfusion requirements should be taken into consideration; for instance, excessive flow leads to pulmonary oedema whereas low flow pumps are prone to thrombus formation due to less vigorous washout; hence the selection of the right operating condition should be determined by the characteristics of the patient.

Equally important, is the selection of an appropriate pressure rise as high pressures increases the risk of intracranial bleeding. In the work by Nishida et al. [189], a flow in the range between $5-5.5$ lt$/$min is considered safe for left ventricular assist devices; higher flows are specially concerning when considering that in a congestive-heart-failure patient the right ventricle was operating at flows in the $3-4$ lt$/$min range. After insertion of a mechanical circulatory device, the cardiac output and venous return will increase and although this is beneficial for the systemic circulation, for the pulmonary circulation it would prove challenging to deal with such increased load [190]. In general, flows of about $4-6$ lt$/$min are considered true assist devices that do not decompress the left ventricle as much as true left ventricle replacement devices with flows as high as 7 lt/min or greater [190]. Optimally, the central venous pressure should be less than 14 mmHg and the mean arterial blood pressure range between $70-80$ mmHg to keep adequate coronary, cerebral and splanchnic blood flows.

Chapter 6

In-vitro Model

The present experimental simulator of cardiovascular loops (SCVL) was developed in collaboration with the research assistant Dr. Akbar Rahideh. In general, SCVLs can be classified into three subdivisions according to the number of actuators used to emulate the human heart as follows: single chamber; twin-chamber; and multi-chamber when more than two actuators are implemented. Our experimental rig falls into the multi-chamber category as we implemented four actuators to represent the human heart. In other available multi-chamber rigs [77, 191, 192], actuation of the heart chambers is achieved by using pneumatic pumps and the circulation loops are opened to atmosphere to regulate the pressure in the system. The present system utilises linear motors to accurately emulate the contraction and filling phases of the atria and ventricles of the human heart, and is a closed-to-atmosphere system to allow for feedback control of the sensed pressures in the systems. It also includes five mechanical heart valves to adequately achieved unidirectional flow; five Hoffman clips used to induce resistance to the flow; and four air-spring capacitors to account for the pressure-volume control in the blood vessels. Water was selected as the working fluid with the purpose of preserving the good functioning of the MCS device. It is worth mentioning that initially a glycol-water mixture was used as the working fluid but it proved detrimental for the MCS device as it completely stop working. The main goals of this SCVL are to simulate the aortic sinus pressure waveform, closer to patophysiological conditions as that found in the clinical setting, including steep rise of the pulse pressure, dicrotic notch which is due to the closure of the aortic valve, and gradual decline of pressure to the aortic diastolic pressure. Also, to mimic diseased conditions with the intention of evaluating the system response while the MCS is placed at AAo and DAo, as described in Chapter 4. These are achieved by using individual actuation for each of the four chambers that constitute the heart by implementing linear motors. Each linear motor consists of a stator and a slider accurately controlled by electromagnetic principles thus allowing accurate trace of the instantaneous location of the slider and therefore precise emulation of contraction and filling phases as found in the native cardiac muscle.

6.1 The cardiovascular simulator

The multi-chamber SCVL can be classified into three main parts: (1) heart model; (2) pulmonary and systemic circulations; and (3) control, measurement and monitoring systems. Fig. 6.1 shows the schematic representation of the multi-chamber SCVL system while Fig. 6.2 shows the schematic representation of the control system.

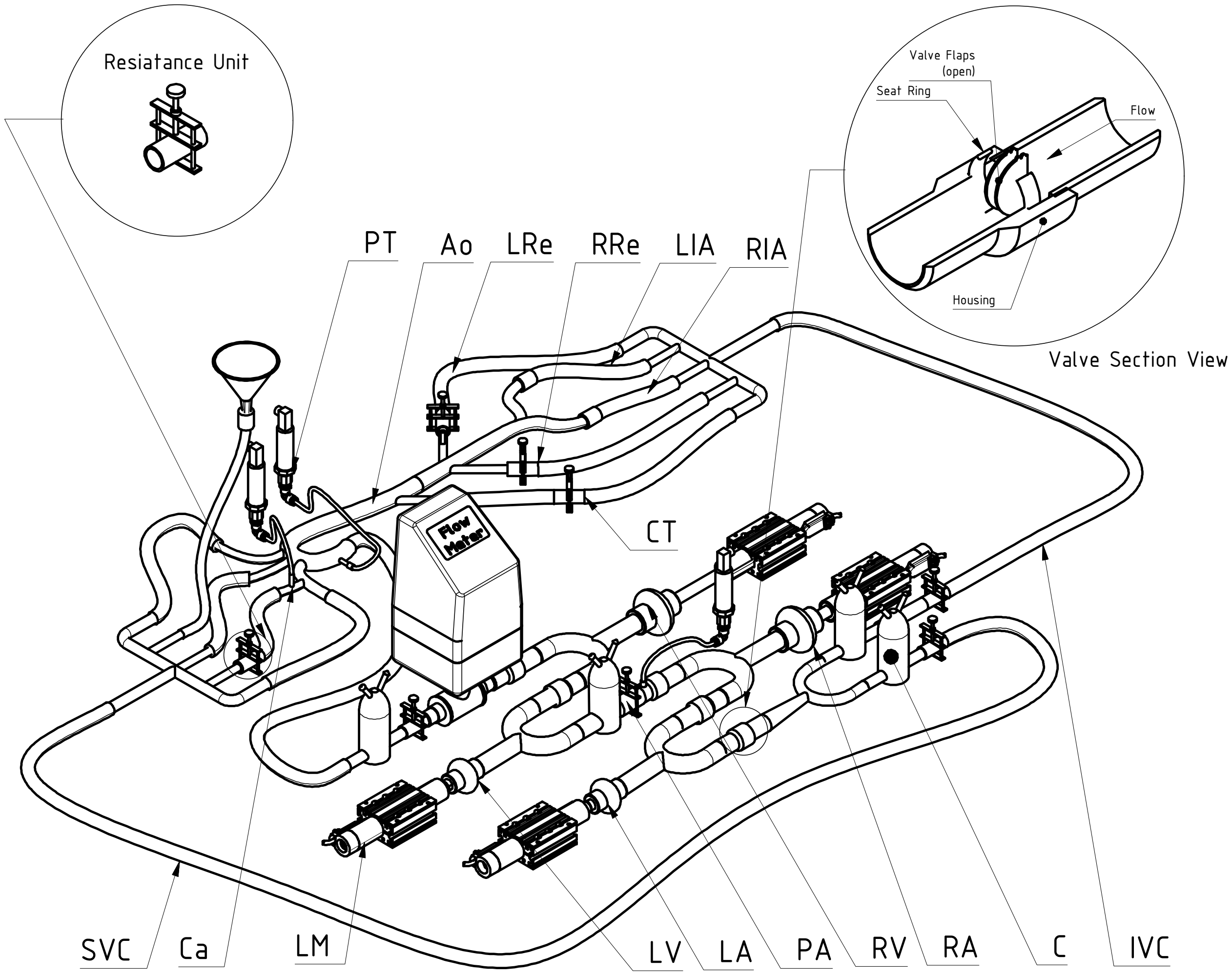

Figure 6.1. Diagrammatic representation of the SCVL. Ao: aorta artery; C: compliance; Ca: carotid artery; CT: celiac trunk; IVC: inferior vena cava; LA: left atrium; LM: linear motor; LV: left ventricle; PA: pulmonary artery; PT: pressure transducer; RA: right atrium; Re: renal artery; RV: right ventricle; SVC: superior vena cava

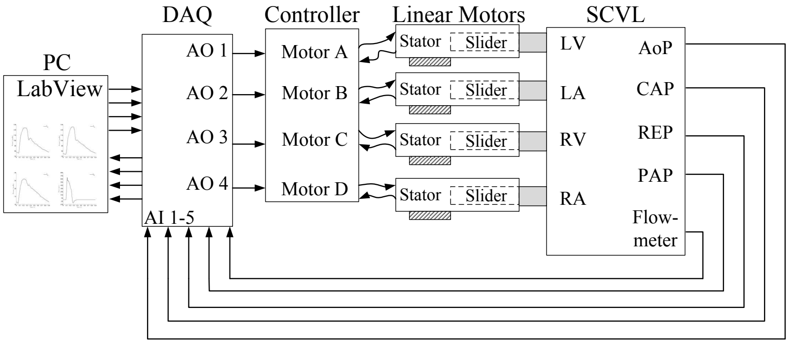

Figure 6.2. Schematic of the control system. AoP, aortic pressure; CAP, carotid artery pressure; DAQ, data acquisition card; LA, left atrium; LV, left ventricle; PAP, pulmonary artery pressure; RA, right atrium; RV, right ventricle.

6.1.1 Heart model

For modelling heart chambers, four rubber gaiters with proper sizes (left ventricle and right ventricle with volume of 120 and 50 ml, respectively) are used to represent the native heart chambers. Each chamber is connected to a separate linear motor. The well-established time-varying elastance model introduced by Suga et al. [88] is used to individually activate the four linear motors representing the ventricles and atria. Each linear motor slider is displaced, according to the time-varying elastance model as described in Eq. 2.5. The displacement of the linear motor representing the left ventricle function in a single cardiac cycle is achieved according Eq. 2.6.

The model for the right ventricle is similar to that for the left ventricle, except the values of parameters are different. The displacement of the linear motor representing the atrium in a single cardiac cycle is achieved according to Eq. 2.7. The time parameters for the linear motors are the same as previously implemented in the mathematical model described in Chapter 2; see Table 2.2.

Four mechanical heart valves corresponding to mitral, pulmonary, tricuspid and aortic are used in the vicinity of each chamber to control unidirectional flow. Additionally, another mechanical valve is set at the end of vena cava before the right atrium to help venous return and to prevent backflow of the working fluid. These five mechanical heart valves are Medtronic's 29mm diameter Hall Easy-Fit Mechanical Valves (Minneapolis, Minnesota, USA).

6.1.2 Systemic and pulmonary circulation

Total systemic and pulmonary resistances are modelled by using adjustable resistors (Hoffman clips screw-type clamp). The level of resistance at various parts of the systemic and pulmonary loops is manually set to mimic different physiological and pathological conditions. The system compliance is modelled by using four air capacitors which consists of a chamber partially filled with both water and compressed air, located one in the ascending aorta, one in the pulmonary circulation, and two in the vena cava artery to control the central venous pressure and venous return and consequently cardiac output (CO). These compliance units are placed in parallel to their respective resistance units as seen in Fig. 6.1. The level of air pressure in each compliance chamber is adjusted via a sphygmomanometer for various physiological conditions. Any change in air pressure results in changing the level of compliance in the system.

Systemic and pulmonary vasculatures are reproduced by using 24-mm diameter rubber tubing. The aorta artery is made out of glass according to the anatomical features of the average adult native system in a similar way to the study conducted by Pantalos et al. [193], including: the ascending aorta; the aortic arch with the brachiocephalic trunk, left common carotid artery, and left subclavian artery; thoracic aorta; abdominal aorta with the celiac trunk and renal arteries; and common iliac arteries. This model of the aorta artery was done with the intention of accurately distributing CO to the upper body, heart, abdomen and lower body.

6.1.3 Control, measurement and monitoring systems

Four identical tubular permanent magnet linear motors (P01-37x120 LinMot, Spreitenbach, Switzerland) are used to drive the four chambers representing the heart. A controller (E400 LinMot, Switzerland) with 4 channels is employed to accurately control the position of the motors by independently controlling the displacement of each slider according to a predefined time-varying elastance function. A high speed, high performance data acquisition card (DAQ) with four analogue outputs, 16 analogue inputs and 48 digital input/outputs (NI PXIe-6368 National Instrument, Budapest, Hungary) is used to, firstly, send the desired displacement trajectories from the PC to the linear motor controller and secondly to read the measurement signals from the pressure transducers and the flow meter to the PC. The desired trajectory generation and monitoring tasks is achieved via NI LabView software (National Instrument, Texas, USA). Four pressure transducers (PMP1400 Druck General Electric Company Billerica, MA, USA) are used to simultaneously measure the pressures at aortic sinus, carotid, renal and pulmonary arteries. An electromagnetic flowmeter (SITRANS F M MAG 1100 F Siemens, Munich, Germany) is employed to measure the flowrate of the ascending aorta, carotid, renal and pulmonary arteries. Fig. 6.2 shows the schematic of the control system.

6.2 Results

In this work, seven cases are studied: 1) control condition; 2) Class III HF; 3) Class IV HF; 4) Class III HF with MCS at DAo; 5) Class IV HF with MCS at DAo; 6) Class III HF with MCS at AAo; 7) Class IV HF with MCS at AAo. In each case, pressure and flow time histories are simultaneously recorded at aortic sinus, carotid, renal and pulmonary arteries together with CO measurement as these are the gold standards of cardiac condition assessment [111]. In all seven cases, the experimental pressure waveforms are compared to the numerical data. Peripheral resistance is measured at the aortic valve sinus as the relationship between mean pressure and mean flow rate. All measured haemodynamic variables are summarised in Table 6.1.

6.2.1 Statistical analyses

For each of the simulated cases, the system was run for 2 minutes prior to the recording of the measured data. This was done with the purpose of allowing the system to settle down. Next, the experimental data was recorded over a 3-minute period to allow for the data capture of at least 180 heart cycles per each simulated case. For the statistical analyses, the first 150 heart cycles were processed. This strategy was implemented because the system presents many systematic and random errors and so each cardiac cycle can be considered as a new measurement. The sources of these errors were identified as follows: 1) the linear motors did not cope well with the early stages of the cardiac cycle given that at these instances load is highest; 2) the rubber tubing used to model the blood vessels were not fixed, hence, they continuously exhibited a jerky motion; 3) the glass material used in the aorta model made the backward propagated waves travel faster generating timing issues; 4) the prosthetic heart valves used to model the atrio-ventricular interface never completely closed, this allowed for leakage to occur at the end of the systolic phase. A moving-average filter was implemented to remove the spikes generated by the linear motors at the beginning of the cardiac cycle and the random motion of the rubber tubing. All processed data exhibited a normal distribution and was found to fall within the 95% confidence limits. In all measured pressure waves the standard error is displayed with the vertical bars. In Fig. 6.3-6.9, the mean pressure over 150 cycles is displayed. The measured waveforms are represented with solid lines, the numerical data with dashed-and-dot lines and the filtered data with dotted lines. Frequency histograms are also provided for all cases.

6.2.2 Simulated cases without MSC device

6.2.2.1 Case 1: Control condition

In this case the linear motors are operating at 66 bpm and the measured CO is 5.1 lt/min. In Fig. 6.3a-h, it can be observed that the SCVL is able to capture the main physiological features of the pressure waveforms as found in the native cardiovascular system, these include: dicrotic notch due to valve closure, and a gradual decline of pressure to the aortic diastolic pressure as seen in Fig. 6.3 (a); increased pulse pressure as the circulating fluid moves away from the heart, as seen in Fig. 6.3 (e) and (g); diastolic pressure decay in all pressure waveforms, as seen in Fig. 6.3 (a), (c), (e) and (g). In general, the mean aortic pressure ($P_{avs,mean}$) is 94 mmHg; mean carotid pressure ($P_{\mathrm{ca,mean}}$) is 94.41 mmHg, mean renal pressure (($P_{\mathrm{re,mean}}$)) is 92.43 mmHg, mean pulmonary artery pressure ($P_{pvs,mean}$) is 18 mmHg.

6.2.2.2 Case 2: Class III HF

Class III HF, is considered as a mild to moderate HF condition and is commonly divided into two further categories: left ventricular diastolic dysfunction (LVDD) and left ventricular systolic dysfunction (LVSD). In this work LVVD was selected because in most hypertensive patients there is co-existing impaired diastolic relaxation and therefore impaired left ventricle diastolic filling [167, 194, 195]. In the clinical setting, hypertension is defined as a systolic blood pressure of 140 mmHg or greater and/or a diastolic blood pressure of 90 mmHg or greater [196]. In most hypertensive patients there is co-existing impaired diastolic relaxation and therefore impaired left ventricle diastolic filling [167, 194, 195]. Zhou et al. [197], reported aortic stiffening as the main factor for developing increased left ventricle afterload and consequent left ventricle hypertrophy and left ventricle dysfunction (LVD).

In order to mimic LVDD, aortic compliance is reduced, TPR is increased, left ventricle elastance is reduced, and left ventricle resting volume is decreased. This is achieved by decreasing displacement of the left ventricle actuator. The linear motors in this case operate at 80 bpm.

In general, there is an increase in both the EDP and ESP at the aortic sinus and carotid pressure waveforms, in comparison to the control condition, as seen in Fig. 6.4(a). Similarly, $P_{pvs,mean}$ has increased from the normal 18 mmHg to 28 mmHg; see Fig. 6.4(c). P_{avs} is 140/100 mmHg and P_{ca} is 142/96 mmHg; CO drops, from 5.1 lt/min in a control condition, to 3.2 lt/min. The dicrotic notch due to valve closure can also be appreciated; seen in Fig. 6.4(a).

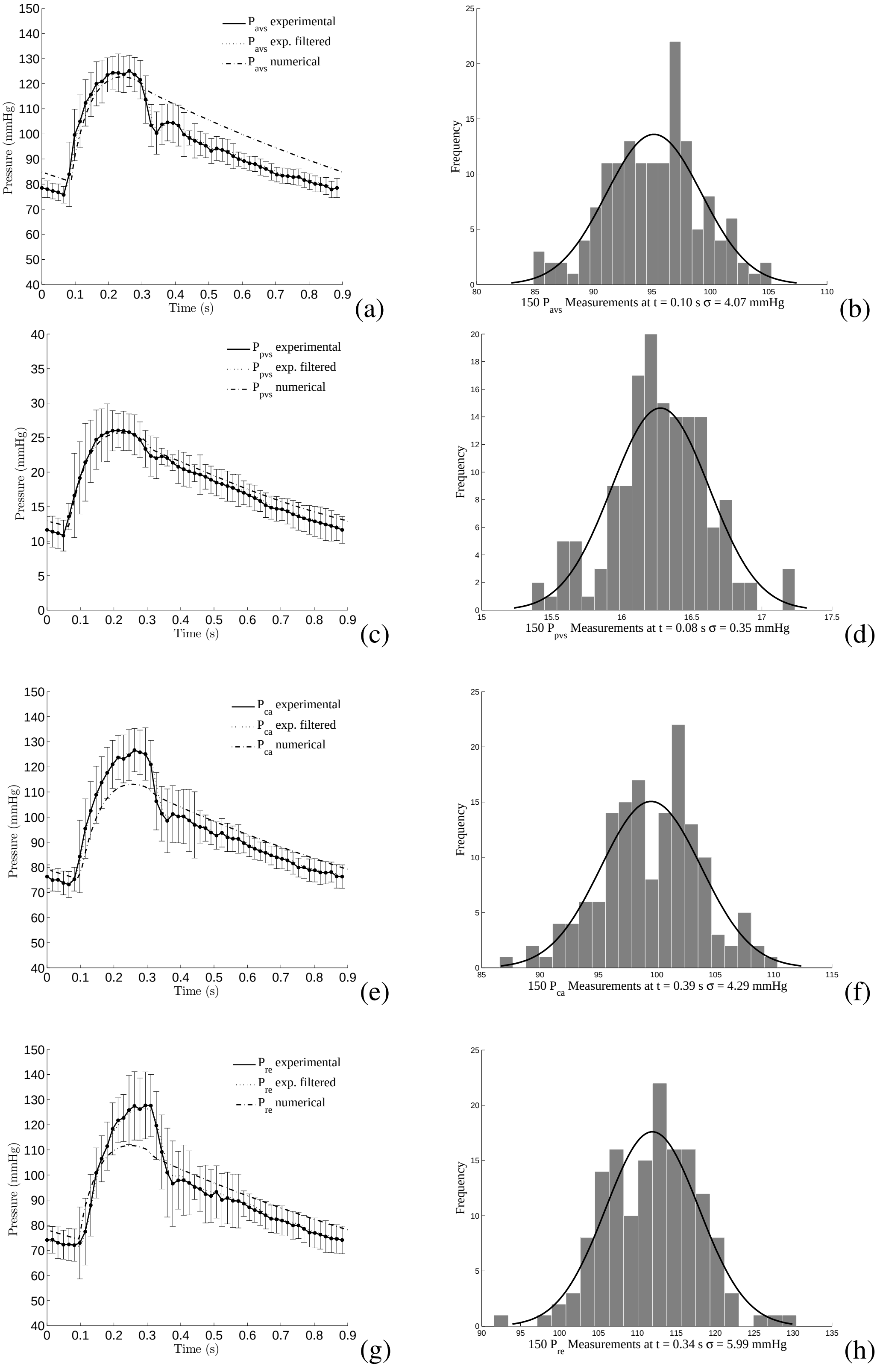

Figure 6.3. Comparison of pressure and flow time histories in aortic, carotid, renal and pulmonary arteries during control condition. The standard error is displayed with the vertical bars. The time of highest standard error is provided in the legend of each histogram.

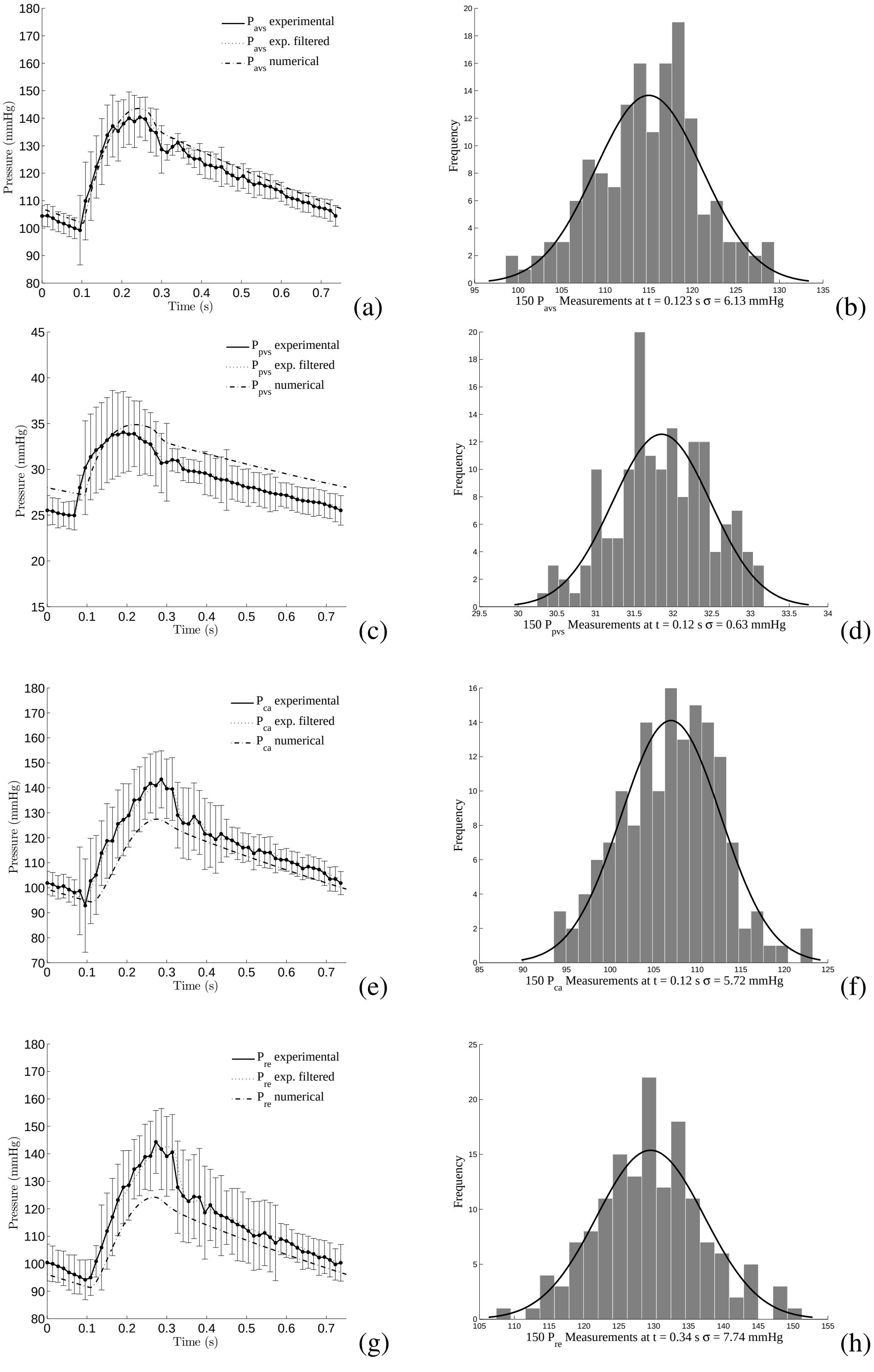

Figure 6.4. Comparison of pressure and flow time histories in aortic, carotid, renal and pulmonary arteries during Class III HF.

6.2.2.3 Case 3: Class IV HF

As previously introduced, a Class IV HF is an advanced form of HF; see Table 1.1; its most common condition is congestive heart failure (CHF). This condition can be defined as a heart that becomes severely weakened as a product of cardiovascular disease; mainly myocardial infarction. As a consequence, the pumping action of the heart is severely depressed resulting in two main effects: reduced CO and damming up of blood in the veins leading to an increase in venous pressure and therefore increase in right atrial pressure [6]. To reproduce a CHF condition, the circulating volume of water is increased; $\mathrm{Elv}_{\mathrm{min}}$ is increased in order to increase the resting left ventricle volume; $\mathrm{Elv}_{\mathrm{max}}$ is decreased by 50% of the normal value with the purpose of mimicking the reduced left ventricle pumping ability. The linear motors in this case are operating at 60 bpm.

In general, CO is 2.6 lt/min while $P_{avs,mean}$ is 85 mmHg. As it is evident in Fig. 6.5(a) and (e), for both aortic sinus and carotid pressure waveforms there is a drop in EDP and ESP, in comparison with the control condition. The pulmonary circulation by contrast, exhibits hypertension where $P_{pvs,mean}$ is 28.7 mmHg. Dicrotic notch due to valve closure can also be appreciated; seen Fig. 6.5(a).

6.2.3 Simulated cases with MSC device

In the following cases the hydrodynamic impact of the MCS described in Chapter 5 is investigated by measuring pressure, flow and resistance at the aortic sinus, carotid, renal and pulmonary arteries. Implementing a MCS device in DAo produces pressure drop upstream of the pump, that is in cerebral and upper limb circulations, and pressure rise downstream of the pump, that is the splanchnic, renal and lower limb circulations. In particular, the pressure drop produced upstream of the MCS device unloads the left ventricle, eventually improving cardiac output, whereas pressure rise produced downstream of the MCS device results in increased blood perfusion rate in the abdominal organs, particularly the liver and kidneys [198–200]. By contrast, the usage of a MSC device in AAo

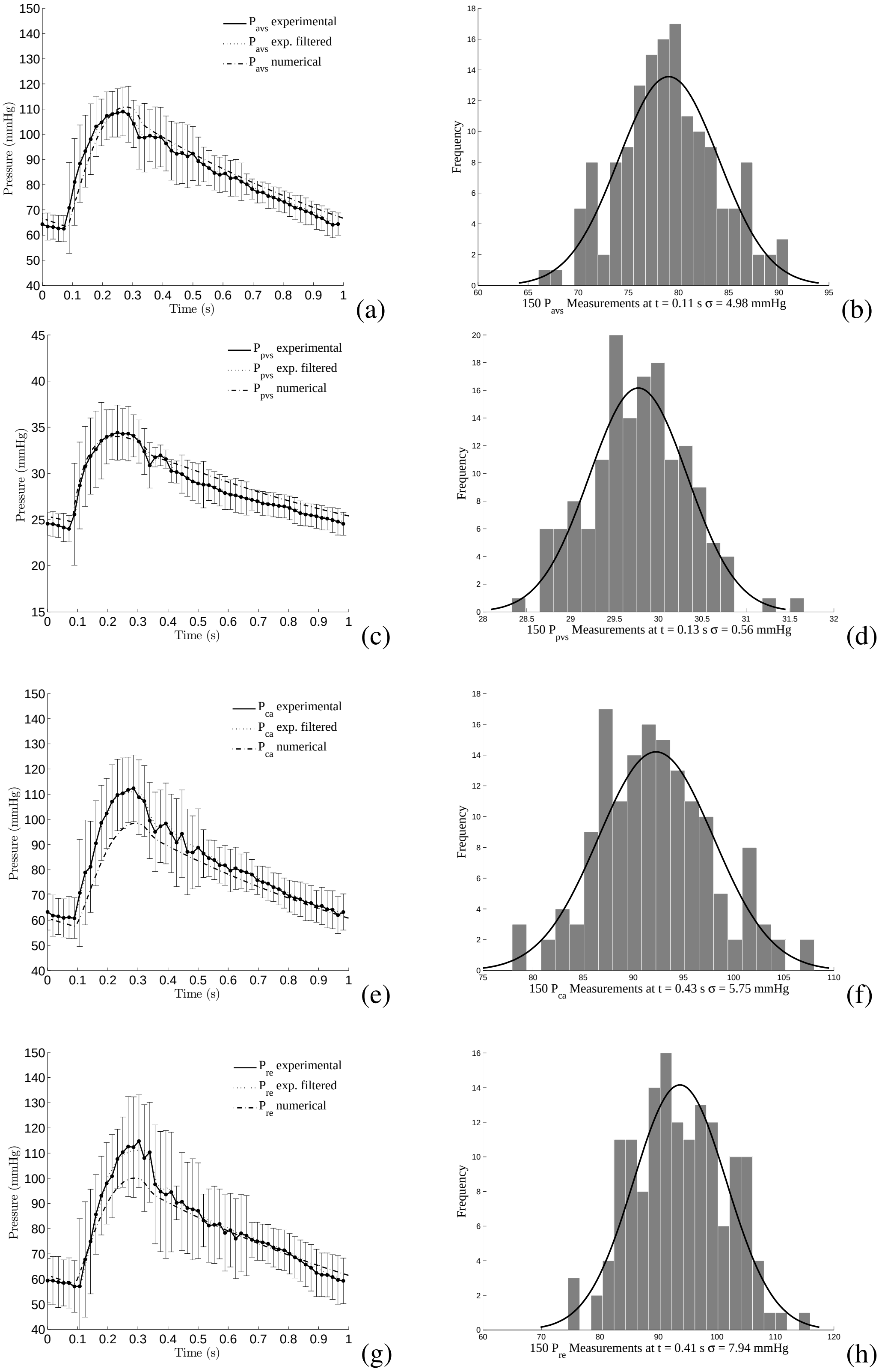

Figure 6.5. Comparison of pressure and flow time histories in aortic, carotid, renal and pulmonary arteries during Class IV HF. The standard error is displayed with the vertical bars. The time of highest standard error is provided in the legend of each histogram.

generates pressure drop in the left ventricle and pressure rise in the cerebral, splanchnic, renal and limbs vascular beds.

6.2.3.1 Case 4: Class III HF with MCS in DA

In Fig. 6.6 (a), it is observed that upon insertion of the MCS at DAo, the pathological aortic sinus pressure waveform has returned to an acceptable level of 118/70 mmHg; and the carotid pressure waveform, presented in Fig. 6.6 (e), has lowered to 120/66 mmHg. A successful re-establishment in CO from 2.7 lt/min to 5.2 lt/min is also observed. Dicrotic notch due to valve closure is less obvious than in the control condition due to the suction generated upstream of the MCS device, as seen in Fig. 6.6 (a). As a general observation, the pressure drop upstream of the MCS device alleviates the high arterial pressures in aortic sinus and carotid artery. Similarly, in the pulmonary artery there is a decreased in $P_{pvs,mean}$ from 28 mmHg to 23 mmHg, as seen in Fig. 6.6(c). However, $P_{\mathrm{re,mean}}$ is elevated from 114.3 mmHg to 137.8 mmHg indicating a potential risk for renal hypertension, as seen in Fig. 6.6(g).

6.2.3.2 Case 5: Class IV HF with MCS in DA

In a similar fashion to Case 4, the MCS insertion at DAo unloaded the vascular beds upstream of the pump and increased the perfusion in the renal loop as seen in Fig. 6.7(g). Central pressure is within a normal-to-low value at 108/60 mmHg and CO is also within a normal limit at 4.82 lt/min in comparison to 2.59 lt/min without MCS.

6.2.3.3 Case 6: Class III HF with MCS in AA

Upon insertion of the MCS in ascending aorta during Class III HF (see Fig. 6.8) it can be observed an optimum LV unloading contrasted by an increased cerebral perfusion with $P_{\mathrm{ca,mean}}$ equal to 133.9 mmHg, hence, falling within the limits for adequately autoregulated perfusion. In general, CO is 5.3 lt/min; $P_{avs,mean}$ is 84.74 mmHg. As it is evident from Fig. 6.5(a) and (e), for both the aortic sinus and carotid pressure waveforms there is

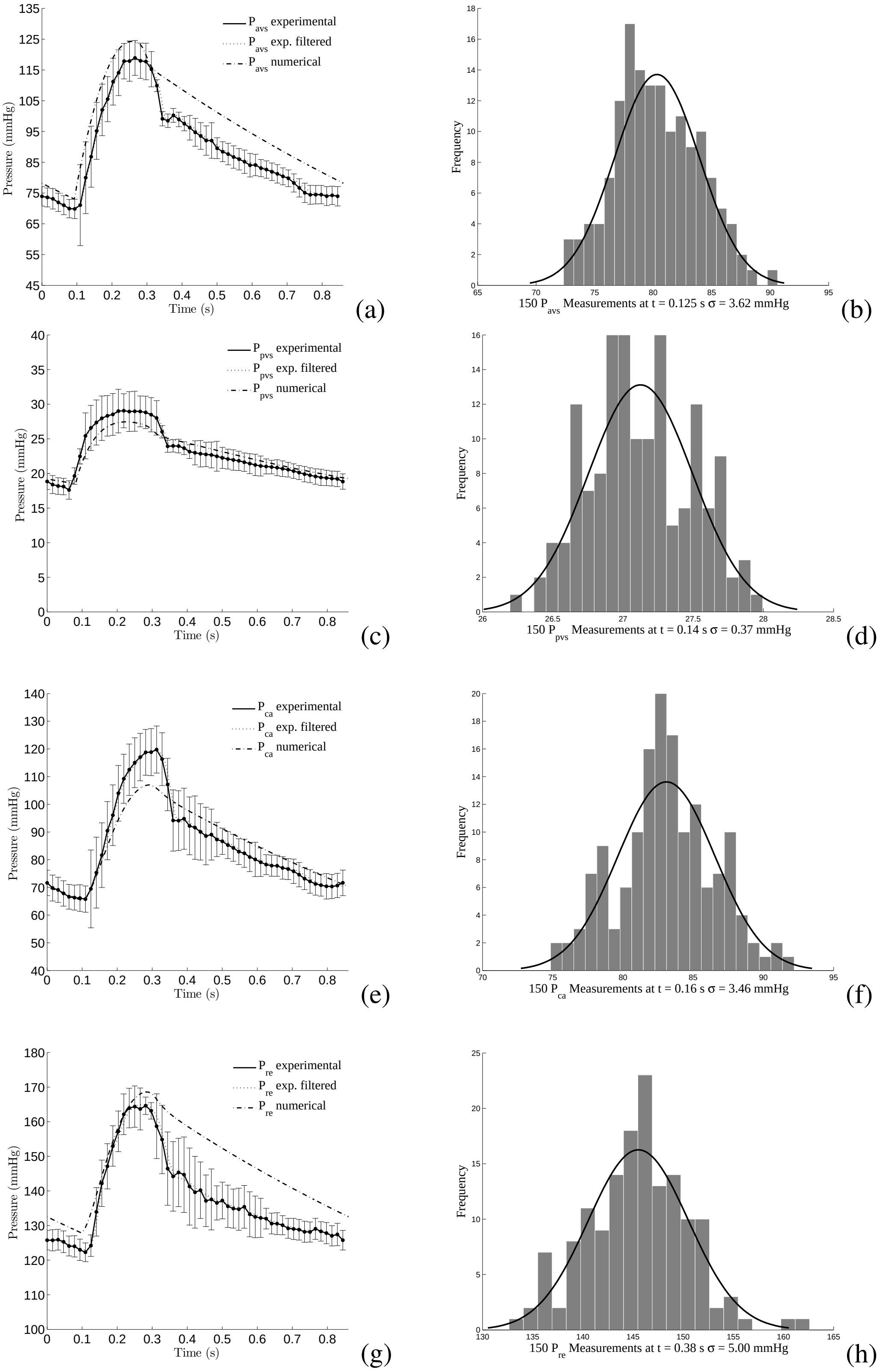

Figure 6.6. Comparison of pressure and flow time histories in aortic, carotid, renal and pulmonary arteries during CHF III upon insertion of MCS in the descending aorta. The standard error is displayed with the vertical bars. The time of highest standard error is provided in the legend of each histogram.

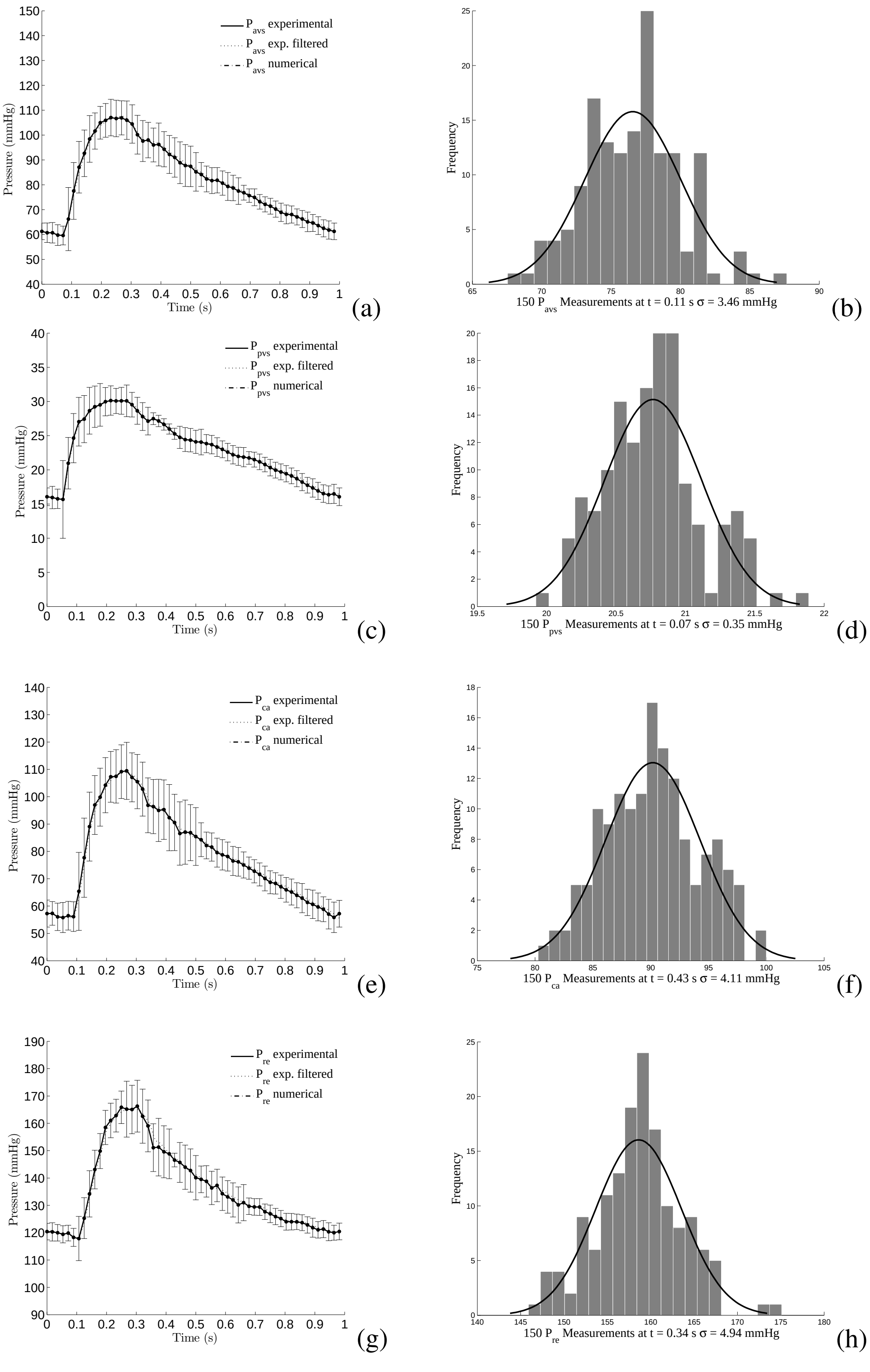

Figure 6.7. Comparison of pressure and flow time histories in aortic, carotid, renal and pulmonary arteries during Class IV HF upon insertion of MCS in the descending aorta. The standard error is displayed with the vertical bars. The time of highest standard error is provided in the legend of each histogram.

a drop in EDP and ESP, in comparison with the control condition. The pulmonary circulation, exhibits a decreased of mean pressure, $P_{pvs,mean}$, from 28.0 mmHg to 23.66 mmHg. Dicrotic notch due to valve closure can not be well distinguished given that the aortic valve remains partially opened during the diastolic phase; see Fig. 6.8(a).

6.2.3.4 Case 7: Class IV HF with MCS in AA

In a similar fashion to Case 6, the MCS insertion in AAo during Class IV HF unloaded LV and increased perfusion to the remaining vascular beds, as seen in Fig. 6.9(a), (c), (e) and (g). Central pressure is within a normal-to-low value at 108/62.4 mmHg and CO is re-established to a normal value at 5.1 lt/min in comparison to the 2.59 lt/min without MCS.

Table 6.1. Summary of hemodynamic variables for the all modelled cases.

Parameter	Control	Class III	Class IV	Class III pump DA	Class IV pump DA	Class III pump AA	Class IV pump AA	Unit
HR	66.67	80.00	60.00	70.00	60.00	70.00	60.00	bmp
LVEDP	4.50	15.00	20.00	8.10	11.00	9.30	11.00	mmHg
LVESP	123.00	139.00	108.80	117.00	107.40	113.50	109.00	mmHg
$P_{\mathrm{avs,s}}$	123.70	140.00	108.70	118.00	107.80	113.30	108.00	mmHg
$P_{\mathrm{avs,d}}$	76.32	99.97	62.46	70.00	59.60	61.00	62.40	mmHg
$\mathrm{AoP}_{\mathrm{mean}}$	94.00	119.40	84.49	89.44	81.74	84.74	84.32	mmHg
Central Pulse Pressure	47.38	40.03	46.24	48.00	48.20	52.30	45.60	mmHg
$P_{\mathrm{ca,s}}$	126.00	141.50	111.00	119.60	108.50	161.20	149.40	mmHg
$P_{\mathrm{ca,d}}$	74.16	95.02	60.72	65.90	55.80	114.70	102.80	mmHg
$P_{\mathrm{ca,mean}}$	94.41	116.50	82.05	85.42	78.94	133.90	122.70	mmHg
$P_{\mathrm{re,s}}$	126.50	142.50	112.00	164.90	165.30	163.30	152.00	mmHg
$P_{\mathrm{re,d}}$	71.53	93.87	56.56	123.30	118.40	112.00	99.00	mmHg
$P_{\mathrm{re,mean}}$	92.43	114.30	79.79	137.80	136.40	131.20	118.30	mmHg
$P_{\mathrm{pvs,s}}$	26.05	32.77	34.80	29.00	30.12	27.00	30.00	mmHg
$P_{\mathrm{pvs,d}}$	10.82	24.12	24.32	17.65	15.67	17.79	16.00	mmHg
$P_{\mathrm{pvs,mean}}$	18.00	28.08	28.60	22.96	23.15	23.66	23.15	mmHg
CO‡	5.50	3.32	2.59	5.20	4.82	5.32	5.10	lt/min
TPR‡	1.26	3.00	3.00	1.03	1.02	0.96	0.99	mmHg.s/ml

‡ Denotes a parameter calculated by using a correction factor of 0.22 given that water is less viscous than blood.

6.3 Discussion

The results show the capability of the multi-chamber SCVL to reproduce the aortic sinus, carotid, renal and pulmonary arteries pressure and flow waveforms in the control, Class III HF and Class IV with and without MCS. Using four tubular permanent magnet linear

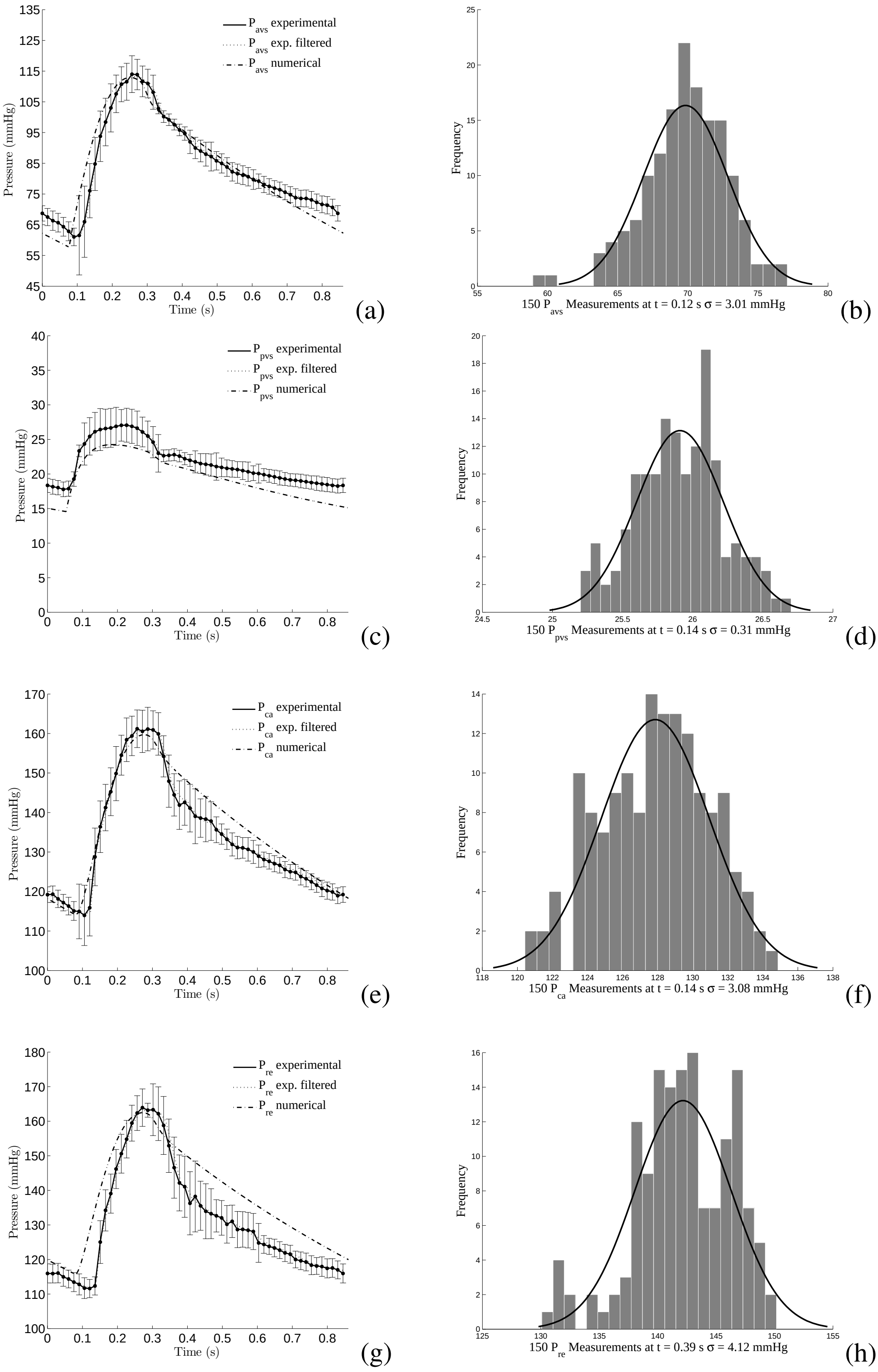

Figure 6.8. Comparison of pressure and flow time histories in aortic, carotid, renal and pulmonary arteries during Class III HF upon insertion of MCS in the ascending aorta. The standard error is displayed with the vertical bars. The time of highest standard error is provided in the legend of each histogram.

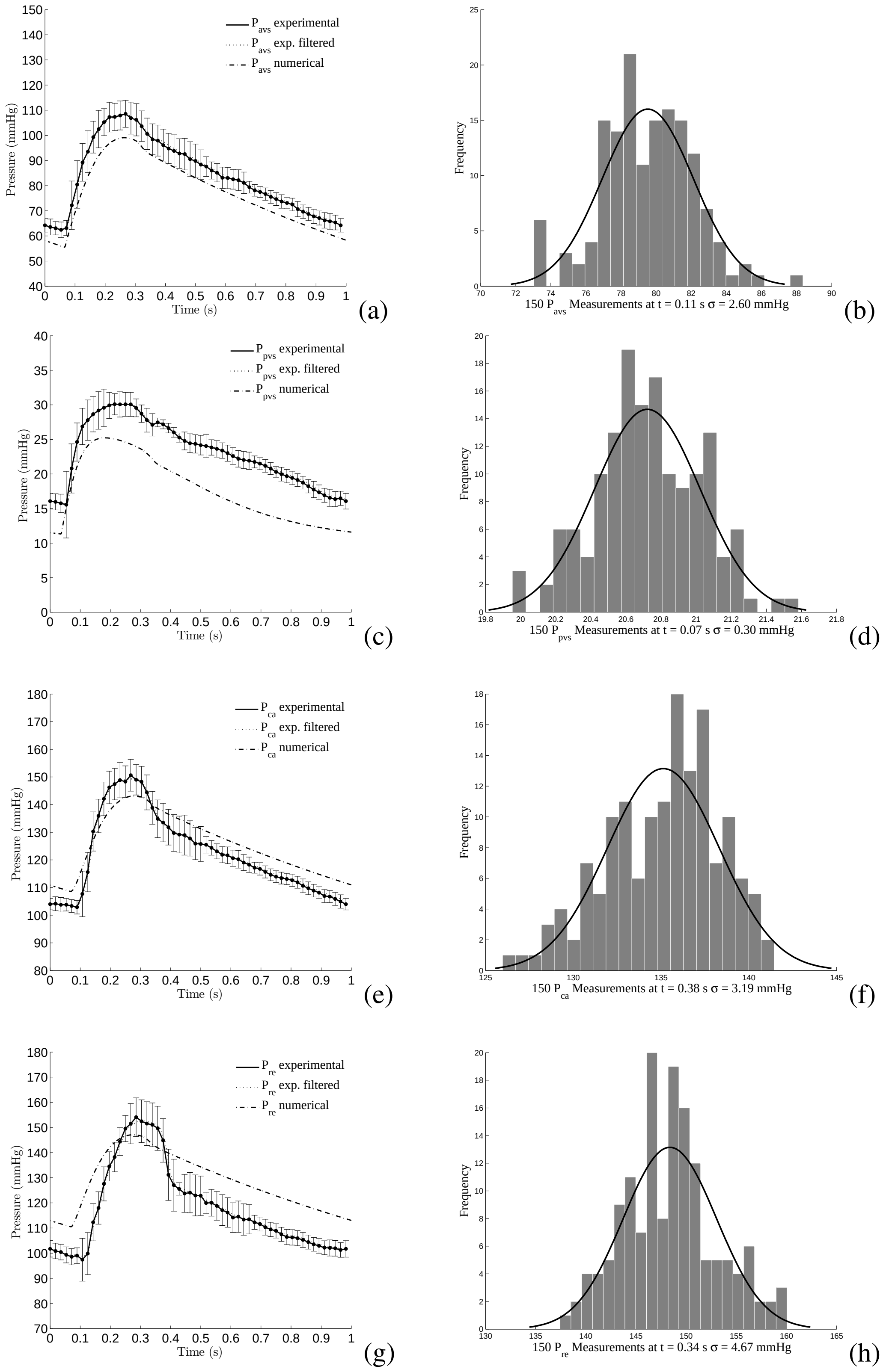

Figure 6.9. Comparison of pressure and flow time histories in aortic, carotid, renal and pulmonary arteries during Class IV HF upon insertion of MCS in the ascending aorta. The standard error is displayed with the vertical bars. The time of highest standard error is provided in the legend of each histogram.

motors, working according to prescribed elastance functions of the native ventricles and atria shows the high success of this technique in emulating the contraction phase and filling phases as found in the native cardiac muscle. A major downside in this work is the implementation of water as the working fluid. Blood differs from water, amongst other factors, by being more viscous, 4 mPa s in comparison with 0.89 mPa s, respectively. Having such difference in viscosity implicated that higher resistances across the entire test rig were necessary to achieve adequate pressure waveforms in all simulated conditions. To compensate for this, a correction factor of 0.22 was implemented in the calculations of TPR and CO; see Table 6.1.

From the statistical analyses, it can be can be observed that for the simulation cases without the MCS device the greatest error occurs at the early stages of the cardiac cycle, that is for T ranging between $0.08 - 0.14$ s; this coincides with the highest load or highest systemic resistance encountered by the linear motor actuating the LV chamber. In the cases with the MCS device, the uncertainties were attenuated at the early cardiac cycle stages and the diastolic phase; this is because the MCS device relieves the load of the linear motor actuating the LV chamber.

One important aspect captured by the SCVL is the augmented pressure at the late systolic phase of the AoPW for the HF simulations; this is due to the increased in systemic resistance and the wave reflections from the periphery or arterial tree [168, 201]. The augmented pulse pressure as the forward wave moves away from the heart is clearly captured by the system; this is, however, not captured by the mathematical model as it is only a lumped parameter representation of the CV system where the arterial stiffness is not accounted for. Finally, the delay between the feet of the aorta, carotid and renal arterial pressures is also captured by the SCVL; see Fig. 6.10 for a schematic representation of the progression of the pressure wave along the aortic tree. From this figure is it noticeable that the onset of the systolic phase is delayed as the wave moves away from the heart.

Table 6.1 shows the haemodynamic variables as found with the multi-chamber SCVL. In general, it can be observed that inserting an MCS device at AAo can be potentially

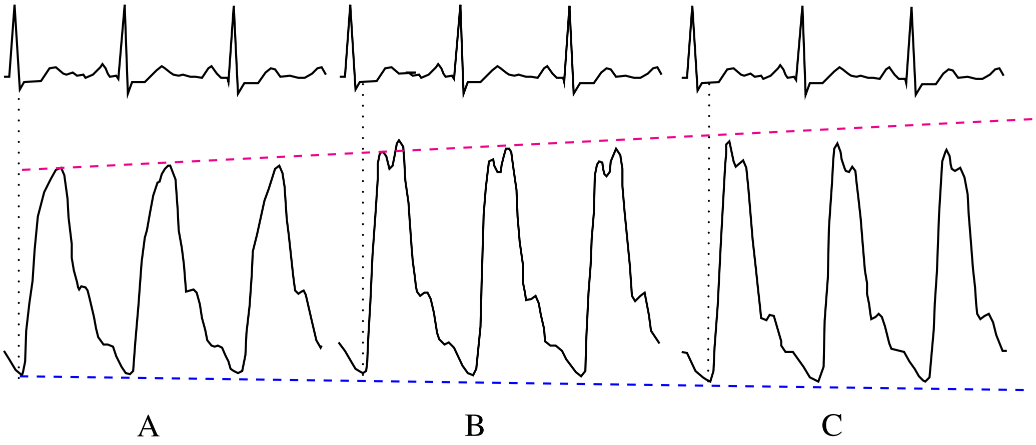

Figure 6.10. Schematic representation of the progression of pressure wave along the aortic tree. A; coronary arteries; B: Abdominal aorta at the level of the renal arteries; C: iliac artery. Adapted from Safar et al. [201].

dangerous as it increases the perfusion of the cerebral vascular bed well above the control values. In all simulated cases the dicrotic notch is captured in the aortic sinus and carotid pressure waveforms although less notorious when the MCS device was inserted at DAo. In comparison to the native pressure waveform, the dicrotic notch on the experimental results seems slightly bigger, this is justified with the implementation of mechanical heart valves as the pressure difference across these devices is higher than that found in the native system [138]. The implementation of glass in the aorta section of the SCVL can be accountable for the steeper rise of the pulse pressure as seen in all pressure waveforms; this is because the stiffness of this material is far greater to what is found in the native vasculature [168].

One of the crucial concerns of implanting a pump in descending aorta is that the perfusion pressure in the brain might be affected by the pressure drop generated upstream the pump. Nevertheless, according to Guyton et al. [6] and different studies conducted by Reitan et al. [198–200], in a native human cardiovascular system cerebral blood flow is well autoregulated for a $P_{ca,mean}$ between 60-140 mmHg, that is, the local blood flow feedback control provides enough blood perfusion within this limit. According to the experimental findings, upon insertion of MCS at DAo $P_{\mathrm{ca,mean}}$ has a value of 85.42 mmHg for Class III HF and 78.94 mmHg for Class IV HF, these values fit well within the range of 60-140 mmHg therefore, the pressure drop in carotid artery will not impose perfusion disturbances in the brain. The pulmonary circulation also benefits from a MCS at DAo since $P_{pvs,mean}$ was decreased by 5 mmHg in both Class III and IV HF.

Chapter 7

Conclusions and Recommendations

7.1 Conclusions

The objectives set up in this work were well accomplished. As a result of the combination of models and proper optimisation of the system parameters, predictions of pathophysiological trends were successfully obtained; see Fig. 7.1 for diagrammatic representation of the stages undertaken in this work. In the following sections the conclusion relevant to the models implemented in this work are presented.

7.1.1 Mathematical model

Haemodynamic variables including pressures, flows and volumes were evaluated in the four cardiovascular chambers. In general, the model followed physiological trends when compared to cycle-averaged parameters but not so closely when compared to pressure time histories along the aorta artery; however, the model is good enough for predicting central artery pressures and flows which ultimately allowed the selection an adequate design point for the MCS device. Evaluation of central hemodynamic variables is essential in the diagnosis and treatment of patients with suspected cardiovascular disease, such as myocardial infarction and heart failure [111]. In clinical practice the conductance catheter intervention continues to be the best technique for the evaluation of cardiac function, in-

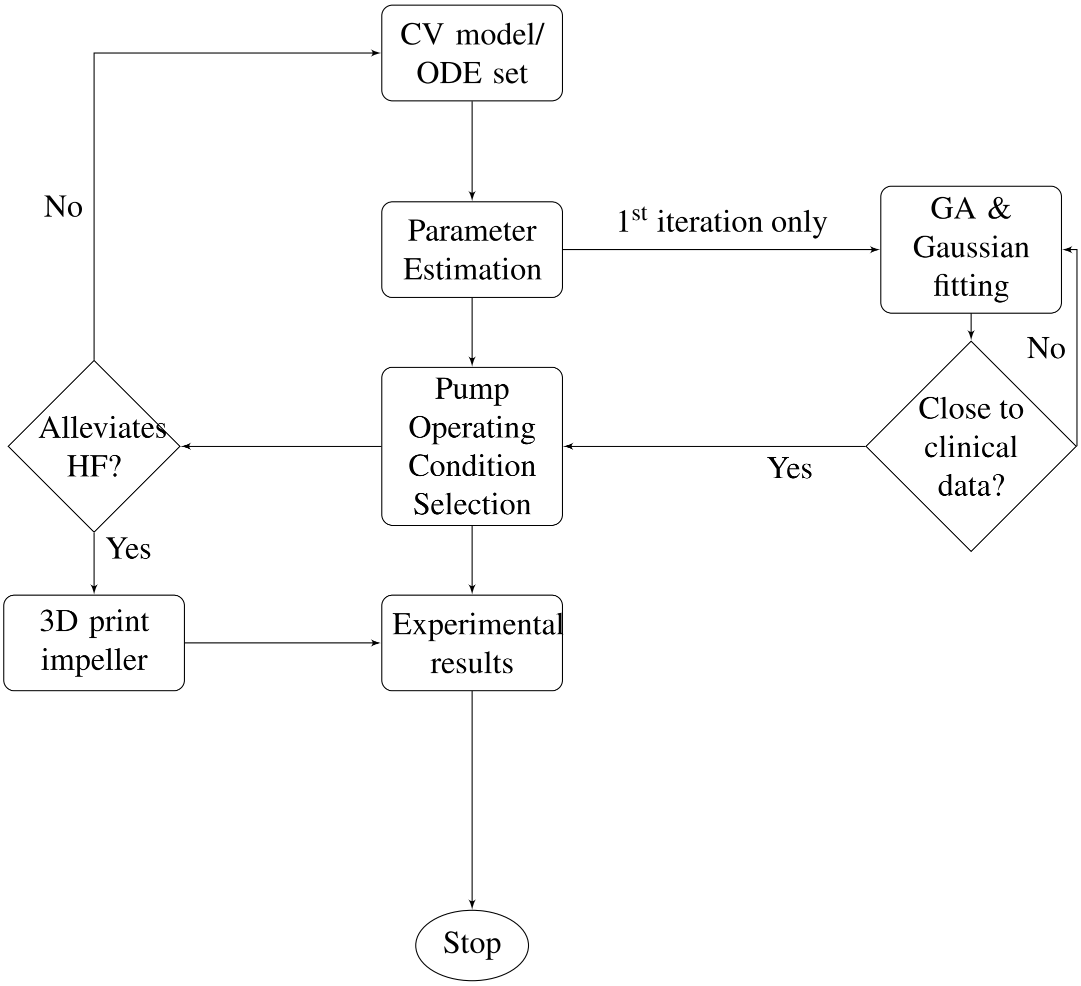

Figure 7.1. Flow chart representing the stages and processes undertaken during this work.

cluding presure; volume and cardiac contractily [202]. However, this procedure has limited clinical applications due to its invasive nature and possible side effects [111, 202]. Imaging techniques such as MRI, although not invasive, tend to underestimate CO in non physiological conditions [202]. Cardiovascular models have the potential to accurately estimate patient specific cardiovascular function [112, 203].

Mathematical models of the human cardiovascular system continue to be relevant tools in the estimation of haemodynamic properties that are almost impossible to measure in the clinical settings. The implementation of GAs for tuning purposes increases the possibility of creating more complex models. In the present model optimal values for the vessel compliance of both systemic and pulmonary circulations were identified. These values fit well a Gaussian distribution and can be used in future works as objective functions, or geometric constraints, to implement a more sophisticated autoregulation system. In this way, not only physiological conditions can be reproduced, but also diseased conditions, and very importantly the use of cardiovascular supportive devices could be evaluated. In the clinical setting, the gold standard of the cardiac condition assessment, mainly LV contractility, is considered to be the dynamic PV loop analysis [202]. Unfortunately this assessment is not routine in every day clinical practice due to its invasive nature and high risk of complications. Clearly, a more dynamic non-invasive method is still missing in the clinical setting and it will perhaps be through mathematical modelling that this could be accomplished [111].

After several iterations, it was found that a pressure difference of 70 mmHg and a flow rate of 5 lt/min produced the closest match to the imposed criteria of alleviating LV high filling pressures, unloading LV and re-establishing a normal CO without compromising cerebral perfusion. The inclusion of a volume reflex to the mathematical model, to account for the autoregulation of blood volume, played a crucial role in the adequate selection of the MCS device design point.

7.1.2 In-vitro model

The multi-chamber SCVL implemented in this work successfully validated the numerical results. The present SCVL is a close-to-atmosphere system and includes models for all four chambers as well as the systemic and pulmonary circulation loops. Using linear motors for displacing individual heart chamber provides a satisfactory technique for emulating different physiological and pathological conditions of the human cardiovascular system. Although the system presented many random and systematic errors the mean measurements predicted, closely enough, important haemodynamic variables.

The selected impeller provided effective circulatory support for Class III and IV HF conditions displaying the capability of this approach for alleviating the high afterload pressure in LV. In particular, it was found that placing the selected impeller at DAo can be more beneficial for a Class III HF condition when compared to the AAo configuration, this is because the mean carotid pressure was found to be elevated.

In general, the results show the capability of in-vitro model to replicate various physiological and pathological conditions with and without an MCS device. Although in-vivo testing is the ideal solution for investigating various MCS device performance, developing more elaborate SCVL could be more cost effective and also could provide cardiologists with reliable outcomes.

7.2 Further Work

Throughout the development of this work many limitations that could improve the accuracy of the results were identified. A summary of these items together with their suggested pathway for improvement is provided below.

7.2.1 Mathematical model

The present mathematical model of CV system was developed with the intention of mimicking several pathophysiological conditions and simulating short-term transient responses to changes induced during the usage of MCS devices. The suggested pathway would be to model cardiac and vascular functions at a molecular level so that more accurate predictions of an MCS device performance in the short- and, most importantly, in the long-term can be made. This should be coupled with a wave propagation model, for the arterial tree mainly, with the intention of representing more adequately the early stages of the systolic AoPW and the entirety of the diastolic portion of the AoPW. In this way, patient-specific data can be input to the model with the main goal of optimising the MCS device design and the surgical implantation site.

7.2.2 In-vitro model

In the present in-vitro model, the implementation of a glass made aorta meant that wave propagations were occurring at a faster rate. One way to improve this difficulty would be to implement a dynamic compliance unit. This system would be composed of a reciprocating piston mechanism and a silicone bellow; see Fig. 7.2. The piston would allow to vary the compliance of the system while the silicone material, due to is elastic property, would delay the fast propagating waves. The Dynamic Compliance model was built at Queen Mary's Workshop (see Fig.7.3) however, due to time constraints it was not possible to test it.

The tests performed with the MCS device were carried out in series with the heart and although this proved beneficial it would be important to test a parallel configuration as well. This is particularly important given that many of the commercial devices have a LV-Apex-to-Aorta bypass configuration; see Table 1.3. The present model uses rubber gaiters for heart chambers therefore, it is not possible to connect a MCS device to its non-rigid walls. With this in mind, a diaphragm pump is recommended for further studies; see Fig. 7.4. This system is composed of rigid walls and a rubber diaphragm. This configuration would allow for the connection of MCS devices across the chamber's rigid walls. This model was built at Queen Mary's Workshop (see Fig.7.5) however, due to time constraints it was not possible to test it.

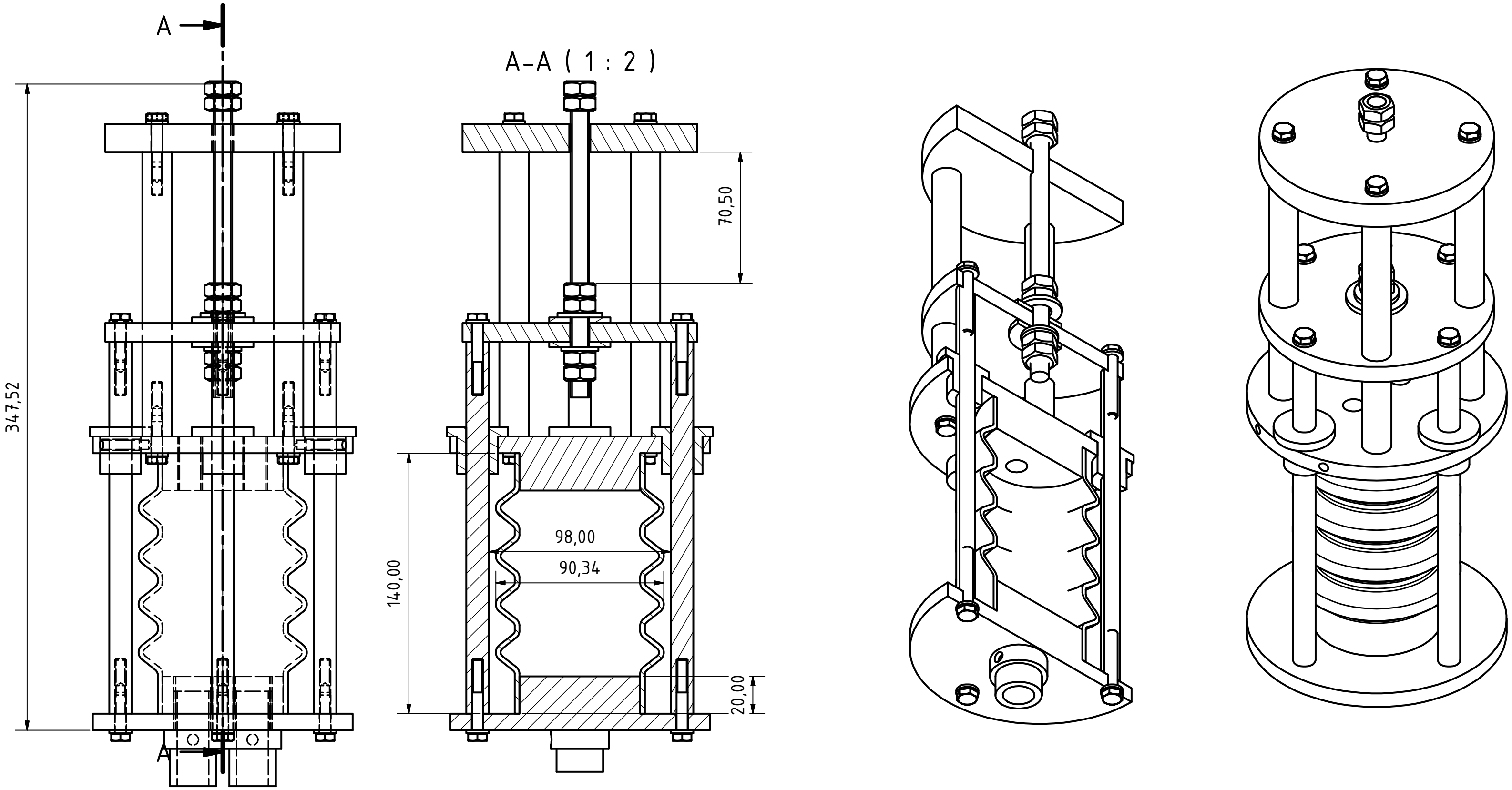

Figure 7.2. Drawing of the proposed dynamic compliance unit.

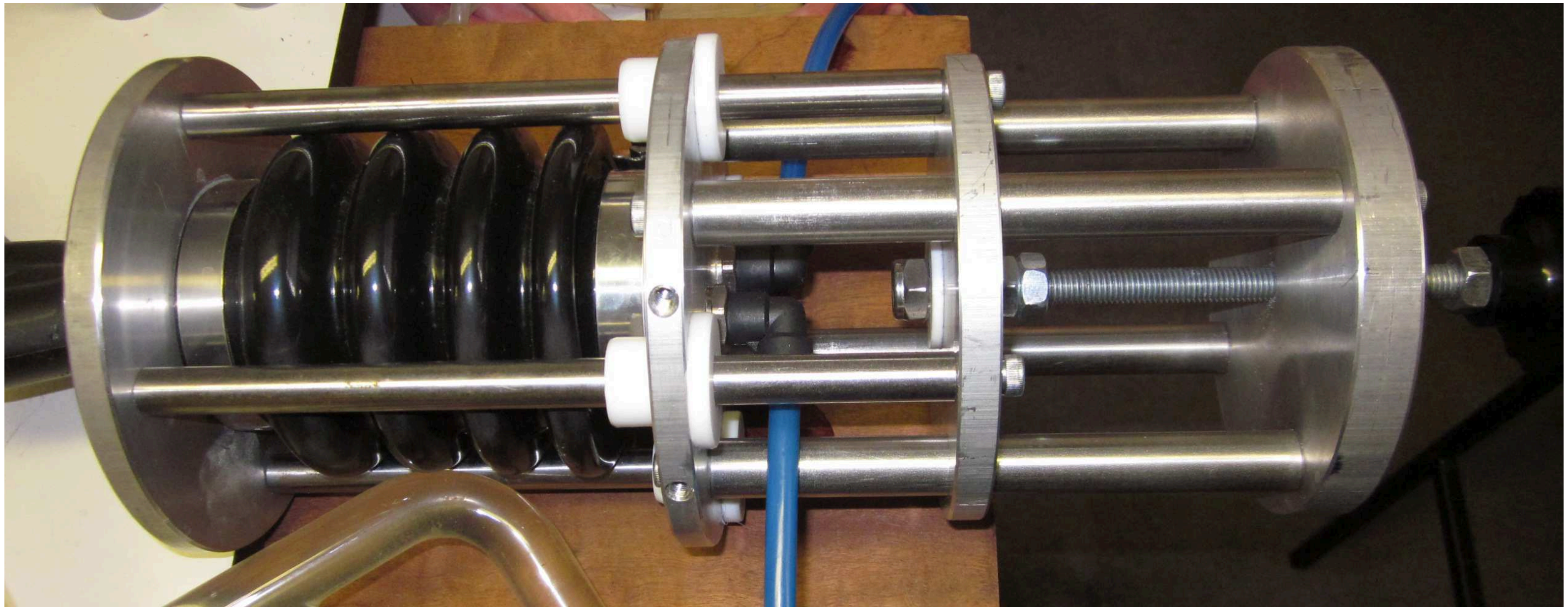

Figure 7.3. Manufactured dynamic compliance unit.

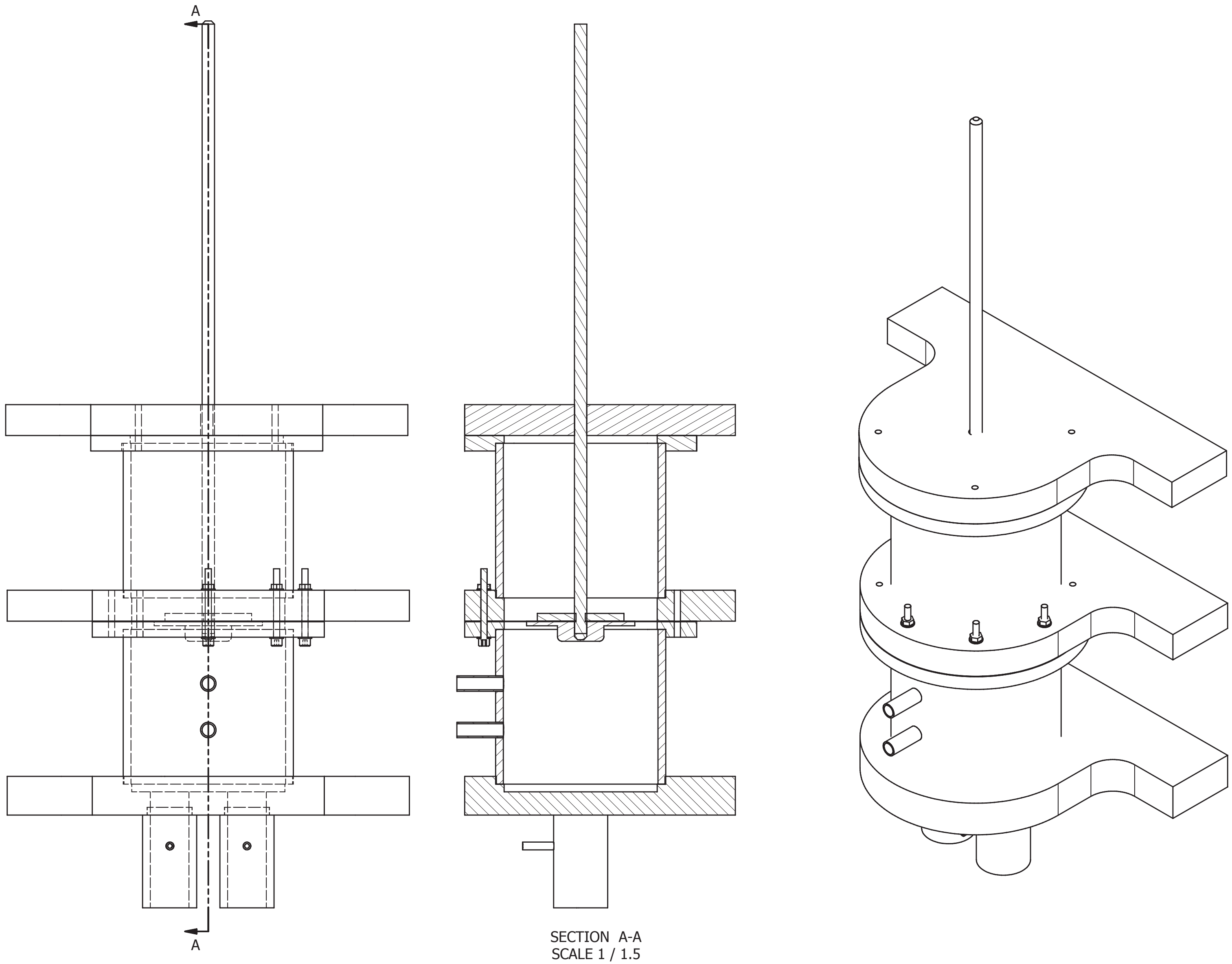

Figure 7.4. Drawing of the proposed diaphragm pump.

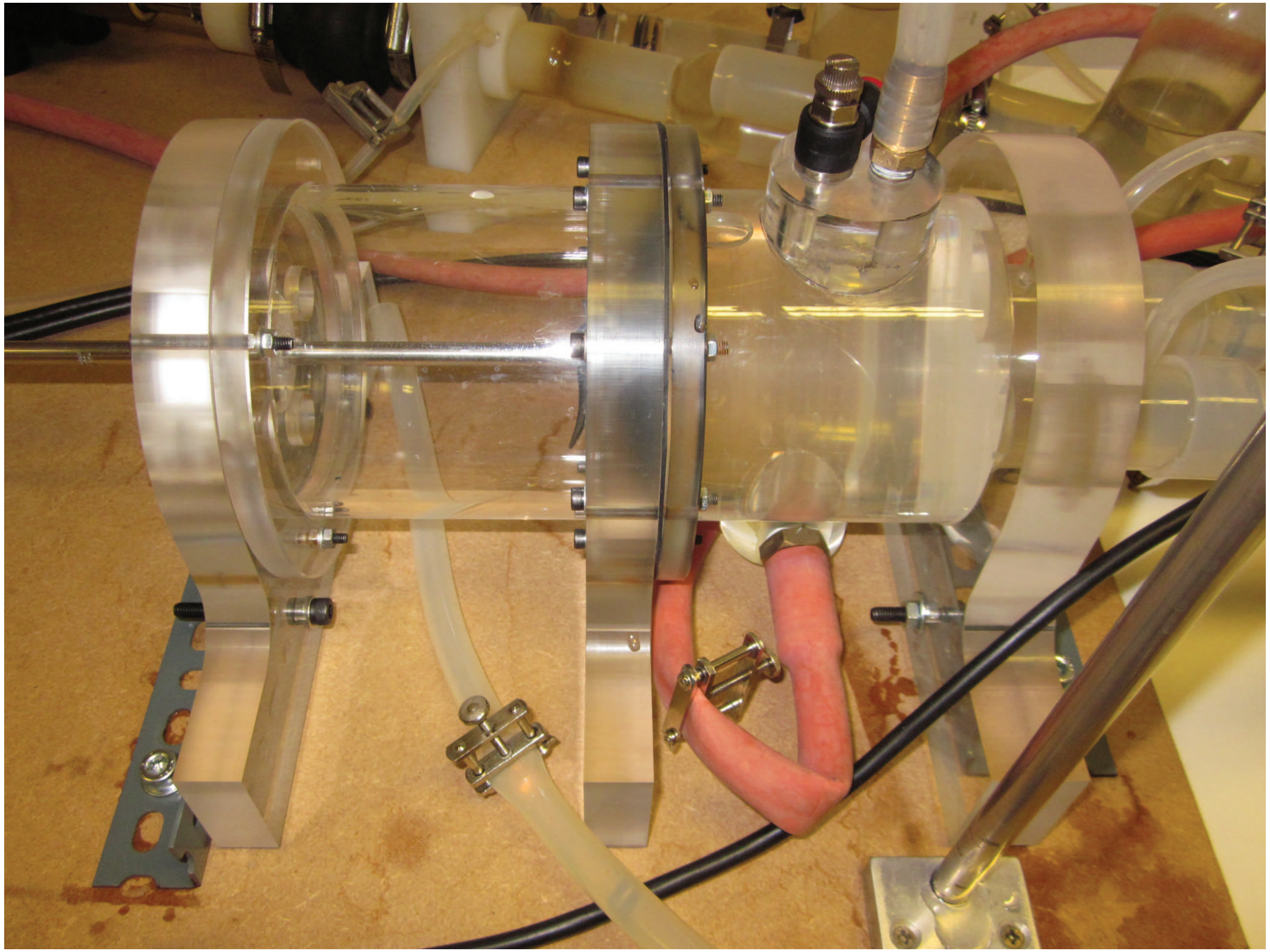

Figure 7.5. Manufactured diaphragm pump with parallel MCS device connection site.

7.2.3 The centrifugal pump

One of the main constraints of having selected an off-the-shelf centrifugal pump was the inability to modify its volute; this in turn, limited the possibilities of investigating many other impeller geometries. In future works, the impeller and the volute should be purposely designed to fit the desirable operating condition. Similarly, the motor's angular speed was not controllable which in turn limited the geometry of the impeller. It is therefore recommended to implement a motor controller that could also allow the measurement of the current and voltage with the intention of calculating the efficiency of the system.

Given that the wall shear stress should not exceed 150 Pa, greater attention should be given to the design and testing of the impeller blades. In terms of testing, an optical method for flow visualisation such as Particle Image Velocimetry coupled to a purposely designed computer analysis program, for the compilation of the velocity data along a boundary and its transformation into shear stress, should be implemented.

7.3 Published Work

The contents of Chapter 6 have been partially published in: In vitro cardiovascular system emulator (bioreactor) for the simulation of normal and diseased conditions with and without mechanical circulatory support. Paula Ruiz, Mohamand Amin Rezaienia, Akbar Rahideh, Thomas R Keeble, Martin T Rothman, Theodosios Korakianitis. Artificial Organs 06/2013; 37(6):549-60.

Appendix A

Model Parameters

Parameter	Control	CHF III	CHF III pump AAo	CHF III pump DAo	CHF IV	CHF IV pump AAo	CHF IV pump DAo
Vcovb,0	100.000	110.000	110.000	120.000	115.000	115.000	115.000
Vcvb,0	450.000	605.000	605.000	660.000	632.500	632.500	632.500
Vsvb,0	1150.000	1320.000	1320.000	1440.000	1380.000	1380.000	1380.000
Vrvd,0	1000.000	1045.000	1045.000	1140.000	1092.500	1092.500	1092.500
Vp,0	550.000	605.000	605.000	660.000	632.500	632.500	632.500
Vulvb,0	400.000	440.000	440.000	480.000	460.000	460.000	460.000
Vllvb,0	500.000	550.000	550.000	600.000	575.000	575.000	575.000
Vsvc,0	100.000	110.000	110.000	120.000	115.000	115.000	115.000
Vivc,0	200.000	220.000	220.000	240.000	230.000	230.000	230.000
Vaorta,0	250.000	275.000	275.000	300.000	287.500	287.500	287.500
Vheart,0	380.000	330.000	330.000	360.000	345.000	345.000	345.000
Vlv0	152.000	132.000	132.000	144.000	138.000	138.000	138.000
Vla0	57.000	49.500	49.500	120.000	51.750	51.750	51.750
Vrv0	114.000	99.000	99.000	660.000	103.500	103.500	103.500
Vra0	57.000	49.500	49.500	49.500	51.750	51.750	51.750
T	0.830	0.750	0.750	1.00	0.660	0.750	0.750
HR	72.289	80.000	80.000	80.000	90.909	80.000	80.000
Ts1	0.273	0.260	0.260	0.260	0.244	0.260	0.260
Ts2	0.410	0.390	0.390	0.390	0.366	0.390	0.390
Tpwb	0.710	0.650	0.650	0.650	0.560	0.640	0.640
Tpww	0.830	0.750	0.750	0.750	0.660	0.750	0.750
Elvs	3.000	3.000	3.000	3.000	3.830	3.900	3.900
Elvd	0.100	1.500	1.500	1.500	2.000	1.900	1.900
Elamax	0.500	1.000	1.000	1.000	1.000	1.000	1.000
Elamin	0.250	0.500	0.500	0.500	0.500	0.500	0.500
Ervs	1.200	1.800	1.800	1.800	1.800	1.800	1.800

Parameter	Control	CHF III	CHF III pump AAo	CHF III pump DAo	CHF IV	CHF IV pump AAo	CHF IV pump DAo
Ervd	0.100	0.100	0.100	0.100	0.100	0.100	0.100
Eramax	0.500	1.000	1.000	1.000	1.000	1.000	1.000
Eramin	0.250	0.250	0.250	0.250	0.250	0.250	0.250
Plv,0	4.000	20.000	12.000	12.000	20.000	20.000	20.000
Pla,0	3.000	3.000	3.000	3.000	3.000	3.000	3.000
Prv,0	3.000	7.000	7.000	7.000	7.000	10.000	7.000
Pra,0	3.000	3.000	3.000	3.000	3.000	3.000	3.000
Pump AAo	0.000	0.000	70.000	0.000	0.000	70.000	0.000
Pump DAo	0.000	0.000	0.000	70.000	0.000	0.000	70.000
T_ref	0.830	0.750	0.750	1.000	0.660	0.750	0.750
Psyst_ref	90.000	90.000	90.000	90.00	90.000	90.000	90.000
Ppul_ref	8.000	8.000	8.000	8.000	8.000	8.000	4.000
G_co	0.035	0.035	0.035	0.035	0.035	0.035	0.035
CO_ref	5.000	5.000	5.000	0.250	5.000	5.000	5.000
G_gfr	1.000	2.000	2.000	2.000	2.000	2.000	2.000
Vra_ref	90.000	90.000	90.000	90.000	90.000	90.000	90.000
G_erv	-0.005	-0.004	-0.004	-0.004	-0.004	-0.004	0.005
G_elv	0.010	0.010	0.010	0.010	0.010	0.010	0.010
G_eld	0.000	0.010	0.010	0.000	0.000	-0.010	0.010
G_r,sar	0.005	0.005	0.005	70.000	0.005	0.005	0.010
G_c,svn	0.050	0.050	0.050	0.750	0.050	0.100	0.100
G_r,par	-0.005	-0.005	-0.005	-0.005	-0.005	-0.005	-0.005
G_c,pvn	-0.050	-0.050	-0.050	-0.050	-0.050	-0.050	-0.050
Qsti	200.000	200.000	200.000	200.000	200.000	200.000	200.000
Qpti	0.180	0.180	0.180	0.180	0.180	0.180	0.180
Qdti	2.000	2.000	2.000	2.000	2.000	2.000	2.000
Qsmi	400.000	400.000	400.000	400.000	400.000	400.000	400.000
Qpmi	0.150	0.150	0.150	0.150	0.150	0.150	0.150
Qdmi	2.000	2.000	2.000	2.00	2.000	2.000	2.000
Qspo	800.000	800.000	800.000	800.000	800.000	800.000	800.000
Qppo	1.500	1.500	1.500	1.500	1.500	1.500	1.500
Qdpo	2.500	2.500	2.500	2.500	2.500	2.500	2.500
Qsao	900.000	900.000	900.000	900.000	900.000	900.000	900.000
Qpao	0.280	0.280	0.280	0.280	0.280	0.280	0.280
Qdao	1.000	1.000	1.000	1.000	1.000	1.000	1.000
Cavs	0.800	0.400	0.200	0.200	0.200	0.500	0.700
Carao	0.120	0.050	0.050	0.050	0.050	0.050	0.050
Ctao	0.120	0.025	0.025	0.025	0.025	0.025	0.025
Cuaao	0.120	0.025	0.025	0.025	0.025	0.025	0.025
Claao	0.120	0.025	0.025	0.025	0.025	0.025	0.025

Parameter	Control	CHF III	CHF III pump AAo	CHF III pump DAo	CHF IV	CHF IV pump AAo	CHF IV pump DAo
Ccoil	0.120	0.025	0.025	0.025	0.025	0.025	0.025
Lavs	0.000	0.000	0.000	0.000	0.000	0.000	0.000
Larao	0.000	0.000	0.000	0.000	0.000	0.000	0.000
Ltao	0.000	0.000	0.000	0.000	0.000	0.000	0.000
Luaao	0.000	0.000	0.000	0.000	0.000	0.000	0.000
Llaao	0.000	0.000	0.000	0.000	0.000	0.000	0.000
Lcoil	0.000	0.000	0.000	1.000	0.000	0.000	0.000
Vavs,0	50.000	45.833	45.833	0.500	47.917	47.917	47.917
Varao,0	50.000	45.833	45.833	0.050	47.917	47.917	47.917
Vtao,0	50.000	45.833	45.833	0.025	47.917	47.917	47.917
Vuaao,0	50.000	45.833	45.833	0.025	47.917	47.917	47.917
Vlaao0	50.000	45.833	45.833	0.025	47.917	47.917	47.917
Vcoil0	50.000	45.833	45.833	0.025	47.917	47.917	47.917
Ravs	0.010	0.100	0.100	0.000	0.100	0.100	0.100
Rarao	0.000	0.010	0.010	0.000	0.010	0.010	0.003
Rtao	0.000	0.010	0.010	0.000	0.010	0.010	0.003
Ruaao	0.000	0.010	0.010	0.000	0.010	0.010	0.300
Rlaao	0.000	0.010	0.010	0.000	0.010	0.010	0.003
Rcoil	0.000	0.010	0.010	0.000	0.010	0.010	0.003
Qavs,0	600.000	600.000	600.000	600.000	600.000	600.000	600.000
Qarao,0	600.000	600.000	600.000	600.000	600.000	600.000	600.000
Qtao,0	600.000	600.000	600.000	600.000	600.000	600.000	600.000
Quaao,0	600.000	600.000	600.000	600.000	600.000	600.000	600.000
Qlaao,0	600.000	600.000	600.000	600.000	600.000	600.000	600.000
Qcoil,0	600.000	600.000	600.000	600.000	600.000	600.000	600.000
Csvc	31.820	31.820	31.820	31.820	31.820	31.820	31.820
Lsvc	0.000	0.000	0.000	0.000	0.000	0.000	0.000
Psvc,0	6.000	6.000	6.000	0.010	6.000	6.000	6.000
Rsvc	0.010	0.010	0.010	0.010	0.010	0.010	0.010
Qsvc,0	600.000	600.000	600.000	0.010	600.000	600.000	600.000
Civc	142.938	142.938	142.938	0.010	142.938	142.938	142.938
Livc	0.000	0.000	0.000	600.000	0.000	0.000	0.000
Pivc,0	6.000	6.000	6.000	600.000	6.000	6.000	6.000
Rivc	0.060	0.060	0.060	600.000	0.060	0.060	0.060
Qivc,0	600.000	600.000	600.000	600.000	600.000	600.000	600.000
Psat_covb,0	114.000	114.000	114.000	600.000	114.000	114.000	114.000
Psta_covb,0	108.000	108.000	108.000	600.000	108.000	108.000	108.000
Psar_covb,0	96.000	96.000	96.000	31.820	96.000	96.000	96.000
Pscp_covb,0	36.000	36.000	36.000	0.000	36.000	36.000	36.000
Psvl_covb,0	24.000	24.000	24.000	6.000	24.000	24.000	24.000

Parameter	**Control**	**CHF III**	**CHF III pump AAo**	**CHF III pump DAo**	**CHF IV**	**CHF IV pump AAo**	**CHF IV pump DAo**
Pssv_covb,0	18.000	18.000	18.000	0.010	18.000	18.000	18.000
Psvn_covb,0	12.000	12.000	12.000	600.000	12.000	12.000	12.000
Vsat_covb,0	10.530	11.583	11.583	142.938	12.110	12.110	12.110
Vsta_covb,0	4.680	5.148	5.148	0.000	5.382	5.382	5.382
Vsar_covb,0	4.680	5.148	5.148	6.000	5.382	5.382	5.382
Vscp_covb,0	3.510	3.861	3.861	0.060	4.037	4.037	4.037
Vsvl_covb,0	8.190	9.009	9.009	600.000	9.419	9.419	9.419
Vssv_covb,0	10.000	11.000	11.000	114.000	11.500	11.500	11.500
Vsvn_covb,0	48.400	53.240	53.240	108.000	55.660	55.660	55.660
Vcs,0	10.000	11.000	11.000	96.000	11.500	11.500	11.500
Csat_covb	0.012	0.007	0.007	36.000	0.007	0.007	0.007
Csta_covb	0.012	0.007	0.007	24.000	0.007	0.007	0.007
Csar_covb	0.012	0.007	0.007	18.000	0.007	0.007	0.007
Cscp_covb	0.012	0.007	0.007	12.000	0.007	0.007	0.007
Csvl_covb	0.019	0.011	0.011	12.636	0.011	0.011	0.011
Cssv_covb	1.640	0.957	0.957	5.616	0.957	0.957	0.957
Csvn_covb	6.012	3.507	3.507	5.616	3.507	3.507	3.507
Qsat_covb,0	577.751	577.751	577.751	4.212	577.751	577.751	577.751
Qsta_covb,0	200.277	200.277	200.277	9.828	200.277	200.277	200.277
Qsar_covb,0	100.000	100.000	100.000	12.000	100.000	100.000	100.000
Qscp_covb,0	200.277	200.277	200.277	58.080	200.277	200.277	200.277
Qsvl_covb,0	577.751	577.751	577.751	12.000	577.751	577.751	577.751
Qssv_covb,0	599.978	599.978	599.978	0.007	599.978	599.978	599.978
Qsvn_covb,0	600.000	600.000	600.000	0.007	600.000	600.000	600.000
Lsat_covb	0.000	0.000	0.000	0.007	0.000	0.000	0.000
Lsta_covb	0.000	0.000	0.000	0.007	0.000	0.000	0.000
Lsar_covb	0.000	0.000	0.000	0.011	0.000	0.000	0.000
Lscp_covb	0.000	0.000	0.000	0.957	0.000	0.000	0.000
Lsvl_covb	0.000	0.000	0.000	3.507	0.000	0.000	0.000
Lssv_covb	0.000	0.000	0.000	577.751	0.000	0.000	0.000
Lsvn_covb	0.000	0.000	0.000	200.277	0.000	0.000	0.000
Rsat_covb	1.392	3.555	3.087	100.000	3.227	3.227	3.423
Rsta_covb	4.100	10.474	9.096	200.277	9.509	9.509	10.085
Rsar_covb	6.000	15.327	13.310	577.751	13.915	13.915	14.758
Rscp_covb	4.100	10.474	9.096	599.978	9.509	9.509	10.085
Rsvl_covb	1.392	3.555	3.087	600.000	3.227	3.227	3.423
Rssv_covb	1.007	2.574	2.235	0.000	2.336	2.336	2.478
Rsvn_covb	1.000	2.555	2.218	0.000	2.319	2.319	2.460
Ccs	1.640	0.957	0.957	0.000	0.957	0.957	0.957
Lcs	0.000	0.000	0.000	0.000	0.000	0.000	0.000

Parameter	**Control**	**CHF III**	**CHF III pump AAo**	**CHF III pump DAo**	**CHF IV**	**CHF IV pump AAo**	**CHF IV pump DAo**
Rcs	1.000	2.554	2.218	0.000	2.319	2.319	2.460
Pcs,0	12.000	12.000	12.000	0.000	12.000	12.000	12.000
Qcs,0	600.000	600.000	600.000	0.000	600.000	600.000	600.000
Psat_cvb,0	120.000	120.000	120.000	3.878	120.000	120.000	120.000
Psta_cvb,0	108.000	108.000	108.000	11.426	108.000	108.000	108.000
Psar_cvb,0	96.000	96.000	96.000	16.720	96.000	96.000	96.000
Pscp_cvb,0	36.000	36.000	36.000	11.426	36.000	36.000	36.000
Psvl_cvb,0	24.000	24.000	24.000	3.878	24.000	24.000	24.000
Pssv_cvb,0	18.000	18.000	18.000	2.807	18.000	18.000	18.000
Psvn_cvb,0	12.000	12.000	12.000	2.787	12.000	12.000	12.000
Vsat_cvb,0	47.385	63.707	63.707	0.957	66.602	66.602	66.602
Vsta_cvb,0	21.060	28.314	28.314	0.000	29.601	29.601	29.601
Vsar_cvb,0	21.060	28.314	28.314	2.787	29.601	29.601	29.601
Vscp_cvb,0	15.795	21.236	21.236	12.000	22.201	22.201	22.201
Vsvl_cvb,0	36.855	49.550	49.550	600.000	51.802	51.802	51.802
Vssv_cvb,0	92.160	123.904	123.904	120.000	129.536	129.536	129.536
Vsvn_cvb,0	215.685	289.977	289.977	108.000	303.157	303.157	303.157
Csat_cvb	0.012	0.007	0.007	36.000	0.007	0.007	0.007
Csta_cvb	0.012	0.007	0.007	24.000	0.007	0.007	0.007
Csar_cvb	0.012	0.007	0.007	18.000	0.007	0.007	0.007
Cscp_cvb	0.012	0.007	0.007	12.000	0.007	0.007	0.007
Csvl_cvb	0.067	0.039	0.049	69.498	0.049	0.049	0.049
Cssv_cvb	12.221	7.129	9.503	30.888	9.503	9.503	9.503
Csvn_cvb	45.012	26.257	35.007	30.888	35.007	35.007	35.007
Qsat_cvb,0	389.988	577.751	577.751	23.166	577.751	577.751	577.751
Qsta_cvb,0	171.632	200.277	200.277	54.054	200.277	200.277	200.277
Qsar_cvb,0	92.308	100.000	100.000	135.168	100.000	100.000	100.000
Qscp_cvb,0	171.632	200.277	200.277	316.338	200.277	200.277	200.277
Qsvl_cvb,0	389.988	577.751	577.751	12.000	577.751	577.751	577.751
Qssv_cvb,0	399.990	599.978	599.978	0.007	599.978	599.978	599.978
Qsvn_cvb,0	400.000	600.000	600.000	0.007	600.000	600.000	600.000
Lsat_cvb	0.000	0.000	0.000	0.007	0.000	0.000	0.000
Lsta_cvb	0.000	0.000	0.000	0.007	0.000	0.000	0.000
Lsar_cvb	0.000	0.000	0.000	0.049	0.000	0.000	0.000
Lscp_cvb	0.000	0.000	0.000	9.503	0.000	0.000	0.000
Lsvl_cvb	0.000	0.000	0.000	35.007	0.000	0.000	0.000
Lssv_cvb	0.000	0.000	0.000	577.751	0.000	0.000	0.000
Lsvn_cvb	0.000	0.000	0.000	200.277	0.000	0.000	0.000
Rsat_cvb	0.374	0.781	0.633	100.000	0.656	0.656	0.752
Rsta_cvb	1.036	2.164	1.527	200.277	1.550	1.550	2.084

Parameter	Control	CHF III	CHF III pump AAo	CHF III pump DAo	CHF IV	CHF IV pump AAo	CHF IV pump DAo
Rsar_cvb	1.500	3.135	2.154	577.751	2.177	2.177	3.019
Rscp_cvb	1.036	2.164	1.527	599.978	1.550	1.550	2.084
Rsvl_cvb	0.374	0.781	0.633	600.000	0.656	0.656	0.752
Rssv_cvb	0.280	0.584	0.507	0.000	0.530	0.530	0.563
Rsvn_cvb	0.278	0.581	0.504	0.000	0.527	0.527	0.559
Psat_ulvb,0	114.000	114.000	114.000	0.000	114.000	114.000	114.000
Psta_ulvb,0	108.000	108.000	108.000	0.000	108.000	108.000	108.000
Psar_ulvb,0	96.000	96.000	96.000	0.000	96.000	96.000	96.000
Pscp_ulvb,0	36.000	36.000	36.000	0.000	36.000	36.000	36.000
Psvl_ulvb,0	24.000	24.000	24.000	0.000	24.000	24.000	24.000
Pssv_ulvb,0	18.000	18.000	18.000	0.852	18.000	18.000	18.000
Psvn_ulvb,0	12.000	12.000	12.000	2.361	12.000	12.000	12.000
Vsat_ulvb,0	42.120	46.332	46.332	3.420	48.438	48.438	48.438
Vsta_ulvb,0	18.720	20.592	20.592	2.361	21.528	21.528	21.528
Vsar_ulvb,0	18.720	20.592	20.592	0.852	21.528	21.528	21.528
Vscp_ulvb,0	14.040	15.444	15.444	0.637	16.146	16.146	16.146
Vsvl_ulvb,0	32.760	36.036	36.036	0.633	37.674	37.674	37.674
Vssv_ulvb,0	81.920	90.112	90.112	114.000	94.208	94.208	94.208
Vsvn_ulvb,0	191.720	210.892	210.892	108.000	220.478	220.478	220.478
Csat_ulvb	0.012	0.007	0.007	36.000	0.007	0.007	0.007
Csta_ulvb	0.012	0.007	0.007	24.000	0.007	0.007	0.007
Csar_ulvb	0.012	0.007	0.007	18.000	0.007	0.007	0.007
Cscp_ulvb	0.012	0.007	0.007	12.000	0.007	0.007	0.007
Csvl_ulvb	0.041	0.024	0.024	50.544	0.024	0.024	0.024
Cssv_ulvb	6.523	3.805	3.805	22.464	3.805	3.805	3.805
Csvn_ulvb	24.012	14.007	14.007	22.464	14.007	14.007	14.007
Qsat_ulvb,0	577.751	577.751	577.751	16.848	577.751	577.751	577.751
Qsta_ulvb,0	200.277	200.277	200.277	39.312	200.277	200.277	200.277
Qsar_ulvb,0	100.000	100.000	100.000	98.304	100.000	100.000	100.000
Qscp_ulvb,0	200.277	200.277	200.277	230.064	200.277	200.277	200.277
Qsvl_ulvb,0	577.751	577.751	577.751	12.000	577.751	577.751	577.751
Qssv_ulvb,0	599.978	599.978	599.978	0.007	599.978	599.978	599.978
Qsvn_ulvb,0	600.000	600.000	600.000	0.007	600.000	600.000	600.000
Lsat_ulvb	0.000	0.000	0.000	0.007	0.000	0.000	0.000
Lsta_ulvb	0.000	0.000	0.000	0.007	0.000	0.000	0.000
Lsar_ulvb	0.000	0.000	0.000	0.024	0.000	0.000	0.000
Lscp_ulvb	0.000	0.000	0.000	3.805	0.000	0.000	0.000
Lsvl_ulvb	0.000	0.000	0.000	14.007	0.000	0.000	0.000
Lssv_ulvb	0.000	0.000	0.000	577.751	0.000	0.000	0.000
Lsvn_ulvb	0.000	0.000	0.000	200.277	0.000	0.000	0.000

Parameter	Control	CHF III	CHF III pump AAo	CHF III pump DAo	CHF IV	CHF IV pump AAo	CHF IV pump DAo
Rsat_ulvb	1.237	2.585	2.245	100.000	2.347	2.347	2.490
Rsta_ulvb	3.645	7.617	6.615	200.277	6.916	6.916	7.335
Rsar_ulvb	5.333	11.147	9.680	577.751	10.120	10.120	10.733
Rscp_ulvb	3.645	7.617	6.615	599.978	6.916	6.916	7.335
Rsvl_ulvb	1.237	2.585	2.245	600.000	2.347	2.347	2.490
Rssv_ulvb	0.896	1.872	1.625	0.000	1.699	1.699	1.802
Rsvn_ulvb	0.889	1.858	1.613	0.000	1.687	1.687	1.789
Psat_svb,0	114.000	114.000	114.000	0.000	114.000	114.000	114.000
Psta_svb,0	108.000	108.000	108.000	0.000	108.000	108.000	108.000
Psar_svb,0	96.000	96.000	96.000	0.000	96.000	96.000	96.000
Pscp_svb,0	36.000	36.000	36.000	0.000	36.000	36.000	36.000
Psvl_svb,0	24.000	24.000	24.000	0.000	24.000	24.000	24.000
Pssv_svb,0	18.000	18.000	18.000	2.820	18.000	18.000	18.000
Psvn_svb,0	12.000	12.000	12.000	8.310	12.000	12.000	12.000
Vsat_svb,0	121.095	138.996	138.996	12.160	145.314	145.314	145.314
Vsta_svb,0	53.820	61.776	61.776	8.310	64.584	64.584	64.584
Vsar_svb,0	53.820	61.776	61.776	2.820	64.584	64.584	64.584
Vscp_svb,0	40.365	46.332	46.332	2.042	48.438	48.438	48.438
Vsvl_svb,0	94.185	108.108	108.108	2.027	113.022	113.022	113.022
Vssv_svb,0	235.520	270.336	270.336	114.000	282.624	282.624	282.624
Vsvn_svb,0	551.195	632.676	632.676	108.000	661.434	661.434	661.434
Csat_svb	0.012	0.007	0.007	36.000	0.007	0.007	0.007
Csta_svb	0.012	0.007	0.007	24.000	0.007	0.007	0.007
Csar_svb	0.012	0.007	0.007	18.000	0.007	0.007	0.007
Cscp_svb	0.012	0.007	0.007	12.000	0.007	0.007	0.007
Csvl_svb	0.121	0.071	0.071	151.632	0.071	0.071	0.071
Cssv_svb	24.430	14.251	14.251	67.392	14.251	14.251	14.251
Csvn_svb	90.012	52.507	52.507	67.392	52.507	52.507	52.507
Qsat_svb,0	577.751	577.751	577.751	50.544	577.751	577.751	577.751
Qsta_svb,0	200.277	200.277	200.277	117.936	200.277	200.277	200.277
Qsar_svb,0	100.000	100.000	100.000	294.912	100.000	100.000	100.000
Qscp_svb,0	200.277	200.277	200.277	690.192	200.277	200.277	200.277
Qsvl_svb,0	577.751	577.751	577.751	12.000	577.751	577.751	577.751
Qssv_svb,0	599.978	599.978	599.978	0.007	599.978	599.978	599.978
Qsvn_svb,0	600.000	600.000	600.000	0.007	600.000	600.000	600.000
Lsat_svb	0.000	0.000	0.000	0.007	0.000	0.000	0.000
Lsta_svb	0.000	0.000	0.000	0.007	0.000	0.000	0.000
Lsar_svb	0.000	0.000	0.000	0.071	0.000	0.000	0.000
Lscp_svb	0.000	0.000	0.000	14.251	0.000	0.000	0.000
Lsvl_svb	0.000	0.000	0.000	52.507	0.000	0.000	0.000

Parameter	Control	CHF III	CHF III pump AAo	CHF III pump DAo	CHF IV	CHF IV pump AAo	CHF IV pump DAo
Lssv_svb	0.000	0.000	0.000	577.751	0.000	0.000	0.000
Lsvn_svb	0.000	0.000	0.000	200.277	0.000	0.000	0.000
Rsat_svb	0.285	0.584	0.507	100.000	0.525	0.525	0.557
Rsta_svb	0.718	1.407	1.222	200.277	1.240	1.240	1.315
Rsar_svb	1.022	1.984	1.723	577.751	1.742	1.742	1.847
Rscp_svb	0.718	1.407	1.222	599.978	1.240	1.240	1.315
Rsvl_svb	0.285	0.584	0.507	600.000	0.525	0.525	0.557
Rssv_svb	0.223	0.467	0.405	0.000	0.424	0.424	0.449
Rsvn_svb	0.222	0.464	0.403	0.000	0.422	0.422	0.447
Psat_rvd,0	114.000	114.000	114.000	0.000	114.000	114.000	114.000
Psta_rvd,0	108.000	108.000	108.000	0.000	108.000	108.000	108.000
Psar_rvd,0	96.000	96.000	96.000	0.000	96.000	96.000	96.000
Pscp_rvd,0	36.000	36.000	36.000	0.000	36.000	36.000	36.000
Psvl_rvd,0	24.000	24.000	24.000	0.000	24.000	24.000	24.000
Pssv_rvd,0	18.000	18.000	18.000	0.626	18.000	18.000	18.000
Psvn_rvd,0	12.000	12.000	12.000	1.449	12.000	12.000	12.000
Vsat_rvd,0	105.300	110.039	110.039	2.027	115.040	115.040	115.040
Vsta_rvd,0	46.800	48.906	48.906	1.449	51.129	51.129	51.129
Vsar_rvd,0	46.800	48.906	48.906	0.626	51.129	51.129	51.129
Vscp_rvd,0	35.100	36.680	36.680	0.509	38.347	38.347	38.347
Vsvl_rvd,0	81.900	85.586	85.586	0.507	89.476	89.476	89.476
Vssv_rvd,0	204.800	214.016	214.016	114.000	223.744	223.744	223.744
Vsvn_rvd,0	479.300	500.869	500.869	108.000	523.635	523.635	523.635
Csat_rvd	0.003	0.002	0.002	36.000	0.002	0.002	0.002
Csta_rvd	0.003	0.002	0.002	24.000	0.002	0.002	0.002
Csar_rvd	0.003	0.002	0.002	18.000	0.002	0.002	0.002
Cscp_rvd	0.003	0.002	0.002	12.000	0.002	0.002	0.002
Csvl_rvd	0.090	0.053	0.053	120.042	0.053	0.053	0.053
Cssv_rvd	19.537	11.397	11.397	53.352	11.397	11.397	11.397
Csvn_rvd	72.003	42.002	42.002	53.352	42.002	42.002	42.002
Qsat_rvd,0	577.751	577.751	577.751	40.014	577.751	577.751	577.751
Qsta_rvd,0	200.277	200.277	200.277	93.366	200.277	200.277	200.277
Qsar_rvd,0	100.000	100.000	100.000	233.472	100.000	100.000	100.000
Qscp_rvd,0	200.277	200.277	200.277	546.402	200.277	200.277	200.277
Qsvl_rvd,0	577.751	577.751	577.751	12.000	577.751	577.751	577.751
Qssv_rvd,0	599.978	599.978	599.978	0.002	599.978	599.978	599.978
Qsvn_rvd,0	600.000	600.000	600.000	0.002	600.000	600.000	600.000
Lsat_rvd	0.000	0.000	0.000	0.002	0.000	0.000	0.000
Lsta_rvd	0.000	0.000	0.000	0.002	0.000	0.000	0.000
Lsar_rvd	0.000	0.000	0.000	0.053	0.000	0.000	0.000

Parameter	**Control**	**CHF III**	**CHF III pump AAo**	**CHF III pump DAo**	**CHF IV**	**CHF IV pump AAo**	**CHF IV pump DAo**
Lscp_rvd	0.000	0.000	0.000	11.397	0.000	0.000	0.000
Lsvl_rvd	0.000	0.000	0.000	42.002	0.000	0.000	0.000
Lssv_rvd	0.000	0.000	0.000	577.751	0.000	0.000	0.000
Lsvn_rvd	0.000	0.000	0.000	200.277	0.000	0.000	0.000
Rsat_rvd	0.356	0.729	0.561	100.000	0.587	0.587	0.696
Rsta_rvd	0.898	1.759	1.654	200.277	1.729	1.729	1.644
Rsar_rvd	1.278	2.481	2.420	577.751	2.530	2.530	2.309
Rscp_rvd	0.898	1.759	1.654	599.978	1.729	1.729	1.644
Rsvl_rvd	0.356	0.729	0.561	600.000	0.587	0.587	0.696
Rssv_rvd	0.279	0.583	0.406	0.000	0.425	0.425	0.562
Rsvn_rvd	0.278	0.581	0.403	0.000	0.422	0.422	0.559
Psat_llvb,0	114.000	114.000	114.000	0.000	114.000	114.000	114.000
Psta_llvb,0	108.000	108.000	108.000	0.000	108.000	108.000	108.000
Psar_llvb,0	96.000	96.000	96.000	0.000	96.000	96.000	96.000
Pscp_llvb,0	36.000	36.000	36.000	0.000	36.000	36.000	36.000
Psvl_llvb,0	24.000	24.000	24.000	0.000	24.000	24.000	24.000
Pssv_llvb,0	18.000	18.000	18.000	0.782	18.000	18.000	18.000
Psvn_llvb,0	12.000	12.000	12.000	1.811	12.000	12.000	12.000
Vsat_llvb,0	52.650	57.915	57.915	2.533	60.548	60.548	60.548
Vsta_llvb,0	23.400	25.740	25.740	1.811	26.910	26.910	26.910
Vsar_llvb,0	23.400	25.740	25.740	0.782	26.910	26.910	26.910
Vscp_llvb,0	17.550	19.305	19.305	0.636	20.183	20.183	20.183
Vsvl_llvb,0	40.950	45.045	45.045	0.633	47.093	47.093	47.093
Vssv_llvb,0	102.400	112.640	112.640	114.000	117.760	117.760	117.760
Vsvn_llvb,0	239.650	263.615	263.615	108.000	275.598	275.598	275.598
Csat_llvb	0.001	0.001	0.001	36.000	0.001	0.001	0.001
Csta_llvb	0.001	0.001	0.001	24.000	0.001	0.001	0.001
Csar_llvb	0.001	0.001	0.001	18.000	0.001	0.001	0.001
Cscp_llvb	0.001	0.001	0.001	12.000	0.001	0.001	0.001
Csvl_llvb	0.038	0.022	0.022	63.180	0.022	0.022	0.022
Cssv_llvb	8.141	4.749	4.749	28.080	4.749	4.749	4.749
Csvn_llvb	30.001	17.501	17.501	28.080	17.501	17.501	17.501
Qsat_llvb,0	577.751	577.751	577.751	21.060	577.751	577.751	577.751
Qsta_llvb,0	200.277	200.277	200.277	49.140	200.277	200.277	200.277
Qsar_llvb,0	100.000	100.000	100.000	122.880	100.000	100.000	100.000
Qscp_llvb,0	200.277	200.277	200.277	287.580	200.277	200.277	200.277
Qsvl_llvb,0	577.751	577.751	577.751	12.000	577.751	577.751	577.751
Qssv_llvb,0	599.978	599.978	599.978	0.001	599.978	599.978	599.978
Qsvn_llvb,0	600.000	600.000	600.000	0.001	600.000	600.000	600.000
Lsat_llvb	0.000	0.000	0.000	0.001	0.000	0.000	0.000

Parameter	Control	CHF III	CHF III pump AAo	CHF III pump DAo	CHF IV	CHF IV pump AAo	CHF IV pump DAo
Lsta_llvb	0.000	0.000	0.000	0.001	0.000	0.000	0.000
Lsar_llvb	0.000	0.000	0.000	0.022	0.000	0.000	0.000
Lscp_llvb	0.000	0.000	0.000	4.749	0.000	0.000	0.000
Lsvl_llvb	0.000	0.000	0.000	17.501	0.000	0.000	0.000
Lssv_llvb	0.000	0.000	0.000	577.751	0.000	0.000	0.000
Lsvn_llvb	0.000	0.000	0.000	200.277	0.000	0.000	0.000
Rsat_llvb	1.546	3.232	2.807	100.000	2.934	2.934	3.112
Rsta_llvb	4.556	9.522	8.269	200.277	8.645	8.645	9.169
Rsar_llvb	6.667	13.933	12.100	577.751	12.650	12.650	13.417
Rscp_llvb	4.556	9.522	8.269	599.978	8.645	8.645	9.169
Rsvl_llvb	1.546	3.232	2.807	600.000	2.934	2.934	3.112
Rssv_llvb	1.119	2.340	2.032	0.000	2.124	2.124	2.253
Rsvn_llvb	1.111	2.322	2.017	0.000	2.108	2.108	2.236
Cpvs	1.200	1.200	1.200	0.000	1.200	1.200	1.200
Cpat	1.200	1.200	1.200	0.000	1.200	1.200	1.200
Cpta	1.200	1.200	1.200	0.000	1.200	1.200	1.200
Cpar	1.200	1.200	1.200	0.000	1.200	1.200	1.200
Cpcp	1.200	1.200	1.200	0.000	1.200	1.200	1.200
Cpvl	1.546	1.546	1.546	3.526	1.546	1.546	1.546
Cpsv	25.276	25.276	25.276	10.387	25.276	25.276	25.276
Cpvn	66.200	66.200	66.200	15.200	66.200	66.200	66.200
Cpvn	25.276	25.276	25.276	10.387	25.276	25.276	25.276
Lpvs	0.000	0.000	0.000	3.526	0.000	0.000	0.000
Lpat	0.000	0.000	0.000	2.552	0.000	0.000	0.000
Lpta	0.000	0.000	0.000	2.533	0.000	0.000	0.000
Lpar	0.001	0.001	0.001	1.200	0.001	0.001	0.001
Lpcp	0.005	0.005	0.005	1.200	0.005	0.005	0.005
Lpvl	0.001	0.001	0.001	1.200	0.001	0.001	0.001
Lpsv	0.000	0.000	0.000	1.200	0.000	0.000	0.000
Lpvn	0.000	0.000	0.000	1.200	0.000	0.000	0.000
Lpvn	0.000	0.000	0.000	1.546	0.000	0.000	0.000
Rpvs	0.002	0.002	0.002	25.276	0.002	0.002	0.002
Rpat	0.002	0.002	0.002	66.200	0.002	0.002	0.002
Rpta	0.032	0.032	0.032	25.276	0.032	0.032	0.032
Rpar	0.127	0.127	0.127	0.000	0.127	0.127	0.127
Rpcp	0.032	0.032	0.032	0.000	0.032	0.032	0.032
Rpvl	0.002	0.002	0.002	0.000	0.002	0.002	0.002
Rpsv	0.002	0.002	0.002	0.001	0.002	0.002	0.002
Rpvn	0.002	0.002	0.002	0.005	0.002	0.002	0.002
Rpvn	0.002	0.002	0.002	0.001	0.002	0.002	0.002

Parameter	Control	CHF III	CHF III pump AAo	CHF III pump DAo	CHF IV	CHF IV pump AAo	CHF IV pump DAo
Ppvs,0	25.000	25.000	25.000	0.000	25.000	25.000	25.000
Ppat,0	22.915	22.915	22.915	0.000	22.915	22.915	22.915
Ppta,0	16.665	16.665	16.665	0.000	16.665	16.665	16.665
Ppar,0	8.333	8.333	8.333	0.002	8.333	8.333	8.333
Ppcp,0	5.208	5.208	5.208	0.002	5.208	5.208	5.208
Ppvl,0	2.083	2.083	2.083	0.032	2.083	2.083	2.083
Ppsv,0	1.043	1.043	1.043	0.127	1.043	1.043	1.043
Ppvn,0	0.625	0.625	0.625	0.032	0.625	0.625	0.625
Ppvn,0	0.415	0.415	0.415	0.002	0.415	0.415	0.415
Qpvs,0	600.000	600.000	600.000	0.002	600.000	600.000	600.000
Qpat,0	550.000	550.000	550.000	0.002	550.000	550.000	550.000
Qpta,0	400.000	400.000	400.000	0.002	400.000	400.000	400.000
Qpar,0	200.000	200.000	200.000	25.000	200.000	200.000	200.000
Qpcp,0	125.000	125.000	125.000	22.915	125.000	125.000	125.000
Qpvl,0	50.000	50.000	50.000	16.665	50.000	50.000	50.000
Qpsv,0	25.000	25.000	25.000	8.333	25.000	25.000	25.000
Qpvn,0	15.000	15.000	15.000	5.208	15.000	15.000	15.000
Qpvn,0	10.000	10.000	10.000	2.083	10.000	10.000	10.000
Vpvs,0	9.680	10.648	10.648	1.043	11.132	11.132	11.132
Vpat,0	57.915	63.707	63.707	0.625	66.602	66.602	66.602
Vpta,0	25.740	28.314	28.314	0.415	29.601	29.601	29.601
Vpar,0	25.740	28.314	28.314	600.000	29.601	29.601	29.601
Vpcp,0	19.305	21.236	21.236	550.000	22.201	22.201	22.201
Vpvl,0	45.045	49.550	49.550	400.000	51.802	51.802	51.802
Vpsv,0	77.220	84.942	84.942	200.000	88.803	88.803	88.803
Vpvn,0	263.615	289.977	289.977	125.000	303.157	303.157	303.157
Vpvn,0	25.740	28.314	28.314	50.000	29.601	29.601	29.601

Appendix B

Impeller Generation - MATLAB Code

```
function[]=Impellergeneration()
clear all
close all
clc

%% ************ Plot Meridional Profile created with ellipses and ...
   bezier curves *******
% recall the pump requirements and geometry parameters
[phi,DP,g,H,Q,mdot,N,w,z,sftrad,...
    shrad,b1,R2,IH,b2,LEsw,TEsw,Nspan,LEoblique,...
    Z_span,R_span,Z_tout,R_tout,Z_bout,R_bout]=CFpumparameters();

MPcolor=[1 0 0
0 1 0
0 0 1
1 0 1
0.749 0.749 0
0 0 0
0 0 0];

mpblade=[50.0 50.0 545 700];
figure(1)
```

```
for i=1:7
set(gcf,'Color', 'w','Position',mpblade)
plot(Z_span(:,i),R_span(:,i),'LineWidth',2,'Color',MPcolor(i,:))
hold on
end
line([Z_span(1,6), Z_span(1,7)],[R_span(1,6), ...
   R_span(1,7)],'LineWidth',2,'Color',[0 0 0])
line([Z_span(1,1), Z_span(1,5)],[R_span(1,1), ...
   R_span(1,5)],'LineWidth',2,'Color',[0 0 0])
line([Z_span(end,1), Z_span(end,5)],[R_span(end,1), ...
   R_span(end,5)],'LineWidth',2,'Color',[0 0 0])
line([Z_span(4,1), Z_span(4,1)],[R_span(4,5), ...
   R_span(4,5)],'LineWidth',2,'Color',[0 0 0])
line([Z_span(end,1), ...
   Z_bout(1)],[R_span(end,1),R_bout(end)],'LineWidth',2,'Color',[0 ...
   0 0])
line([Z_span(end,5), ...
   Z_tout(end)],[R_span(end,5),R_tout(end)],'LineWidth',2,'Color',[0 ...
   0 0])
line([Z_bout(end), ...
   Z_tout(end)],[R_bout(end),R_tout(end)],'LineWidth',2,'Color',[0 ...
   0 0])
xlim([-16 1])
ylim([0 20])
annotation('textbox',...
    [0.255045871559633 0.603285715179784 0.223853204884661 ...
       0.0442857133916447],...
    'String',{'32^{\circ} LE inclination'});
annotation('line',[0.475229357798165 0.491743119266055],...
    [0.602857142857143 0.537142857142857]);
xlabel('Z')
ylabel('R')
legend('span01','span02','span03','span04',...
    'span05','Location','SouthEast')
```

```
% title('Blade Meridional Profile')
print('-depsc','-r600','Mprofile')
%% Plot blade wrap angle
[xWATD,yWATD]=ThetaDefinition();
ColorDef=[1 0 0
0 1 0
0 0 1
1 0 1
0.749 0.749 0];
angle=[50.0 50.0 700 540];
figure(2)
for i=1:Nspan
set(gcf,'Color', 'w','Position',angle)
plot(xWATD(:,i),yWATD(:,i),'LineWidth',2,'Color',ColorDef(i,:))
hold on
ylabel('Theta (degree)')
end
xlabel('M-prime')
legend('span01','span02','span03','span04','span05','Location','SouthEast')
% title('Wrap Angle')
% print('-depsc','-r600','wrapangle')



%% Construct Blade Surface: Pressure and Suction sides
[xdr_span,ydr_span,xdl_span,ydl_span]=PSsides();

sectionx=xdl_span;
sectionxt=xdr_span;
sectiony=ydl_span;
sectionyt=ydr_span;
sectionz=Z_span(:,1:5);
sectionzt=sectionz;

secx_bladetip=[xdl_span(:,5),xdr_span(:,5)];
```

```
secy_bladetip=[ydl_span(:,5),ydr_span(:,5)];
secz_bladetip=[Z_span(:,5),Z_span(:,5)];

secx_bladehub=[xdl_span(:,1),xdr_span(:,1)];
secy_bladehub=[ydl_span(:,1),ydr_span(:,1)];
secz_bladehub=[Z_span(:,1),Z_span(:,1)];

secx_bladeTE=[xdl_span(end,1),xdr_span(end,1);...
    xdl_span(end,2),xdr_span(end,2);...
    xdl_span(end,3),xdr_span(end,3);...
    xdl_span(end,4),xdr_span(end,4);...
    xdl_span(end,5),xdr_span(end,4)];

secy_bladeTE=[ydl_span(end,1),ydr_span(end,1);...
    ydl_span(end,2),ydr_span(end,2);...
    ydl_span(end,3),ydr_span(end,3);...
    ydl_span(end,4),ydr_span(end,4);...
    ydl_span(end,5),ydr_span(end,4)];

secz_bladeTE=[Z_span(end,1),Z_span(end,1);...
    Z_span(end,2),Z_span(end,2);...
    Z_span(end,3),Z_span(end,3);...
    Z_span(end,4),Z_span(end,4);...
    Z_span(end,5),Z_span(end,5)];

figure(3)
set(gcf,'Color', 'w','Position',angle)
surf(sectionx,sectiony,-sectionz,'FaceColor',[1 1 1]);%blade
view([131 40]);
% view([-226 22]);
hold on
surf(sectionxt,sectionyt,-sectionzt,'FaceColor',[1 1 1]);%blade
surf(secx_bladetip,secy_bladetip,-secz_bladetip,'FaceColor',[0.5 ...
   0.5 0.5]);%blade
```

```
surf(secx_bladehub,secy_bladehub,−secz_bladehub,'FaceColor',[1 1 ...
   1]);%blade
surf(secx_bladeTE,secy_bladeTE,−secz_bladeTE,'FaceColor',[1 1 1]);%blad
% title('Spanwise Loft')
xlabel('x','Interpreter','latex','FontSize',16,'FontName','Times');
ylabel('y','Interpreter','latex','FontSize',16,'FontName','Times');
zlabel('z','Interpreter','latex','FontSize',16,'FontName','Times');
print('−deps','−r600','bladeloft')%Use for black and white figure
% print('−depsc','−r600','bladeloft')
%% Plot the Flow Path

[sectionxfp,sectionyfp,sectionzfp,sectionxtfp,...
    sectionytfp,sectionztfp,sectionx_outlet,...
    sectiony_outlet,sectionz_outlet,x_fpshaft,...
    y_fpshaft,z_fpshaft,x_shroud,y_shroud,...
    z_shroud,x_tdiff,y_tdiff,z_tdiff,x_tout,...
    y_tout,z_tout,x_bdiff,y_bdiff,z_bdiff,...
    x_hub,y_hub,z_hub,x_bout,y_bout,z_bout]=FlowPath();
figure(4)
set(gcf,'Color', 'w','Position',angle)
surf(sectionxfp,sectionyfp,−sectionzfp,'FaceColor',[1 1 1]);%flow ...
   passage
hold on
surf(sectionxtfp,sectionytfp,−sectionztfp,'FaceColor',[1 1 ...
   1]);%flow passage
surf(sectionx_outlet,sectiony_outlet,−sectionz_outlet,'FaceColor',[1 ...
   1 1]);%flow passage
surf(x_fpshaft,y_fpshaft,z_fpshaft,'FaceColor',[1 1 1]);%flow passage
surf(x_tdiff,y_tdiff,z_tdiff,'FaceColor',[1 1 1]);%flow passage
surf(x_tout,y_tout,z_tout,'FaceColor',[1 1 1]);%flow passage
surf(x_bout,y_bout,z_bout,'FaceColor',[1 1 1]);%flow passage
surf(x_bdiff,y_bdiff,z_bdiff,'FaceColor',[1 1 1]);%flow passage
surf(x_hub,y_hub,z_hub,'FaceColor',[1 1 1]);%flow passage
```

```
% surf(x_shroud,y_shroud,z_shroud,'FaceColor',[1 1 ...
   1],'FaceAlpha',0.5);%flow passage
surf(sectionx,sectiony,−sectionz,'FaceColor',[1 1 1]);%blade
surf(sectionxt,sectionyt,−sectionzt,'FaceColor',[1 1 1]);%blade
surf(secx_bladetip,secy_bladetip,−secz_bladetip,'FaceColor',[0.5 1 ...
   1]);%blade
surf(secx_bladehub,secy_bladehub,−secz_bladehub,'FaceColor',[0.1 1 ...
   1]);%blade
surf(secx_bladeTE,secy_bladeTE,−secz_bladeTE,'FaceColor',[1 1 ...
   1]);%blade
view([131 40]);
xlabel('x','Interpreter','latex','FontSize',16,'FontName','Times');
ylabel('y','Interpreter','latex','FontSize',16,'FontName','Times');
zlabel('z','Interpreter','latex','FontSize',16,'FontName','Times');
% print('−deps','−r600','flowpath')%Use for black and white figure
% print('−depsc','−r600','flowpath')%Use for color figure


%%  Summary of calculated pump parameters
[beta1,beta2,Z]=ioangles();
iarea=pi∗((R_span(1,5)∗2e−3−R_span(1,1)∗2e−3)/4)^2;
oarea=pi∗R2∗2∗−b2;

% ∗∗∗∗∗∗∗∗∗∗∗∗∗∗∗∗∗∗∗∗∗∗ Results ∗∗∗∗∗∗∗∗∗∗∗∗∗∗∗∗∗∗∗∗∗∗∗∗∗∗∗∗∗∗∗∗∗∗∗
fprintf(' ______________________________Table. Summary of ...
   calculated pump parameters _________________________________\n')
fprintf(' ...
   _____________________________________________________________________________
fprintf(' Description                           Symbol              ...
   Value            Units   \n')
fprintf(' ...
   _____________________________________________________________________________
fprintf(' Flow                                  Q                   ...
   %3f               m^3/s\n',Q)
```

```
fprintf(' Rotational speed                              rpm             ...
   %0.2f            rev/min\n',N)
fprintf(' Pressure difference                           DP              ...
   %0.2f            Pa\n',DP)
fprintf(' Static head                                   H               ...
   %0.2f            m\n',H)
fprintf(' Hub diameter                                  D,h             ...
   %0.2f            mm\n',R_span(1,1)*2)
fprintf(' Tip diameter                                  D,t             ...
   %0.2f            mm\n',R_span(1,5)*2)
fprintf(' Exit diameter                                 D2              ...
   %0.2f            mm\n',R2*2000)
fprintf(' Inlet blade angle at hub                      B1,h            ...
   %0.2f            degree\n',-beta1(1))
fprintf(' Inlet blade angle at span 2                   B1,s02          ...
   %0.2f            degree\n',-beta1(2))
fprintf(' Inlet blade angle at span 3                   B1,s03          ...
   %0.2f            degree\n',-beta1(3))
fprintf(' Inlet blade angle at span 4                   B1,s04          ...
   %0.2f            degree\n',-beta1(4))
fprintf(' Inlet blade angle at tip                      B1,t            ...
   %0.2f            degree\n',-beta1(5))
fprintf(' Mean inlet blade angle                        B1,mean         ...
   %0.2f            degree\n',mean(beta1)*-1)
fprintf(' Exit blade angle                              B2              ...
   %0.2f            degree\n',-beta2)
fprintf(' Inlet area                                    A1              ...
   %32f             m^2\n',iarea)
fprintf(' Exit area                                     A2              ...
   %3f              m^2\n',oarea)
fprintf(' Inlet width                                   b1              ...
   %0.2f            mm\n',b1*1000)
fprintf(' Exit width                                    b2              ...
   %0.2f            mm\n',-b2*1000)
```

```
fprintf(' Number of vanes                            Z                    ...
   %0.1f              dimensioless\n',Z)
fprintf(' ...
   ________________________________________________________________________________




end



function [phi,DP,g,H,Q,mdot,N,w,z,sftrad,...
    shrad,b1,R2,IH,b2,LEsw,TEsw,Nspan,LEoblique,...
    Z_span,R_span,Z_tout,R_tout,Z_bout,R_bout]=CFpumparameters();
%************ Requirements ***********************
dp=60;                        % Pressure difference in mmHg
DP=dp*1.01325e5/760;          % Pressure difference in Pascal [kg/m.s^2]

rho=1060;                     % water density [kg/m^3]
g=9.81;                       % [m/s^2]
H=DP/(rho*g);                 % Head [m]
q=5;                          % Volume flow rate in lt/min
Q=q/(1000*60);                % Volume flow rate in m^3/s

mdot=Q*rho;                   % mass flow rate in kg/s
N=1500;                       % Rotational speed in rpm
w=N*2*pi/60;                  % Rotational speed in rad/s
z=5;                         % Number of blade sets. Note: value...
                              % obtained heuristically using CFX
D2=30e-3;                     % Exit diameter in meter
U2=w*D2/2;                    % exit speed in m/s
R3=(D2/2)*1.10;               % Flow passage exit diameter. 10% ...
   larger than R2
```

```
%************* Assumptions *************************
eta=0.8;                   % Target efficiency
psi=(g*H)/(eta*U2^2);      % Head coefficient
phi=psi/tand(85.24);        % flow coefficient
% phi=0.042;              % flow coefficient

bb2=(Q/(pi*D2*U2*phi));    % exit blade width

%% ************ Impeller dimensions *****************
sftrad=3.5e-3;                  % shaft radius
shrad=9.5e-3;                   % shroud radius
b1=shrad-sftrad;                % blade width at LE
R2=D2/2;                        % impeller exit radius
IH=12.6e-3;                     % impeller height
b2=-bb2;                        % blade width at TE
b3=-3.5e-3;                          % flow passage exit height
LEsw=b1/4;                      % LE span width
TEsw=b2/4;                      % TE span width

%% ************ Calculate Meridional profile of the Blade with ...
   ellipse ************

Nspan=5;                     % Number of blade spans
center=[-IH,R2];
a_profile=linspace(IH,(IH+4*TEsw),Nspan);
b_hub=R2-sftrad;
b_profile=linspace(b_hub,(b_hub-4*LEsw),Nspan);
phi=0;
LEang1=32; %LE inclination angle in degree
LEoblique=LEang1*ones(1,5)*pi/180;
th0=3*pi/2;
Np=100;
```

```
theta_profile=zeros(Np,Nspan);  %size preallocation
x_medprof=zeros(Np,Nspan);      %size preallocation
y_medprof=zeros(Np,Nspan);      %size preallocation
for i=1:Nspan
theta_profile(:,i)=linspace(th0+LEoblique(i),2*pi,Np);
[x_medprof(:,i),y_medprof(:,i)]=MPellipse(a_profile(i),...
    b_profile(i),phi,center(1,1),center(1,2),theta_profile(:,i));
end

%% ************ Calculate Meridional profile of the Blade with ...
   bezier curve ******

MPEspan01=[x_medprof(1,1)*1e3 y_medprof(1,1)*1e3
−2.430796 8.240053
−0.131960 12.365806
0.0 R2*1e3];

MPEspan02=[x_medprof(1,2)*1e3 y_medprof(1,2)*1e3
−3.351704 9.37263
−1.319757 12.942479
TEsw*1e3 R2*1e3];

MPEspan03=[x_medprof(1,3)*1e3 y_medprof(1,3)*1e3
−4.454421 10.034303
−2.307186 12.750931
TEsw*2e3 R2*1e3];

MPEspan04=[x_medprof(1,4)*1e3 y_medprof(1,4)*1e3
−5.37582 11.196277
−3.596377 12.994438
TEsw*3e3 R2*1e3];

MPEspan05=[x_medprof(1,5)*1e3 y_medprof(1,5)*1e3
−5.9172 11.941994
```

```
−4.522485 14.142688
TEsw*4e3 R2*1e3];

diffuserb=[−14 2
−10.498090 2.755456
−7.758556 4.122178
x_medprof(1,1)*1e3 y_medprof(1,1)*1e3 ];



diffusert=[−14 10
−12.112202 9.899723
−8.758477 9.831319
x_medprof(1,5)*1e3 y_medprof(1,5)*1e3];

Npd=15; %Number of points in cut−off TE
Z_tout=linspace(b2*1e3,b3*1e3,Npd);
R_tout=linspace(R2*1e3,R3*1e3,Npd);

Z_bout(1,1:Npd)=0;
R_bout=linspace(R2*1e3,R3*1e3,Npd);

P0=[MPEspan01(1,:);MPEspan02(1,:);MPEspan03(1,:);...
    MPEspan04(1,:);MPEspan05(1,:);diffuserb(1,:);...
    diffusert(1,:)];
P1=[MPEspan01(2,:);MPEspan02(2,:);MPEspan03(2,:);...
    MPEspan04(2,:);MPEspan05(2,:);diffuserb(2,:);...
    diffusert(2,:)];
P2=[MPEspan01(3,:);MPEspan02(3,:);MPEspan03(3,:);...
    MPEspan04(3,:);MPEspan05(3,:);diffuserb(3,:);...
    diffusert(3,:)];
P3=[MPEspan01(4,:);MPEspan02(4,:);MPEspan03(4,:);...
    MPEspan04(4,:);MPEspan05(4,:);diffuserb(4,:);...
    diffusert(4,:)];
```

```
Npb=100;%Number of points in bezier curve
x_Mprofile=zeros(Npb,Nspan);
y_Mprofile=zeros(Npb,Nspan);
Z_span=zeros(Npb,Nspan);
R_span=zeros(Npb,Nspan);

for i=1:7;
   [x_Mprofile(:,i),y_Mprofile(1:Npb,i)]=MPbezier(P0(i,:),...
   P1(i,:),P2(i,:),P3(i,:));
   Z_span(:,i)=x_Mprofile(:,i);
   R_span(:,i)=y_Mprofile(:,i);

end



function[beta1,beta2,Z]=ioangles()



% recall the pump requirements and geometry parameters
[phi,DP,g,H,Q,mdot,N,w,z,sftrad,...
    shrad,b1,R2,IH,b2,LEsw,TEsw,Nspan,LEoblique,...
    Z_span,R_span,Z_tout,R_tout,Z_bout,R_bout]=CFpumparameters();

tau=1.0e-3;
d1t=R_span(1,5)*2e-3;
d1h=R_span(1,1)*2e-3;
dspan=linspace(d1h-b2,d1t+b2,4);

%% Inlet Angle: 1. Calculate individual flow channels' width, where ...
   the number of flow
% channels is Nspan-1.
% 2. Calculate U1, Sb1, & Cm1.
b1htotal=0;
b1ntotal=0;
```

```
Cm1=0;
for i=1:(Nspan-1)
    b1h=sqrt((Z_span(1,i)*1e-3-Z_span(1,i+1)*1e-3)^2+...
        (R_span(1,i)*1e-3-R_span(1,i+1)*1e-3)^2);
    b1htotal=b1htotal+b1h;
    bn1=sqrt((R_span(1,i)*1e-3-R_span(1,i+1)*1e-3)^2);
    b1ntotal=b1ntotal+bn1;
    Sb1=1-((tau*z)/(pi*dspan(i)));
Cm1s=Q/(4*pi*dspan(i)*bn1*Sb1);
Cm1=Cm1+Cm1s;

end

% If the leading edge (LE) is oblique D1 varies in different flow lines
% therefore C1 is slightly higher than Cm1 and W1 is considerably ...
   reduced
for i=1:Nspan
U1=w*R_span(1,i)*1e-3;
Ku=0.9; % Best value for Ku is 0.9 which implies a LE small prerotation
Cu1=U1-Ku*U1;
beta1(:,i)=-(atan(Cm1/(U1-Cu1))*(180/pi));
end



oarea=pi*R2*2*-b2;
U2=w*R2;
Cm2=Q/oarea;
Cu2=H*g/U2;
beta2=-90+(atan(Cm2/(U2-Cu2))*(180/pi));



Z=abs(round(6.5*((R2*1000+R_span(1,1))/(R2*1000-R_span(1,1)))*sin((beta1(1,1)*...
    (pi/180)+beta2*(pi/180))/2))); % Calculates number of blade sets
```

```
end



function [dZdS,dRdS,Mprime,Mprofile]=MCDefinition()

[phi,DP,g,H,Q,mdot,N,w,z,sftrad,...
    shrad,b1,R2,IH,b2,LEsw,TEsw,Nspan,LEoblique,...
    Z_span,R_span,Z_tout,R_tout,Z_bout,R_bout]=CFpumparameters();
%% ****** Blade meridional profile in meridional coordinate ...
   definiton *********
Npb=100;%Number of points in curve
dZdS=zeros(Npb,Nspan);
dRdS=zeros(Npb,Nspan);

for i=1:Nspan
    dZdS(:,i)=gradient(Z_span(:,i));
    dRdS(:,i)=gradient(R_span(:,i));
    Mprofile=cumtrapz(sqrt(dZdS.^2+dRdS.^2));
end
for i=1:Nspan
Mprime(:,i)=cumtrapz((sqrt(dZdS(:,i).^2+dRdS(:,i).^2))./R_span(:,i));
end



function [x,y]=MPbezier(P0,P1,P2,P3)

% Cubic bezier curve with 4 control points P0,P1,P2,P3
t=linspace(0,1,100); % linearly space parameterization
profile=zeros(length(t),2); % Size preallocation
for k=1:length(t)%120 points
    profile(k,:)=(-P0 + 3*(P1-P2) + P3)*t(k).^3 + ...
       3*(P0-2*P1+P2)*t(k).^2 + 3*(P1-P0)*t(k) + P0;
end
```

```
x=profile(:,1);

y=profile(:,2);



function [x,y]=MPellipse(a,b,phi,x0,y0,th)



x=a*cos(th)*cos(phi)-b*sin(th)*sin(phi)+x0;

y=a*cos(th)*sin(phi)+b*sin(th)*cos(phi)+y0;



end



function [xdr_span,ydr_span,xdl_span,ydl_span]=PSsides()

% recall the pump requirements and geometry parameters

[phi,DP,g,H,Q,mdot,N,w,z,sftrad,...

    shrad,b1,R2,IH,b2,LEsw,TEsw,Nspan,LEoblique,...

    Z_span,R_span,Z_tout,R_tout,Z_bout,R_bout]=CFpumparameters();

[dZdS,dRdS,Mprime,Mprofile]=MCDefinition();

[xWATD,yWATD]=ThetaDefinition();

[Thickness]=ThkDefinition();

%% ***** Coordinate transformation (Cartesian definition):

%**************** Construction of LE ellipse ************

NpLE=10; %Length ratio of LE's ellipse

%size allocation

Npb=100;%Number of points in bezier curve

xdr_span=zeros(Npb,Nspan);

ydr_span=zeros(Npb,Nspan);

xdl_span=zeros(Npb,Nspan);

ydl_span=zeros(Npb,Nspan);
```

```
for i=1:Nspan
a_span=sqrt(xWATD(NpLE,i)^2−xWATD(1,i)^2);
b_span=Thickness(NpLE,i);
ke_span=a_span/b_span;
xm_span=ke_span.*b_span−xWATD(1:NpLE,i);
ym_span=1/ke_span.*sqrt((ke_span*b_span)^2−xm_span.^2);

%***** Construction of pressure and suction sides *******
yt_span=[ym_span;Thickness((NpLE+1):end,i)];
y_ssi_span=yWATD(:,i)+yt_span;
y_psi_span=yWATD(:,i)−yt_span;

xdr_span(:,i)=R_span(:,i).*cos(y_ssi_span*pi/180);
ydr_span(:,i)=R_span(:,i).*sin(y_ssi_span*pi/180);
xdl_span(:,i)=R_span(:,i).*cos(y_psi_span*pi/180);
ydl_span(:,i)=R_span(:,i).*sin(y_psi_span*pi/180);
end



function [xWATD,yWATD]=ThetaDefinition()

% recall the pump requirements and geometry parameters
[dZdS,dRdS,Mprime,Mprofile]=MCDefinition();

[phi,DP,g,H,Q,mdot,N,w,z,sftrad,...
    shrad,b1,R2,IH,b2,LEsw,TEsw,Nspan,LEoblique,...
    Z_span,R_span,Z_tout,R_tout,Z_bout,R_bout]=CFpumparameters();

[beta1,beta2,Z]=ioangles();
%**** @ span01
THDspan1=[0 0
   Mprime(25,1)  −beta1(1)
   Mprime(50,1) 75
```

```
   Mprime(end,1) —beta2];

%**** @ span02
THDspan2=[0 0
   Mprime(25,2)  —beta1(2)
   Mprime(75,2) 75
   Mprime(end,2) —beta2];

%**** @ span03
THDspan3=[0 0
   Mprime(25,3)  —beta1(3)
   Mprime(75,3) 70
   Mprime(end,3) —beta2];

%**** @ span04
THDspan4=[0 0
   Mprime(25,4)  —beta1(4)
   Mprime(75,4) 70
   Mprime(end,4) —beta2];

%**** @ span05
THDspan5=[0 0
   Mprime(25,5)  —beta1(5)
   Mprime(75,5) 70
   Mprime(end,5) —beta2];

P0=[THDspan1(1,:);THDspan2(1,:);...
    THDspan3(1,:);THDspan4(1,:);THDspan5(1,:)];
P1=[THDspan1(2,:);THDspan2(2,:);...
    THDspan3(2,:);THDspan4(2,:);THDspan5(2,:)];
P2=[THDspan1(3,:);THDspan2(3,:);...
    THDspan3(3,:);THDspan4(3,:);THDspan5(3,:)];
P3=[THDspan1(4,:);THDspan2(4,:);...
    THDspan3(4,:);THDspan4(4,:);THDspan5(4,:)];
```

```
Npb=100;%Number of points in bezier curve
x_data=zeros(Npb,Nspan);
y_data=zeros(Npb,Nspan);
xWATD=zeros(Npb,Nspan);
yWATD=zeros(Npb,Nspan);

% Camber line coordinates
for i=1:Nspan;
   [x_data(:,i),y_data(1:Npb,i)]=MPbezier(P0(i,:),...
       P1(i,:),P2(i,:),P3(i,:));
   xWATD(:,i)=x_data(:,i);
   yWATD(:,i)=y_data(:,i);

end



function [Thickness]=ThkDefinition()

% recall the pump requirements and geometry parameters
[phi,DP,g,H,Q,mdot,N,w,z,sftrad,...
    shrad,b1,R2,IH,b2,LEsw,TEsw,Nspan,LEoblique,...
    Z_span,R_span,Z_tout,R_tout,Z_bout,R_bout]=CFpumparameters();
[dZdS,dRdS,Mprime,Mprofile]=MCDefinition();

Dthk=linspace(18,9,4);
%**** @ span01
thkspan1=[Mprofile(1,1) Dthk(1)
Mprofile(25,1)  Dthk(4)
Mprofile(75,1)  Dthk(4)
Mprofile(end,1) Dthk(4)];
%**** @ span02
thkspan2=[Mprofile(1,2) Dthk(1)
Mprofile(25,2)  Dthk(4)
```

```
Mprofile(75,2)  Dthk(4)
Mprofile(end,2) Dthk(4)];
%**** @ span03
thkspan3=[Mprofile(1,3) Dthk(1)
Mprofile(25,3)  Dthk(4)
Mprofile(75,3)  Dthk(4)
Mprofile(end,3) Dthk(4)];
%**** @ span04
thkspan4=[Mprofile(1,4) Dthk(1)
Mprofile(25,4)  Dthk(4)
Mprofile(75,4)  Dthk(4)
Mprofile(end,4) Dthk(4)];
%**** @ span05
thkspan5=[Mprofile(1,5) Dthk(1)
Mprofile(25,5)  Dthk(4)
Mprofile(75,5)  Dthk(4)
Mprofile(end,5) Dthk(4)];



P0=[thkspan1(1,:);thkspan2(1,:);...
    thkspan3(1,:);thkspan4(1,:);thkspan5(1,:)];
P1=[thkspan1(2,:);thkspan2(2,:);...
    thkspan3(2,:);thkspan4(2,:);thkspan5(2,:)];
P2=[thkspan1(3,:);thkspan2(3,:);...
    thkspan3(3,:);thkspan4(3,:);thkspan5(3,:)];
P3=[thkspan1(4,:);thkspan2(4,:);...
    thkspan3(4,:);thkspan4(4,:);thkspan5(4,:)];

Npb=100;%Number of points in bezier curve
x_thkdata=zeros(Npb,Nspan);
y_thkdata=zeros(Npb,Nspan);
xTHKD=zeros(Npb,Nspan);
yTHKD=zeros(Npb,Nspan);
```

```
for i=1:Nspan;
   [x_thkdata(:,i),y_thkdata(1:Npb,i)]=MPbezier(P0(i,:),...
       P1(i,:),P2(i,:),P3(i,:));
%    xTHKD(:,i)=x_thkdata(:,i);
   Thickness(:,i)=(y_thkdata(:,i))/2;
end




function[sectionxfp,sectionyfp,sectionzfp,sectionxtfp,sectionytfp,sectionztfp,...
sectionx_outlet,sectiony_outlet,sectionz_outlet,x_fpshaft,y_fpshaft,z_fpshaft,...
x_shroud,y_shroud,z_shroud,x_tdiff,y_tdiff,z_tdiff,...
x_tout,y_tout,z_tout,x_bdiff,y_bdiff,z_bdiff,...
x_hub,y_hub,z_hub,x_bout,y_bout,z_bout]=FlowPath();



[xdr_span,ydr_span,xdl_span,ydl_span]=PSsides();

% recall the pump requirements and geometry parameters
[phic,DP,g,H,Q,mdot,N,w,z,sftrad,...
    shrad,b1,R2,IH,b2,LEsw,TEsw,Nspan,LEoblique,...
    Z_span,R_span,Z_tout,R_tout,Z_bout,R_bout]=CFpumparameters();

[dZdS,dRdS,Mprime,Mprofile]=MCDefinition();
[xWATD,yWATD]=ThetaDefinition();
[Thickness]=ThkDefinition();

%% FP: Flow Path construction from span 01 and 05 based on Z=11 ...
   blades FPOA=360/Z



% FPOA: flow path offset angle
```

```
%size allocation
Npb=100;%Number of points in bezier curve
xdrfp_span=zeros(Npb,Nspan);
ydrfp_span=zeros(Npb,Nspan);
xdlfp_span=zeros(Npb,Nspan);
ydlfp_span=zeros(Npb,Nspan);

%**************** Construction of Flow Path pressure and suction ...
   sides ***********
for i=1:Nspan
FPOA=360/z*0.5;
yfp_ssi_span(:,i)=yWATD(:,i)+FPOA;
yfp_psi_span(:,i)=yWATD(:,i)-FPOA;
xdrfp_span(:,i)=R_span(:,i).*cos(yfp_ssi_span(:,i)*pi/180);
ydrfp_span(:,i)=R_span(:,i).*sin(yfp_ssi_span(:,i)*pi/180);
xdlfp_span(:,i)=R_span(:,i).*cos(yfp_psi_span(:,i)*pi/180);
ydlfp_span(:,i)=R_span(:,i).*sin(yfp_psi_span(:,i)*pi/180);

end

%% **************** Construction of Flow Path Inlet and Outlet ...
   diffusers ************
%**************** Inlet Flow *******************
xdlfp_bdiff=R_span(:,6).*cos(FPOA*pi/180);
ydlfp_bdiff=R_span(:,6).*sin(FPOA*pi/180);
xdrfp_bdiff=R_span(:,6).*cos(-FPOA*pi/180);
ydrfp_bdiff=R_span(:,6).*sin(-FPOA*pi/180);

xdlfp_tdiff=R_span(:,7).*cos(FPOA*pi/180);
ydlfp_tdiff=R_span(:,7).*sin(FPOA*pi/180);
xdrfp_tdiff=R_span(:,7).*cos(-FPOA*pi/180);
ydrfp_tdiff=R_span(:,7).*sin(-FPOA*pi/180);

%**************** Outlet Flow *******************
```

```
xdlfp_bout=R_bout.*cos(yfp_ssi_span(end,1)*pi/180);
ydlfp_bout=R_bout.*sin(yfp_ssi_span(end,1)*pi/180);
xdrfp_bout=R_bout.*cos(yfp_ssi_span(end,1)*pi/180);
ydrfp_bout=R_bout.*sin(yfp_ssi_span(end,1)*pi/180);

xdlfp_tout=R_tout.*cos(yfp_psi_span(end,1)*pi/180);
ydlfp_tout=R_tout.*sin(yfp_psi_span(end,1)*pi/180);
xdrfp_tout=R_tout.*cos(yfp_psi_span(end,1)*pi/180);
ydrfp_tout=R_tout.*sin(yfp_psi_span(end,1)*pi/180);



%**************** Inlet  ****************
th_dshaft=linspace(-FPOA*pi/180,FPOA*pi/180,20);
x_dshaft=(R_span(1,6).*cos(th_dshaft))';
y_dshaft=(R_span(1,6).*sin(th_dshaft))';
z_dshaft=(linspace(Z_span(1,6),Z_span(1,6),20))';

th_deye=linspace(-FPOA*pi/180,FPOA*pi/180,20);
x_deye=(R_span(1,7).*cos(th_deye))';
y_deye=(R_span(1,7).*sin(th_deye))';
z_deye=z_dshaft;

%******** for loop to create inlet made out of 20 curves ******
Ncurves=20;
topradii=linspace(R_span(1,6),R_span(1,7),Ncurves);
th_top=linspace(-FPOA*pi/180,FPOA*pi/180,Ncurves);

for i=1:20
    x_fpshaft(:,i)=topradii(i).*cos(th_top);
    y_fpshaft(:,i)=topradii(i).*sin(th_top);
    z_fpshaft(:,i)=-z_dshaft;
end
```

```
for ii=1:length(Z_span)
    x_tdiff(:,ii)=R_span(ii,7).*cos(th_top);
    y_tdiff(:,ii)=R_span(ii,7).*sin(th_top);
    z_tdiff(1:Ncurves,ii)=-Z_span(ii,7);
end


for jj=1:length(yfp_psi_span)
    theta_span05(jj,:)=linspace(yfp_psi_span(jj,5),yfp_ssi_span(jj,5),Ncurves);
    x_shroud(:,jj)=R_span(jj,5).*cos(theta_span05(jj,:)*pi/180);
    y_shroud(:,jj)=R_span(jj,5).*sin(theta_span05(jj,:)*pi/180);
    z_shroud(1:Ncurves,jj)=-Z_span(jj,5);
end

for kk=1:length(Z_tout)
    x_tout(:,kk)=R_tout(kk).*cos(theta_span05(end,:)*pi/180);
    y_tout(:,kk)=R_tout(kk).*sin(theta_span05(end,:)*pi/180);
    z_tout(1:Ncurves,kk)=-Z_tout(kk);
end


for iii=1:length(Z_span)
    x_bdiff(:,iii)=R_span(iii,6).*cos(th_top);
    y_bdiff(:,iii)=R_span(iii,6).*sin(th_top);
    z_bdiff(1:Ncurves,iii)=-Z_span(iii,6);
end

for jjj=1:length(yfp_psi_span)
    theta_span01(jjj,:)=linspace(yfp_psi_span(jjj,1),yfp_ssi_span(jjj,1),Ncurves)
    x_hub(:,jjj)=R_span(jjj,1).*cos(theta_span01(jjj,:)*pi/180);
    y_hub(:,jjj)=R_span(jjj,1).*sin(theta_span01(jjj,:)*pi/180);
    z_hub(1:Ncurves,jjj)=-Z_span(jjj,1);
end
```

```
for kkk=1:length(Z_bout)
    x_bout(:,kkk)=R_bout(kkk).*cos(theta_span01(end,:)*pi/180);
    y_bout(:,kkk)=R_bout(kkk).*sin(theta_span01(end,:)*pi/180);
    z_bout(1:Ncurves,kkk)=-Z_bout(kkk);
end

%*************** Outlet ***************
th_doutbott=linspace(yfp_psi_span(end,5)*pi/180,yfp_ssi_span(end,1)*pi/180,20);
x_doutbott=(R_bout(end).*cos(th_doutbott))';
y_doutbott=(R_bout(end).*sin(th_doutbott))';
z_doutbott=(linspace(Z_bout(1),Z_bout(1),20))';

th_douttop=th_doutbott;
x_douttop=(R_tout(end).*cos(th_douttop))';
y_douttop=(R_tout(end).*sin(th_douttop))';
z_douttop=(linspace(Z_tout(end),Z_tout(end),20))';



secx_lfpb=[xdlfp_bdiff;xdrfp_span(:,1);xdrfp_bout'];
secx_lfpt=[xdlfp_tdiff;xdrfp_span(:,5);xdlfp_bout'];
secy_lfpb=[ydlfp_bdiff;ydrfp_span(:,1);ydrfp_bout'];
secy_lfpt=[ydlfp_tdiff;ydrfp_span(:,5);ydlfp_bout'];
secz_lfpb=[Z_span(:,6);Z_span(:,1);Z_bout'];
secz_lfpt=[Z_span(:,7);Z_span(:,5);Z_tout'];

secx_rfpb=[xdrfp_bdiff;xdlfp_span(:,1);xdlfp_tout'];
secx_rfpt=[xdrfp_tdiff;xdlfp_span(:,5);xdrfp_tout'];
secy_rfpb=[ydrfp_bdiff;ydlfp_span(:,1);ydlfp_tout'];
secy_rfpt=[ydrfp_tdiff;ydlfp_span(:,5);ydrfp_tout'];
secz_rfpb=[Z_span(:,6);Z_span(:,1);Z_bout'];
secz_rfpt=[Z_span(:,7);Z_span(:,5);Z_tout'];
```

```
sectionxfp=[secx_rfpb,secx_rfpt];
sectionyfp=[secy_rfpb,secy_rfpt];
sectionzfp=[secz_rfpb,secz_rfpt];

sectionxtfp=[secx_lfpb,secx_lfpt];
sectionytfp=[secy_lfpb,secy_lfpt];
sectionztfp=[secz_lfpb,secz_lfpt];


sectionx_outlet=[x_doutbott,x_douttop];
sectiony_outlet=[y_doutbott,y_douttop];
sectionz_outlet=[z_doutbott,z_douttop];



end
```

Bibliography

[1] S. Morgan, H. Smith, I. Simpson, G. Liddiard, H. Raphael, R. Pickering, and D. Mant, “Prevalence and clinical characteristics of left ventricular dysfunction among elderly patients in general practice setting: cross sectional survey,” *BMJ*, vol. 318, pp. 368–372, 2 1999. 1

[2] S. Stewart, A. Jenkins, S. Buchan, A. McGuire, S. Capewell, and J. J. McMurray, “The current cost of heart failure to the national health service in the uk,” *European Journal of Heart Failure*, vol. 4, no. 3, pp. 361–371, 2002. 1

[3] V. L. Roger, A. S. Go, D. M. Lloyd-Jones, E. J. Benjamin, J. D. Berry, W. B. Borden, D. M. Bravata, S. Dai, E. S. Ford, C. S. Fox, H. J. Fullerton, C. Gillespie, S. M. Hailpern, J. A. Heit, V. J. Howard, B. M. Kissela, S. J. Kittner, D. T. Lackland, J. H. Lichtman, L. D. Lisabeth, D. M. Makuc, G. M. Marcus, A. Marelli, D. B. Matchar, C. S. Moy, D. Mozaffarian, M. E. Mussolino, G. Nichol, N. P. Paynter, E. Z. Soliman, P. D. Sorlie, N. Sotoodehnia, T. N. Turan, S. S. Virani, N. D. Wong, D. Woo, and M. B. Turner, “Heart disease and stroke statistics —2012 update: A report from the american heart association,” *Circulation*, vol. 125, no. 1, pp. e2–e220, 2012. 1

[4] P. A. McKee, W. P. Castelli, P. M. McNamara, and W. B. Kannel, “The Natural History of Congestive Heart Failure: The Framingham Study,” *New England Journal of Medicine*, vol. 285, no. 26, pp. 1441–1446, 1971. 1

[5] R. Levick, *An Introduction to Cardiovascular Physiology*. Hodder Arnold, 4th ed., 2003. x, xii, 2, 5, 6, 8, 43, 50, 70

[6] A. Guyton and J. Hall, *Textbook of Medical Physiology*. Philadelphia, PA, USA: Elsevier Saunders, 2006. x, xiii, 2, 3, 7, 8, 35, 45, 46, 56, 77, 117, 126

[7] L. Waite, *Biofluid Mechanics in Cardiovascular System*. McGraw-Hill, 2006. 2

[8] J. Batzel, B. Giuseppe, R. Mukkamala, and K. H. Chon, "Modeling and disentangling physiological mechanisms: linear and nonlinear identification of techniques for analysis of cardiovascular regulation," *Philosophical Transactions of the Royal American Society*, vol. 367, pp. 1377 – 1391, 2009. 7

[9] P. R. Kalra, S. D. Anker, and A. J. S. Coats, "Water and sodium regulation in chronic heart failure: the role of natriuretic peptides and vasopressin," *Cardiovascular Research*, vol. 51, no. 3, pp. 495–509, 2001. 7, 11, 14

[10] M. A. Lee, M. Bohm, M. Paul, and D. Ganten, "Tissue renin-angiotensin systems - their role in cardiovascular-disease," *Circulation*, vol. 87, no. 5, pp. 7–13, 1993. 8, 11

[11] D. Kasper, E. Braunwald, A. Fauci, S. Hauser, D. Longo, J. Jameson, and J. Loscalzo, *Harrison's principles of internal medicine*, ch. Part 9: Disorders of the Cardiovascular System, pp. 1538–1540. McGraw-Hill Medical Publishing Division, 17th, ed., 2008. 8

[12] J. N. Cohn, "The management of chronic heart failure," *New England Journal of Medicine*, vol. 335, no. 7, pp. 490–498, 1996. 9, 15

[13] M. Gheorghiade, R. J. Cody, G. S. Francis, W. J. McKenna, J. B. Young, and R. O. Bonow, "Current medical therapy for advanced heart failure," *American Heart Journal*, vol. 135, no. 6, Supplement, pp. S231 – S248, 1998. 9, 10, 11, 71

[14] R. Holland, B. Rechel, K. Stepien, I. Harvey, and I. Brooksby, “Patients’ self-assessed functional status in heart failure by new york heart association class: A prognostic predictor of hospitalizations, quality of life and death,” *Journal of Cardiac Failure*, vol. 16, no. 2, pp. 150 – 156, 2010. 9

[15] T. C. C. of the New York Heart Association, *Nomenclature and criteria for diagnosis of diseases of the heart and blood vessels.* Boston, MA: Little, Brown, 1964. 10

[16] K. W. Dauterman, A. S. Go, R. Rowell, T. Gebretsadik, S. Gettner, and B. M. Massie, “Congestive heart failure with preserved systolic function in a statewide sample of community hospitals,” *Journal of Cardiac Failure*, vol. 7, no. 3, pp. 221 – 228, 2001. 10

[17] S. A. Hunt, W. T. Abraham, M. H. Chin, A. M. Feldman, G. S. Francis, T. G. Ganiats, M. Jessup, M. A. Konstam, D. M. Mancini, K. Michl, J. A. Oates, P. S. Rahko, M. A. Silver, L. W. Stevenson, C. W. Yancy, A. C. Cardiology, and A. M. H. A. T. Force, “Acc/aha 2005 guideline update for the diagnosis and management of chronic heart failure in the adult,” *Circulation*, vol. 112, no. 12, pp. E154–235, 2005. 11

[18] R. W. Schrier, “Role of diminished renal function in cardiovascular mortality: Marker or pathogenetic factor?,” *Journal of the American College of Cardiology*, vol. 47, no. 1, pp. 1 – 8, 2006. x, 11, 12, 13

[19] M. Packer, W. H. Lee, P. D. Kessler, S. S. Gottlieb, J. L. Bernstein, and M. L. Kukin, “Role of neurohormal mechanisms in determining survival in patients with severe chronic heart failure,” *Circulation*, vol. 75, no. 5, pp. 80–92, 1987. 11

[20] M. E. Leithe, R. D. Margorien, J. B. Hermiller, D. V. Unverferth, and C. V. Leier, “Relationship between central hemodynamics and regional blood flow in normal

subjects and in patients with congestive heart failure," *Circulation*, vol. 69, no. 1, pp. 57–64, 1984. 11, 77

[21] J. O. Davis and R. H. Freeman, "Mechanisms regulating renin release," *Physiological Reviews*, vol. 56, no. 1, pp. 1–56, 1976. 11, 14

[22] M. A. Creager, J. L. Halperin, D. B. Bernard, D. P. Faxon, C. D. Melidossian, H. Gavras, and T. J. Ryan, "Acute regional circulatory and renal hemodynamic-effects of converting-enzyme inhibition in patients with congestive heart-failure," *Circulation*, vol. 64, no. 3, pp. 483–489, 1981.

[23] R. J. Cody, A. B. Covit, G. L. Schaer, J. H. Laragh, J. E. Sealey, and J. Feldschuh, "Sodium and water-balance in chronic congestive-heart-failure," *Journal of Clinical Investigation*, vol. 77, no. 5, pp. 1441–1452, 1986. 11, 14

[24] R. Zelis and S. F. Flaim, "Alterations in vasomotor tone in congestive heart-failure," *Progress in Cardiovascular Diseases*, vol. 24, no. 6, pp. 437–459, 1982. 11

[25] C. Curtiss, J. N. Cohn, T. Vrobel, and J. A. Franciosa, "Role of renin-angiotensin system in systemic vasoconstriction of chronic congestive heart-failure," *Circulation*, vol. 58, no. 5, pp. 763–770, 1978. 11

[26] J. D. Hosenpud and B. H. Greenberg, eds., *Congestive Heart Failure*. Lippincott Williams & Wilkins, third edition ed., 2007. 12, 13, 14

[27] M. Mukoyama, K. Nakao, K. Hosoda, S. Suga, Y. Saito, Y. Ogawa, G. Shirakami, M. Jougasaki, K. Obata, H. Yasue, Y. Kambayashi, K. Inouye, and H. Imura, "Brain natriuretic peptide as a novel cardiac hormone in humans - evidence for an exquisite dual natriuretic peptide system, atrial-natriuretic-peptide and brain natriuretic peptide," *Journal of Clinical Investigation*, vol. 87, no. 4, pp. 1402–1412, 1991. 12

[28] S. P. D'Souza, M. Davis, and G. F. Baxter, "Autocrine and paracrine actions of natriuretic peptides in the heart," *Pharmacology & Therapeutics*, vol. 101, no. 2, pp. 113 – 129, 2004. 12

[29] D. L. Dries, D. V. Exner, M. J. Domanski, B. Greenberg, and L. W. Stevenson, "The prognostic implications of renal insufficiency in asymptomatic and symptomatic patients with left ventricular systolic dysfunction," *Journal of the American College of Cardiology*, vol. 35, no. 3, pp. 681 – 689, 2000. 13

[30] H. M. Krumholz, Y.-T. Chen, V. Vaccarino, Y. Wang, M. J. Radford, W. Bradford, and R. I. Horwitz, "Correlates and impact on outcomes of worsening renal function in patients ≥ 65 years of age with heart failure," *The American Journal of Cardiology*, vol. 85, no. 9, pp. 1110 – 1113, 2000. 13

[31] S. S. Gottlieb, W. Abraham, J. Butler, D. E. Forman, E. Loh, B. M. Massie, C. M. O'Connor, M. W. Rich, L. W. Stevenson, J. Young, and H. M. Krumholz, "The prognostic importance of different definitions of worsening renal function in congestive heart failure," *Journal of Cardiac Failure*, vol. 8, no. 3, pp. 136 – 141, 2002. 13

[32] G. F. DiBona and U. C. Kopp, "Neural control of renal function," *Physiological Reviews*, vol. 77, no. 1, pp. 75–197, 1997. 14

[33] G. F. DiBona, "Neural control of the kidney - past, present, and future," *Hypertension*, vol. 41, no. 3, pp. 621–624, 2003. 14, 45

[34] J. P. Henry, O. H. Gauer, and J. L. Reeves, "Evidence of the atrial location of receptors influencing urine flow," *Circulation Research*, vol. 4, no. 1, pp. 85–90, 1956. 14

[35] G. G. Blume, C. J. Mcleod, M. E. Barnes, J. B. Seward, P. A. Pellikka, P. M. Bastiansen, and T. S. Tsang, "Left atrial function: physiology, assessment, and clinical

implications," *European Journal of Echocardiography*, vol. 12, no. 6, pp. 421–430, 2011. 14

[36] I. H. Zucker, A. J. Gorman, K. G. Cornish, and M. Lang, "Impaired atrial receptor modulation or renal nerve activity in dogs with chronic volume overload1," *Cardiovascular Research*, vol. 19, no. 7, pp. 411–418, 1985. 14

[37] M. Volpe, C. Tritto, N. Deluca, A. F. Mele, G. Lembo, S. Rubattu, M. Romano, P. Decampora, I. Enea, B. Ricciardelli, B. Trimarco, and M. Condorelli, "Failure of atrial-natriuretic-factor to increase with saline load in patients with dilated cardiomyopathy and mild heart-failure," *Journal of Clinical Investigation*, vol. 88, no. 5, pp. 1481–1489, 1991. 14

[38] E. A. Rose, A. J. Moskowitz, M. Packer, J. A. Sollano, D. L. Williams, A. R. Tierney, D. F. Heitjan, P. Meier, D. D. Ascheim, R. G. Levitan, A. D. Weinberg, L. W. Stevenson, P. A. Shapiro, R. M. Lazar, J. T. Watson, D. J. Goldstein, and A. C. Gelijns, "The REMATCH trial: rationale, design, and end points," *The Annals of Thoracic Surgery*, vol. 67, no. 3, pp. 723 – 730, 1999. 15, 17

[39] T. S. Investigators, "Effect of enalapril on survival in patients with reduced left-ventricular ejection fractions and congestive-heart-failure," *New England Journal of Medicine*, vol. 325, no. 5, pp. 293–302, 1991. 15

[40] M. S. Slaughter, F. D. Pagani, J. G. Rogers, L. W. Miller, B. Sun, S. D. Russell, R. C. Starling, L. Chen, A. J. Boyle, S. Chillcott, R. M. Adamson, M. S. Blood, M. T. Camacho, K. A. Idrissi, M. Petty, M. Sobieski, S. Wright, T. J. Myers, and D. J. Farrar, "Clinical management of continuous-flow left ventricular assist devices in advanced heart failure," *The Journal of heart and lung transplantation*, vol. 29, pp. S1 – S39, 2010. 15

[41] O. Frazier, M. P. Macris, T. J. Myers, J. Duncan, B. Radovančević, P. S. M., and

D. A. Cooley, “Improved survival after extended bridge to cardiac transplantation,” *The Annals of thoracic surgery*, vol. 57, pp. 1416 – 1422, 1994. 15

[42] S. A. Hunt, O. H. Frazier, and T. J. Myers, “Mechanical circulatory support and cardiac transplantation,” *Circulation*, vol. 97, no. 20, pp. 2079–2090, 1998. x, 15, 18, 19, 20, 27, 28

[43] M. E. DeBakey, “Development of mechanical heart devices,” *The Annals of Thoracic Surgery*, vol. 79, no. 6, pp. S2228 – S2231, 2005. 15, 16

[44] S. D. Moulopoulos, “Intra-aortic balloon counterpulsation 50 years later: Initial conception and consequent ideas,” *Artificial Organs*, vol. 35, no. 9, pp. 843–848, 2011. 16

[45] D. A. Cooley, D. Liotta, G. L. Hallman, R. D. Bloodwell, R. D. Leachman, and J. D. Milam, “Orthotopic cardiac prosthesis for two-staged cardiac replacement,” *The American Journal of Cardiology*, vol. 24, no. 5, pp. 723 – 730, 1969. 16

[46] J. Norman, D. Cooley, B. Kahan, A. Keats, E. Massin, R. Solis, W. Luper, M. Brook, T. Klima, O. Frazier, J. Hacker, J. Duncan, C. Dacso, D. Winston, and G. Reul, “Total support of the circulation of a patient with post-cardiotomy stone-heart syndrome by a partial artificial heart (ALVAD) for 5 days followed by heart and kidney transplantation,” *The Lancet*, vol. 311, no. 8074, pp. 1125 – 1127, 1978. 16

[47] J. Norman, J. Fuqua, R. Trono, C. Hibbs, C. Edmonds, S. Igo, M. Brewer, D. Holub, and D. Cooley, “An intracorporeal (abdominal) left ventricular assist device: Initial clinical trials (LX),” in *Assisted Circulation* (F. Unger, ed.), pp. 107–126, Springer Berlin Heidelberg, 1979. 16

[48] Y. Nosé, M. Yoshikawa, S. Murabayashi, and T. Takano, “Development of rotary blood pump technology: Past, present, and future,” *Artificial Organs*, vol. 24, no. 6, pp. 412–420, 2000. 16

[49] K. E. Johnson, M. B. Liska, L. D. Joyce, and R. W. Emery, “Registry report. use of total artificial hearts: summary of world experience, 1969-1991,” *ASAIO journal (American Society for Artificial Internal Organs : 1992)*, vol. 38, no. 3, pp. M486–92, 1992. 16

[50] A. M. Feldman, ed., *Heart Failure: Device Management*, ch. Left Ventricular Assist Devices for Acute and Chronic Heart Failure, p. 141. West Sussex, UK: John Wiley & Sons, Ltd., 2010. 17

[51] O. H. Frazier, T. J. Myers, I. D. Gregoric, T. Khan, R. Delgado, M. Croitoru, K. Miller, R. Jarvik, and S. Westaby, “Initial clinical experience with the jarvik 2000 implantable axial-flow left ventricular assist system,” *Circulation*, vol. 105, no. 24, pp. 2855–2860, 2002. 17

[52] J. W. Long, A. G. Kfoury, M. S. Slaughter, M. Silver, C. Milano, J. Rogers, R. Delgado, and O. Frazier, “Long-term destination therapy with the heartmate xve left ventricular assist device: improved outcomes since the rematch study,” *Congestive Heart Failure*, vol. 11, no. 3, pp. 133–138, 2005. x, 17, 18, 27

[53] D. Gagnon, M. Petty, and J. R. Lahpor, “HeartMate® family of left ventricular assist systems,” *Perfusion*, vol. 15, no. 4, pp. 345–354, 2000. 17, 18, 27

[54] A. Pavie, N. Reiss, and S. Aubert, “Implantation technique of the novacor left ventricular assist device,” *Multimedia Manual of Cardio-Thoracic Surgery*, vol. 2007, no. 0219, 2007. 18, 27

[55] M. C. Deng, M. Loebe, A. El-Banayosy, E. Gronda, P. G. Jansen, M. Vigano, G. M. Wieselthaler, B. Reichart, E. Vitali, A. Pavie, *et al.*, “Mechanical circulatory support for advanced heart failure effect of patient selection on outcome,” *Circulation*, vol. 103, no. 2, pp. 231–237, 2001. x, 18

[56] D. J. Farrar and J. D. Hill, “Univentricular and biventricular thoratec VAD support

as a bridge to transplantation," *The Annals of Thoracic Surgery*, vol. 55, no. 1, pp. 276–282, 1993. x, 19, 27

[57] W. Konertz, H. Hotz, M. Schneider, M. Redlin, and H. Reul, "Clinical experience with the MEDOSHIA-VAD System in Infants and Children: A Preliminary Report," *The Annals of Thoracic Surgery*, vol. 63, no. 4, pp. 1138 – 1143, 1997. x, 19, 20, 27

[58] J. G. Copeland, R. G. Smith, F. A. Arabia, P. E. Nolan, G. K. Sethi, P. H. Tsau, D. McClellan, and M. J. Slepian, "Cardiac replacement with a total artificial heart as a bridge to transplantation," *New England Journal of Medicine*, vol. 351, no. 9, pp. 859–867, 2004. xi, 20, 27

[59] B. P. Griffith, R. L. Kormos, H. S. Borovetz, K. Litwak, J. F. Antaki, V. L. Poirier, and K. C. Butler, "HeartMate II left ventricular assist system: from concept to first clinical use," *The Annals of Thoracic Surgery*, vol. 71, no. 3, Supplement 1, pp. S116 – S120, 2001. xi, 21, 28

[60] D. J. Goldstein, "Worldwide Experience With the MicroMed DeBakey Ventricular Assist Device™ as a Bridge to Transplantation," *Circulation*, vol. 108, no. 10 suppl 1, pp. II–272–II–277, 2003. 21, 28

[61] G. P. Noon and M. Loebe, "Current status of the micromed debakey noon ventricular assist device," *Texas Heart Institute Journal*, vol. 37, no. 6, p. 652, 2010. 21, 28

[62] M. E. DeBakey, "A miniature implantable axial flow ventricular assist device," *The Annals of Thoracic Surgery*, vol. 68, no. 2, pp. 637 – 640, 1999. xi, 22, 28

[63] O. H. Frazier, T. J. Myers, S. Westaby, and I. D. Gregoric, "Use of the jarvik 2000 left ventricular assist system as a bridge to heart transplantation or as destination therapy for patients with chronic heart failure," *Annals of Surgery*, vol. 237, no. 5, pp. 631–636, 2003. xi, 22, 28

[64] S. Westaby, M. Siegenthaler, F. Beyersdorf, M. Massetti, J. Pepper, A. Khayat, R. Hetzer, and O. H. Frazier, “Destination therapy with a rotary blood pump and novel power delivery,” *European Journal of Cardio-Thoracic Surgery*, vol. 37, no. 2, pp. 350–356, 2010. 22, 28

[65] C. Schmid, T. D. Tjan, C. Etz, C. Schmidt, F. Wenzelburger, M. Wilhelm, M. Rothenburger, G. Drees, and H. H. Scheld, “First clinical experience with the incor left ventricular assist device,” *The Journal of Heart and Lung Transplantation*, vol. 24, no. 9, pp. 1188 – 1194, 2005. xi, 23, 28

[66] R. Hetzer, Y. Weng, E. V. Potapov, M. Pasic, T. Drews, M. Jurmann, E. Hennig, and M. J, “First experiences with a novel magnetically suspended axial flow left ventricular assist device,” *European Journal of Cardio-thoracic Surgery*, vol. 25, no. 6, pp. 964–970, 2004. xi, 23

[67] M. Strueber, G. O’Driscoll, P. Jansz, A. Khaghani, W. C. Levy, and G. M. Wieselthaler, “Multicenter evaluation of an intrapericardial left ventricular assist system,” *Journal of the American College of Cardiology*, vol. 57, no. 12, pp. 1375 – 1382, 2011. 24, 29, 78

[68] HeartWare Inc., USA, *HeartWare® Ventricular Assist System Instructions for Use*, November 2012. xi, 24, 29

[69] M. Morshuis, A. El-Banayosy, L. Arusoglu, R. Koerfer, R. Hetzer, G. Wieselthaler, A. Pavie, and C. Nojiri, “European experience of duraheart™ magnetically levitated centrifugal left ventricular assist system,” *European Journal of Cardio-Thoracic Surgery*, vol. 35, no. 6, pp. 1020–1028, 2009. xi, 25, 29

[70] P. Ayre, S. Vidakovic, G. Tansley, P. Watterson, and N. Lovell, “Sensorless flow and head estimation in the ventrassist rotary blood pump,” *Artificial Organs*, vol. 24, no. 8, pp. 585 – 588, 2000. 25, 30

[71] D. Esmore, P. Spratt, R. Larbalestier, S. Tsui, A. Fiane, P. Ruygrok, D. Meyers, and J. Woodard, “VentrAssist™ left ventricular assist device: clinical trial results and clinical development plan update,” *European Journal of Cardio-Thoracic Surgery*, vol. 32, no. 5, pp. 735–744, 2007. xi, 25, 30

[72] D. Timms, “A review of clinical ventricular assist devices,” *Medical Engineering & Physics*, vol. 33, no. 9, pp. 1041 – 1047, 2011. 25, 29

[73] K. Yamazaki, S. Kihara, T. Akimoto, O. Tagusari, A. Kawai, M. Umezu, J. Tomioka, R. Kormos, B. Griffith, and H. Kurosawa, “EVAHEART™: An implantable centrifugal blood pump for long-term circulatory support,” *The Japanese Journal of Thoracic and Cardiovascular Surgery*, vol. 50, no. 11, pp. 461–465, 2002. 26, 29

[74] S. Agarwal and K. M. High, “Newer-generation ventricular assist devices,” *Best Practice & Research Clinical Anaesthesiology*, vol. 26, no. 2, pp. 117 – 130, 2012. Mechanical Circulatory Support. 26, 29, 78

[75] B. Meyns, S. Klotz, A. Simon, W. Droogne, F. Rega, B. Griffith, R. Dowling, M. J. Zucker, and D. Burkhoff, “Proof of concept: Hemodynamic response to long-term partial ventricular support with the synergy pocket micro-pump,” *Journal of the American College of Cardiology*, vol. 54, no. 1, pp. 79 – 86, 2009. 26, 30

[76] HeartWare™ International, Inc., USA, *CircuLite™ Overview*, December 2013. xi, 26, 30

[77] D. L. Timms, S. D. Gregory, N. A. Greatrex, M. J. Pearcy, J. F. Fraser, and U. Steinseifer, “A compact mock circulation loop for the in vitro testing of cardiovascular devices,” *Artificial Organs*, vol. 35, pp. 384–391, 2011. xi, 26, 107

[78] M. S. Slaughter, J. G. Rogers, C. A. Milano, S. D. Russell, J. V. Conte, D. Feldman, B. Sun, A. J. Tatooles, R. M. Delgado, J. W. Long, T. C. Wozniak, W. Ghumman,

D. J. Farrar, and O. H. Frazier, “Advanced heart failure treated with continuous-flow left ventricular assist device,” *New England Journal of Medicine*, vol. 361, no. 23, pp. 2241–2251, 2009. 27, 28

[79] J. Copeland, A. Pavie, D. Duveau, W. Keon, R. Masters, R. Pifarre, R. Smith, and F. Arabia, “Bridge to transplantation with the CardioWest total artificial heart: the international experience 1993 to 1995,” *Journal of Heart and Lung Transplantion*, vol. 15, pp. 94 – 99, 1996. 27

[80] L. W. Miller, F. D. Pagani, S. D. Russell, R. John, A. J. Boyle, K. D. Aaronson, J. V. Conte, Y. Naka, D. Mancini, R. M. Delgado, T. E. MacGillivray, D. J. Farrar, and O. Frazier, “Use of a continuous-flow device in patients awaiting heart transplantation,” *New England Journal of Medicine*, vol. 357, no. 9, pp. 885–896, 2007. 28

[81] K. A. Pennings, J. R. Martina, B. F. Rodermans, J. R. Lahpor, F. N. van de Vosse, B. A. de Mol, and M. C. Rutten, “Pump Flow Estimation From Pressure Head and Power Uptake for the HeartAssist5, HeartMate II, and HeartWare VADs,” *ASAIO Journal*, vol. 59, pp. 420 – 426, 2013. 28

[82] O. Frazier, T. J. Myers, S. Westaby, and I. D. Gregoric, “Clinical experience with an implantable, intracardiac, continuous flow circulatory support device: physiologic implications and their relationship to patient selection,” *The Annals of Thoracic Surgery*, vol. 77, no. 1, pp. 133 – 142, 2004. 28

[83] T. Yagdi, E. Oguz, F. Ayik, S. Ertugay, S. Nalbantgil, C. Engin, and M. Ozbaran, “Ventricular assist system applications in end-stage heart failure,” *Transplantation Proceedings*, vol. 43, no. 3, pp. 923 – 926, 2011. 28

[84] T. Akimoto, K. Yamazaki, P. Litwak, K. N. Litwak, O. Tagusari, T. Mori, J. F. Antaki, M. V. Kameneva, M. J. Watach, M. Umezu, J. Tomioka, R. L. Kormos, H. Koyanagi, and B. P. Griffith, “Continuously maintaining positive flow avoids

endocardial suction of a rotary blood pump with left ventricular bypass," *Artificial Organs*, vol. 24, no. 8, pp. 606–610, 2000. 29, 78

[85] T. Akimoto, K. N. Litwak, K. Yamazaki, P. Litwak, S.-i. Kihara, O. Tagusari, S.-i. Yamazaki, M. V. Kameneva, M. J. Watach, M. Umezu, J. Tomioka, R. L. Kormos, H. Koyanagi, and B. P. Griffith, "The role of diastolic pump flow in centrifugal blood pump hemodynamics," *Artificial Organs*, vol. 25, no. 9, pp. 724 – 727, 2001. 29, 78

[86] R. M. Lazar, P. A. Shapiro, B. E. Jaski, M. K. Parides, R. C. Bourge, J. T. Watson, L. Damme, W. Dembitsky, J. D. Hosenpud, L. Gupta, A. Tierney, T. Kraus, and Y. Naka, "Neurological events during long-term mechanical circulatory support for heart failure - the randomized evaluation of mechanical assistance for the treatment of congestive heart failure (REMATCH) experience," *Circulation*, vol. 109, no. 20, 2004. 31

[87] G. S. Murphy, E. A. Hessel, and R. C. Groom, "Optimal perfusion during cardiopulmonary bypass: An evidence-based approach," *Anesthesia and Analgesia*, vol. 108, no. 5, pp. 1394–1417, 2009. 31

[88] H. Suga, K. Sagawa, and A. Shoukas, "Load independence of the instantaneous pressure-volume ratio of the canine left ventricle and effects of epinephrine and heart rate on the ratio," *Circulation Research*, vol. 32, pp. 314–322, 1973. 33, 34, 110

[89] G. Pennati, M. Bellotti, and R. Fumero, "Mathematical modelling of the human foetal cardiovascular system based on doppler ultrasound data," *Medical Engineering & Physics*, vol. 19, no. 4, pp. 327 – 335, 1997.

[90] F. Y. Chen, D. B. Lautz, B. J. deGuzman, L. Aklog, R. M. Ahmad, R. G. Laurence, G. S. Couper, L. H. Cohn, and T. A. McMahon, "An Engineering Model of Dy-

namic Cardiomyoplasty. I.," *Annals of Biomedical Engineering*, vol. 26, pp. 441–453, 1998.

[91] X. Xiao, E. Ozawa, Y. Huang, and R. Kamm, "Model-based assessment of cardiovascular health from noninvasive measurements," *Annals of Biomedical Engineering*, vol. 30, pp. 612–623, 2002. 33

[92] B. W. Smith, J. G. Chase, R. I. Nokes, G. M. Shaw, and G. Wake, "Minimal haemodynamic system model including ventricular interaction and valve dynamics," *Medical Engineering & Physics*, vol. 26, no. 2, pp. 131 – 139, 2004. 33, 34, 35, 70

[93] R. Fogliardi, R. Burattini, S. G. Shroff, and K. B. Campbell, "Fit to diastolic arterial pressure by third-order lumped model yields unreliable estimates of arterial compliance," *Medical Engineering & Physics*, vol. 18, no. 3, pp. 225 – 233, 1996. 33

[94] R. Pietrabissa, S. Mantero, T. Marotta, and L. Menicanti, "A lumped parameter model to evaluate the fluid dynamics of different coronary bypasses," *Medical Engineering & Physics*, vol. 18, no. 6, pp. 477 – 484, 1996.

[95] R. Cole, C. Lucas, W. Cascio, and T. Johnson, "A labview™ model incorporating an open-loop arterial impedance and a closed-loop circulatory system," *Annals of Biomedical Engineering*, vol. 33, pp. 1555–1573, 2005.

[96] P. Segers, E. R. Rietzschel, M. L. De Buyzere, N. Stergiopulos, N. Westerhof, L. M. Van Bortel, T. Gillebert, and P. R. Verdonck, "Three- and four-element windkessel models: assessment of their fitting performance in a large cohort of healthy middle-aged individuals," *Proceedings of the Institution of Mechanical Engineers Part H-Journal of Engineering in Medicine*, vol. 222, no. H4, pp. 417–428, 2008. 33

[97] G. Pennati and R. Fumero, "Scaling approach to study the changes through the

gestation of human fetal cardiac and circulatory behaviors," *Annals of Biomedical Engineering*, vol. 28, pp. 442–452, 2000. 33

[98] K. Peterson, E. T. Ozawa, G. M. Pantalos, and M. K. Sharp, "Numerical simulation of the influence of gravity and posture on cardiac performance," *Annals of Biomedical Engineering*, vol. 30, pp. 247–259, 2002.

[99] T. Korakianitis and Y. Shi, "A concentrated parameter model for the human cardiovascular system including heart valve dynamics and atrioventricular interaction," *Medical Engineering & Physics*, vol. 28, pp. 613–628, 2006.

[100] T. Korakianitis and Y. Shi, "Effects of atrial contraction, atrioventricular interaction and heart valve dynamics on human cardiovascular system response," *Medical Engineering & Physics*, vol. 28, no. 8, pp. 762–779, 2006. 34, 35, 49, 66

[101] T. Korakianitis and Y. Shi, "Numerical simulation of cardiovascular dynamics with healthy and diseased heart valves," *Journal of Biomechanics*, vol. 39, no. 11, pp. 1964–1982, 2006. 33, 35

[102] Y. Shi and T. Korakianitis, "Numerical simulation of cardiovascular dynamics with left heart failure and in-series pulsatile ventricular assist device," *Artificial Organs*, vol. 30, no. 12, pp. 929–948, 2006. 33

[103] Y. Shi, T. Korakianitis, and C. Bowles, "Numerical simulation of cardiovascular dynamics with different types of VAD assistance," *Journal of Biomechanics*, vol. 40, no. 13, pp. 2919 – 2933, 2007.

[104] T. Korakianitis and Y. Shi, "Numerical comparison of hemodynamics with atrium to aorta and ventricular apex to aorta VAD support," *ASAIO Journal*, vol. 53, no. 5, pp. 537–548, 2007.

[105] E. Lim, S. Dokos, S. L. Cloherty, R. F. Salamonsen, D. G. Mason, J. A. Reizes, and N. H. Lovell, "Parameter-optimized model of cardiovascular-rotary blood pump

interactions," *IEEE Transactions on Biomedical Engineering*, vol. 57, pp. 254–266, FEB 2010. 33

[106] M. S. Olufsen, C. S. Peskin, W. Y. Kim, E. M. Pedersen, A. Nadim, and J. Larsen, "Numerical simulation and experimental validation of blood flow in arteries with structured-tree outflow conditions," *Annals of Biomedical Engineering*, vol. 28, pp. 1281–1299, 2000. 33

[107] H. Kim, K. Jansen, and C. Taylor, "Incorporating autoregulatory mechanisms of the cardiovascular system in three-dimensional finite element models of arterial blood flow," *Annals of Biomedical Engineering*, vol. 38, pp. 2314–2330, 2010. 45

[108] R. L. Spilker and C. A. Taylor, "Tuning multidomain hemodynamic simulations to match physiological measurements," *Annals of Biomedical Engineering*, vol. 38, no. 8, pp. 2635–2648, 2010.

[109] P. Blanco, J. Leiva, R. Feijóo, and G. Buscaglia, "Black-box decomposition approach for computational hemodynamics: One-dimensional models," *Computer Methods in Applied Mechanics and Engineering*, vol. 200, no. 13-16, pp. 1389 – 1405, 2011.

[110] M. Willemet, V. Lacroix, and E. Marchandise, "Inlet boundary conditions for blood flow simulations in truncated arterial networks," *Journal of Biomechanics*, vol. 44, no. 5, pp. 897 – 903, 2011. 33

[111] R. Mukkamala and D. Xu, "Continuous and less invasive central hemodynamic monitoring by blood pressure waveform analysis," *American Journal of Physiology-Heart and Circulatory Physiology*, vol. 299, no. 3, pp. H584–H599, 2010. 33, 59, 112, 128, 130

[112] A. Tsanas, J. Y. Goulermas, V. Vartela, D. Tsiapras, G. Theodorakis, A. C. Fisher, and P. Sfirakis, "The windkessel model revisited: A qualitative analysis of the cir-

culatory system," *Medical Engineering & Physics*, vol. 31, no. 5, pp. 581 – 588, 2009. 33, 35, 130

[113] M. D. Feldman, P. H. Pak, C. C. Wu, H. L. Haber, C. M. Heesch, J. D. Bergin, E. R. Powers, T. D. Cowart, W. Johnson, A. M. Feldman, and D. A. Kass, "Acute cardiovascular effects of OPC-18790 in patients with congestive heart failure : Time- and dose-dependence analysis based on pressure-volume relations," *Circulation*, vol. 93, no. 3, pp. 474–483, 1996. 34

[114] G. J. Langewouters, K. H. Wesseling, and W. J. A. Goedrd, "The static elastic properties of 45 human thoracic and 20 abdominal aortas in vitro and the parameters of a new model," *Journal of Biomechanics*, vol. 17, no. 6, pp. 425 – 435, 1984. 34

[115] S. G. Shroff, J. S. Janicki, and K. T. Weber, "Evidence and quantitation of left ventricular systolic resistance," *American Journal of Physiology —Heart and Circulation Physiology*, vol. 249, no. 2, pp. H358–370, 1985. 34

[116] T. E. Claessens, D. Georgakopoulos, M. Afanasyeva, S. J. Vermeersch, H. D. Millar, N. Stergiopulos, N. Westerhof, P. R. Verdonck, and P. Segers, "Nonlinear isochrones in murine left ventricular pressure-volume loops: how well does the time-varying elastance concept hold?," *American Journal of Physiology —Heart and Circulation Physiology*, vol. 290, no. 4, pp. H1474–1483, 2006. 34

[117] K. B. Campbell, A. M. Simpson, S. G. Campbell, H. L. Granzier, and B. K. Slinker, "Dynamic left ventricular elastance: a model for integrating cardiac muscle contraction into ventricular pressure-volume relationships," *Journal of Applied Physiology*, vol. 104, no. 4, pp. 958–975, 2008. 34

[118] J.-W. Lankhaar, F. A. Rövekamp, P. Steendijk, B. E. Westerhof, T. Kind, A. Vonk-Noordegraaf, and N. Westerhof, "Modeling the instantaneous pressure-volume relation of the left ventricle: A comparison of six models," *Annals of Biomedical Engineering*, vol. 37, pp. 1710–1726, 2009. 34, 70

[119] H. Senzaki, C.-H. Chen, and D. A. Kass, “Single-beat estimation of end-systolic pressure-volume relation in humans: A new method with the potential for noninvasive application,” *Circulation*, vol. 94, no. 10, pp. 2497–2506, 1996. 34

[120] S. Patrick, S. Paul, S. Nikos, and W. Nico, “Predicting systolic and diastolic aortic blood pressure and stroke volume in the intact sheep,” *Journal of Biomechanics*, vol. 34, no. 1, pp. 41 – 50, 2001.

[121] N. Westerhof, N. Stergiopulos, and M. Noble, *Snapshots of Hemodynamics: An Aid for Clinical Research and Graduate Education*, vol. 18. Springer US, 2005. 34

[122] T. Cochrane, “Simple model of circulatory system dynamics including heart valve mechanics,” *Journal of Biomedical Engineering*, vol. 13, no. 4, pp. 335 – 340, 1991. 35

[123] T. Cochrane, C. J. Kenyon, P. V. Lawford, M. M. Black, J. B. Chambers, and D. C. Sprigings, “Validation of the orifice formula for estimating effective heart-valve opening area,” *Clinical Physics and Physiological Measurement*, vol. 12, no. 1, pp. 21–37, 1991. 35

[124] D. Garcia, P. J. C. Barenbrug, P. Pibarot, A. L. A. J. Dekker, F. H. van der Veen, J. G. Maessen, J. G. Dumesnil, and L. G. Durand, “A ventricular-vascular coupling model in presence of aortic stenosis,” *American Journal of Physiology - Heart and Circulation Physiology*, vol. 288, no. 4, pp. H1874–1884, 2005. 35

[125] J. Palladino and A. Noordergraaf, “Defining muscle elastance as a parameter,” in *Engineering in Medicine and Biology Society, 2007. EMBS 2007. 29th Annual International Conference of the IEEE*, pp. 5315 –5318, 22-26 2007. 35

[126] P. Segers, N. Stergiopulos, P. Verdonck, and N. Westerhof, “Mathematical model analysis of heart-arterial interaction in hypertension,” *Proceedings of the 23rd Annual International Conference of the IEEE Engineering in Medicine and Biology Society, Vols 1-4*, vol. 23, pp. 192–195, 2001. 35

[127] F. Bauer, M. Jones, T. Shiota, M. Firstenberg, X. Jian, H. Tsujino, J. Yong, M. Sitges, L. Cardon, A. Zetts, and J. Thomas, "Left ventricular outflow tract mean systolic acceleration as a surrogatefor the slope of the left ventricular end-systolic pressure-volume relationship," *Journal of the American College of Cardiology*, vol. 40, no. 7, pp. 1320 – 1327, 2002. 35, 49

[128] J. Werner, D. Böhringer, and M. Hexamer, "Simulation and Prediction of Cardiotherapeutical Phenomena from a Pulsatile Model Coupled to the Guyton Circulation Model," *IEEE Transaction on Biomedical Engineering*, vol. 49, no. 5, pp. 430–439, 2002. 35

[129] E. Lanzarone, P. Liani, G. Baselli, and M. Costantino, "Model of arterial tree and peripheral control for the study of physiological and assisted circulation," *Medical Engineering & Physics*, vol. 29, no. 5, pp. 542 – 555, 2007. 35

[130] E. Lim, S. Dokos, S. L. Cloherty, R. F. Salamonsen, D. G. Mason, J. A. Reizes, and N. H. Lovell, "Parameter-optimized model of cardiovascular-rotary blood pump interactions," *IEEE Transactions on Biomedical Engineering*, vol. 57, no. 2, pp. 254–266, 2010.

[131] E. Lim, A.-H. H. Alomari, A. V. Savkin, S. Dokos, J. F. Fraser, D. L. Timms, D. G. Mason, and N. H. Lovell, "A method for control of an implantable rotary blood pump for heart failure patients using noninvasive measurements," *Artificial Organs*, vol. 35, no. 8, 2011. 35

[132] T. Korakianitis and Y. Shi, "A concentrated parameter model for the human cardiovascular system including heart valve dynamics and atrioventricular interaction," *Medical Engineering & Physics*, vol. 28, pp. 613–628, July 2006. 36, 37, 39

[133] T. Korakianitis and Y. Shi, "Effects of atrial contraction, atrioventricular interaction, and heart valve dynamics on human cardiovascular system response," *Medical Engineering & Physics*, vol. 28, pp. 762–779, August 2006.

[134] T. Korakianitis and Y. Shi, “Numerical simulation of cardiovascular dynamics with healthy and diseased heart valves,” *Journal of Biomechanics*, vol. 39, pp. 1964–1982, August 2006.

[135] Y. Shi and T. Korakianitis, “Numerical simulation of cardiovascular dynamics with left heart failure and in-series pulsatile ventricular assist device,” *Artificial Organs*, vol. 30, pp. 929–948, December 2006.

[136] T. Korakianitis and Y. Shi, “Numerical comparison of hemodynamics with atrium to aorta and ventricular apex to aorta VAD support,” *ASAIO Journal*, vol. 53, pp. 537–548, September/October 2007.

[137] Y. Shi, T. Korakianitis, and C. Bowles, “Numerical simulation of cardiovascular dynamics with different types of VAD assistance,” *Journal of Biomechanics*, vol. 40, pp. 2919–2933, October 2007. 36, 37, 39

[138] J. She, M. Li, L. Huan, and Y. Yu, “Dynamic characteristics of prosthetic heart valves,” *Medical Engineering & Physics*, vol. 17, no. 4, pp. 273 – 281, 1995. 38, 39, 126

[139] F. Luca, A. Quarteroni, and A. Veneziani, *Cardiovascular Mathematics: Modeling and simulation of the circulatory system*. Springer, 2009. 39

[140] E. Sandblom and M. Axelsson, “The venous circulation: A piscine perspective,” *Comparative Biochemistry and Physiology a-Molecular & Integrative Physiology*, vol. 148, no. 4, pp. 785–801, 2007. xii, 43

[141] T. Heldt, E. Shim, R. Kamm, and R. Mark, “Computational modeling of cardiovascular response to orthostatic stress,” *Journal of Applied Physiology*, vol. 92, pp. 1239–1254, 2002. xii, 43, 45, 46, 49

[142] E. B. Shim, H. M. Jun, C. H. Leem, S. Matusuoka, and A. Noma, “A new integrated method for analyzing heart mechanics using a cell-hemodynamics-

autonomic nerve control coupled model of the cardiovascular system," *Progress in Biophysics & Molecular Biology*, vol. 96, no. 1-3, pp. 44–59, 2008. xii, 43, 45

[143] T. Heldt, *Computational Models of Cardiovascular Response to Orthostatic Stress*. PhD thesis, Massachusetts Institute of Technology, 2004. 43, 60, 70

[144] A. C. Guyton, "Determination of cardiac output by equating venous return curves with cardiac response curves," *Physiological reviews*, vol. 35, no. 1, pp. 123–9, 1955. xii, 44

[145] M. J. Davis and M. A. Hill, "Signaling mechanisms underlying the vascular myogenic response," *Physiological Reviews*, vol. 79, no. 2, pp. 387–423, 1999. 45

[146] D. M. Bers, "Cardiac excitation-contraction coupling," *Nature*, vol. 415, no. 6868, pp. 198–205, 2002. 45

[147] K. Lu, J. Clark, Jr, F. GhorBel, D. Ware, and A. Bidani, "A human cardiopulmonary system model applied to the analysis of the valsalva maneuver," *American Journal of Physiology —Heart and Circulation Physiology*, vol. 281, pp. H2661–H2679, 2001. 45, 49

[148] P. Ataee, G. A. Dumont, W. T. Boyce, and IEEE, "Baroreflex modeling in the genesis of stress reactivity using sigmoidal characteristic," in *American Control Conference*, pp. 3566–3571, 2010. 45

[149] A. C. Guyton, H. J. Granger, and T. G. Coleman, "Circulation —overall regulation," *Annual Review of Physiology*, vol. 34, pp. 13–44, 1972. 45

[150] T. E. Jackson, A. C. Guyton, and J. E. Hall, "Transient response of glomerular-filtration rate and renal blood flow to step changes in arterial pressure," *American Journal of Physiology*, vol. 233, no. 5, pp. F396–F402, 1977.

[151] J. P. Gilmore, K. G. Cornish, S. D. Rogers, and W. L. Joyner, "Direct evidence for

myogenic auto-regulation of the renal micro-circulation in the hamster," *Circulation Research*, vol. 47, no. 2, pp. 226–230, 1980.

[152] M. Shahin and S. Maka, "A transfer function method for the assessment of nervous system modulation of long term dynamics of blood pressure," in *Communication Control and Computing Technologies (ICCCT), 2010 IEEE International Conference on*, pp. 560 –564, oct. 2010. 45

[153] R. Bailon, G. Laouini, C. Grao, M. Orini, P. Laguna, and O. Meste, "The integral pulse frequency modulation model with time-varying threshold: Application to heart rate variability analysis during exercise stress testing," *IEEE Transactions on Biomedical Engineering*, vol. 58, no. 3, pp. 642–652, 2011. 47

[154] M. Takeuchi, Y. Igarashi, S. Tomimoto, M. Odake, T. Hayashi, T. Tsukamoto, K. Hata, H. Takaoka, and H. Fukuzaki, "Single-beat estimation of the slope of the end-systolic pressure volume relation in the human left-ventricle," *Circulation*, vol. 83, no. 1, pp. 202–212, 1991. 49

[155] S. Nakatani, M. Garcia, M. Firstenberg, L. Rodriguez, R. Grimm, N. Greenberg, P. McCarthy, P. Vandervoort, and J. Thomas, "Noninvasive assessment of left atrial maximum dP/dt by a combination of transmitral and pulmonary venous flow," *Journal of the American College of Cardiology*, vol. 34, no. 3, pp. 795 – 801, 1999.

[156] J. Thomas, J. Zhou, N. Greenberg, G. Bibawy, P. McCarthy, and P. VanDervoort, "Physical and physiological determinants of pulmonary venous flow: Numerical analysis," *American Journal of Physiology —Heart and Circulation Physiology*, vol. 272, no. 41, pp. H2453–H2465, 1997.

[157] D. R. Hose, A. J. Narracott, J. M. T. Penrose, D. Baguley, I. P. Jones, and P. V. Lawford, "Fundamental mechanics of aortic heart valve closure," *Journal of Biomechanics*, vol. 39, no. 5, pp. 958–967, 2006. 52

[158] F. Liang, S. Takagi, R. Himeno, and H. Liu, “Biomechanical characterization of ventricular-arterial coupling during aging: A multi-scale model study,” *Journal of Biomechanics*, vol. 42, no. 6, pp. 692 – 704, 2009. 49, 82

[159] A. Rahideh, T. Korakianitis, P. Ruiz, T. Keeble, and M. T. Rothman, “Optimal brushless DC motor design using genetic algorithms,” *Journal of Magnetism and Magnetic Materials*, vol. 322, pp. 3680–3687, Nov 2010. xiii, 51, 52, 53

[160] D. A. Coley, *An Introduction to Genetic Algorithms for Scientists and Engineers*. Covent Garden, London: World Scientific, 2003. 52, 53

[161] P. Segers, P. Verdonck, Y. Deryck, S. Brimioulle, R. Naeije, S. Carlier, and N. Stergiopulos, “Pulse pressure method and the area method for the estimation of total arterial compliance in dogs: Sensitivity to wave reflection intensity,” *Annals of Biomedical Engineering*, vol. 27, pp. 480–485, 1999. 52

[162] C. Quick, D. Berger, D. Hettrick, and A. Noordergraaf, “True arterial system compliance estimated from apparent arterial compliance,” *Annals of Biomedical Engineering*, vol. 28, pp. 291–301, 2000.

[163] E. Kung, A. Les, C. Figueroa, F. Medina, K. Arcaute, R. Wicker, M. McConnell, and C. Taylor, “In vitro validation of finite element analysis of blood flow in deformable models,” *Annals of Biomedical Engineering*, vol. 39, pp. 1947–1960, 2011. 52

[164] M. Westwood, L. Anderson, D. Firmin, P. Gatehouse, C. Charrier, B. Wonke, and D. Pennell, “A single breath-hold multiecho T2* cardiovascular magnetic resonance technique for diagnosis of myocardial iron overload,” *Journal of Magnetic Resonance Imaging*, vol. 18, no. 1, pp. 33–39, 2003. 52

[165] G. F. Uler, O. A. Mohammed, and C. S. Koh, “Utilizing genetic algorithms for the optimal-design of electromagnetic devices,” *IEEE Transactions on Magnetics*, vol. 30, no. 6, pp. 4296–4298, 1994. 53

[166] M. Longmore, I. Wilkinson, and E. Török, *Oxford Handbook of Clinical Medicine, fifth edition.* Oxford University Press, 2001. 70

[167] G. Schillaci, L. Pasqualini, P. Verdecchia, G. Vaudo, S. Marchesi, C. Porcellati, G. de Simone, and E. Mannarino, "Prognostic significance of left ventricular diastolic dysfunction in essential hypertension," *Journal of the American College of Cardiology*, vol. 39, no. 12, pp. 2005 – 2011, 2002. 70, 114

[168] S. J. Denardo, R. Nandyala, G. L. Freeman, G. L. Pierce, and W. W. Nichols, "Pulse wave analysis of the aortic pressure waveform in severe left ventricular systolic dysfunction," *Circulation-Heart Failure*, vol. 3, no. 1, pp. 149–156, 2010. xiv, 71, 72, 73, 125, 126

[169] K. Berenji, M. H. Drazner, B. A. Rothermel, and J. A. Hill, "Does load-induced ventricular hypertrophy progress to systolic heart failure?," *American Journal of Physiology —Heart and Circulatory Physiology*, vol. 289, no. 1, pp. H8–H16, 2005. 71

[170] N. Moorjani, S. Westaby, J. Narula, P. A. Catarino, R. Brittin, T. J. Kemp, N. Narula, and P. H. Sugden, "Effects of left ventricular volume overload on mitochondrial and death-receptor mediated apoptotic pathways in the transition to heart failure," *The American Journal of Cardiology*, vol. 103, no. 9, pp. 1261 – 1268, 2009. 71

[171] S. R. Houser, V. P. III, and J. Weisser, "Abnormalities of calcium cycling in the hypertrophied and failing heart," *Journal of Molecular and Cellular Cardiology*, vol. 32, no. 9, pp. 1595 – 1607, 2000. 71

[172] P. Ruiz, M. A. Rezaienia, A. Rahideh, T. R. Keeble, M. T. Rothman, and T. Korakianitis, "In vitro cardiovascular system emulator (bioreactor) for the simulation of normal and diseased conditions with and without mechanical circulatory support," *Artificial Organs*, vol. 37, no. 6, pp. 549–560, 2013. 71

[173] L. Leverett, J. Hellums, C. Alfrey, and E. Lynch, "Red blood cell damage by shear stress," *Biophysical Journal*, vol. 12, no. 3, pp. 257 – 273, 1972. 79, 105

[174] A. J. Stepanoff, *Centrifugal and Axial Flow Pumps: Theory, Design, and Application*. New York: John Wiley & Sons, Inc., second edition ed., 1962. xiv, 80, 81, 90

[175] A. Kovaáts, *Design and Performance of Centrifugal and Axial Flow Pumps and Compressors*. Pergamon Press, 1964. 80, 81

[176] J. Tuzson, *Centrifugal Pump Design*. Wiley-Interscience, 2000. xiv, 80, 84, 85, 96

[177] K. Srinivasan, *Rotodynamic Pumps (Centrifugal and Axial)*. New Delhi: New Age International Publishers, 2008. 81, 86, 87, 88

[178] A. R. Curtas, H. G. Wood, P. E. Allaire, J. C. McDaniel, S. W. Day, and D. B. Olsen, "Computational fluid dynamics modeling of impeller designs for the HeartQuest left ventricular assist device," *ASAIO Journal*, vol. 48, no. 5, pp. 552–561, 2002. 84

[179] W.-G. Li, "Effects of viscosity of fluids on centrifugal pump performance and flow pattern in the impeller," *International Journal of Heat and Fluid Flow*, vol. 21, no. 2, pp. 207 – 212, 2000. 84

[180] D. Timms, *Design, development and evaluation of centrifugal ventricular assist devices*. PhD thesis, Queensland University of Technology, Brisbane, Queensland, Australia, 2005. 84

[181] T. Miloş, "CAD procedure for blade design of centrifugal pump impeller ussing conformal mapping method," in *5th National Conference of Romanian Hydropower Engineers*, vol. 70 of *d*, (Bucharest), pp. 213–220, May 2008. xiv, 88, 89

[182] M. A. Fernández, L. Formagia, J.-F. Gerbeau, and A. Quartenori, *Cardiovascular Mathematics: Modeling and simulation of the circulatory system*, vol. 1, ch. The derivation of the equations for fluids and structure, pp. 77–121. Milano: Srpringer, 2009. 90

[183] J. D. Anderson Jr, *Computational Fluid Dynamics: The Basics with Applications*. New York: McGraw-Hill, Inc., 1995. xv, 92

[184] F. M. White, *Fluid Mechanics*. New York: McGraw-Hill, fifth edition ed., 2005. xv, 95

[185] M. Schobeiri, *Turbomachinery Flow Physics and Dynamic Performance*. Berlin: Springer, 2005. 96

[186] ANSYS, Inc, Canonsburg, PA, *ANSYS CFX-Solver Theory Guide*, release 12.1 ed., November 2009. 96, 97

[187] S. P. Sutera, "Flow-induced trauma to blood cells.," *Circulation Research*, vol. 41, no. 1, pp. 2–8, 1977. 105

[188] R. Paul, J. Apel, S. Klaus, F. Schügner, P. Schwindke, and H. Reul, "Shear stress related blood damage in laminar couette flow," *Artificial Organs*, vol. 27, no. 6, pp. 517–529, 2003. 105

[189] H. Nishida, K. Yamazaki, M. Endo, H. Koyanaghi, K. Tajima, K. Higuchi, and T. Mori, "Development of the implantable centrifugal right ventricular assist device: combined use with LVAD as an alternative to the total artificial heart," *Journal of Congestive Heart Failure and Circulatory Support*, vol. 1, no. 4, pp. 213–217, 2001. 106

[190] P. L. DiGiorgi, V. Rao, Y. Naka, and M. C. Oz, "Which patient, which pump?," *Journal of Heart and Lung Transplantation*, vol. 22, no. 3, pp. 221–235, 2003. 106

[191] D. Timms, M. Hayne, K. McNeil, and A. Galbraith, "A complete mock circulation loop for the evaluation of left, right, and biventricular assist devices," *Artificial Organs*, vol. 29, no. 7, pp. 564–572, 2005. 107

[192] Y. Liu, P. J. Allaire, H. Wood, and D. Olsen, "Design and initial testing of a mock human circulatory loop for left ventricular assist device performance testing," *Artificial Organs*, vol. 29, no. 4, pp. 341–345, 2005. 107

[193] G. M. Pantalos, C. Ionan, S. C. Koenig, K. J. Gillars, T. Horrell, S. Sahetya, J. Colyer, and L. A. Gray, "Expanded pediatric cardiovascular simulator for research and training," *ASAIO Journal*, vol. 56, no. 1, pp. 67–72, 2010. 111

[194] K. Wachtell, V. Palmieri, E. Gerdts, J. N. Bella, G. P. Aurigemma, V. Papademetriou, B. Dahlöf, T. Aalto, H. Ibsen, J. E. Rokkedal, and R. B. Devereux, "Prognostic significance of left ventricular diastolic dysfunction in patients with left ventricular hypertrophy and systemic hypertension (the LIFE Study)," *The American Journal of Cardiology*, vol. 106, no. 7, pp. 999 – 1005, 2010. 114

[195] M. T. Lonnebakken, E. Gerdts, K. Boman, K. Wachtell, B. Dahlof, and R. B. Devereux, "In-treatment stroke volume predicts cardiovascular risk in hypertension," *Journal of Hypertension*, vol. 29, no. 8, pp. 1508–1514, 2011. 114

[196] A. Chobanian, G. Bakris, H. Black, W. Cushman, L. Green, J. Izzo, Jr, D. Jones, B. Materson, S. Oparil, J. Wright, Jr, and E. Roccella, "The seventh report of the joint national committee on prevention, detection, evaluation, and treatment of high blood pressure: The JNC 7 report," *Journal of the American Medical Association*, vol. 289, no. 219, pp. 2560 – 2571, 2003. 114

[197] R.-H. Zhou, A. E. Vendrov, I. Tchivilev, X.-L. Niu, K. C. Molnar, M. Rojas, J. D. Carter, H. Tong, G. A. Stouffer, N. R. Madamanchi, and M. S. Runge, "Mitochondrial oxidative stress in aortic stiffening with age the role of smooth muscle

cell function," *Arteriosclerosis thrombosis and vascular biology*, vol. 32, no. 3, pp. 745–755, 2012. 114

[198] O. Reitan, S. Steen, and H. Ohlin, "Hemodynamic effects of a new percutaneous circulatory support device in a left ventricular failure model," *ASAIO Journal*, vol. 49, pp. 731–736, 2003. 117, 126

[199] O. Reitan, H. Ohlin, B. Peterzen, H. Granfeldt, S. Steen, and H. Emanuelsson, "Initial tests with a new cardiac assist device," *ASAIO Journal*, vol. 45, pp. 317–321, 1999.

[200] O. Reitan, J. Sternby, and H. Ohlin, "Hydrodynamic properties of a new percutaneous intra-aortic axial flow pump," *ASAIO Journal*, vol. 46, pp. 323–329, 2000. 117, 126

[201] M. E. Safar, J. Blacher, and P. Jankowski, "Arterial stiffness, pulse pressure, and cardiovascular disease-is it possible to break the vicious circle?," *Atherosclerosis*, vol. 218, no. 2, pp. 263–271, 2011. xvii, 125, 126

[202] H. Y. Lin, D. Freed, T. W. R. Lee, R. C. Arora, A. Ali, W. Almoustadi, B. Xiang, F. Wang, S. Large, S. B. King, B. Tomanek, and G. H. Tian, "Quantitative assessment of cardiac output and left ventricular function by noninvasive phase-contrast and cine mri: Validation study with invasive pressure-volume loop analysis in a swine model," *Journal of Magnetic Resonance Imaging*, vol. 34, no. 1, pp. 203–210, 2011. 130

[203] P. V. Lawford, A. V. Narracott, K. McCormack, J. Bisbal, C. Martin, B. Brook, M. Zachariou, P. Kohl, K. Fletcher, and V. Diaz-Zuccarini, "Virtual physiological human: training challenges," *Philosophical Transactions of the Royal Society a-Mathematical Physical and Engineering Sciences*, vol. 368, no. 1921, pp. 2841–2851, 2010. 130